

THESE

présentée

A LA FACULTE DES SCIENCES DE L'UNIVERSITE DE ROUEN

en vue de l'obtention du Doctorat

Discipline : Physique

Spécialité : Energétique

par

Feng XU

**Diffusion d'un Faisceau Quelconque par un Sphéroïde et
Mesure en Ligne de la Vapeur Humide par l'Extinction
Spectrale de la Lumière**

Soutenue le 13 Mars 2007

Directeurs de thèse

Maître de Conférences **Kuanfang REN**

CNRS UMR 6614 – CORIA

Université de Rouen

Professeur **Xiaoshu CAI**

IPTFM

Université des Sciences et
Technologies de Shanghai, Chine.

Membres du jury

Rapporteurs

Xiang'e HAN

Professeur, Université de Xidian, Chine.

James A. LOCK

Professeur, Université de Cleveland, Etats-Unis.

Cameron TROPEA

Professeur, Université Technique de Darmstadt, Allemagne.

Examineurs

Xiaoshu CAI

Professeur, Université des Sciences et Technologies de
Shanghai, Chine.

Gérard GOUESBET

Professeur, Institut National des Sciences Appliquées de Rouen
(INSA de Rouen), France.

Gérard GREHAN

Directeur de Recherche au Centre National de la Recherche
Scientifique (CNRS), France.

Cafer OZKUL

Professeur (Doyen), Université de Rouen, France.

Kuanfang REN

Maître de Conférences, Université de Rouen, France.

Invité

Jean-marc DOREY

Ingénieur de Recherche, Electricité de France, R&D, France.

THESIS

submitted to

THE FACULTY OF SCIENCES OF ROUEN UNIVERSITY

for the degree of

Doctor of Philosophy

Discipline : Physics Speciality : Energy

by

Feng XU

Shaped Beam Scattering by a Spheroid and Online Wet Steam Measurement by Using Spectral Light Extinction Method

Defensed on 13 March 2007

Supervisors

Associate Professor **Kuan Fang REN**

CNRS UMR 6614 – CORIA

Rouen University

Professor **Xiao Shu CAI**

IPTFM

University of Shanghai for Science and
Technology

Members of Defence Committee

Reviewers

Xiang'e HAN

Professor, Xidian University, China.

James A. LOCK

Professor, Cleveland State University, USA.

Cameron TROPEA

Professor, Darmstadt University of Technology, Germany.

Examinators

Xiaoshu CAI

Professor, University of Shanghai for Science and
Technology, China.

Gérard GOUESBET

Professor, National Institute of Applied Sciences of Rouen
(INSA of Rouen), France.

Gérard GREHAN

Director of Research in National Center for Scientific Research
(CNRS), France.

Cafer OZKUL

Professor (Dean), Rouen University, France.

Kuanfang REN

Associate Professor, Rouen University, France.

Invited

Jean-marc DOREY

Engineer of Research, Electricity of France, R&D, France.

To my mother & father

To Judy

Acknowledgements

This thesis is the fruit of Sino-French collaboration between the two laboratories UMR 6614/CORIA¹ (CNRS²-Université et INSA³ de Rouen, France) and IPTFM⁴ (University of Shanghai for Science and Technology, China).

I am greatly indebted to my supervisor, Dr. Kuanfang REN, for his excellent guidance, unyielding support and enthusiastic encouragement during my Ph.D studies. His creative ideas and excellent insight into the physical phenomenon have brought me to the higher level of thinking during the research.

I also would like to express sincere gratitude to my co-supervisor, Professor Xiaoshu CAI, for his encouragement and supports. The confidence and freedom he gave me has boosted all my interests in light scattering studies since I followed him for research in Oct. 2001.

I sincerely wish to express my special gratitude to Mr. Jean-marc DOREY, Engineer of Research in EDF R&D, for his support for my thesis work and the organization of joint projects for online wet steam measurement.

I'm so grateful to Professor Gérard GOUESBET, for his appreciation of my thesis work and his carefulness and patience in helping me correct the manuscripts of the journal papers and the thesis. I also thank him for his kindness in helping me invite Professor James A. Lock to be on the jury and review the thesis.

Thanks are also due to the reviewers, Professor Xiang'e HAN, Professor James A. LOCK, and Professor Cameron TROPEA for many useful suggestions regarding the text. I would express my respect for them for their high scientific competence, their carefulness in reading the manuscript, and their very precious comments. The manuscript has been revised according to their remarks. Special respects are shown to Professor James A. LOCK, a well known scientist in the field of light scattering theory, to accept to review my thesis and come to my defence from USA, making me feel quite honored. Thanks are also forwarded to Professor & Dean Cafer OZKUL, and Dr. Gérard GREHAN for their serving on the examination committee.

1. Complexe de Recherche Interprofessionnel en Aérotherochimie;
2. Centre National de la Recherche Scientifique;
3. Institut National des Sciences Appliquées;
4. Institute of Particle and Two-phase Flow Measurement.

I would like to acknowledge Ms. Nathalie FOUET, the secretary in library of CORIA, for helping me index a great number of references for my research. Without her warmhearted aids, I can hardly work so efficiently in a foreign country during a relatively short time, two years.

Most of all, I would like to thank my family for their tremendous sacrifices, unwavering support and encouragement throughout, which have always been my greatest source of strength and inspiration. Here I should also be grateful to a lady in Australia, Ms. Judy, for all the feelings she has communicated to me in the past two years.

Finally, I acknowledge the supports for this thesis from the French Embassy in China (Project 4B2-007), EDF, the Natural Science Foundation of China (Project 50336050), and Ministry of Science and Technology of China (“863” Program 2006AA03Z349). And I would like to express my thanks to Ms. BEAULIEU of CROUS of Haute-Normandie, for her assistance during my stay in France.

Résumé

La théorie de Lorenz-Mie généralisée (TLMG) est développée pour la description de la diffusion d'un faisceau incident quelconque par un sphéroïde homogène. Les expressions analytiques d'amplitude des champs diffusés, des sections efficaces de diffusion, d'absorption, et d'extinction, de pression de radiation sont obtenues et des calculs numériques sont présentés. Pour enlever la contrainte de la TLMG dans les calculs numériques pour un sphéroïde de grande taille, l'optique géométrique classique est étendu au cas d'un faisceau gaussien diffusé par un sphéroïde. En ce qui concerne l'expérience, un système optique sur la base de l'extinction spectrale de la lumière est développé et appliqué à la mesure de vapeur humide dans une turbine à EDF. L'influence de la diffusion multiple sur le spectre d'extinction et celle de la diffusion des particules situés dans le bord de zone de la mesure sont analysées en utilisant le modèle de Monte Carlo.

Mots clés : Diffusion de la lumière, Théorie de Lorenz-Mie, Sphéroïde, Optique géométrique, Pression de radiation, Extinction de la lumière, Métrologie optique, Vapeur humide

Abstract

The generalized Lorenz-Mie theory (GLMT) is developed to describe the interaction between an arbitrary shaped beam and a homogeneous spheroid. Analytical expressions of the amplitudes of the scattering fields, the scattering, absorption and extinction crosssections, and the radiation pressure are obtained. The numerical results are also presented. To overcome the drawback of the GLMT in numerical calculation for a large spheroid, the classical geometrical optics is extended to the case of Gaussian beam scattering by a spheroid. In experimental aspect, an optical system on the basis of the spectral light extinction method is developed and used for wet steam measurement in EDF. The influences of the scattering by the particles in the edge measurement zone and of the multiple scattering on the extinction spectrum are analyzed by using the Monte Carlo method.

Key words : Light Scattering, Lorenz-Mie theory, Spheroid, Geometrical optics, Radiation pressure, Light extinction, Optical particle sizing, Wet steam

Table of Contents

List of Symbols and Abbreviations	1
General Introduction	11
Part I. Shaped Beam Scattering by a Homogeneous Spheroid	
1. Introduction	
1.1 Shaped beam.....	16
1.2 Spheroid	16
1.3 Rigorous theory.....	17
1.4 Geometrical optics	18
1.5 Organization of Part I.....	20
2. Generalized Lorenz-Mie Theory for Shaped Beam Scattering by a Spheroid	
2.1 Theory	21
2.1.1 Beam expansion in the spherical coordinates.....	22
2.1.2 Far-field scattering	25
2.1.3 Extinction and scattering crosssections.....	26
2.1.4 Radiation pressure	28
2.2 Beam shape coefficients for an arbitrary shaped beam.....	31
2.2.1 Spherical beam shape coefficients	31
2.2.2 Spheroidal beam shape coefficients	33
2.2.3 Applicability of the classical localization principle	36
2.2.4 Field reconstruction from spheroidal beam shape coefficients.....	38
2.2.5 Validation of beam shape coefficients	40
2.3 Special cases.....	45
2.3.1 Plane wave incidence	45
2.3.2 Spherical particle scattering	47
2.4 Numerical results.....	48
2.4.1 Far-field scattering	49

2.4.2	Scattering and extinction crosssections.....	54
2.4.3	Radiation Pressure.....	58
2.5	Conclusion.....	72
3.	Geometrical Optics Approximation of Gaussian Beam Scattering by a Spheroid	
3.1	Gaussian beam scattering by a sphere.....	74
3.1.1	Extension of geometrical optics approximation.....	75
3.1.2	Numerical results and discussion.....	81
3.1.3	Evaluation of surface wave influence.....	91
3.2	Gaussian beam scattering by a spheroid.....	94
3.2.1	Description of the method.....	96
3.2.2	Numerical results and discussion.....	102
3.3	Conclusion.....	113
Part II.	Online Wet Steam Measurement by Using Light Extinction Method	
4.	Introduction	
4.1	Development of light extinction method.....	117
4.2	Influence of some factors.....	124
4.2.1	Refractive index.....	124
4.2.2	Multiple scattering, dependent scattering, and forward scattering.....	125
4.2.3	Non-sphericity of the particle.....	127
4.3	Inversion algorithms.....	127
4.4	Organization of Part II.....	124
5.	Spectral Light Extinction Method	
5.1	Basic principle.....	125
5.2	Inversion algorithms.....	129
5.2.1	Phillips-Twomey-NNLS algorithm.....	130
5.2.2	Optimized regularization technique.....	131
5.3	Presentation of the software TURACE 5.0.....	133
5.4	Numerical investigation of inversion algorithms.....	134
5.4.1	Rosin-Rammler distribution.....	134

5.4.2	Inversion without measurement errors	135
5.4.3	Inversion with measurement errors	140
5.5	Conclusion.....	147
6.	Sensibility Analysis of Measurement System	
6.1	Stability of the light source	148
6.1.1	Calibration of the system.....	150
6.1.2	Mean standart deviation of intensity	152
6.1.3	Measurement results.....	154
6.2	Sensibility of extinction spectrum to variation of concentration	158
6.2.1	Measurement of spectrum variation of water and milk emulsion	159
6.2.2	Measurement of concentration variation of standard polystyrene particles	164
6.3	Size and concentration measurement of standard polystyrene particles	168
6.3.1	Experimental setup.....	168
6.3.2	Measurements.....	169
6.4	Conclusion.....	176
7.	Wet Steam Measurement	
7.1	Wetness	178
7.2	Experimental setup.....	179
7.3	Measurements.....	181
7.3	Conclusion.....	187
8.	Particle Sizing in High Concentration	
8.1	Monte Carlo method.....	188
8.2	Numerical studies	189
8.2.1	Evaluation of multiple scattering	189
8.2.2	Influence of scattering from particles in edge zone	190
8.2.3	Influence of multiple scattering.....	197
8.3	Experimental studies	202
8.3.1	Polystyrene particles.....	202
8.3.2	Wet steam.....	206
8.4	Conclusion.....	208

9. Conclusions and Perspectives

9.1 Theory209

9.2 Experiment210

Appendices

Appendix A Computation of eigenvalues λ_{mn} and expansion coefficients d_r^{mn} 212

Appendix B Spheroidal vector wave functions214

Appendix C Orthogonality relations for some functions216

Appendix D Spherical vector wave functions219

Appendix E Electromagnetic fields of an astigmatic elliptical Gaussian beam.....221

Appendix F Presentation of the Software TURACE 5.0.....222

Appendix G Characteristics of the spectrometers226

Appendix H Characteristics of the light sources227

References228

Publication List of the Author.....242

中文摘要.....245

List of Symbols and Abbreviations

Roman Symbols

a	:	albedo factor; semimajor axis length of the spheroid
a_n	:	Mie coefficients;
A	:	coefficient matrix;
A_n^m	:	coefficients describing the scattered fields;
b	:	semiminor axis length of the spheroid;
b_n	:	Mie coefficients;
B_n^m	:	coefficients describing the scattered fields;
B_w	:	boxcar of wavelength;
c	:	size parameter of the spheroid; weight coefficients multiplied with the B-splines;
c_m	:	light speed in the medium;
C	:	constant equal to $-3Z/2$;
C_n^m	:	coefficients describing the internal fields;
C_n^{pw}	:	plane wave term;
C_{abs}	:	absorption crosssection;
C_{ext}	:	extinction crosssection;
C_{sca}	:	scattering crosssection;
C_n	:	number concentration of particles;
$C_{pr, x}$:	radiation pressure crosssection in the x direction;
$C_{pr, y}$:	radiation pressure crosssection in the y direction;
$C_{pr, z}$:	radiation pressure crosssection in the z direction;
C_v	:	volume concentration of particles;
\bar{C}_v	:	mean volume concentration;
d	:	diameter of the spherical particle;
d_r^{mn}	:	expansion coefficients of the spheroidal angular functions;
D	:	diameter of the particle;
D_1	:	diameter of the incident light bundle;

D_2	:	diameter of the detector;
D_3	:	opening diameter of the diaphragm;
D_{32}	:	Sauter mean diameter;
$D_{v_{50}}$:	volume mean diameter;
$D_{n_{50}}$:	number mean diameter;
D_G	:	divergence factor;
D_n^m	:	coefficients describing the internal fields;
\bar{D}_{32}	:	mean inversed Sauter mean diameters;
ΔD	:	length of diameter interval;
\bar{D}	:	characteristic diameter of the Rosin-Rammler distribution;
E	:	extinction spectrum (ratio);
ΔE	:	deviation of the extinction;
\mathbf{E}	:	electric field;
f	:	semifocal length of the spheroid; focal length of the lens;
f_{mn}	:	beam shape coefficients of plane wave;
g_{mn}	:	beam shape coefficients of plane wave;
F	:	objective function for optimization;
F_x	:	x component of the propagation direction of a Gaussian ray;
F_y	:	y component of the propagation direction of a Gaussian ray;
F_z	:	z component of the propagation direction of a Gaussian ray;
g	:	asymmetry parameter;
$g_{n,TE}^m$:	spherical beam shape coefficients;
$g_{n,TM}^m$:	spherical beam shape coefficients;
$G_{n,TE}^m$:	spheroidal beam shape coefficients;
$G_{n,TM}^m$:	spheroidal beam shape coefficients;
H	:	smoothing matrix;
\mathbf{H}	:	magnetic field;
\mathbf{i}	:	unit vector in x direction;
I	:	transmitted intensity;

	:	identity matrix;
I_0	:	incidence intensity;
I_M	:	intensity detected from channel Master;
I_S	:	intensity detected from channel Slave;
$I_{\text{trans.}}$:	transmitted intensity;
$\Delta I_{\text{diff.}}$:	diffused intensity;
\bar{I}	:	mean intensity;
\mathbf{j}	:	unit vector in y direction;
k	:	wavenumber;
J_{mn}^p	:	factor in analytical expressions of radiation pressure crosssection;
		order of the B -spline;
		order of the matrix;
K	:	distribution factor of the Rosin-Rammler distribution;
K_{mn}^p	:	factor in analytical expressions of radiation pressure crosssection;
\mathbf{k}	:	unit vectors in z direction;
k_0	:	wavenumber in free space;
L	:	distance from the diaphragm to the detector;
L_p	:	path of a ray undergoing $p-1$ internal reflections inside the particle;
L_{mn}^p	:	factor in analytical expressions of radiation pressure crosssection;
m_f	:	mass of the liquid phase of water;
m_g	:	mass of the vapor phase of water;
\mathbf{m}_{mn}	:	spherical vector wave functions;
\hat{m}	:	relative refractive index of the particle;
m_r	:	real part of the relative refractive index;
m_i	:	imaginary part of the relative refractive index;
\hat{m}_1	:	refractive index of the medium;
\hat{m}_Π	:	refractive index of the particle;
M_{mn}^p	:	factor in analytical expressions of radiation pressure crosssection;
\mathbf{M}_{mn}	:	Spheroidal vector wave functions;
$n(D)$:	normalized number frequency distribution;
N	:	number of the particles;

		number of modals of particle size distribution;
N_{mn}	:	normalization factor of d_r^{mn} ;
N_w	:	Number of wavelength;
$N(D)$:	number frequency distribution;
\mathbf{n}	:	unit vector outward normal;
\mathbf{n}_{mn}	:	spherical vector wave functions;
\mathbf{N}_{mn}	:	spheroidal vector wave functions;
$N_{j,k}$:	B -spline of order k with bearing interval $[D_j, D_{j+k}]$;
O_{mn}^p	:	factor in analytical expressions of radiation pressure crosssection;
O_P	:	particle's center;
O_B	:	beam's center;
O_{P-xyz}	:	Cartesian coordinate system of the particle;
O_{B-uvw}	:	Cartesian coordinate system of the beam;
$O_{P-u'v'w'}$:	Cartesian coordinate system of the beam with origin moved to O_P ;
p	:	order of a ray;
P_{mn}^p	:	factor in analytical expressions of radiation pressure crosssection;
P_{HG}	:	Henry-Greenstein phase function;
P_n^m	:	associated Legendre functions of the first kind;
q_1, q_2	:	random number;
Q_{mn}^p	:	factor in analytical expressions of radiation pressure crosssection;
Q_{ext}	:	extinction efficiency;
Q_{sca}	:	scattering efficiency;
r	:	radius of the spherical particle;
		projection radius of a sphere/spheroid along the z axis;
		polar spherical coordinate;
r_1, r_2	:	Fresnel reflection coefficients;
R	:	curvature radius of the wavefront;
R_{mn}^p	:	factor in analytical expressions of radiation pressure crosssection;
R_Q	:	coefficient of the extinction ratio;
R_s	:	distance from the observation point to the particle center;
R_{mn}	:	spheroidal radial functions of order m and degree n ;

S	:	a spherical surface;
S_{mn}^p	:	factor in analytical expressions of radiation pressure crosssection;
S_d	:	amplitude of the diffracted ray;
S_j	:	amplitude function;
S_{mn}	:	spheroidal angular functions of order m and degree n ;
S_G	:	initial amplitude of a Gaussian ray reaching the surface of the particle;
S_n	:	Sample number for averaging;
T	:	transmission spectrum (ratio);
T_0	:	initial transmittance ratio;
T_{mn}^p	:	factor in analytical expressions of radiation pressure crosssection;
T_I	:	integration time of acquisition;
ΔT	:	time interval of acquisition;
U	:	objective function of in Generalized Cross-Validation method;
U_{mn}^p	:	factor in analytical expressions of radiation pressure crosssection;
v_0	:	volume of the emulsion or suspension;
v_m	:	volume of protein molecules in the milk;
$v(D)$:	normalized volume frequency distribution;
$V(D)$:	volume frequency distribution;
V_{mn}^p	:	factor in analytical expressions of radiation pressure crosssection;
$V_a(D)$:	volume accumulation distribution;
w	:	local waist radius of the circular Gaussian beam;
W	:	E/C ;
w_0	:	waist radius of the circular Gaussian beam;
w_{0u}	:	waist radius of the elliptical Gaussian beam along the x axis;
w_{0v}	:	waist radius of the elliptical Gaussian beam along the y axis;
w_u	:	location of the beam waists along the u axis;
w_v	:	location of the beam waists along the v axis;
(x_0, y_0, z_0)	:	coordinates of the beam center O_B in the particle's coordinates O_P -xyz;
Y_T	:	theoretical wetness;
Y_M	:	measured wetness;
z_n	:	n th-order Hankel function of the first kind;

	:	n th-order Bessel function of the first kind;
z_R	:	Rayleigh length;
Z	:	length of the measurement zone.

Greek Symbols

α	:	dimensionless size parameter of the spherical particle;
β	:	angle between the z axis and the propagating direction of a Gaussian ray;
γ	:	Lagrange factor;
δ_r	:	relative deviation;
δ_a	:	absolute deviation;
$\varepsilon_1, \varepsilon_2$:	amplitude attenuation factors;
η	:	polar spheroidal coordinate;
θ	:	scattering angle;
		polar spherical coordinate;
Θ_{bd}	:	incidence angle of the beam;
Θ_{pl}	:	incidence angle of the plane wave;
θ_i	:	incidence angle of a ray;
θ_r	:	refraction angle;
θ_p	:	scattering angle for a ray of order p ;
θ'_p	:	deviation angle for a ray of order p ;
θ_{rg}	:	position of geometric rainbow of primary order for a spheroid;
$\Delta\theta_{rg}$:	deviation of the primary geometrical rainbow from a sphere for a spheroid;
$\theta_{rg, o}$:	position of geometric rainbow of primary order for a sphere;
θ_c	:	critical angle;
$\theta_{1/2}$:	half collection angle of the detector;
$\Delta\theta_1$:	solid angle;
$\Delta\theta_2$:	solid angle;
κ	:	aspect ratio;
λ	:	wavelength;

λ_0	:	wavelength in the vacuum;
λ_{mn}	:	eigenvalues of the differential equation with respect to R_{mn} and S_{mn} ;
μ_0	:	permeability of free space;
ξ	:	polar spheroidal coordinate;
	:	optical thickness;
ξ_p	:	attenuation factor due to the optical path;
π_n^m	:	generalized Legendre functions;
ρ_r	:	density ratio of the two phases of the water;
ρ_g	:	density of the vapor phase of the water;
ρ_f	:	density of the liquid phase of water;
σ	:	mean standard deviation of the average intensity;
σ_i	:	standard deviation of the intensity with respect to each wavelength;
σ_r	:	relative mean standard deviation of the average intensity;
σ_λ	:	mean standard deviation of the intensity with respect to the wavelength;
$\sigma_{\lambda, r}$:	relative mean standard deviation of the intensity with respect to the wavelength;
τ	:	turbidity;
	:	angle formed by the z axis and the line from particle center to the intersection point of Gaussian ray and the surface of the particle;
$\tau_{rg, o}$:	incidence angle corresponding to the geometrical rainbow angle for a sphere;
$\tau'_{rg, o}$:	refraction angle corresponding to the geometrical rainbow angle for a sphere;
τ_n^m	:	generalized Legendre functions;
ϕ	:	polar spherical or spheroidal coordinate;
Φ_{bd}	:	polarization angle of the beam;
Φ	:	light flux;
ϕ_p	:	combined phase shift;
ϕ_i	:	phase of the Gaussian beam;
$\phi_{p, pl}$:	combined phase shift for plane wave;

$\phi_{p,PH}$:	phase shift due to the optical path;
$\phi_{p,FL}$:	phase shift due to the focal lines;
$\Delta\phi_{p,T,j}$:	additional phase shifts brought in by total reflection;
ψ_{mn}	:	scalar eigenfunctions to the scalar wave equation;
ω	:	circular frequency of light;
$\Delta\Omega_1$:	solid angle;
$\Delta\Omega_2$:	solid angle.

Subscripts or superscripts

emn	:	even item;
<i>i</i>	:	incident;
<i>j</i>	:	perpendicular ($j=1$) and parallel ($j=2$) components; <i>j</i> th kind;
I	:	region outside the particle;
II	:	region inside the particle;
min	:	minimum;
max	:	maximum;
o	:	sphere;
<i>s</i>	:	scattered;
<i>t</i>	:	internal;
T	:	transformation of matrix;
<i>x, y, and z</i>	:	components in <i>x, y, and z</i> direction;
$\xi, \eta, \text{ and } \phi$:	components in $\xi, \eta, \text{ and } \phi$ direction;
omn	:	odd item;
'	:	first derivative;
*	:	complex conjugate.

Mathematical operators

Im	:	imaginary part;
----	---	-----------------

min	:	minimization;
Re	:	real part;
∇^2	:	Laplace operator;
T	:	transformation of matrix;
Tr	:	trace of a matrix;
'	:	first derivative;
*	:	complex conjugate;
...	:	norm of a matrix.

Abbreviations

CCD	:	charged-coupled device;
GCV	:	Generalized Cross-Validation;
GLMT	:	generalized Lorenz-Mie theory;
GO	:	geometrical optics;
MSD	:	mean standard deviation;
NFD	:	number frequency distribution;
NNLS	:	non-negative least square;
ORT	:	optimized regularization technique;
PSD	:	particle size distribution;
RPCS	:	radiation pressure crosssection;
RPF	:	radiation pressure force;
R-R	:	Rosin-Rammler;
SD	:	standard deviation;
SLEM	:	spectral light extinction method;
SMD	:	Sauter mean diameter;
VFD	:	volume frequency distribution.

General Introduction

Light scattering theory and its application in particle and particle system characterization have been the interests of many researchers in the past several decades. Since the rigorous theory, Lorenz-Mie theory, was developed in the beginning of the last century, a solid theoretical basis has been laid down for many optical instruments, which are characterized by rapid, accurate, and non-intrusive measurement.

Although the sphere finds most applications in the particle shape modeling in many occasions of optical measurements, more particles existing in nature or generated in industrial processes are non-spherical. As a first order extension of the sphere, the spheroid is considered to model some of them. However, the extension of the light scattering theory from sphere to spheroid is not a straightforward step. More difficult is the further extension from plane wave incidence to shaped beam incidence, which is the objective of the current thesis aiming at establishing a systematic theory for arbitrary shaped beam scattering by a spheroid.

To overcome the drawback of rigorous theory in practical numerical calculation of the scattered fields for large spheroids, the classical geometrical optics is also developed by the author in the current thesis. By using the extended geometrical optics, the position of the primary order geometric rainbow for a spheroid of any aspect ratio κ can be predicted. Deviations of the primary order rainbow position predicted by Moebius formula, which is applicable only when the aspect ratio of the spheroid κ approach much to unity (typically, $|\kappa-1|\leq 0.05$), can be evaluated.

As an important application occasion of the light scattering theory, wet steam measurement by using spectral light extinction method becomes the second part of the thesis. In large steam turbines used for electrical power production, the steam enters the low-pressure turbine cylinders as a dry superheated steam but exhausts to the condenser as a two-phase mixture of saturated steam and small liquid droplets. The occurrence of condensation phenomena in wet steam two-phase flow caused by the droplets degrades the efficiency of the turbine and makes corrosion damage to the turbine blades. In geothermal power plants and nuclear power plants, its harm to the economic characteristics and the security of steam turbine units is especially

remarkable due to the existence of the saturated steam. Therefore, it is greatly significant to investigate the behavior of wet steam two-phase flow in steam turbines. In the thesis, an online particle size distribution and wetness measurement system is developed on the basis of the spectral light extinction method and it is successfully applied in experiments.

The thesis is organized as follows, theoretical development of two independent theories, generalized Lorenz-Mie theory and geometrical optics, for the description of shaped beam scattering by a spheroid, is presented in part I (Chapters 1~3). Development of an optical system designed on the basis of spectral light extinction method and its application in wet steam measurement, are presented in Part II (Chapters 4~8). And a conclusion of the thesis is given in Chapter 9.

Part I.

Shaped Beam Scattering by a Homogeneous
Spheroid

Chapter 1. Introduction

Numbers of optical phenomena in the nature, such as the rainbow, the glory, the sky blue and the evening glow have inspired our infinite poetic imagination. Some of them even become the belief to many ordinary people. Thanks to Rayleigh (1881), Mie (1908), Debye (1909), and other physicists' efforts in the development of light scattering theory in the past two centuries, the mechanism of scattering gradually becomes clear to us.

Thanks to our understanding of scattering, more and more non-intrusive optical instruments have been invented and developed for particle and particle system characterization. For examples, by using rainbow refractometry, the temperature and the composition of a single droplet or the droplet system can be known (Wilms et al., 2004; Wilms, 2005; Vetrano et al., 2005); By measuring the morphology dependent resonances, droplet size, evaporation rate, surface tension, viscosity, as well as species concentration in a multicomponent droplet can be determined (Chen et al., 1996). Through exerting optical force, mechanical rigidity of a soft cell can be measured (Guck et al., 2000, 2001).

To provide a theoretical basis for these optical methods of measurement, relevant scattering theories have been developed. Among all the theories established for light scattering description, rigorous theory and geometrical optics are two of the most widely applied methods in practical situations. In the current thesis, the main concern centers on the interaction between a single particle and the laser beam, which is the basis for various modern optical instruments developed for particle characterization, such as laser Doppler anemometry (Durst et al., 1981), dual-cylindrical wave particle analyzer (Naqwi et al., 1990, 1992), laser imaging particle analyzer (Schaub et al., 1991), optical tweezer (Ashkin, 1970, 1980; Ashkin and Dziedzic, 1987, 1989; Ashkin et al., 1987), etc.

The first part of the current thesis is contributed to the shaped beam scattering by a spheroid. We will give a discussion in the upcoming sections on the several aspects involved, including the shaped beam and the spheroid, and the theories developed for describing their interaction in history, including rigorous theory and geometrical optics.

1.1 Shaped beam

The name of “laser beam” in the current thesis can be viewed as equivalent to “arbitrary shaped beam”. With the development of laser optics, more and more beams of different shapes and profiles have been applied to the optical instruments, e.g., the circular and elliptical Gaussian beams, high-order Hermite-Gaussian beams, Laguerre-Gaussian beam, etc. When we develop a theory for describing shaped beam scattering by a single particle, the expansion of the shaped beam in coordinates adapted to the particle is important. Among all the beams, the most commonly used one is the Gaussian beam working on the fundamental mode TEM_{00} , whose description has been given by Davis (1979), Gouesbet and Gréhan (1988) and Barton and Alexander (1989). The description of high-order Hermite-Gaussian beam (TEM_{mn}) can be derived by performing partial derivatives of the fundamental spatial mode TEM_{00} (Barton, 1997). And the description of the Laguerre-Gaussian beams is not involved, since they can be expressed in terms of a summation of the Hermite-Gaussian beams (Siegman, 1971). Once the electric and magnetic fields in the coordinates of the particle are determined, the remaining task is straightforward: establishing the equations ensuring the continuity of the tangential components of the electric and magnetic vectors across the surface of the particle and then solving the equation set.

1.2 Spheroid

Light scattering by non-spherical particles has been the interests of many researchers in the past several decades. As one of the non-spherical particles, the spheroid provides first order appropriate model in many practical situations. For example, in atomization under high Weber numbers (typically $We > 100$), the droplets acted by the aerodynamic drag forces are deformed into the oblate spheroidal shape during the period between the primary atomization and the secondary breakup (Hsiang and Faeth, 1992). By the action of inertial forces, falling droplets at low Reynolds number also possess the oblate spheroidal shape (Taylor and Acrivos, 1964). For some aerodynamic particle sizing instruments, the droplets suspended in an accelerated sample airstream are deformed from spherical to oblate spheroidal shape (Secker et al., 2000a, b; Secker et al. 2001). Brenn and Frohn’ experiment shows that free oscillation of fundamental mode ($n=2$) of the droplet in a gaseous medium cause its surface to approach the spheroidal shape (Brenn

and Frohn, 1993). The spheroid also provides a suitable model in some biological experiments. For example, under the action of the optical stretcher (Guck et al., 2000, 2001), which uses two counter-propagating laser beams to stretch a soft red blood cell by optical force, the cell is deformed to a shape approximate to the prolate spheroid in its initial and intermediary period of deformation.

Since the spheroid can serve as the model for the studies of the deformed particles in many cases, its scattering characteristics should be theoretically known before its measurements and diagnoses by using various optical instruments, which is the motivation of the thesis. By using both rigorous theory and geometrical optics, the far-field scattering, the rainbow position, scattering and extinction coefficients, and the optical force will be studied for a spheroid, prolate or oblate, transparent or absorbing, illuminated by arbitrary shaped beam.

1.3 Rigorous theory

The rigorous theory of shaped beam scattering by a spheroid is developed from the theories of shaped beam scattering by a sphere and of plane wave scattering by a spheroid. To find the solution to Maxwell's equation by using variable separation and boundary condition methods, it is primarily necessary to expand the shaped beam in the coordinates generated from the shape of the particle. To this aim, Kim and Lee (1983) used the complex-source-point method, Barton (1988) combined the particle's geometry with the incident fields and introduced the surface integral method, while Gouesbet et al. (1988) developed the generalized Lorenz-Mie theory (GLMT), which employs a set of beam shape coefficients (BSCs) to describe the incident beam. GLMT has found the most conventional applications in laser particle characterization because of its clearer physical interpretation in beam description: the BSCs are independent of the geometry of the spherical particle.

The rigorous theory for plane wave scattering by a homogeneous spheroid was first developed by Asano and Yamamoto (1975). By using the surface integral method, Barton (1995) first extended such a theory to the case of arbitrary beam incidence and studied the internal and near-surface fields for a spheroid. Thereafter, theories for shaped beam scattering by a layered spheroid or a spheroid with an embedded source is developed accordingly (Barton, 2000, 2001).

Within the framework of the GLMT (Gouesbet et al., 1988), on-axis and off-axis Gaussian beam scattering by a spheroid has also been studied (Han and Wu, 2001; Han et al., 2003). But the propagation direction of the incident beam is assumed to be parallel to the symmetrical axis of the spheroid.

This thesis contributes to the development of a systematic rigorous theory to describe the shaped beam scattering by a spheroid. Both the profile of the beam and its incident angle can be arbitrary. Analytical expressions of the scattering amplitudes, the scattering and extinction coefficients, and radiation pressure force are then yielded for a spheroid.

1.4 Geometrical optics

Although GLMT can serve as a rigorous theory in describing the interaction between the incident beam and spheroid, hardly can it be applied to the practical calculation for a homogeneous spheroid of projection radius larger than $\sim 5 \mu\text{m}$ ($r \geq \sim 5$) or axis ratio larger than ~ 3 ($a/b \geq \sim 3$). This is mainly due to the mathematical difficulties in numerical evaluation of radial spheroidal functions of the second kind for the spheroid of large size or axis ratio (Li et al., 1998).

In face of such a difficulty, the geometrical optics (GO) is expected to work instead of the rigorous theory. In GO approximation, the final scattering intensities are calculated from the superposition of the complex amplitudes of the diffracted rays, the externally reflected rays and the refracted rays experiencing finite internal reflections inside the particle (van de Hulst, 1957). Due to its advantages of more straightforward physical interpretation of scattering phenomenon and much higher efficiency in numerical calculations, GO can be applied in the studies of non-spherical and large particle scattering when no rigorous theory exists or rigorous theory can hardly achieve. The unique requirement is that the particle should be at least ten times larger than the wavelength, which is just the incapability range of the rigorous theory.

Many authors have contributed to the development of GO approximation to light scattering. Glantschnig and Chen (1980) have simplified the intensity calculation by superposing the amplitudes of the externally reflected rays and the directly transmitted rays into that of diffracted ray and thus obtained a formula to describe the scattering by a pure water droplet in

the forward angular range $[0^\circ, 60^\circ]$. Aiming at practical particle sizing, Kuster et al. (1991) derived a more compact formula by simply considering the contribution of the diffracted and direct transmitted rays. Ungut et al. (1981) made a detailed comparison of the GO approximation with Mie theory in forward scattering calculation. They found good agreement of the two theories can be achieved at the scattering angles within $[0^\circ, 20^\circ]$ for a transparent spherical particle of size parameter greater than ~ 6 . Xu et al. (2003, 2004a) extended GO to plane wave scattering by an absorbing homogeneous or a coated particle. Comparison with Mie and Aden-Kerker theory (Mie, 1908; Aden and Kerker, 1951) indicates that GO can be used for scattering calculation for both transparent and weakly absorbing particles in the near forward directions.

However, all the aforementioned papers concern the plane wave scattering by a spherical particle. As to the shaped beam illumination, only Chevaillier et al. (1986, 1990) extended the Fraunhofer diffraction theory to describe Gaussian beam scattering by an opaque circular disk. But their method is only valid for scattering angles less than $\sim 6^\circ$. Moreover, the numerical method adopted for performing the diffraction integral has the requirement that the local beam waist radius w should be larger than the disk radius a . With respect to the particle, Hovenac et al. (1991) applied ray theory to study forward scattering of the plane wave by a spheroid, while Lock (1996a, b) gave a general formula for amplitude calculation of the specularly reflected and directly transmitted rays from a spheroid with arbitrary orientation. In rainbow studies, GO has also found practical applications, particularly in the studies of droplet and elliptical cylinder scattering (Walker, 1976; Fraster, 1993; Adler et al., 1998). However, because of the difficulties in divergence factor calculation and ray-tracing program design for a three-dimensional object, these methods can hardly handle the emergent rays experiencing more than one internal reflection inside the non-spherical particles. In this thesis, an extension of GO to describe Gaussian beam scattering by a spheroid will be given. The beam is assumed to have nose-on incidence on the spheroid so that the beam axis coincides with the rotationally axis of symmetry of the particle. In this case, calculations of the divergence factor, the phase shift, etc. for a three-dimensional object can be simplified into the two-dimensional domain. In this case, prediction of the geometrical rainbow position is made for a spheroid of large axis ratio, which is the theoretical basis of rainbow thermometry.

1.5 Organization of Part I

The first part of the present thesis is organized into 2 chapters: Chapter 2 is contributed to the development of the GLMT for shaped beam scattering by a spheroid. And Chapter 3 is contributed to the development of GO approximation of Gaussian beam scattering by a spheroid.

Note should be paid to that most work stated in Chapters 2 and 3 has been published in the journal papers by the author (Xu et al. 2006a, b, 2007a-c). Nevertheless, to ensure the completeness and the coherence of the thesis, the work is reorganized for presentation.

Chapter 2. Generalized Lorenz-Mie Theory for Shaped Beam Scattering by a Spheroid

In this chapter, we develop the generalized Lorenz-Mie theory (GLMT) for shaped beam scattering by a spheroid. First, the general theory is presented and analytical expressions of the scattered fields, scattering, extinction and the radiation pressure crosssections are given. Then, our efforts are devoted to the expansion of the incident shaped beam of arbitrary orientation and location in terms of the vector spheroidal wave functions in a given spheroidal coordinates. Evaluation method of the beam shape coefficients (BSCs) in spheroidal coordinates is discussed and comparison of the reconstructed fields with the original ones is made. Finally, the demonstration calculations and numerical results from the current theory are presented. The plane wave, circular Gaussian beam, elliptical Gaussian beam are employed as the incident beams for calculations.

2.1 Theory

We consider a monochromatic, arbitrarily oriented shaped beam incident on a spheroid with semimajor and semiminor axes a and b , respectively (Fig. 2.1). In its own Cartesian coordinate system O_B-uvw , the beam is polarized in the u direction at the waist. The spheroid, prolate or oblate, is surrounded by a homogeneous, nonmagnetic and lossless medium. The time-dependent part of the electromagnetic field is assumed to be $\exp(-i\omega t)$. Outside and inside the particle, the electromagnetic fields must satisfy vector wave equations (or Helmholtz equations) as follows:

$$\begin{cases} \nabla^2 \mathbf{E} + k^2 \mathbf{E} = 0 \\ \nabla^2 \mathbf{H} + k^2 \mathbf{H} = 0 \end{cases}, \quad (2-1)$$

where $k = 2\pi / \lambda$ is the wavenumber. Assuming that $k_0 = 2\pi / \lambda_0$ is the wavenumber of light in free space, we have wavenumbers $k_I = k_0 \hat{m}_I$ and $k_{II} = k_0 \hat{m}_{II}$ outside and inside of the spheroid respectively, and the refractive indices \hat{m}_I and \hat{m}_{II} of the medium and of the spheroid,

respectively.

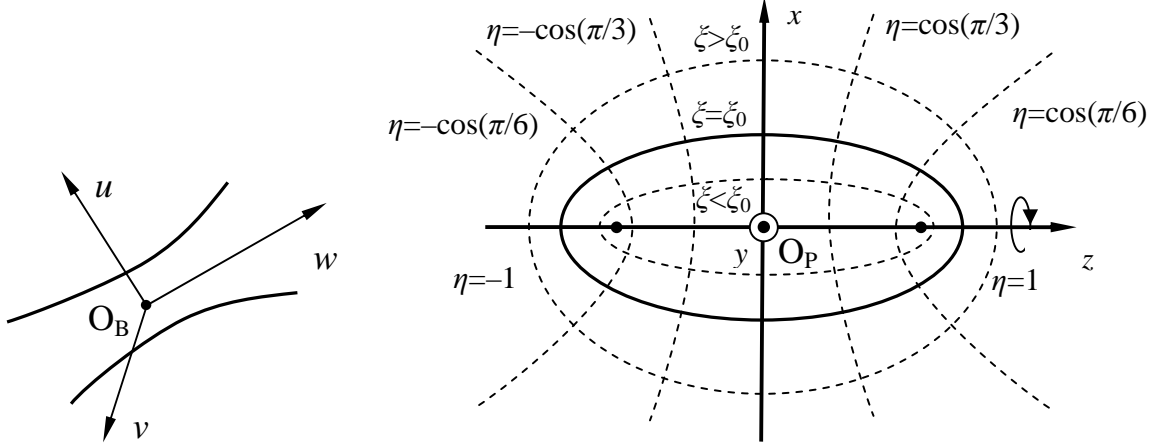


Fig. 2.1 Coordinate systems: O_B-uvw is attached to the incident shaped beam and O_P-xyz is attached to the spheroid.

Solutions of vector wave equation (2-1) can be found by applying the variable separation method (VSM) to the following scalar wave equation:

$$\nabla^2 \psi + k^2 \psi = 0. \quad (2-2)$$

The relationship between the scalar function ψ and the spheroidal vector wave functions will be given in Subsection 2.1.1.

2.1.1 Beam expansion in spheroidal coordinates

By using the VSM, solutions to the scalar wave function denoted by Eq.(2-2) in the prolate spheroidal coordinates (ξ, η, ϕ) are the scalar eigenfunctions expressed in the following form:

$$\psi_{mn} = S_{|m|n}(c, \eta) R_{|m|n}(c, \xi) \exp(im\phi), \quad (2-3)$$

where the dimensionless parameter c is defined by $c=kf$, with f being the semifocal length of the spheroid. The spheroidal angular functions $S_{mn}(c, \eta)$ and the spheroidal radial functions $R_{mn}(c, \xi)$, satisfy the following differential equations (Flammer, 1957):

$$\frac{d}{d\xi} \left[(\xi^2 - 1) \frac{dR_{mn}(c, \xi)}{d\xi} \right] - \left[\lambda_{mn}(c) - c^2 \xi^2 - \frac{m^2}{\xi^2 - 1} \right] R_{mn}(c, \xi) = 0, \quad (2-4)$$

$$\frac{d}{d\eta} \left[(1 - \eta^2) \frac{dS_{mn}(c, \eta)}{d\eta} \right] + \left[\lambda_{mn}(c) - c^2 \eta^2 - \frac{m^2}{1 - \eta^2} \right] S_{mn}(c, \eta) = 0. \quad (2-5)$$

In Eq. (2-4) and Eq. (2-5), λ_{mn} is a separation constant. The discrete values of λ_{mn} ($n=m, m+1, \dots$) are the eigenvalues ensuring finite solution at $\eta=\pm 1$ for the differential equations. Methods on the computation of λ_{mn} have been reviewed by Li et al. (1998). And the method used by us is proposed by Hodge (1970) and given in Appendix A.

Attention should be paid to the fact that all the equations and expressions pertaining to the prolate spheroidal system can be converted to their counterparts in the oblate system through replacements of the parameters c and ξ by $-ic$ and $i\xi$, respectively. Therefore, in this chapter, we only present the formulation for a prolate spheroid for convenience.

The spheroidal vector wave functions (\mathbf{M}_{mn} , \mathbf{N}_{mn}) (see Appendix B for their complete expressions), as solutions to the vector wave equation (2-1), are then generated by following vector operations on the scalar function ψ_{mn} :

$$\mathbf{M}_{mn} = \nabla \times (\mathbf{r} \psi_{mn}). \quad (2-6)$$

$$\mathbf{N}_{mn} = \frac{1}{k} \nabla \times \mathbf{M}_{mn}. \quad (2-7)$$

The incident fields can be expanded in terms of spheroidal vector wave functions ($\mathbf{M}_{mn}^{(i)}$, $\mathbf{N}_{mn}^{(i)}$) as follows:

$$\mathbf{E}^{(i)} = \sum_{m=-\infty}^{\infty} \sum_{n=|m|, n \neq 0}^{\infty} i^{n+1} \left[iG_{n,TE}^m \mathbf{M}_{mn}^{(i)}(c_1; \xi, \eta, \phi) + G_{n,TM}^m \mathbf{N}_{mn}^{(i)}(c_1; \xi, \eta, \phi) \right], \quad (2-8)$$

$$\mathbf{H}^{(i)} = -\frac{ik_1}{\omega\mu_0} \sum_{m=-\infty}^{\infty} \sum_{n=|m|, n \neq 0}^{\infty} i^{n+1} \left[G_{n,TM}^m \mathbf{M}_{mn}^{(i)}(c_1; \xi, \eta, \phi) + iG_{n,TE}^m \mathbf{N}_{mn}^{(i)}(c_1; \xi, \eta, \phi) \right], \quad (2-9)$$

where μ_0 is the permeability of free space and $G_{n,TE}^m$ and $G_{n,TM}^m$ are the BSCs in spheroidal coordinates, or more briefly, spheroidal BSCs. Their computation will be discussed in Section 2.2.

Likewise, the scattered fields ($\mathbf{E}^{(s)}$, $\mathbf{H}^{(s)}$) are expressed in terms of the spheroidal vector wave functions ($\mathbf{M}_{mn}^{(s)}$, $\mathbf{N}_{mn}^{(s)}$) as follows:

$$\mathbf{E}^{(s)} = \sum_{m=-\infty}^{\infty} \sum_{n=|m|, n \neq 0}^{\infty} i^{n+1} \left[B_n^m \mathbf{M}_{mn}^{(s)}(c_1; \xi, \eta, \phi) + A_n^m \mathbf{N}_{mn}^{(s)}(c_1; \xi, \eta, \phi) \right], \quad (2-10)$$

$$\mathbf{H}^{(s)} = -\frac{ik_1}{\omega\mu_0} \sum_{m=-\infty}^{\infty} \sum_{n=|m|, n \neq 0}^{\infty} i^{n+1} \left[A_n^m \mathbf{M}_{mn}^{(s)}(c_1; \xi, \eta, \phi) + B_n^m \mathbf{N}_{mn}^{(s)}(c_1; \xi, \eta, \phi) \right]. \quad (2-11)$$

And the internal fields ($\mathbf{E}^{(t)}$, $\mathbf{H}^{(t)}$) read as

$$\mathbf{E}^{(t)} = \sum_{m=-\infty}^{\infty} \sum_{n=|m|, n \neq 0}^{\infty} i^{n+1} \left[D_n^m \mathbf{M}_{mn}^{(t)}(c_{II}; \xi, \eta, \phi) + C_n^m \mathbf{N}_{mn}^{(t)}(c_{II}; \xi, \eta, \phi) \right], \quad (2-12)$$

$$\mathbf{H}^{(t)} = -\frac{ik_{II}}{\omega\mu_0} \sum_{m=-\infty}^{\infty} \sum_{n=|m|, n \neq 0}^{\infty} i^{n+1} \left[C_n^m \mathbf{M}_{mn}^{(t)}(c_{II}; \xi, \eta, \phi) + D_n^m \mathbf{N}_{mn}^{(t)}(c_{II}; \xi, \eta, \phi) \right]. \quad (2-13)$$

The spheroidal vector functions describing the incident and internal fields, ($\mathbf{M}_{mn}^{(i)}$, $\mathbf{N}_{mn}^{(i)}$) and ($\mathbf{M}_{mn}^{(t)}$, $\mathbf{N}_{mn}^{(t)}$), are associated with $R_{mn}^{(1)}$, the radial function of the first kind that is finite at the origin of the spheroidal coordinates $\zeta=0$. The spheroidal vector functions for the scattered fields ($\mathbf{M}_{mn}^{(s)}$, $\mathbf{N}_{mn}^{(s)}$) are associated with $R_{mn}^{(3)}$, the radial function of the third kind ensuring that the scattered wave becomes a spherical diverging wave when the spheroidal radial coordinate ζ tends to infinity, as it should.

The unknown coefficients A_n^m , B_n^m , C_n^m , and D_n^m describing the scattered and internal fields can be determined from the following boundary conditions ensuring the continuity of tangential components of electric and magnetic vectors across the surface of the spheroid $\xi = \xi_0$:

$$E_\eta^{(i)} + E_\eta^{(s)} = E_\eta^{(t)}, \quad (2-14)$$

$$E_\phi^{(i)} + E_\phi^{(s)} = E_\phi^{(t)}, \quad (2-15)$$

$$H_\eta^{(i)} + H_\eta^{(s)} = H_\eta^{(t)}, \quad (2-16)$$

$$H_\phi^{(i)} + H_\phi^{(s)} = H_\phi^{(t)}. \quad (2-17)$$

We use the method proposed by Asano and Yamamoto (1975) to determine these coefficients. Namely, the η and ϕ components of the spheroidal harmonics are multiplied by

$\left\{ \left[(\xi_0^2 - 1) + (1 - \eta^2) \right]^{5/2} \right\}$ and $\left\{ \begin{array}{l} (\xi_0^2 - 1)^{-1/2} (\xi_0^2 - \eta^2) \\ (\xi_0^2 + 1)^{-1/2} (\xi_0^2 + \eta^2) \end{array} \right\}$ for the $\left\{ \begin{array}{l} \text{prolate} \\ \text{oblate} \end{array} \right\}$ spheroid. Afterward, the

spheroidal angular functions S_{mn} are expanded in terms of the associated Legendre functions of the first kind $P_n^m(\cos \theta)$. By virtue of the orthogonality of the P_n^m 's, a set of equations corresponding to Eqs. (2-14)-(2-17) can be obtained and solved to obtain the coefficients A_n^m , B_n^m , C_n^m , and D_n^m . This step is the similar as that for the case of plane wave incidence (Li et al., 1998, 2001, 2002; Yong and Sebak, 2006). The only modification is the implantation of the negative mode of the spheroidal vector wave function into the equation group corresponding to

the TM mode and the substitution of $\left\{ \begin{array}{l} f_{mn} \\ g_{mn} \end{array} \right\}$ by $\left\{ \begin{array}{l} -iG_{n,TE}^m \\ -G_{n,TM}^m \end{array} \right\}$ for positive m 's and by $\left\{ \begin{array}{l} iG_{n,TE}^m \\ -G_{n,TM}^m \end{array} \right\}$ for

negative m 's.

2.1.2 Far-field scattering

When the spheroidal radial coordinate ξ tends to infinity ($\xi \rightarrow \infty$), the associated spheroidal surface becomes a spherical one. In this case, we have $f\xi \rightarrow r$ ($c_1\xi \rightarrow k_1r$) and $\eta \rightarrow \cos \theta$. The ξ component of the spheroidal vector wave functions becomes negligible generating a transverse wave. And the η and ϕ components ($\mathbf{M}_{mn}^{(s)}$, $\mathbf{N}_{mn}^{(s)}$) have the following asymptotic behaviors:

$$M_{mn,\eta}^{(s)} = -(-i)^n \frac{e^{ik_1r}}{k_1r} \frac{mS_{|m|n}(c_1, \cos \theta)}{\sin \theta} \exp(im\phi), \quad (2-18)$$

$$M_{mn,\phi}^{(s)} = -(-i)^{n+1} \frac{e^{ik_1r}}{k_1r} \frac{dS_{|m|n}(c_1, \cos \theta)}{d\theta} \exp(im\phi), \quad (2-19)$$

$$N_{mn,\eta}^{(s)} = -(-i)^n \frac{e^{ik_1r}}{k_1r} \frac{dS_{|m|n}(c_1, \cos \theta)}{d\theta} \exp(im\phi), \quad (2-20)$$

$$N_{mn,\phi}^{(s)} = -(-i)^{n+1} \frac{e^{ik_1r}}{k_1r} \frac{mS_{|m|n}(c_1, \cos \theta)}{\sin \theta} \exp(im\phi). \quad (2-21)$$

Substituting Eqs. (2-18)-(2-21) into Eqs.(2-10) and (2-11) yields the far-field electromagnetic components as follows:

$$E_{\eta}^{(s)} = -\frac{i}{k_1 r} e^{ik_1 r} S_1, \quad (2-22)$$

$$E_{\phi}^{(s)} = -\frac{1}{k_1 r} e^{ik_1 r} S_2, \quad (2-23)$$

$$H_{\eta}^{(s)} = \frac{k_1}{\omega \mu_0} E_{\phi}^{(s)}, \quad (2-24)$$

$$H_{\phi}^{(s)} = -\frac{k_1}{\omega \mu_0} E_{\eta}^{(s)}, \quad (2-25)$$

where S_1 and S_2 are the complex amplitude functions calculated by

$$S_1 = \sum_{m=-\infty}^{\infty} \sum_{n=|m|, n \neq 0}^{\infty} \left[A_n^m \frac{m S_{|m|n}(c_1, \cos \theta)}{\sin \theta} + B_n^m \frac{d S_{|m|n}(c_1, \cos \theta)}{d \theta} \right] \exp(im\phi), \quad (2-26)$$

$$S_2 = \sum_{m=-\infty}^{\infty} \sum_{n=|m|, n \neq 0}^{\infty} \left[A_n^m \frac{d S_{|m|n}(c_1, \cos \theta)}{d \theta} + B_n^m \frac{m S_{|m|n}(c_1, \cos \theta)}{\sin \theta} \right] \exp(im\phi). \quad (2-27)$$

2.1.3 Extinction and scattering crosssections

For a particle of arbitrary shape, the scattering and extinction crosssections are defined as follows (Born and Wolf, 1999):

$$C_{sca} = \text{Re} \left\{ \iint_{\Sigma} (\mathbf{E}^{(s)} \times \mathbf{H}^{(s)*}) \cdot \mathbf{n} dS \right\}, \quad (2-28)$$

$$C_{ext} = -\text{Re} \left\{ \iint_{\Sigma} (\mathbf{E}^{(i)} \times \mathbf{H}^{(s)*} + \mathbf{E}^{(s)} \times \mathbf{H}^{(i)*}) \cdot \mathbf{n} dS \right\}, \quad (2-29)$$

where S may denote a spherical surface of a sphere with radius r , containing the particle and centered at a point inside the particle, \mathbf{n} is the unit vector outward normal with respect to S , Re denotes the real part of the integral results and the asterisk denotes the complex conjugate. We take the center of the spheroid as the center of such a sphere.

When the spheroidal radial coordinate ζ tends to infinity ($\zeta \rightarrow \infty$), the spheroidal surface characterized by the spheroidal radial coordinate ζ becomes a spherical one ($c\zeta$ tends to kr and η tends to $\cos\theta$) and the radial components of the spheroidal vector wave functions become zero. Using such a spherical surface to perform the integral of Eqs. (2-28) and (2-29), we have

$$C_{sca} = \int_0^\pi \int_0^{2\pi} \frac{1}{2} \operatorname{Re} \left(E_\eta^{(s)} H_\phi^{(s)*} - E_\phi^{(s)} H_\eta^{(s)*} \right) r^2 \sin \theta d\theta d\phi, \quad (2-30)$$

$$C_{ext} = \int_0^\pi \int_0^{2\pi} \frac{1}{2} \operatorname{Re} \left(E_\phi^{(i)} H_\eta^{(s)} + E_\phi^{(s)} H_\eta^{(i)*} - E_\eta^{(i)} H_\phi^{(s)} - E_\eta^{(s)} H_\phi^{(i)*} \right) r^2 \sin \theta d\theta d\phi, \quad (2-31)$$

Substituting into Eqs. (2-30) and (2-31) the asymptotic behaviors of $(\mathbf{M}_{mn}^{(s)}, \mathbf{N}_{mn}^{(s)})$ as indicated by Eqs. (2-18)-(2-21) and those of $(\mathbf{M}_{mn}^{(i)}, \mathbf{N}_{mn}^{(i)})$ as follows:

$$M_{mn,\eta}^{(i)} = -\frac{1}{2} \left[(-i)^n \frac{e^{ik_1 r}}{k_1 r} - i^n \frac{e^{-ik_1 r}}{k_1 r} \right] \frac{m S_{|m|n}(c_1, \cos \theta)}{\sin \theta} \exp(im\phi), \quad (2-32)$$

$$M_{mn,\phi}^{(i)} = -\frac{1}{2} \left[(-i)^{n+1} \frac{e^{ik_1 r}}{k_1 r} + i^{n+1} \frac{e^{-ik_1 r}}{k_1 r} \right] \frac{dS_{|m|n}(c_1, \cos \theta)}{d\theta} \exp(im\phi), \quad (2-33)$$

$$N_{mn,\eta}^{(i)} = -\frac{1}{2} \left[(-i)^n \frac{e^{ik_1 r}}{k_1 r} - i^n \frac{e^{-ik_1 r}}{k_1 r} \right] \frac{dS_{|m|n}(c_1, \cos \theta)}{d\theta} \exp(im\phi), \quad (2-34)$$

$$N_{mn,\phi}^{(i)} = -\frac{1}{2} \left[(-i)^{n+1} \frac{e^{ik_1 r}}{k_1 r} + i^{n+1} \frac{e^{-ik_1 r}}{k_1 r} \right] \frac{m S_{|m|n}(c_1, \cos \theta)}{\sin \theta} \exp(im\phi), \quad (2-35)$$

and invoking orthogonality relations for the exponentials $\exp(im\phi)$ and the generalized Legendre functions τ_n^m and π_n^m as follows (Gouesbet et al., 1988):

$$\int_0^{2\pi} \exp[i(m-m')\phi] d\phi = 2\pi \delta_{mm'}, \quad (2-36)$$

$$\int_0^\pi (\tau_n^m \tau_{n'}^m + m^2 \pi_n^m \pi_{n'}^m) \sin \theta d\theta = \frac{2n(n+1)(n+m)!}{(2n+1)(n-m)!} \delta_{nn'}, \quad (2-37)$$

$$\int_0^\pi (\tau_n^m \pi_n^m + \tau_{n'}^m \pi_{n'}^m) \sin \theta d\theta = 0, \quad (2-38)$$

where

$$\tau_n^m = \frac{dP_n^m(\cos \theta)}{d\theta}, \quad (2-39)$$

$$\pi_n^m = \frac{P_n^m(\cos \theta)}{\sin \theta}, \quad (2-40)$$

we can finally obtain the following analytical expressions of the scattering and extinction crosssections after some algebra:

$$C_{sca} = \frac{\lambda^2}{\pi} \operatorname{Re} \left[\sum_{p=-\infty}^{+\infty} \sum_{n=|p| \neq 0}^{+\infty} \sum_{n'=|p| \neq 0}^{+\infty} \Pi_{nn'}^p \left(A_n^p A_{n'}^{p,*} + B_n^p B_{n'}^{p,*} \right) \right], \quad (2-41)$$

$$C_{ext} = \frac{\lambda^2}{\pi} \operatorname{Re} \left[\sum_{p=-\infty}^{+\infty} \sum_{n=|p| \neq 0}^{+\infty} \sum_{n'=|p| \neq 0}^{+\infty} \Pi_{nn'}^p \left(A_n^p G_{n',TM}^{p,*} + B_n^p G_{n',TE}^{p,*} \right) \right], \quad (2-42)$$

where

$$\Pi_{nn'}^p = \begin{cases} 0, & |n - n'| = \text{odd} \\ \sum_{r=0,1}^{\infty} r \frac{(r+|p|)(r+|p|+1)(r+2|p|)!}{2r+2|p|+1} \frac{d_r^{|p|n} d_r^{|p|n'}}{r!}, & |n - n'| = \text{even} \end{cases}. \quad (2-43)$$

2.1.4 Radiation pressure

The radiation pressure force (RPF) exerted by the beam on the particle is proportional to the net momentum removed from the incident beam. If we use the radiation pressure crosssections (RPCS) $C_{pr, x}$, $C_{pr, y}$, and $C_{pr, z}$ to characterize the transverse (along the x and y axes) and longitudinal (along the z axis) components of RPF respectively, they can be related to the integral of the absorption crosssection, C_{abs} , by (Gouesbet et al. 1988)

$$C_{pr, x} = c_m F_x = \overline{\sin \theta \cos \phi} C_{abs}, \quad (2-44)$$

$$C_{pr, y} = c_m F_y = \overline{\sin \theta \sin \phi} C_{abs}, \quad (2-45)$$

$$C_{pr, z} = c_m F_z = \overline{\cos \theta} C_{abs}, \quad (2-46)$$

where c_m denotes the light speed in the surrounding medium and F_x , F_y and F_z denote the three components of RPF along the x , y , and z axes respectively.

Since the time-averaged Poynting vector \mathbf{S} can be obtained from the incident and scattered electromagnetic fields outside the particle as follows (Bohren and Huffman, 1983):

$$\mathbf{S} = \frac{c_m}{8\pi} \left(\mathbf{E}^{(i)} \times \mathbf{H}^{(i)*} + \mathbf{E}^{(s)} \times \mathbf{H}^{(s)*} + \mathbf{E}^{(i)} \times \mathbf{H}^{(s)*} + \mathbf{E}^{(s)} \times \mathbf{H}^{(i)*} \right), \quad (2-47)$$

and the energy absorbed by the particle is negative to the integral result of the Poynting vector over a closed surface around the particle, we have the following integral for the absorption crosssection:

$$C_{\text{abs}} = -\text{Re} \left\{ \iint_{\Sigma} \left(\mathbf{E}^{(s)} \times \mathbf{H}^{(s)*} + \mathbf{E}^{(i)} \times \mathbf{H}^{(s)*} + \mathbf{E}^{(s)} \times \mathbf{H}^{(i)*} \right) \cdot \mathbf{n} dS \right\}. \quad (2-48)$$

Note that the integral result of the first term of the Poynting vector (Eq.(2-47)) over a closed surface of the particle is zero.

When the spheroidal radial coordinate ζ tends to infinity ($\zeta \rightarrow \infty$), the spheroidal surface characterized by the spheroidal radial coordinate ζ becomes a spherical one ($c\zeta$ tends to kr and η tends to $\cos\theta$) and the radial components of the spheroidal vector wave functions become zero. Using such a spherical surface to perform the integral of Eq.(2-48), we have the following expression for C_{abs} :

$$C_{\text{abs}} = \int_0^\pi \int_0^{2\pi} \frac{1}{2} \text{Re} \left(E_\phi^{(i)} H_\eta^{(s)} + E_\phi^{(s)} H_\eta^{(i)*} - E_\eta^{(i)} H_\phi^{(s)} - E_\eta^{(s)} H_\phi^{(i)*} - E_\eta^{(s)} H_\phi^{(s)*} + E_\phi^{(s)} H_\eta^{(s)*} \right) r^2 \sin\theta d\theta d\phi. \quad (2-49)$$

Substituting Eq.(2-49) into Eqs. (2-44)-(2-46) yields the following expressions of RPCS:

$$C_{\text{pr},x} = \int_0^\pi \int_0^{2\pi} \frac{1}{2} \text{Re} \left(E_\phi^{(i)} H_\eta^{(s)} + E_\phi^{(s)} H_\eta^{(i)*} - E_\eta^{(i)} H_\phi^{(s)} - E_\eta^{(s)} H_\phi^{(i)*} - E_\eta^{(s)} H_\phi^{(s)*} + E_\phi^{(s)} H_\eta^{(s)*} \right) r^2 \sin^2\theta \cos\phi d\theta d\phi, \quad (2-50)$$

$$C_{\text{pr},y} = \int_0^\pi \int_0^{2\pi} \frac{1}{2} \text{Re} \left(E_\phi^{(i)} H_\eta^{(s)} + E_\phi^{(s)} H_\eta^{(i)*} - E_\eta^{(i)} H_\phi^{(s)} - E_\eta^{(s)} H_\phi^{(i)*} - E_\eta^{(s)} H_\phi^{(s)*} + E_\phi^{(s)} H_\eta^{(s)*} \right) r^2 \sin^2\theta \sin\phi d\theta d\phi, \quad (2-51)$$

$$C_{\text{pr},z} = \int_0^\pi \int_0^{2\pi} \frac{1}{2} \text{Re} \left(E_\phi^{(i)} H_\eta^{(s)} + E_\phi^{(s)} H_\eta^{(i)*} - E_\eta^{(i)} H_\phi^{(s)} - E_\eta^{(s)} H_\phi^{(i)*} - E_\eta^{(s)} H_\phi^{(s)*} + E_\phi^{(s)} H_\eta^{(s)*} \right) r^2 \sin\theta \cos\theta d\theta d\phi. \quad (2-52)$$

Substituting Eqs. (2-18)-(2-21) and (2-32)-(2-35), which are the asymptotic behaviors of η and ϕ components of the spheroidal vector wave functions describing the scattering and incident waves, into Eqs.(2-8)-(2-11), using Eqs.(2-50)-(2-52), and invoking the orthogonality relations

listed in Appendix C for the generalized angular functions $\frac{S_{mn}(c_1, \cos\theta)}{\sin\theta}$,

as well as the exponentials $\exp(im\phi)$, we can obtain the following analytical

expressions of RPCS after a great deal of algebra:

$$C_{pr,x} = \frac{\lambda^2}{4\pi} \sum_{p=1}^{+\infty} \sum_{n=p-1 \neq 0}^{+\infty} \sum_{n'=p}^{+\infty} \operatorname{Re} \left[L_{nn'}^{p-1} (2U_{nn'}^{p-1} - S_{nn'}^{p-1}) + L_{n'n}^{-p} (2U_{n'n}^{-p} - S_{n'n}^{-p}) + iM_{nn'}^{p-1} (2V_{nn'}^{p-1} - T_{nn'}^{p-1}) + iM_{n'n}^{-p} (2V_{n'n}^{-p} - T_{n'n}^{-p}) \right], \quad (2-53)$$

$$C_{pr,y} = \frac{\lambda^2}{4\pi} \sum_{p=1}^{+\infty} \sum_{n=p-1 \neq 0}^{+\infty} \sum_{n'=p}^{+\infty} \operatorname{Im} \left[L_{nn'}^{p-1} (2U_{nn'}^{p-1} - S_{nn'}^{p-1}) + L_{n'n}^{-p} (2U_{n'n}^{-p} - S_{n'n}^{-p}) + iM_{nn'}^{p-1} (2V_{nn'}^{p-1} - T_{nn'}^{p-1}) + iM_{n'n}^{-p} (2V_{n'n}^{-p} - T_{n'n}^{-p}) \right], \quad (2-54)$$

$$C_{pr,z} = \frac{\lambda^2}{4\pi} \sum_{p=-\infty}^{+\infty} \sum_{n=|p| \neq 0}^{+\infty} \sum_{n'=|p| \neq 0}^{+\infty} \operatorname{Re} \left[J_{nn'}^p (O_{nn'}^p + P_{nn'}^p) + ipK_{nn'}^p (Q_{nn'}^p - R_{nn'}^p) \right], \quad (2-55)$$

where $J_{nn'}^p$, $K_{nn'}^p$, $L_{nn'}^p$, and $M_{nn'}^p$ are expressed by Eqs. (B9)-(B12) in Appendix C and $O_{nn'}^p - V_{nn'}^p$ are given by

$$O_{nn'}^p = G_{n, TM}^p A_{n'}^{p,*} + G_{n', TM}^{p,*} A_n^p - 2A_n^p A_{n'}^{p,*}, \quad (2-56)$$

$$P_{nn'}^p = G_{n, TE}^p B_{n'}^{p,*} + G_{n', TE}^{p,*} B_n^p - 2B_n^p B_{n'}^{p,*}, \quad (2-57)$$

$$Q_{nn'}^p = G_{n, TE}^p A_{n'}^{p,*} + G_{n', TM}^{p,*} B_n^p - 2A_{n'}^{p,*} B_n^p, \quad (2-58)$$

$$R_{nn'}^p = G_{n, TM}^p B_{n'}^{p,*} + G_{n', TE}^{p,*} A_n^p - 2A_n^p B_{n'}^{p,*}, \quad (2-59)$$

$$S_{nn'}^p = A_n^p G_{n', TM}^{p+1,*} + A_{n'}^{p+1,*} G_{n, TM}^p + B_n^p G_{n', TE}^{p+1,*} + B_{n'}^{p+1,*} G_{n, TE}^p, \quad (2-60)$$

$$T_{nn'}^p = B_n^p G_{n', TM}^{p+1,*} + B_{n'}^{p+1,*} G_{n, TE}^p - A_n^p G_{n', TE}^{p+1,*} - A_{n'}^{p+1,*} G_{n, TM}^p, \quad (2-61)$$

$$U_{nn'}^p = A_n^p A_{n'}^{p+1,*} + B_n^p B_{n'}^{p+1,*}, \quad (2-62)$$

$$V_{nn'}^p = A_{n'}^{p+1,*} B_n^p - A_n^p B_{n'}^{p+1,*}. \quad (2-63)$$

Four kinds of coefficients can be identified in the analytical solution of RPF, the scattering coefficients (A_n^p , B_n^p) which are determined by the particle properties (including size, axis ratio and the relative refractive index), the geometrical coefficients $J_{nn'}^p$, $K_{nn'}^p$, $L_{nn'}^p$, and $M_{nn'}^p$ which depend only on the eccentricity parameter of the spheroid (c_1), the beam shape coefficients ($G_{n, TE}^p$, $G_{n, TM}^p$) which are determined by the beam properties in spheroidal coordinates, and the

cross-terms of the beam shape coefficients and the geometrical coefficients, $O_{mn}^p - V_{mn}^p$.

2.2 Beam shape coefficients for an arbitrary shaped beam

Theoretically, any shaped beam can be expanded in terms of spheroidal vector wave functions as indicated by Eqs.(2-8)-(2-9). And the spheroidal BSCs can be evaluated directly by using the orthogonality relations of the spheroidal vector wave functions. But this incurs a quite involved and tedious mathematical process. An alternative way is to use our good knowledge of spherical BSCs and establish a relation between the spheroidal and spherical BSCs. Nevertheless, it is not a straightforward step. In shaped beam scattering by a spherical particle, the z axis of particle's Cartesian coordinates can be set along propagation direction of the incident beam so that the incidence angle is zero. For a spheroid, however, the z axis must be symmetrical axis of the spheroid to generate the spheroidal vector wave functions. In this case, the BSC evaluation method in spherical coordinates for the beam of incidence angle being zero should be generalized to the case of beam of arbitrary incidence angle.

In this section, we first discuss the evaluation of the spherical BSCs. Then a transformation relation from spherical BSCs ($g_{n,TE}^m, g_{n,TM}^m$) to spheroidal ones ($G_{n,TE}^m, G_{n,TM}^m$) is given.

2.2.1 Spherical beam shape coefficients

By using the VSM, solutions to the scalar wave equation (2-2) in the spherical coordinates (r, θ, ϕ) are the scalar eigenfunctions written in the following form:

$$\psi_{mn} = z_n(r) P_n^{|m|}(\cos \theta) \exp(im\phi), \quad (2-64)$$

where $z_n(r)$ is the spherical Bessel function and $P_n^m(\cos \theta)$ is the associated Legendre function of the first kind (Arfken, 1985).

Then the spherical vector wave functions ($\mathbf{m}_{mn}, \mathbf{n}_{mn}$) (see Appendix D for their complete expressions), as solutions to the vector wave Eq. (2-1), are generated by following vector operations on the scalar function ψ_{mn} :

$$\mathbf{m}_{mn} = \nabla \times (\mathbf{r} \psi_{mn}). \quad (2-65)$$

$$\mathbf{n}_{mn} = \frac{1}{k} \nabla \times \mathbf{m}_{mn}. \quad (2-66)$$

Finally the incident, scattered and internal fields can be expressed as an infinite series of these vector functions. We note that for the descriptions of the incident and scattered fields, the spherical Bessel function of the first kind is adopted in the scalar function Eq.(2-64), while for the description of the internal field, the Hankel function of the first kind is used.

In the GLMT for a sphere (Gouesbet et al., 1988), two Bromwich scalar potentials, U_{TM} and U_{TE} , are introduced to describe the incident fields $(\mathbf{E}^{(i)}, \mathbf{H}^{(i)})$. Such a description is essentially equivalent to the following beam expansion in terms of the spherical vector wave functions $(\mathbf{m}_{mn}^{(i)}, \mathbf{n}_{mn}^{(i)})$:

$$\mathbf{E}^{(i)} = \sum_{m=-\infty}^{+\infty} \sum_{n=|m|, n \neq 0}^{+\infty} c_{n,pw} i^{n+1} \left(i g_{n,TE}^m \mathbf{m}_{mn}^{(i)}(r, \theta, \phi) + g_{n,TM}^m \mathbf{n}_{mn}^{(i)}(r, \theta, \phi) \right), \quad (2-67)$$

$$\mathbf{H}^{(i)} = -\frac{ik_1}{\omega \mu_0} \sum_{m=-\infty}^{+\infty} \sum_{n=|m|, n \neq 0}^{+\infty} c_{n,pw} i^{n+1} \left(g_{n,TM}^m \mathbf{m}_{mn}^{(i)}(r, \theta, \phi) + i g_{n,TE}^m \mathbf{n}_{mn}^{(i)}(r, \theta, \phi) \right), \quad (2-68)$$

where the plane wave term $c_{n,pw}$ reads as

$$c_{n,pw} = \frac{2n+1}{n(n+1)}, \quad (2-69)$$

and $g_{n,TM}^m$ and $g_{n,TE}^m$ are the BSCs in spherical coordinates (or more briefly, spherical BSCs). In the same manner as done for the incident field, expressions of the scattered and internal fields can also be obtained from their description by U_{TM} and U_{TE} in the spherical coordinates (Gouesbet et al., 1988).

By using the orthogonality relation of the associated Legendre function $P_n^m(\cos \theta)$ of the first kind and Ferrer's definition and that of the exponential function $\exp(im\phi)$, the spherical BSCs can be formulated in as a double integral of the r components of the incident electric and magnetic fields $E_r^{(i)}$ and $H_r^{(i)}$ (Maheu et al., 1988; Barton, 1988):

$$g_{n,TM}^m = \frac{(-i)^{n+1} (n-|m|)!}{4\pi (n+|m|)!} \frac{k_1 r}{z_n(k_1 r)} \int_0^\pi \int_0^{2\pi} \frac{E_r^{(i)}(r, \theta, \phi)}{E_0} P_n^{|m|}(\cos \theta) \sin \theta \exp(-im\phi) d\theta d\phi, \quad (2-70)$$

$$g_{n,TE}^m = \frac{(-i)^{n+1} (n-|m|)!}{4\pi (n+|m|)!} \frac{k_1 r}{z_n(k_1 r)} \int_0^\pi \int_0^{2\pi} \frac{H_r^{(i)}(r, \theta, \phi)}{H_0} P_n^{|m|}(\cos \theta) \sin \theta \exp(-im\phi) d\theta d\phi. \quad (2-71)$$

Evidently, the coefficients evaluated by these integrals depend on the radial coordinate r , but they should not be. Therefore in numerical calculation the value of r must be carefully chosen to ensure the fast convergence of the integral and the independence of the BSCs (Ren, 1995).

To eliminate the r -dependence of the BSCs, the following triple integrals of $E_r^{(i)}$ and $H_r^{(i)}$ are introduced (Gouesbet and Lock, 1994):

$$g_{n,TM}^m = \frac{(2n+1)(-i)^{n+1} (n-|m|)!}{2\pi^2 (n+|m|)!} \int_0^\infty k_1 r z_n(k_1 r) \int_0^{2\pi} \exp(-im\phi) \int_0^\pi \frac{E_r^{(i)}(r, \theta, \phi)}{E_0} P_n^{|m|}(\cos \theta) \sin \theta d\theta d\phi d(k_1 r), \quad (2-72)$$

$$g_{n,TE}^m = \frac{(2n+1)(-i)^{n+1} (n-|m|)!}{2\pi^2 (n+|m|)!} \int_0^\infty k_1 r z_n(k_1 r) \int_0^{2\pi} \exp(-im\phi) \int_0^\pi \frac{H_r^{(i)}(r, \theta, \phi)}{H_0} P_n^{|m|}(\cos \theta) \sin \theta d\theta d\phi d(k_1 r). \quad (2-73)$$

A detailed discussion of the quadrature method is given by Gouesbet et al. (1996). Particularly when the coordinates of the beam are parallel to that of the particle, the most efficient technique for BSC evaluation is known as the localized approximation (Ren et al., 1998; Gouesbet, 1999).

2.2.2 Spheroidal beam shape coefficients

In GLMT for a sphere, we set the three axes of the beam coordinates u , v , and w parallel to their counterparts x , y , and z axes of the particle coordinates, respectively. Such a setting of the Cartesian coordinate system for a spherical particle will not cause any inconvenience for the generation of spherical wave functions owing to the spherical symmetry of the spherical particle. For a spheroidal particle, however, the z axis of its Cartesian coordinate system should be the rotation axis of symmetry of the spheroid to generate the spheroidal vector wave functions. Thus we should discuss the BSC evaluation method in a given coordinate system for arbitrary incident beam.

To explain more clearly, the geometry of the beam and the particle illustrated in Fig. 2.1 is replotted in Fig. 2.2. The shaped beam polarized in the u direction propagates along the w direction in its own Cartesian coordinates O_B-uvw . After coordinate translation, the beam center

O_B can be moved to the particle center O_P so that $O_P-u'v'w'$ is brought in. Taking the symmetrical axis of the spheroid as the z axis, we set the x axis of the Cartesian coordinates of the particle in the plane formed by the w' and z axes. In this way the Cartesian coordinates of the particle O_P-xyz are determined. Then the beam center O_B is assumed to locate at (x_0, y_0, z_0) in O_P-xyz . We use Θ_{bd} to characterize the propagation direction of the beam relative to the O_P-yz plane and Φ_{bd} to characterize the polarization direction of its electric field relative to the O_P-xz plane, as illustrated in Fig. 2.2. In the present Chapter Θ_{bd} and Φ_{bd} are also called the incidence angle and the polarization angle, respectively.

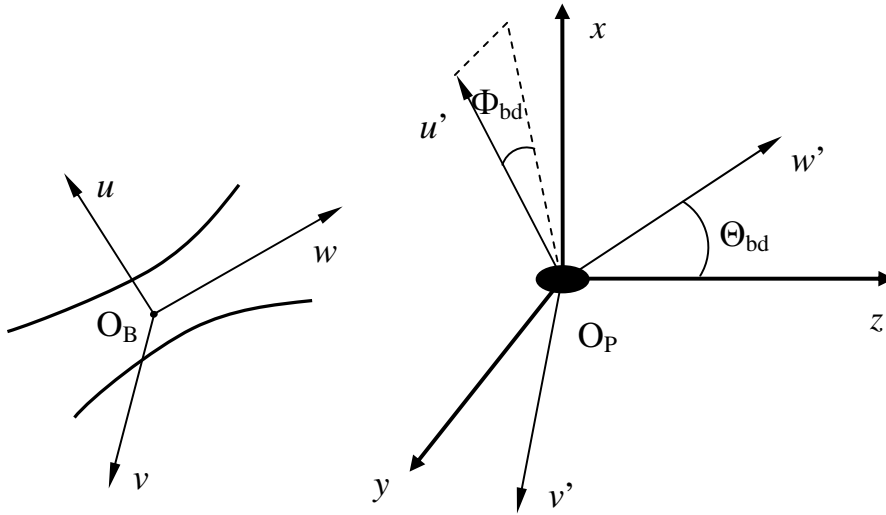


Fig. 2.2 Geometry of Cartesian coordinates of the beam and spheroid. O_P-xyz is the Cartesian coordinates of the particle and $O_P-u'v'w'$ is paprally translated from the beam coordinates O_B-uvw . The beam center O_B locates at (x_0, y_0, z_0) in O_P-xyz .

With the aid of such an angle set (Θ_{bd}, Φ_{bd}) , the two systems can be related by a conversion matrix A as follows (Xu et al., 2007a):

$$\begin{pmatrix} x - x_0 \\ y - y_0 \\ z - z_0 \end{pmatrix} = A \begin{pmatrix} u \\ v \\ w \end{pmatrix}, \quad (2-74)$$

where A reads as

$$A = \begin{pmatrix} \cos \Theta_{bd} \cos \Phi_{bd} & -\cos \Theta_{bd} \sin \Phi_{bd} & \sin \Theta_{bd} \\ \sin \Phi_{bd} & \cos \Phi_{bd} & 0 \\ -\sin \Theta_{bd} \cos \Phi_{bd} & \sin \Theta_{bd} \sin \Phi_{bd} & \cos \Theta_{bd} \end{pmatrix}. \quad (2-75)$$

On the basis of such a transformation, the description of the incident fields $\mathbf{E}^{(i)}(E_u, E_v, E_w)$ and $\mathbf{H}^{(i)}(H_u, H_v, H_w)$ in the beam coordinates $O_B\text{-}uvw$ can be transformed to their counterparts $\mathbf{E}^{(i)}(E_x, E_y, E_z)$ and $\mathbf{H}^{(i)}(H_x, H_y, H_z)$ in particle coordinates $O_P\text{-}xyz$:

$$\begin{cases} E_x = \cos \Theta_{bd} \cos \Phi_{bd} E_u - \cos \Theta_{bd} \sin \Phi_{bd} E_v + \sin \Theta_{bd} E_w \\ E_y = \sin \Phi_{bd} E_u + \cos \Phi_{bd} E_v \\ E_z = -\sin \Theta_{bd} \cos \Phi_{bd} E_u + \sin \Theta_{bd} \sin \Phi_{bd} E_v + \cos \Theta_{bd} E_w \end{cases}. \quad (2-76)$$

Via projection, the x , y and z components of the incident fields can be transformed to the spherical coordinates (r, θ, ϕ) . And for the BSC evaluation, only the r components of incident electromagnetic fields are required:

$$E_r^{(i)} = \sin \theta \cos \phi E_x + \sin \theta \sin \phi E_y + \cos \theta E_z, \quad (2-77)$$

$$H_r^{(i)} = \sin \theta \cos \phi H_x + \sin \theta \sin \phi H_y + \cos \theta H_z. \quad (2-78)$$

Substituting Eqs. (2-77) and (2-78), respectively, into Eqs.(2-72) and (2-73) yields the spherical BSCs, $(g_{n,TE}^m, g_{n,TM}^m)$.

Through expansion of the spherical harmonics $P_n^m(\cos \theta)z_n(kr)$ into summation of spheroidal ones $S_{mn}(c, \eta)R_{mn}(c, \xi)$ and invoking the relationship between the unit vectors in spherical and spheroidal coordinates, Han et al. (2001a, 2003) obtained the relations between the spherical vector wave functions $(\mathbf{m}_{mn}, \mathbf{n}_{mn})$ and the spheroidal ones $(\mathbf{M}_{mn}, \mathbf{N}_{mn})$ for positive mode of m . However, for the scattering of a spheroid with arbitrary orientation and location in a shaped beam, both positive and negative modes of m are needed. Therefore the relations between $(\mathbf{m}_{mn}, \mathbf{n}_{mn})$ and $(\mathbf{M}_{mn}, \mathbf{N}_{mn})$ for all modes of m are necessary. After a careful derivation, following relation is found:

$$\mathbf{m}_{mn}^{(i)}(r, \theta, \phi) = \sum_{l=|m|, |m|+1}^{\infty} \frac{2(n+|m|)!}{(2n+1)(n-|m|)!} \frac{i^{l-n}}{N_{|m|l}} d_{n-|m|l}^{m|l} \mathbf{M}_{ml}^{(i)}(c; \xi, \eta, \phi), \quad (2-79)$$

$$\mathbf{n}_{mn}^{(i)}(r, \theta, \phi) = \sum_{l=|m|, |m|+1}^{\infty} ' \frac{2(n+|m|)!}{(2n+1)(n-|m|)!} \frac{i^{l-n}}{N_{|m|l}} d_{n-|m|}^{|m|l} \mathbf{N}_{ml}^{(i)}(c; \xi, \eta, \phi), \quad (2-80)$$

where the prime on the sum symbol indicates that the summation starts from $\begin{Bmatrix} 0 \\ 1 \end{Bmatrix}$ over $\begin{Bmatrix} \text{even} \\ \text{odd} \end{Bmatrix}$ indices of r when $(n-|m|)$ is $\begin{Bmatrix} \text{even} \\ \text{odd} \end{Bmatrix}$.

Substitution of Eqs.(2-79) and (2-80) into Eqs. (2-67)-(2-68) leads to the beam expansion in terms of spheroidal vector wave functions as indicated by Eqs. (2-8)-(2-9), with the spheroidal BSCs determined by:

$$G_{n,TE}^m = \frac{1}{N_{|m|n}(c_1)} \sum_{r=0,1}^{\infty} ' g_{r+|m|,TE}^m \frac{2(r+2|m|)!}{(r+|m|)(r+|m|+1)r!} d_r^{|m|n}(c_1), \quad (2-81)$$

$$G_{n,TM}^m = \frac{1}{N_{|m|n}(c_1)} \sum_{r=0,1}^{\infty} ' g_{r+|m|,TM}^m \frac{2(r+2|m|)!}{(r+|m|)(r+|m|+1)r!} d_r^{|m|n}(c_1). \quad (2-82)$$

Since the spheroidal angular functions S_{mn} can be expressed as the following sums of infinite series of the Legendre functions:

$$S_{mn}(c, \eta) = \sum_{r=0,1}^{\infty} ' d_r^{mn}(c) P_{|m|+r}^m(\cos \theta), \quad (2-83)$$

the expansion coefficients d_r^{mn} in the prolate spheroidal coordinates can be determined by solving a recurrence relationship obtained by substituting Eq. (2-83) into Eq.(2-5) (see Appendix A). And they can be normalized by N_{mn} :

$$N_{mn}(c) = \sum_{r=0,1}^{\infty} ' \frac{2(r+2|m|)!}{(2r+2|m|+1)r!} [d_r^{mn}(c)]^2. \quad (2-84)$$

2.2.3 Applicability of the classical localization principle

In addition to the quadrature method, the localized approximation which is based on the localization principle of van de Hulst (1957) is widely employed as an approximate method to evaluate the BSCs because of its high efficiency in computation (Gouesbet, 1990; Gouesbet et al., 1995; Maheu et al., 1989; Ren et al., 1992). Mathematically, it takes the operations of

$r=(n+1/2)/k_1$ and $\theta \rightarrow \pi/2$ on the r components of electromagnetic fields to simplify the integral.

From the viewpoint of the localization principle, each partial wave of order n in the particle's coordinate system corresponds to a localized ray (actually an annular bundle of rays) passing the origin of the spherical particle at a distance of $r=(n+1/2)/k_1$ along the positive direction of the z axis. Therefore, to employ the localization principle, there exists a premise that the beam containing the localized rays also propagates along the positive direction of the z axis in the particle's Cartesian coordinate system and has the same polarization direction (along the x axis) as the localized rays. Such a premise can be satisfied by the spherical particle when we set the beam coordinate system O_B-uvw parallel to the particle coordinate system O_P-xyz , as done in Lorenz-Mie theory and GLMT.

However, for a spheroidal particle, the z axis of its Cartesian coordinate system is defined by its symmetrical axis and the Cartesian coordinates of the beam and spheroid are not parallel to each other, as discussed in Subsection 2.2.2. In this case, the localization principle method cannot be applied. We take a beam obliquely incident on the spheroid for example. The localized rays contained in the beam propagate along positive direction of the w axis in its own coordinates O_B-uvw , while the partial waves in the particle's coordinates O_P-xyz require that the localized rays propagate along the z axis. Therefore the localization principle is invalid and we are forced to adopt the quadrature method instead for BSC evaluation.

As a straightforward proof to reveal the inapplicability of the localization principle, a plane wave is provided to be incident along the x axis of the Cartesian system of the particle; therefore we have $E_z=1$ and $E_y=E_x=0$. Substitution of these components of electromagnetic fields into Eq. (2-77) yields $E_r = \cos \theta E_z$. With a further localization operation of $\theta \rightarrow \pi/2$, we have $g_{n, TM}^m = 0$, which inevitably makes the all reconstructed radial components of the electric field identical to zero, obviously inconsistent with the original description of the incident fields.

Moreover, in localization principle, the localized ray is assumed to propagate along straight lines, which means that inaccuracies will be incurred when the beam is extremely focused. This will be exemplified in Subsection 2.2.5.

2.2.4 Field reconstruction from spheroidal beam shape coefficients

To verify the accuracy of the evaluated BSCs in spheroidal coordinates, comparison of the reconstructed fields can be made with the original ones. All the components of the incident fields can be reconstructed from spheroidal BSCs via following formulas, which originate from Eqs. (2-8) and (2-9):

$$E_{\xi} = \sum_{m=-\infty}^{\infty} \sum_{n=|m|, n \neq 0}^{\infty} i^{n+1} \left[iG_{n,TE}^m M_{mn,\xi}^{(i)} + G_{n,TM}^m N_{mn,\xi}^{(i)} \right], \quad (2-85)$$

$$E_{\eta} = \sum_{m=-\infty}^{\infty} \sum_{n=|m|, n \neq 0}^{\infty} i^{n+1} \left[iG_{n,TE}^m M_{mn,\eta}^{(i)} + G_{n,TM}^m N_{mn,\eta}^{(i)} \right], \quad (2-86)$$

$$E_{\phi} = \sum_{m=-\infty}^{\infty} \sum_{n=|m|, n \neq 0}^{\infty} i^{n+1} \left[iG_{n,TE}^m M_{mn,\phi}^{(i)} + G_{n,TM}^m N_{mn,\phi}^{(i)} \right], \quad (2-87)$$

$$H_{\xi} = -\frac{ik_1}{\omega\mu_0} \sum_{m=-\infty}^{\infty} \sum_{n=|m|, n \neq 0}^{\infty} i^{n+1} \left[G_{n,TM}^m M_{mn,\xi}^{(i)} + iG_{n,TE}^m N_{mn,\xi}^{(i)} \right], \quad (2-88)$$

$$H_{\eta} = -\frac{ik_1}{\omega\mu_0} \sum_{m=-\infty}^{\infty} \sum_{n=|m|, n \neq 0}^{\infty} i^{n+1} \left[G_{n,TM}^m M_{mn,\eta}^{(i)} + iG_{n,TE}^m N_{mn,\eta}^{(i)} \right], \quad (2-89)$$

$$H_{\phi} = -\frac{ik_1}{\omega\mu_0} \sum_{m=-\infty}^{\infty} \sum_{n=|m|, n \neq 0}^{\infty} i^{n+1} \left[G_{n,TM}^m M_{mn,\phi}^{(i)} + iG_{n,TE}^m N_{mn,\phi}^{(i)} \right], \quad (2-90)$$

where the ξ , η , and ϕ components of the spheroidal vector wave functions $\mathbf{M}_{mn}^{(i)}$ and $\mathbf{N}_{mn}^{(i)}$ are listed in Appendix B.

Our objective is to directly compare original and reconstructed incident electromagnetic fields in Cartesian coordinates; therefore the description of the incident field in the spheroidal coordinates (ξ, η, ϕ) should be transformed to its counterpart in the Cartesian system (x, y, z) via unit vector relationship as follows (Korn and Korn, 1968):

$$\begin{pmatrix} E_x \\ E_y \\ E_z \end{pmatrix} = \begin{pmatrix} \xi \left(\frac{1-\eta^2}{\xi^2 \mp \eta^2} \right)^{\frac{1}{2}} \cos \phi & -\eta \left(\frac{\xi^2 \mp 1}{\xi^2 \mp \eta^2} \right)^{\frac{1}{2}} \cos \phi & -\sin \phi \\ \xi \left(\frac{1-\eta^2}{\xi^2 \mp \eta^2} \right)^{\frac{1}{2}} \sin \phi & -\eta \left(\frac{\xi^2 \mp 1}{\xi^2 \mp \eta^2} \right)^{\frac{1}{2}} \sin \phi & \cos \phi \\ \eta \left(\frac{\xi^2 \mp 1}{\xi^2 \mp \eta^2} \right)^{\frac{1}{2}} & \xi \left(\frac{1-\eta^2}{\xi^2 \mp \eta^2} \right)^{\frac{1}{2}} & 0 \end{pmatrix} \times \begin{Bmatrix} E_\xi \\ E_\eta \\ E_\phi \end{Bmatrix}. \quad (2-91)$$

The Cartesian coordinates (x, y, z) should also be converted to spheroidal ones (ξ, η, ϕ) via the following coordinate transformation for a prolate spheroid:

$$\eta = \frac{2z}{\sqrt{x^2 + y^2 + z^2 + f^2 + 2fz} + \sqrt{x^2 + y^2 + z^2 + f^2 - 2fz}}, \quad (2-92)$$

$$\xi = \frac{\sqrt{x^2 + y^2 + z^2 + f^2 + 2fz} + \sqrt{x^2 + y^2 + z^2 + f^2 - 2fz}}{2f}, \quad (2-93)$$

and the following transformation for an oblate one:

$$\eta = \frac{\sqrt{2}z}{\sqrt{y^2 + z^2 + x^2 - f^2} + \sqrt{y^4 + 2y^2z^2 + 2y^2x^2 - 2y^2f^2 + z^4 + 2x^2z^2 + 2f^2z^2 + x^4 - 2f^2x^2 + f^4}}, \quad (2-94)$$

$$\xi = \frac{\sqrt{y^2 + z^2 + x^2 - f^2} + \sqrt{y^4 + 2y^2z^2 + 2y^2x^2 - 2y^2f^2 + z^4 + 2x^2z^2 + 2f^2z^2 + x^4 - 2f^2x^2 + f^4}}{\sqrt{2}f}. \quad (2-95)$$

In addition, for both prolate and oblate spheroids, ϕ can be calculated by

$$\begin{cases} \phi = \arctan(y/x), & x>0, y>0 \\ \phi = 2\pi + \arctan(y/x), & x>0, y<0 \\ \phi = \pi + \arctan(y/x), & x<0, y>0 \\ \phi = \pi + \arctan(y/x), & x<0, y<0 \end{cases}, \quad (2-96)$$

Equations (2-91)-(2-96) are used for the reconstruction of electromagnetic fields from BSCs at any point (x, y, z) of the Cartesian coordinates. Essentially, Eqs. (2-92)-(2-96) are calculated from the inverse relationship between Cartesian coordinates (x, y, z) and the spheroidal ones (ξ, η, ϕ) .

η , ϕ) as follows (Flammer, 1957):

$$\begin{cases} x = f(1-\eta^2)^{\frac{1}{2}}(\xi^2 \mp 1)^{\frac{1}{2}} \cos \phi \\ y = f(1-\eta^2)^{\frac{1}{2}}(\xi^2 \mp 1)^{\frac{1}{2}} \sin \phi, \\ z = f\eta\xi \end{cases} \quad (2-97)$$

where ξ , η , and ϕ have the ranges $\begin{Bmatrix} 1 \\ 0 \end{Bmatrix} \leq \xi \leq \infty$, $-1 \leq \eta \leq 1$, and $0 \leq \phi \leq 2\pi$, respectively. The

lower limit of the radial coordinate $\begin{Bmatrix} 1 \\ 0 \end{Bmatrix}$ refers to the $\begin{Bmatrix} \text{prolate} \\ \text{oblate} \end{Bmatrix}$ spheroid, as does the operation of $\{\mp\}$ in Eqs. (2-91) and (2-97).

As to the electromagnetic field reconstruction, it is noteworthy that an arbitrary set of the BSCs can be used to reconstruct the electromagnetic fields, well satisfying the Maxwell equations. Although the description of the incident beam, e.g., Davis's first-order (Davis, 1979) or Barton and Alexander's fifth-order (Barton and Alexander, 1989) description of the Gaussian beam, might not be strictly Maxwellian, different methods (Gouesbet et al., 1988) for BSC evaluation, including the quadrature method, finite series, or localized approximation, actually serve as different wave filters to extract the Maxwellian components from the original non-Maxwellian description of the incident fields described by the finite-order approximation. To evaluate the quality of BSCs from these different filters, the best criterion is to compare the reconstructed Maxwellian fields from them with the original ones. The set of BSCs leading to a best fit of these two fields can be considered as the best solution.

2.2.5 Validation of beam shape coefficients

First, we compare the spheroidal BSCs obtained by the proposed method with those obtained by Asano and Yamamoto (1975) for oblique incidence of the plane wave. In the paper of Asano and Yamamoto (1975), two basic polarization modes for plane wave incidence are discussed, i.e. the TM and TE modes, which correspond to the polarization angle Φ_{bd} defined in the present theory as 0° and -90° . Furthermore, the incidence angle defined by Asano and

Yamamoto is equivalent to Θ_{bd} defined in the present theory.

Table 2.1 Spheroidal beam shape coefficients for an oblique incident plane wave of $\lambda_0=0.6328 \mu\text{m}$, $w_0 \rightarrow \infty$, $\Theta_{bd}=45^\circ$ and $\Phi_{bd}=0^\circ$. The beam center O_B has the coordinates $x_0=y_0=z_0=0 \mu\text{m}$ in particle's coordinates $O_P\text{-}xyz$ and the spheroid has the eccentricity parameter $c_1=1.0$.

n, m	$iG_{n,TE}^m$	$G_{n,TM}^m$	f_{mn}	g_{mn}
$n=1, m=0$	(0, 0)	(1.1079, 0)	0	-1.1079
$n=2, m=0$	(0, 0)	(1.2124, 0)	0	-1.2124
$n=3, m=0$	(0, 0)	(0.9845, 0)	0	-0.9845
$n=1, m=1$	(-0.7607, 0)	(-0.5466, 0)	1.5213	1.0932
$n=2, m=1$	(-0.3031, 0)	(-0.0046, 0)	0.6063	0.0092
$n=3, m=1$	(-0.1183, 0)	(0.1698, 0)	0.2365	-0.3396
$n=2, m=2$	(-0.1477, 0)	(-0.1055, 0)	0.2953	0.2110
$n=3, m=2$	(-0.0740, 0)	(-0.0267, 0)	0.1480	0.0535
$n=3, m=3$	(-0.0182, 0)	(-0.0130, 0)	0.0364	0.0259

Table 2.2 Spheroidal beam shape coefficients of a parallel incidence of Gaussian beam of $\lambda_0=0.6328 \mu\text{m}$, $w_0=3\lambda_0$, and $\Theta_{bd}=\Phi_{bd}=0$. The beam center O_B has the coordinates in particle's coordinates $O_P\text{-}xyz$ $x_0=y_0=z_0=0 \mu\text{m}$ and the spheroid has the eccentricity parameter $c_1=1.0$. Attention should be paid to that in such a case of on-axis incidence, only the terms of $m=\pm 1$ in BSCs are involved and all the other coefficients of $|m|\neq 1$ are equal to zero.

n, m	$iG_{n,TE}^m$	$iG_{n,TE}^{-m}$	$G_{n,TM}^m$	$G_{n,TM}^{-m}$
$n=1, m=1$	(-0.7548, 0)	(0.7548, 0)	(-0.7548, 0)	(-0.7548, 0)
$n=2, m=1$	(-0.4196, 0)	(0.4196, 0)	(-0.4196, 0)	(-0.4196, 0)
$n=3, m=1$	(-0.2876, 0)	(0.2876, 0)	(-0.2876, 0)	(-0.2876, 0)
$n=4, m=1$	(-0.2184, 0)	(0.2184, 0)	(-0.2184, 0)	(-0.2184, 0)
$n=5, m=1$	(-0.1703, 0)	(0.1703, 0)	(-0.1703, 0)	(-0.1703, 0)
$n=6, m=1$	(-0.1396, 0)	(0.1396, 0)	(-0.1396, 0)	(-0.1396, 0)
$n=7, m=1$	(-0.1153, 0)	(0.1153, 0)	(-0.1153, 0)	(-0.1153, 0)
$n=8, m=1$	(-0.0974, 0)	(0.0974, 0)	(-0.0974, 0)	(-0.0974, 0)
$n=9, m=1$	(-0.0824, 0)	(0.0824, 0)	(-0.0824, 0)	(-0.0824, 0)
$n=10, m=1$	(-0.0705, 0)	(0.0705, 0)	(-0.0705, 0)	(-0.0705, 0)

Let a plane wave with the incidence angle $\Theta_{bd}=45^\circ$ and polarization angle $\Phi_{bd}=0^\circ$ incident on a spheroid of the eccentricity parameter 1.0 ($c_1=1.0$); the numerical results of spheroidal BSCs

($G_{n,TE}^m, G_{n,TM}^m$) can be found in Table 2.1. They are compared with the BSCs (f_{mn}, g_{mn}) obtained by Asano and Yamamoto (1975). Only the BSCs of positive modes (m) are given, since the negative ones ($-m$) can be obtained from those of positive ones via the following relationship:

$$\begin{cases} G_{n,TM}^m = G_{n,TM}^{-m} = -g_{mn} / 2, & m \geq 1 \\ G_{n,TM}^m = -g_{mn}, & m = 0 \end{cases}, \quad (2-98)$$

$$\begin{cases} G_{n,TE}^m = -G_{n,TE}^{-m} = if_{mn} / 2, & m \geq 1 \\ G_{n,TE}^m = if_{mn} = 0, & m = 0 \end{cases}. \quad (2-99)$$

When the polarization angle Φ_{bd} is -90° , we obtain

$$\begin{cases} G_{n,TM}^m = -G_{n,TM}^{-m} = -if_{mn} / 2, & m \geq 1 \\ G_{n,TM}^m = -if_{mn}, & m = 0 \end{cases}, \quad (2-100)$$

$$\begin{cases} G_{n,TE}^m = G_{n,TE}^{-m} = -g_{mn} / 2, & m \geq 1 \\ G_{n,TE}^m = -g_{mn} = 0, & m = 0 \end{cases}. \quad (2-101)$$

Eqs. (2-98)-(2-99) will be used in Subsection 2.3.1 to yield the same results of plane wave expansion in spheroidal coordinates as described by Asano and Yamamoto (1975) as the TM mode, while Eqs. (2-100) and (2-101) lead to the TE mode.

Second, we discuss the symmetry relationship between the BSCs of positive mode (+ m) and those of negative mode ($-m$) in spheroidal coordinates. The circular Gaussian beam is used for our demonstration calculation. The description of its electromagnetic fields can be recovered from that of an elliptical Gaussian beam (or ‘‘laser sheet,’’ described in Appendix E) by setting the beam-waist radii equal along the u and v axes, namely, $w_{0u}=w_{0v}$, and setting the astigmatism to be zero ($w_u=w_v=0$).

Consider such a beam of waist radius $w_0=3\lambda_0$ ($\lambda_0=0.6328 \mu\text{m}$) propagating along the positive z axis ($\Theta_{bd}=0^\circ$) and incident on a spheroid of eccentricity parameter $c_1=1.0$, its electric field polarized in the x direction ($\Phi_{bd}=0^\circ$), and its center located at $x_0=y_0=z_0=0 \mu\text{m}$, and we can find the following relationship for spheroidal BSCs of positive mode $m=1$ and negative mode $m=-1$ (some results are listed Table 2.2):

$$G_{n,TE}^{+1} = -G_{n,TE}^{-1} = \frac{1}{2} i g_{1n}, \quad (2-102)$$

$$G_{n,TM}^1 = G_{n,TM}^{-1} = \frac{1}{2} g_{1n}. \quad (2-103)$$

Actually, as indicated by Eqs. (2-81) and (2-82), the spheroidal BSCs are an infinite series of the spherical ones. Therefore all the symmetry relationships (Ren et al., 1994) between the spherical BSCs $g_{n,TE/TM}^{+m}$ and $g_{n,TE/TM}^{-m}$ for some shaped beam, e.g., a circular Gaussian beam or a laser sheet, are inherited by spheroidal BSCs. However, the premise is that the Cartesian coordinates of the beam and the particle are parallel to each other, namely, $\Theta_{bd}=\Phi_{bd}=0^\circ$.

Third, we use the spheroidal BSCs to reconstruct the incident fields. An extremely focused Gaussian beam of $w_0=1.0$ $\lambda_0=0.6328$ μm (with the far-field divergence angle $\theta_d=\lambda_0/(\pi w_0)=18.24^\circ$) is assumed to propagate along the z axis ($\Theta_{bd}=0^\circ$), its electric field is polarized in the x direction ($\Phi_{bd}=0^\circ$), and its center is located at $x_0=y_0=z_0=0$ μm . It is expanded in the spheroidal coordinates corresponding to a particle of eccentricity parameter $c_1=1$. As shown in Fig. 2.3, the reconstructed field of E_x from the BSCs calculated by the localization principle deviates $\sim 5\%$ from the original one near the beam axis while the reconstructed field E_x from BSCs calculated by quadrature coincides well with the original one. As analyzed in Subsection 2.2.3, such a deviation is caused by the localization principle, which supposed all the localized rays propagate along the positive z axis. Strictly speaking, it can be satisfied only when on-axis plane wave incidence is concerned. Because of the change of the wavefront curvature radius during the propagation, the geometrical rays contained in a Gaussian beam do not propagate along straight lines, especially when the beam is extremely focused and has a large divergence angle. Our numerical results show that for on-axis beam incidence, a good reconstruction can be achieved when the divergence angle of the Gaussian beam is less than $\theta_d \leq 5^\circ$.

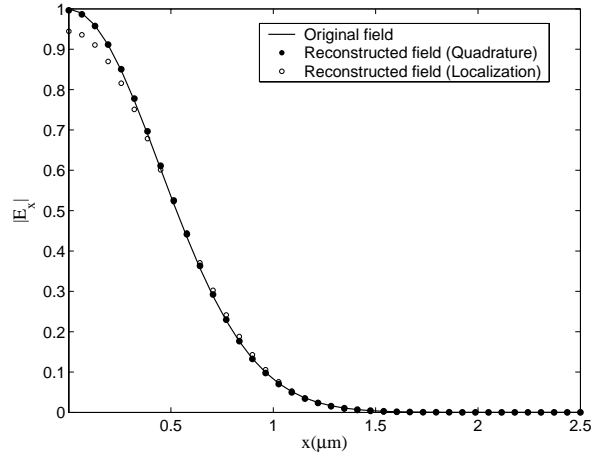


Fig. 2.3 Reconstruction of $E_x(x, 0, 0)$ of a highly focused Gaussian beam with $w_0=\lambda_0=0.6328 \mu\text{m}$ from the spheroidal BSCs calculated by localization principle and quadrature method. Location of the beam center is $x_0=y_0=z_0=0$ and the angle set is $(\Theta_{\text{bd}}=\Phi_{\text{bd}}=0^\circ)$.

To exemplify numerically the inapplicability of the localized principle in the case of oblique incidence, comparison of the reconstructed fields from localization principle and quadrature method are made for an astigmatic laser sheet of $w_{0u}=1.0 \mu\text{m}$, $w_{0v}=1.5 \mu\text{m}$, and $\Theta_{\text{bd}}=\Phi_{\text{bd}}=45^\circ$. The locations of the waists along the u and v axes, w_u and w_v , are set as 0 and 5 μm , respectively. As illustrated by Fig. 2.4, the reconstructed x component of the Maxwellian electric field from the BSCs calculated by the localization principle deviates much from the original one at the plane $\phi=0^\circ$, while the BSCs calculated by quadrature method again lead to satisfactory reconstruction.

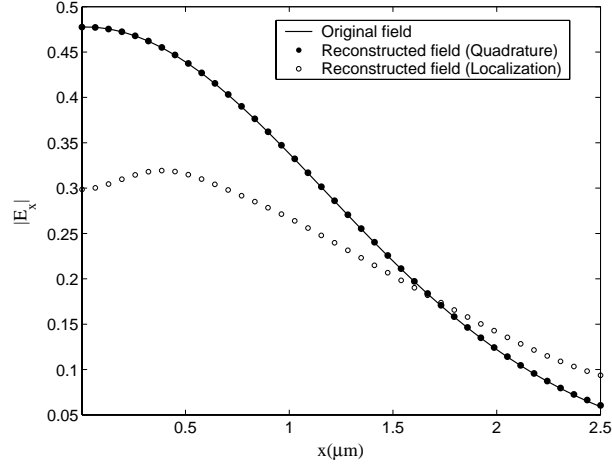


Fig. 2.4 Reconstruction of $E_x(x, 0, 0)$ of an astigmatic elliptical Gaussian beam from the spheroidal BSCs calculated by localization principle and quadrature method. The beam has the waist radii of $w_{0u}=1.0 \mu\text{m}$, $w_{0v}=1.5 \mu\text{m}$, wavelength $\lambda_0=0.6328 \mu\text{m}$ and the center location $x_0=y_0=z_0=0$. The angle set of the beam is $\Theta_{bd}=45^\circ$ and $\Phi_{bd}=45^\circ$. The locations of the waists along u- and v- axes, w_u and w_v , are set as 0 and $5 \mu\text{m}$, respectively.

2.3 Special cases

The results for an arbitrarily oriented shaped beam scattering by a spheroid should also stand for the special case of a beam scattering by a sphere as well as for oblique plane wave scattering by a spheroid. As a check, we demonstrate in this subsection that these special cases can be recovered from the above spheroidal scattering theory.

2.3.1 Plane wave incidence

The spheroidal vector wave functions are related to the odd and even terms as follows:

$$\mathbf{M}_{mn} = \mathbf{M}_{emn} + i\mathbf{M}_{omn}, \quad (2-104)$$

$$\mathbf{N}_{mn} = \mathbf{N}_{emn} + i\mathbf{N}_{omn}. \quad (2-105)$$

The complete expressions of the odd and even terms of $(\mathbf{M}_{mn}, \mathbf{N}_{mn})$ are given in Appendix B. As indicated by Eq.(2-3), in spheroidal coordinates the scalar function ψ is defined by angular and radial functions of absolute mode $|m|$. Therefore they have the following symmetry relationships:

$$\begin{cases} \mathbf{M}_{emn} = \mathbf{M}_{e(-m)n} \\ \mathbf{M}_{omn} = -\mathbf{M}_{o(-m)n} \end{cases}, \quad (2-106)$$

$$\begin{cases} \mathbf{N}_{emn} = \mathbf{N}_{e(-m)n} \\ \mathbf{N}_{omn} = -\mathbf{N}_{o(-m)n} \end{cases}. \quad (2-107)$$

Accordingly, Eqs.(2-8) and (2-9) can be rewritten as

$$\mathbf{E}^{(i)} = \sum_{m=0}^{\infty} \sum_{n=m, n \neq 0}^{\infty} i^{n+1} \frac{(2-\delta_{0m})}{2} \left[i(G_{n,TE}^m + G_{n,TE}^{-m}) \mathbf{M}_{emn}^{(i)} - (G_{n,TE}^m - G_{n,TE}^{-m}) \mathbf{M}_{omn}^{(i)} \right. \\ \left. + (G_{n,TM}^m + G_{n,TM}^{-m}) \mathbf{N}_{emn}^{(i)} + (G_{n,TM}^m - G_{n,TM}^{-m}) i \mathbf{N}_{omn}^{(i)} \right], \quad (2-108)$$

$$\mathbf{H}^{(i)} = -\frac{ik_1}{\omega\mu_0} \sum_{m=0}^{\infty} \sum_{n=m, n \neq 0}^{\infty} i^{n+1} \frac{(2-\delta_{0m})}{2} \left[(G_{n,TM}^m + G_{n,TM}^{-m}) \mathbf{M}_{emn}^{(i)} + (G_{n,TM}^m - G_{n,TM}^{-m}) i \mathbf{M}_{omn}^{(i)} \right. \\ \left. + i(G_{n,TE}^m + G_{n,TE}^{-m}) \mathbf{N}_{emn}^{(i)} - (G_{n,TE}^m - G_{n,TE}^{-m}) \mathbf{N}_{omn}^{(i)} \right]. \quad (2-109)$$

Since for the case of plane wave incidence of the TM mode that corresponds to $\Theta_{bd}=\zeta$ (ζ is the incidence angle, see Asano and Yamamoto (1975)) and $\Phi_{bd}=0^\circ$, the symmetry relationships indicated by Eqs.(2-98)-(2-99) are found for the spheroidal BSCs of positive mode $+m$ and negative mode $-m$. Substituting them into Eqs.(2-108) and (2-109), we have

$$\mathbf{E}^{(i)} = \sum_{m=0}^{+\infty} \sum_{n=m, n \neq 0}^{+\infty} i^n (f_{mn} \mathbf{M}_{omn}^{(i)} - ig_{mn} \mathbf{N}_{emn}^{(i)}), \quad (2-110)$$

$$\mathbf{H}^{(i)} = -\frac{k_1}{\omega\mu_0} \sum_{m=0}^{+\infty} \sum_{n=m, n \neq 0}^{+\infty} i^n (g_{mn} \mathbf{M}_{emn}^{(i)} + if_{mn} \mathbf{N}_{omn}^{(i)}), \quad (2-111)$$

which are exactly same with Asano and Yamamoto's expansion for plane wave incidence, with the following description in Cartesian coordinates of the particle:

$$\mathbf{E}^{(i)} = -(\mathbf{i} \cos \zeta - \mathbf{k} \sin \zeta) \exp[ik_1(x \sin \zeta + z \cos \zeta)], \quad (2-112)$$

$$\mathbf{H}^{(i)} = -\frac{k_1}{\omega\mu_0} \mathbf{j} \exp[ik_1(x \sin \zeta + z \cos \zeta)]. \quad (2-113)$$

Next, let $\Theta_{bd}=\zeta$ and $\Phi_{bd}=-90^\circ$ and use the symmetry relationships indicated by Eqs. (2-100) and (2-101), Eqs.(2-108) and (2-109) become

$$\mathbf{E}^{(i)} = \sum_{m=0}^{\infty} \sum_{n=m, n \neq 0}^{\infty} i^n [g_{mn} \mathbf{M}_{emn}^{(i)} + f_{mn} i \mathbf{N}_{omn}^{(i)}], \quad (2-114)$$

$$\mathbf{H}^{(i)} = \frac{k_1}{\omega\mu_0} \sum_{m=0}^{\infty} \sum_{n=m, n \neq 0}^{\infty} i^n [f_{mn} \mathbf{M}_{omn}^{r(i)} - ig_{mn} \mathbf{N}_{emn}^{r(i)}]. \quad (2-115)$$

Namely the TE mode description for plane wave incidence is then recovered, leading to the

description in Cartesian coordinates of the particle as follows:

$$\mathbf{E}^{(i)} = -\mathbf{j} \exp[ik_1(x \sin \zeta + z \cos \zeta)], \quad (2-116)$$

$$\mathbf{H}^{(i)} = \frac{k_1}{\omega\mu_0} (\mathbf{i} \cos \zeta - \mathbf{k} \sin \zeta) \exp[ik_1(x \sin \zeta + z \cos \zeta)]. \quad (2-117)$$

Eqs. (2-114)-(2-117) agree with Asano and Yamamoto's description of incident fields of the TE mode indicated by Eqs. (2-21)-(2-23).

Similar retrievals also exist for the internal and scattering fields ($\mathbf{E}^{(i)}$, $\mathbf{H}^{(i)}$) and ($\mathbf{E}^{(s)}$, $\mathbf{H}^{(s)}$). Thus we conclude that the current theory is consistent with the case of plane wave scattering by a spheroid.

2.3.2 Spherical particle scattering

When $a/b=1$, the spheroid becomes a sphere. In this case, the semifocal length of the spheroid f and the dimensionless eccentricity parameter of the spheroid c_1 also tend to zero. The spheroidal expansion coefficients become

$$d_{n-|m|}^{l|m|}(0) = \begin{cases} 0 & n \neq l \\ 1 & n = l \end{cases}. \quad (2-118)$$

Replacing r by $l-m$ and substituting l by n , Eqs. (2-79) and (2-80) become

$$\mathbf{m}_{mn}^{(i)}(r, \theta, \phi) = \frac{2(n+|m|)!}{(2n+1)(n-|m|)! N_{|m|n}} \mathbf{M}_{mn}^{(i)}(0; \eta, \xi, \phi), \quad (2-119)$$

$$\mathbf{n}_{mn}^{(i)}(r, \theta, \phi) = \frac{2(n+|m|)!}{(2n+1)(n-|m|)! N_{|m|n}} \mathbf{N}_{mn}^{(i)}(0; \eta, \xi, \phi). \quad (2-120)$$

Also, the spheroidal BSCs expressed by Eqs. (2-81) and (2-82) become

$$G_{n,TE}^m = \frac{1}{N_{|m|n}} \frac{2(n+|m|)!}{n(n+1)(n-|m|)!}, \quad (2-121)$$

$$G_{n,TM}^m = \frac{1}{N_{|m|n}} \frac{2(n+|m|)!}{n(n+1)(n-|m|)!}, \quad (2-122)$$

where

$$N_{|m|} = \frac{2(n+|m|)!}{(2n+1)(n-|m|)!}. \quad (2-123)$$

Therefore the BSCs become

$$G_{n,TE}^m = C_n^{pw} g_{n,TE}^m, \quad (2-124)$$

$$G_{n,TM}^m = C_n^{pw} g_{n,TM}^m, \quad (2-125)$$

where the plane wave term C_n^{pw} is given by Eq.(2-69).

Meanwhile, substituting Eq. (2-123) into Eqs. (2-119) and (2-120) leads to the degeneracy of the spheroidal vector wave functions to the spherical ones:

$$\mathbf{m}_{mn}^{(i)}(r, \theta, \phi) = \mathbf{M}_{mn}^{(i)}(0; \eta, \xi, \phi), \quad (2-126)$$

$$\mathbf{n}_{mn}^{(i)}(r, \theta, \phi) = \mathbf{N}_{mn}^{(i)}(0; \eta, \xi, \phi), \quad (2-127)$$

Substituting Eqs.(2-124)-(2-127) into the incident field expansion in spheroidal coordinates indicated by Eqs. (2-8) and (2-9) leads to the field description in spherical coordinates indicated by Eqs.(2-67) and (2-68). And similar retrievals also exist for the internal and scattered fields. Thus we can end this part of the discussion with the conclusion that arbitrary shaped beam scattering by a sphere can be recovered from the theory for a spheroid when the semifocal length becomes zero.

2.4 Numerical results

The general Lorenz-Mie theory for a spheroid has been developed in Sections 2.1-2.2. Two special cases, plane wave scattering by a spheroid and shaped beam scattering by a sphere are found retrievable from the current theory. In this section, we carry out the numerical validation of the current theory. On such a basis, more demonstration calculations of far-field scattering, extinction crosssection, and radiation pressure force are performed for the cases of interests to us.

2.4.1 Far-field scattering

To compare with Asano and Yamamoto's results for the special case of plane wave incidence (Asano and Yamamoto, 1975), we calculate the far-field plane wave scattering by a prolate spheroid of axis ratio $a/b=2.0$ and eccentricity parameter $c_1=1.0$. The particle is assumed to be a small water droplet suspended in air so that the relative refractive index $\hat{m} = \hat{m}_{\text{II}} / \hat{m}_1 = 1.333$. The plane wave of wavelength $\lambda_0=0.6328 \mu\text{m}$ has the incidence angle $\Theta_{\text{bd}}=45^\circ$ and polarization angle $\Phi_{\text{bd}}=-90^\circ$, corresponding to the TE mode (Asano and Yamamoto, 1975). The scattering patterns illustrated in Fig. 2.5 are the same as those in Fig. 6 given by Asano and Yamamoto (1975). A rotation of angle from $\Phi_{\text{bd}}=-90^\circ$ to $\Phi_{\text{bd}}=0^\circ$ brings out the TM mode, which has the scattering profiles shown in Fig. 2.6, being the same as Fig. 8 given by Asano and Yamamoto (1975).

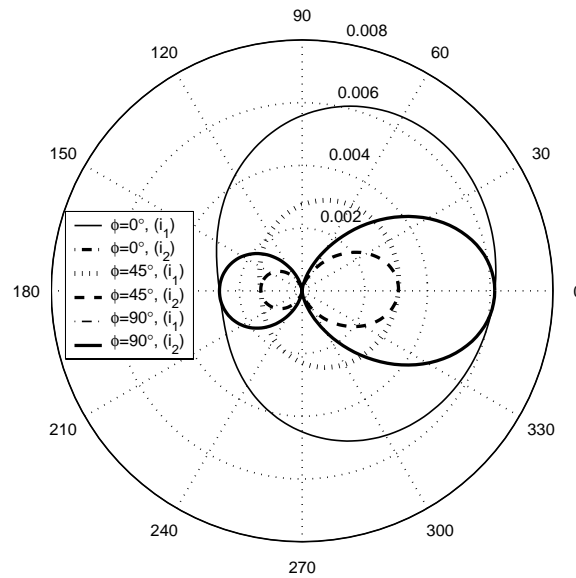


Fig. 2.5 Plane wave scattering by a prolate spheroid of $a/b=2.0$ and eccentricity parameter $c_1=1$. The particle is assumed to be a small water droplet suspended in the air so that the relative refractive index $\hat{m}=\hat{m}_{\text{II}}/\hat{m}_1=1.333$. The plane wave of wavelength $\lambda_0=0.6328 \mu\text{m}$ has the incidence angle $\Theta_{\text{bd}}=45^\circ$ and polarization angle $\Phi_{\text{bd}}=-90^\circ$, corresponding to the TE mode. The figure is same as Fig. 6 given by given by Asano and Yamamoto (1975). Note that for $\phi=0^\circ$ and $\phi=90^\circ$, $i_2=0$.

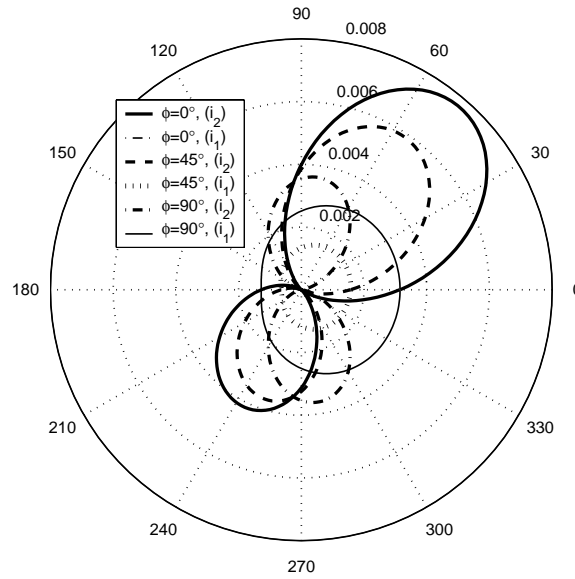


Fig. 2.6 Same as Fig. 2.5 but for TM mode. This figure is same as Asano's Fig. 8 given by Asano and Yamamoto (1975). Note that for $\phi = 0^\circ$, $i_1 = 0$.

Then, we compare the numerical results of the scattered fields of a spheroid of axis ratio $a/b \rightarrow 1$ to those obtained by GLMT for a sphere in the case of on-axis laser sheet illumination. A laser sheet of waist radii $w_{0x} = 1.0 \mu\text{m}$ and $w_{0y} = 1.5 \mu\text{m}$, and wavelength $\lambda_0 = 0.6328 \mu\text{m}$ is incident on a prolate spheroid of axis ratio $a/b = 1.0001$ and semiminor axis length $0.5 \mu\text{m}$ ($b = 0.5 \mu\text{m}$). The electromagnetic fields of a laser sheet are given in Appendix E. The scattering patterns for the three azimuthal angles $\phi = 0^\circ$, 45° and 90° are presented in Fig. 2.7 and compared with those obtained by the GLMT for a sphere of radius $0.5 \mu\text{m}$ ($r = 0.5 \mu\text{m}$) and the same refractive index. As a result, excellent agreement is found, since the axis ratio of the spheroid a/b tends to 1 in this case.

When the sphere deviates more from the sphere, e.g., for a prolate spheroid of axis ratio $a/b = 1.2$, its scattering pattern at the forward angles differ only slightly from that of a spherical particle, as seen from the comparison of Fig. 2.7 with Fig. 2.8. This is because the prolate spheroids with $a/b = 1.2$ (Fig. 2.8) and $a/b = 1.0001$ (Fig. 2.7) have the same projection area (πb^2) for forward diffraction. At larger angles, the scattered intensities are obviously different since the scattering patterns are dominated by reflection and refraction, which are greatly affected by the surface curvature of the particle. As to the oblate spheroid, the forward diffraction is enhanced due to a

larger projection area ($=\pi a^2$), as indicated by Fig. 2.9.

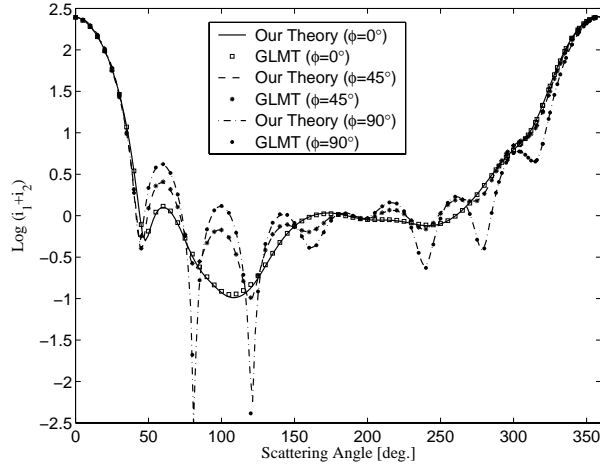


Fig. 2.7 Laser sheet scattering by a prolate spheroid of refractive index $\hat{m}=1.33$, axis ratio $a/b=1.0001$, and semi-minor axis $b=0.5 \mu\text{m}$. The parameters for the beam are $w_{0x}=1.0 \mu\text{m}$, $w_{0y}=1.5 \mu\text{m}$, $\lambda_0=0.6328 \mu\text{m}$, $\Theta_{\text{bd}}=\Phi_{\text{bd}}=0^\circ$. Its center O_B has coordinates $x_0=y_0=0.5 \mu\text{m}$ and $z_0=0.0 \mu\text{m}$ in the particle system $O_P\text{-}xyz$. The particle is assumed to be suspended in the air. In the GLMT's calculation for the sphere, its radius is given as $r=0.5 \mu\text{m}$.

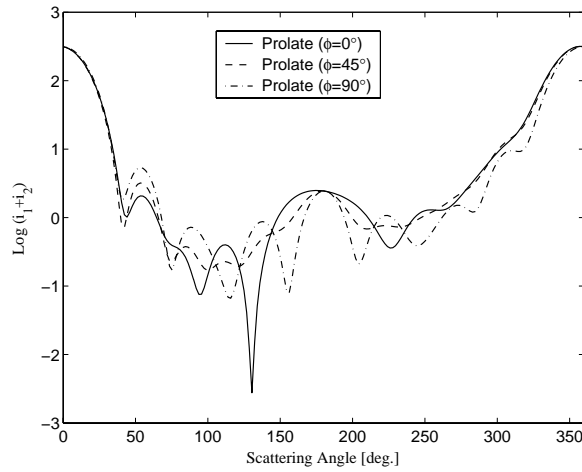


Fig. 2.8 Laser sheet scattering by a prolate water spheroid of refractive index $\hat{m}=1.33$, axis ratio $a/b=1.2$, semi-minor axis $b=0.5 \mu\text{m}$. The parameters for the beam are $w_{0x}=1.0 \mu\text{m}$, $w_{0y}=1.5 \mu\text{m}$, $\lambda_0=0.6328 \mu\text{m}$, $\Theta_{\text{bd}}=\Phi_{\text{bd}}=0^\circ$. Its center O_B has the coordinates $x_0=y_0=0.5 \mu\text{m}$ and $z_0=0.0 \mu\text{m}$ in the particle system $O_P\text{-}xyz$. The particle is assumed to be suspended in the air.

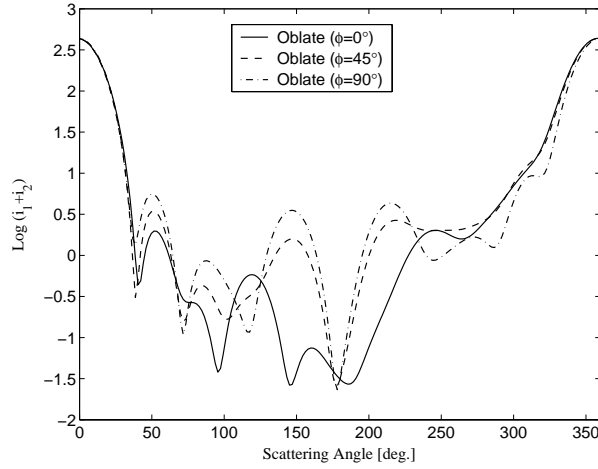


Fig. 2.9 Same as Fig. 2.8, but for an oblate spheroid of $a/b=1.2$.

Finally, we examine the scattering diagram for different incident angles. Keeping the polarization angle Φ_{bd} being 0° and changing the incident angle Θ_{bd} from 0° to 45° , and then to 90° , we find that the main peak at the scattering plane $\phi=0^\circ$ moves from 0° to 45° (Fig. 2.10) and then to 90° (Fig. 2.11). Attention should be paid to the fact that for the special case of side-on incidence ($\Theta_{bd}=90^\circ$ and $\Phi_{bd}=0^\circ$, Fig. 2.11), the scattering plane $\phi=0^\circ$ is where \mathbf{H}_i lies in and is perpendicular to the incident plane defined in the coordinates of the beam. And the scattering plane $\phi=90^\circ$ is the incident plane where \mathbf{E}_i lies in. Both the scattering intensities and the incident intensities of the beam at these two planes have peaks along the propagation direction of the beam (corresponding to the scattering angle $\theta=90^\circ$). For the incident fields, the peak is due to the Gaussian distribution of amplitude while for the scattered fields it is due to the diffraction, although it is not as remarkable as that in the plane $\phi=0^\circ$. However, in the scattering plane of $\phi=45^\circ$ (Fig. 2.11) neither the incident fields nor the scattered ones keep such a peak.

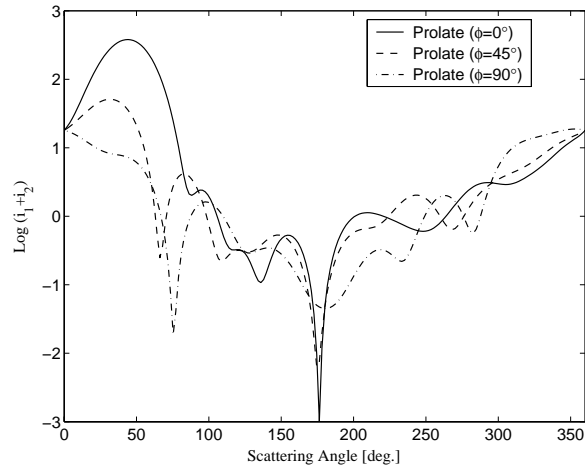


Fig. 2.10 Same as Fig. 2.8 but $\Theta_{bd}=45^\circ$.

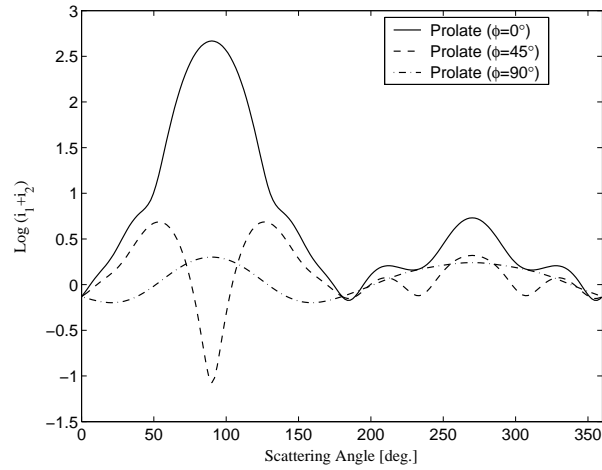


Fig. 2.11 Same as Fig. 2.8 but $\Theta_{bd}=90^\circ$.

In addition, changing the refractive index from $\hat{m}=1.333$ to $\hat{m}=1.333+0.1i$ weakens scattering intensities at all scattering angles due to absorption by the particle, as observed from a comparison of Fig. 2.12 with Fig. 2.11.

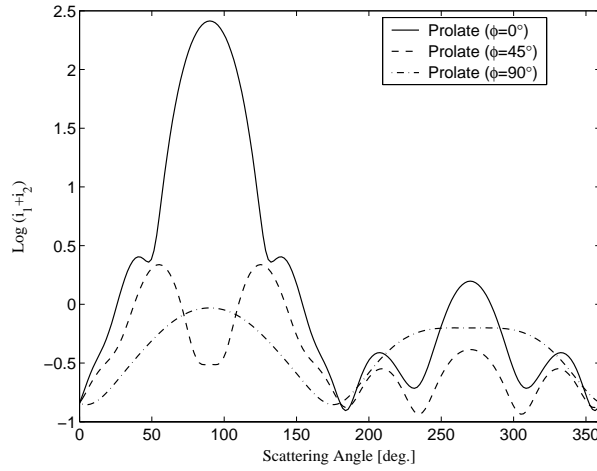


Fig. 2.12 Same as Fig. 2.11 but $\hat{m}=1.333+0.1i$.

2.4.2 Scattering and extinction crosssections

To verify our formulas of scattering and extinction crosssections, numerical calculations have been done in the case of plane wave illumination. And good agreement with the results obtained by Asano and Yamamoto (1975) has been found.

Then, scattering and extinction crosssections versus the axis ratio a/b for the prolate spheroids of same semiminor axis length $0.5 \mu\text{m}$ ($b=0.5 \mu\text{m}$) illuminated by a laser sheet are calculated and illustrated in Fig. 2.13 and Fig. 2.14. The beam of wavelength $\lambda_0=0.6328 \mu\text{m}$ is assumed to have an incidence angle $\Theta_{\text{bd}}=0^\circ$ and polarization angle $\Phi_{\text{bd}}=0^\circ$. The beam waist radii along the u and v axes are 1.0 and $1.5 \mu\text{m}$, respectively ($w_{0u}=1.0 \mu\text{m}$ and $w_{0v}=1.5 \mu\text{m}$). The center of the beam is located at O_P . Five curves are plotted in Fig. 2.13 and Fig. 2.14 for different refractive indices $\hat{m} = 1.333, 1.333+0.005i, 1.333+0.01i, 1.333+0.05i, \text{ and } 1.333+0.1i$. An interesting phenomenon is that when the axis ratio a/b increases from 1 to 2, the scattering and extinction crosssections C_{ext} and C_{sca} first increase to a stable value corresponding to the axis ratio around 1.4, and then decreases rapidly with the growth of a/b . But for oblique incidence, when the incidence angle is $\Theta_{\text{bd}}=45^\circ$, only monotonically increasing relations between C_{sca} and C_{ext} and a/b are found, as indicated by Fig. 2.15 and Fig. 2.16. These relations are also observed for plane wave parallel incidence along the z axis and oblique incidence.

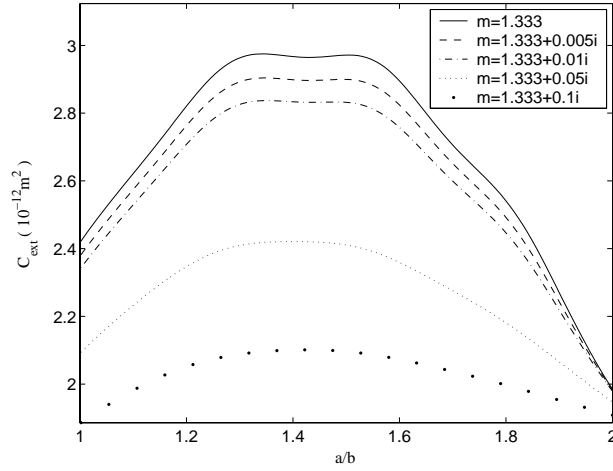


Fig. 2.13 Extinction crosssection C_{ext} versus axis ratio a/b of the spheroid. The beam with parameters $\Theta_{\text{bd}}=0^\circ$, $\Phi_{\text{bd}}=0^\circ$, $x_0=y_0=z_0=0 \mu\text{m}$, $w_{0x}=1.0 \mu\text{m}$, $w_{0y}=1.5 \mu\text{m}$, and $\lambda_0=0.6328 \mu\text{m}$ illuminates the prolate spheroid of semi-minor axis length $b=0.5 \mu\text{m}$. The particle is assumed suspended in the air. Five curves are plotted in the figures for particles of refractive indices $\hat{m}=1.333$, $1.333+0.005i$, $1.333+0.01i$, $1.333+0.05i$, and $1.333+0.1i$, respectively.

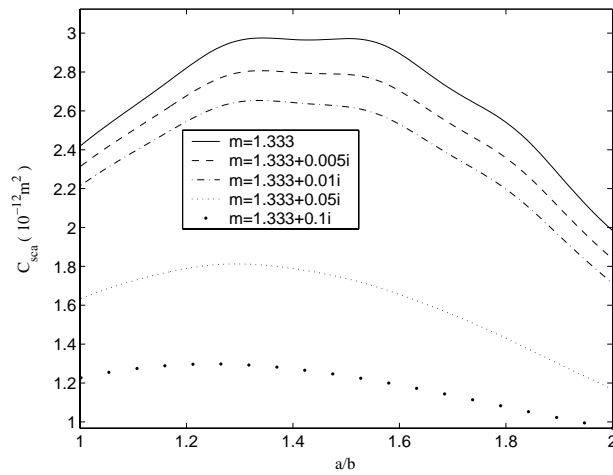


Fig. 2.14 Scattering crosssection C_{sca} versus axis ratio a/b of the spheroid. Parameters of the incident beam and the prolate spheroid are the same as those in Fig. 2.13.

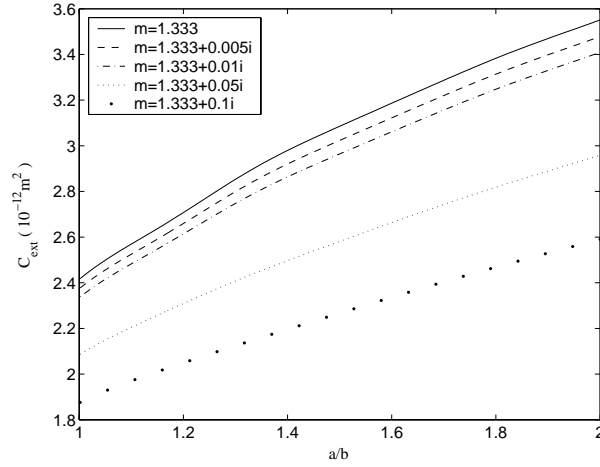


Fig. 2.15 Extinction crosssection C_{ext} versus axis ratio a/b of the spheroid. Parameters of the incident beam and the prolate spheroid are the same as those in Fig. 2.13 except $\Theta_{\text{bd}}=45^\circ$.

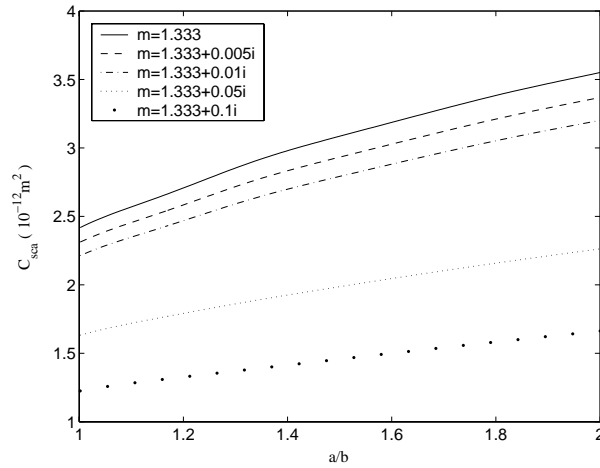


Fig. 2.16 Scattering crosssection C_{sca} versus axis ratio a/b of the spheroid. Parameters of the incident beam and the prolate spheroid are the same as those in Fig. 2.15.

Next, we study the behavior of scattering crosssection versus the eccentricity parameter of the spheroid, c_1 . The same laser sheet as the one used in Fig. 2.13- Fig. 2.16 illuminates the prolate spheroid of semiminor axis length $b=0.5\mu\text{m}$ and axis ratio $a/b=2.0$. We use a real refractive index $\hat{m}=1.333$ so that $C_{\text{ext}}=C_{\text{sca}}$. Five curves are plotted for the incidence angles $\Theta_{\text{bd}}=0^\circ, 22.5^\circ, 45^\circ, 67.5^\circ,$ and 90° , respectively. We can observe in Fig. 2.17 that the differences among the C_{sca} curves associated with $\Theta_{\text{bd}}=45^\circ, 67.5^\circ,$ and 90° are much less significant than those among the curves associated with $\Theta_{\text{bd}}=0^\circ, 22.5^\circ,$ and 45° . Such a phenomenon is also observed for plane

wave incidence, which is obtained by taking the beam-waist radii to be infinity. This means that for the small prolate droplet of eccentricity parameter $c_1 \leq 10$, the quantity of the scattered energy is not affected too much by the incidence angle when Θ_{bd} is larger than 45° .

Finally, we study the scattering crosssection for different polarization angles. The incidence angle is kept to be $\Theta_{bd}=45^\circ$ and the polarization angles Φ_{bd} varies from 0° to 45° , and then to 90° , the curves of C_{sca} do not change much for $1 \leq c_1 \leq 10$, as indicated by Fig. 2.18. This means that quantity of the scattered energy by small prolate droplets is not sensitive to the polarization angle Φ_{bd} in the current case.

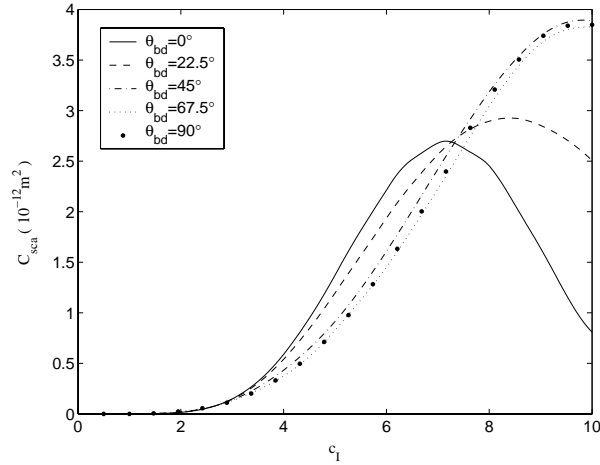


Fig. 2.17 Scattering crosssection C_{sca} versus eccentricity parameter c_1 of a spheroidal droplet. The beam with parameters $\Phi_{bd}=0^\circ$, $x_0=y_0=z_0=0 \mu\text{m}$, $w_{0x}=1.0 \mu\text{m}$, $w_{0y}=1.5 \mu\text{m}$, and $\lambda_0=0.6328 \mu\text{m}$ illuminates the prolate spheroid of axis ratio $a/b=2.0$ and refractive index $\hat{m}=1.33$. The particle is assumed to be suspended in the air. Five curves are plotted in the figure for the incidence angles $\Theta_{bd}=0^\circ$, 22.5° , 45° , 67.5° , and 90° , respectively.

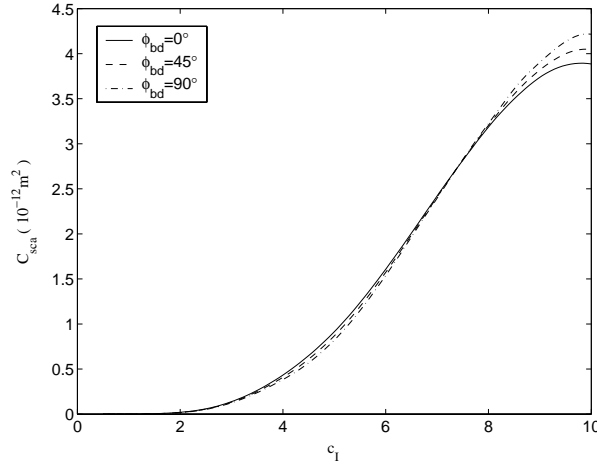


Fig. 2.18 Scattering crosssection C_{sca} versus eccentricity parameter c_1 of a spheroidal water droplet. The beam with parameters $\Theta_{\text{bd}}=45^\circ$, $x_0=y_0=z_0=0 \mu\text{m}$, $w_{0x}=1.0 \mu\text{m}$, $w_{0y}=1.5 \mu\text{m}$ and $\lambda_0=0.6328 \mu\text{m}$ illuminates the prolate spheroid of axis ratio $a/b=2.0$ and refractive index $\hat{m}=1.33$. The particle is assumed suspended in the air. Three curves are plotted in the figure for polarization angles $\Phi_{\text{bd}}=0^\circ$, 45° , and 90° , respectively.

2.4.3 Radiation Pressure

Relying on the theory developed in Subsection 2.1.4, this subsection presents some numerical results for RPCS calculation. Except for the red blood cell levitated by the beam from a sapphire laser used for the numerical simulation of the ‘‘Optical Stretcher’’ in Subsection 2.4.3.2, the particle used for calculation in the remaining parts is the slightly volatile silicone oil of refractive index $\hat{m}=1.5$ (Ashkin and Dziedzic, 1977). It is levitated in the air by the beam from an argon-ion laser of the wavelength $\lambda_0=0.5145 \mu\text{m}$ (Ashkin, 1970).

Since the prolate and oblate spheroids are formed by rotating an ellipse around its major axis and minor axis respectively, these two axes are the symmetrical axes for the prolate and oblate spheroids, respectively. When the beam propagates parallelly to the symmetrical axis of the spheroid, the end-on incidence is brought in and when it propagates vertically to the symmetrical axis, the side-on incidence is brought in. For the end-on incidence, when the projection radius r is used to characterize the projection area of the spheroid, we have $r=b$ for the prolate spheroid and $r=a$ for the oblate one. Such a radius can be related to the eccentricity parameter by $c_1 = k_1 r \sqrt{(a/b)^2 - 1}$ for the prolate spheroid and by $c_1 = k_1 r \sqrt{1 - 1/(a/b)^2}$ for the oblate one. The influence of the particle size characterized by r on the RPF is studied for a given

axis ratio a/b . To study RPF in the experiment of the “Optical Stretcher”, the RPCS are calculated for a given volume of a soft and spherical red blood cell (RBC) acted on by two counter-propagating laser beams and deformed to the spheroidal shape. Besides, influences of the incidence and polarization angles as well as the beam center location are also be studied in the present subsection.

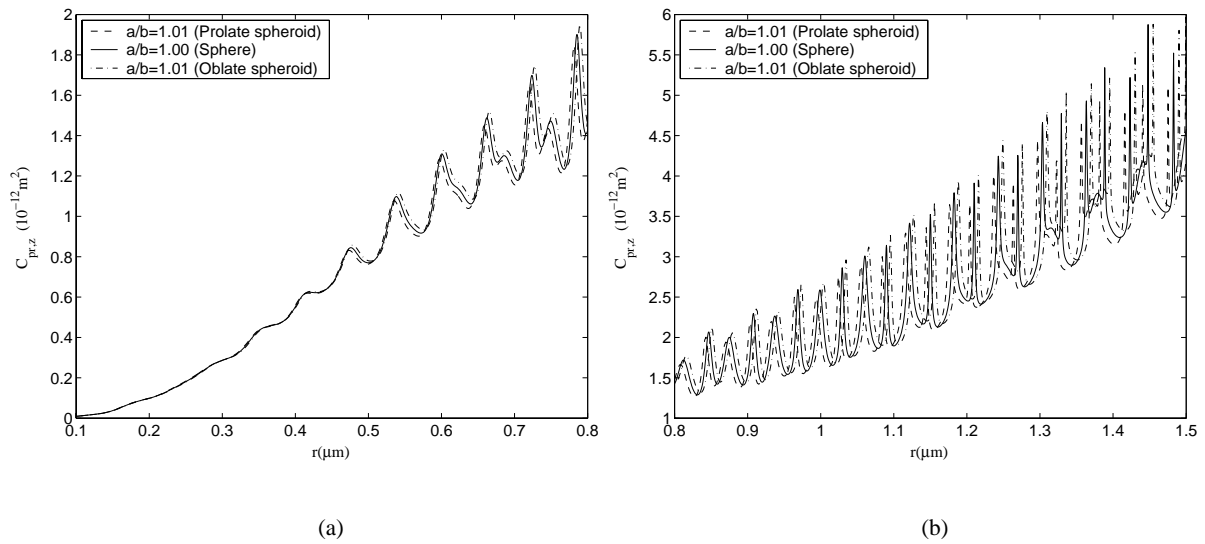
Since the description of the beam is significant for the RPF calculation in some cases (Ren et al., 1996), here it is necessary to point out that throughout the present subsection, Davis’s first order approximation (Davis, 1979) is used to describe the electromagnetic beams. Additionally, because of its high efficiency, the localized approximation (Ren et al., 1998; Gouesbet, 1999) is used for BSCs evaluation when the end-on incidence is involved and the electric field of the beam is polarized in the O_P-xz plane ($\Theta_{bd} = \Phi_{bd} = 0$). In other situations the classical localization principle has been found inapplicable, as discussed in Subsection 2.2.3, therefore quadrature method (Gouesbet et al., 1996) is used instead.

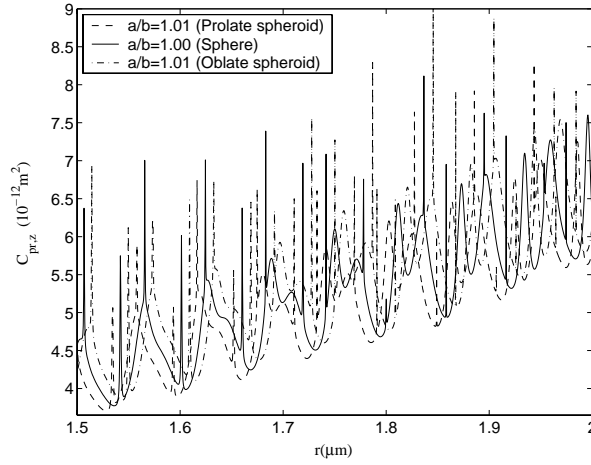
2.4.3.1 Radiation pressure force versus particle size

In this subsection, we predict the radiation pressure exerted on a spheroid by an end-on incident plane wave. Both prolate and oblate spheroids are used for calculation. The results are compared to those obtained by the GLMT for the spherical particle of an exact axis ratio $a/b=1.0$. With the resolution of r being $\Delta r \sim 2.5 \times 10^{-4} \mu\text{m}$, 8000 equidistant points within the interval $0.1 \mu\text{m} \leq r \leq 2.0 \mu\text{m}$ are used in RPCS calculation, since in such a range it is easier to recognize the position difference of the resonances between a spheroid and a sphere.

As indicated in Fig. 2.19, when compared to the RPCS curve versus the particle size for the sphere, the RPCS curve for the prolate spheroid of the axis ratio $a/b=1.01$ has a back- and downward shift. Such a shift becomes up- and forward for the oblate spheroid of the same axis ratio. Moreover, these shifts are enlarged when the spheroid deviates more from the sphere, e.g., $a/b=1.1$, as shown by Fig. 2.20 (note that for the clarity of Fig. 2.20, the RPCS curves of the prolate and oblate spheroids have been offset by the factors 2×10^{-12} and -2×10^{-12} respectively). After a careful identification, we can find in Fig. 2.20 that when the sphere changes to the prolate spheroid, the points A_2 , B_2 , and C_2 on the RPCS curve shift to A_3 , B_3 , and C_3 respectively, which implies an inward compression of the RPCS curve of the sphere.

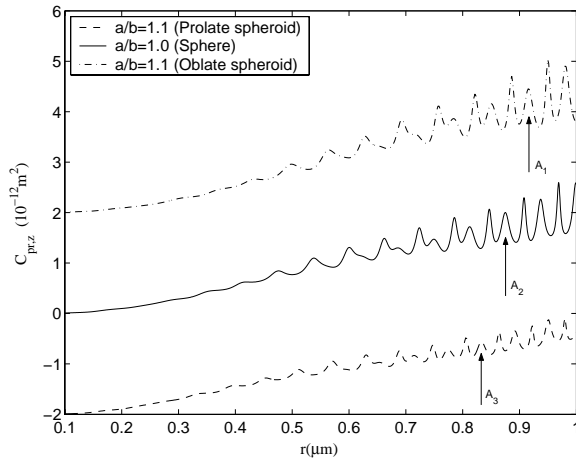
In contrast, when the sphere changes to the oblate spheroid, the outward stretching is brought in and in this case the points A_2 , B_2 , and C_2 are found to shift to A_1 , B_1 , and C_1 respectively. Comparison of the distance between the two points A_1 and A_2 (or A_2 and A_3) to that between B_1 and B_2 (or B_2 and B_3) shows that large particles have more obvious shift than small ones. Comparison of the RPCS values at the points corresponding to the same order of the resonances shows that the resonance strength is enhanced by the oblate spheroid but is reduced by the prolate one. Comparison of the RPCS curves in Fig. 2.20 to those in Fig. 2.19 shows that for the prolate spheroid increasing its axis ratio makes the resonances weaker in strength, narrower in width and more difficult to identify. But for the oblate spheroid, increasing the axis ratio makes the resonances stronger, wider and easier to identify. Besides, as for the spherical particle, increasing the size of the spheroid makes the resonances stronger but narrower.



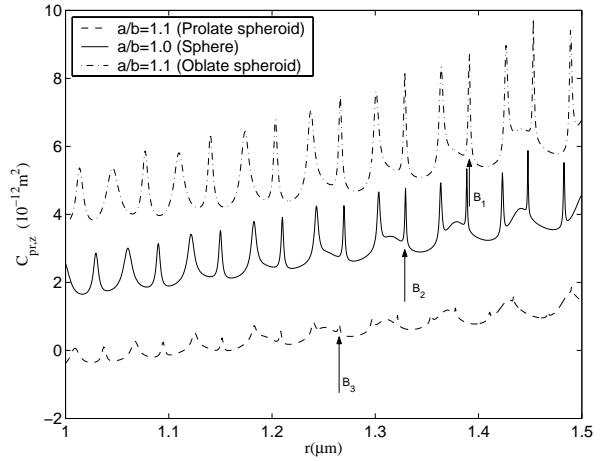


(c)

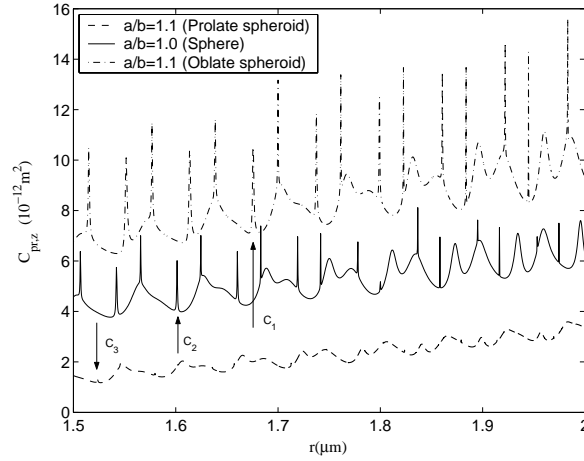
Fig. 2.19 Comparison of the longitudinal RPCS $C_{pr,z}$ exerted by a plane wave on the spheroid of axis ratio $a/b=1.01$ to that on the sphere. The incidence and polarization angles of the plane wave are assumed to be 0° . The particles have the same relative refractive index $\hat{m}=1.5$. The dashed curve is for the prolate spheroid of semiminor axis length equal to the radius of the projection area ($r=b$) and the dash-dot curve is for the oblate spheroid of semimajor axis length equal to the radius of the projection area ($r=a$). The results are compared with the GLMT's radiation pressure predictions for the sphere of radius r . (1) Fig. 2.19(a) is for $0.1 \mu\text{m} \leq r \leq 0.8 \mu\text{m}$; (2) Fig. 2.19(b) is for $0.8 \mu\text{m} \leq r \leq 1.5 \mu\text{m}$; (3) Fig. 2.19(c) is for $1.5 \mu\text{m} \leq r \leq 2.0 \mu\text{m}$.



(a)



(b)



(c)

Fig. 2.20 Same as Fig. 2.19 but for the axis ratio $a/b=1.1$. (1) Fig. 2.20(a) is for $0.1 \mu\text{m} \leq r \leq 1.0 \mu\text{m}$; (2) Fig.20(b) is for $1.0 \mu\text{m} \leq r \leq 1.5 \mu\text{m}$; (3) Fig.20(c) is for $1.5 \mu\text{m} \leq r \leq 2.0 \mu\text{m}$. For clarity and convenient identification, the RPCS curves of the prolate and oblate spheroids have been offset by the factors 2×10^{-12} and -2×10^{-12} , respectively.

2.4.3.2 Radiation pressure force versus axis ratio

In the preceding subsection, the axis ratio of the spheroid is taken to be constant and the behavior of the RPCS curves versus the particle size is discussed. In this subsection, the volume of the particle is given and kept constant during the deformation of a spherical particle to a spheroidal one. In this way, we numerically simulate the experiment of the ‘‘Optical Stretcher’’ (Guck et al., 2000) for a RBC acted on by two end-on incident counter-propagating Gaussian beams of TEM_{00} mode. These two beams are identical except for the opposite propagation directions. The RBC is located where beam sections are identical. Provided that the hemoglobin filled in the soft RBC is incompressible, its volume will not change in the process of deformation.

As described by Guck et al. (2000), such a spherical RBC of radius $r=3.32 \mu\text{m}$ (volume $V_0=153.3 \mu\text{m}^3$) and refractive index $\hat{m}_2=1.380$ is in a buffer of refractive index $\hat{m}_1=1.335$. A cw-Ti: sapphire laser is used to produce the beam of wavelength $\lambda_0=0.785 \mu\text{m}$. The beam is assumed to be extremely focused to the waist radius $w_0=0.5\lambda_0$ and its center O_B is located on the z axis. The ratio of the local waist radius to the particle radius is 1.10 ($w/r=1.10$). We calculate the RPCS for the axis ratio $1.00 \leq a/b \leq 1.23$, corresponding to the linear expansions along the z

axis of $0 \leq \Delta z_0 \leq 0.8 \mu\text{m}$ and the linear contraction along the y axis of $0 \leq \Delta y_0 \leq 0.6 \mu\text{m}$ (Guck et al., 2000). As indicated by the solid curve in Fig. 2.21, the longitudinal RPCS, $C_{\text{pr}, z}$, presents a linearly increasing relationship with the growth of the axis ratio a/b . Its absolute value rises from $3.45 \times 10^{-15} \text{ m}^2$ for $a/b=1.00$ to $4.17 \times 10^{-15} \text{ m}^2$ for $a/b=1.23$. This means that for an “Optical Stretcher” with a given beam power, the RPF exerted on the RBC gradually increase by 20% when it is deformed from a sphere to a prolate spheroid of $a/b=1.23$. Since a normal RBC has the radius between $3 \mu\text{m}$ and $4 \mu\text{m}$, in Fig. 2.21, we also plot the RPCS curves for the RBCs of the radii $r=3.00 \mu\text{m}$, $3.64 \mu\text{m}$, and $3.96 \mu\text{m}$, respectively. These cells are still assumed to be located at the position $w/r=1.1$. Their RPCS curves show a similar increase. Therefore we may suppose that, in the experiment of the “Optical Stretcher” using extremely focused beams, the linear deformation of a spherical RBC is not only the contribution of the beam power increasing but also the contribution of particle shape changing itself during the deformation.

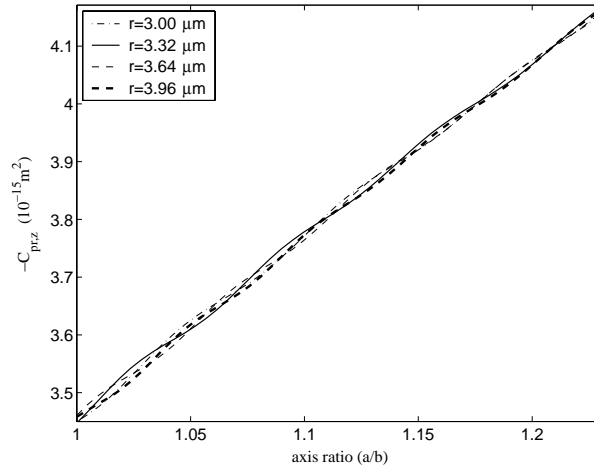


Fig. 2.21 Longitudinal RPCS versus the axis ratio for a red blood cell (RBC) of radii 3.00, 3.32, 3.64 and 3.96 μm , located on the beam axis with the location characterized by $w/r=1.1$. The RBC of refractive index 1.380 is in the buffer of refractive index 1.335, and is deformed from the spherical shape to the spheroidal one under the action of two counter-propagating laser beams in the TEM_{00} mode. The volume of the particle remains constant during the deformation. The circular Gaussian beam has a waist radius $w_0=0.5\lambda$. Note that $C_{\text{pr}, z}$ plotted in Fig. 2.21 represents the RPCS of beam A, which propagates in the direction of the positive z axis. The incidence and polarization angles of the beams are $\Theta_{\text{bd}}=\Phi_{\text{bd}}=0$. Beam B, which has the same axis as Beam A but opposite propagation direction, has RPCS of same value as Beam A but with opposite sign.

Note should be paid to the fact that, for the RBC of radius $3.32 \mu\text{m}$, when the linear expansion along the z axis ($\Delta z_0=2\Delta a$) increases from 0 to $0.8 \mu\text{m}$ and the linear contraction along the y axis

($\Delta y_0=2\Delta b$) increases from 0 to $0.6 \mu\text{m}$ (corresponding to $a/b=1.23$), the volume of the particle decreases from the original value $V_0=153.3 \mu\text{m}^3$ to $V_1=142.1 \mu\text{m}^3$, which means the deviation error increasing from 0% to 7.3%. This is contradictory to the constant volume assumption during the deformation and means that the spheroidal model is more appropriate for a slightly deformed RBC. It has been found that (Guck et al., 2001), when a RBC deviates much from the spherical shape, only its two ends possess the shape partly similar to their counterparts of a spheroid, while the shape of its middle part is more approximate to a cylinder of finite length. Therefore it can be expected that the less a cell deviates from the spherical shape, the better it can be modeled by the spheroid.

2.4.3.3 Radiation pressure force versus incidence and polarization angles

For a sphere, due to its spherical symmetry, once it is located on the beam axis the RPF keeps constant in the beam propagation direction for all incidence angles Θ_{bd} and polarization angles Φ_{bd} . However, in general this is not the case for the spheroidal particle due to its unique symmetrical axis along the z axis. Further on, at an oblique incidence angle, different polarization angles also imply different ray trajectories inside the spheroid so that the resultant RPF should change accordingly. In this subsection we exemplify the influence of both incidence and polarization angles of the beam on the RPF exerted on a spheroid. When the spheroid with an arbitrary location and orientation in the beam moves toward the beam center O_B , rotation might happen. In this case, we need to evaluate the RPF versus the angles Θ_{bd} and Φ_{bd} , respectively.

First, let a TEM_{00} circular Gaussian beam incident on a prolate spheroid at different incidence angles within $[0^\circ, 90^\circ]$. Such a range is representative for the characterization of the influence of the incidence angle on the RPF. The RPCS for $90^\circ \leq \Theta_{\text{bd}} \leq 180^\circ$ is identical to its counterpart corresponding to $180^\circ - \Theta_{\text{bd}}$ except for an opposite sign for $C_{\text{pr}, z}$. And the RPCS for $-180^\circ \leq \Theta_{\text{bd}} \leq 0^\circ$ is identical to its counterpart corresponding to $-\Theta_{\text{bd}}$, except for an opposite sign for $C_{\text{pr}, x}$. A Gaussian beam of waist radius $w_0=2\lambda$ is used for numerical calculations. The polarization angle of the beam is assumed to be 0° ($\Phi_{\text{bd}}=0^\circ$). The semiminor axis length and the axis ratio of the spheroid are equal to $0.5 \mu\text{m}$ and 2.0, respectively. The centers of the beam and the spheroid are assumed to coincide with each other so that O_B has the coordinates $x_0=y_0=z_0=0$

μm in $O_p\text{-}xyz$. As can be found in Fig. 2.22a, the components of RPCS $C_{pr,z}$ and $C_{pr,x}$ change obviously with the incidence angle Θ_{bd} and have the maxima $3.4 \times 10^{-13} \text{ m}^2$ and $5.6 \times 10^{-13} \text{ m}^2$, respectively, corresponding to the end-on incidence ($\Theta_{bd}=0^\circ$) and side-on incidence ($\Theta_{bd}=90^\circ$) are concerned, respectively. Meanwhile, $C_{pr,z}$ and $C_{pr,x}$ are identical to zero at $\Theta_{bd}=90^\circ$ and 0° , respectively, as it should. The resultant RPCS, which is calculated from $C_{pr,z}$ and $C_{pr,x}$ by using $C_{pr, \text{resultant}} = \sqrt{C_{pr,x}^2 + C_{pr,z}^2}$ ($C_{pr,y}=0$ for the current case), also changes with the incidence angle and has its maximum 6.0×10^{-13} at $\sim 48^\circ$.

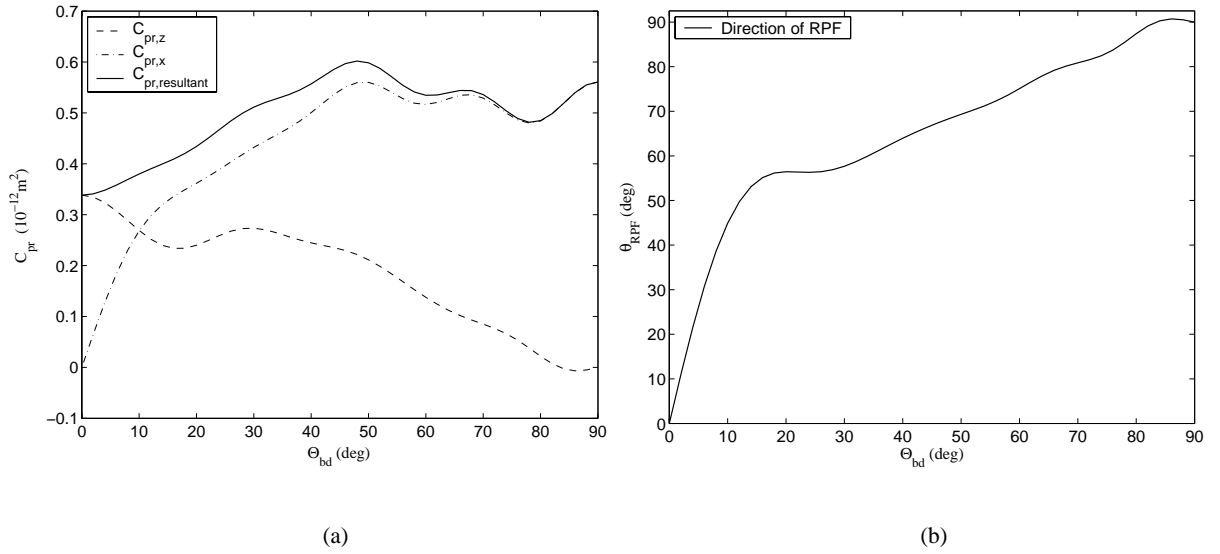


Fig. 2.22 RPCS versus the incidence angle Θ_{bd} . The polarization angle Φ_{bd} is assumed to be 0. The circular Gaussian beam of waist radius $w_0=2\lambda$ is assumed to illuminate a prolate spheroid of axis ratio $a/b=2.0$, with semiminor axis length $b=0.5 \mu\text{m}$ and relative refractive index $\hat{m}=1.5$. Note that $C_{pr,y}$ is equal to zero and hence its curve is not plotted. (1): In Fig. 2.22(a) is plotted the RPCS curve versus Θ_{bd} , including the longitudinal component of RPCS $C_{pr,z}$, the transverse one $C_{pr,x}$, as well as the resultant one; (2): In Fig. 2.22(b) is plotted the direction of the resultant RPF (in $O_p\text{-}xy$ plane) exerted on the spheroid. Note that θ is formed by the direction of the resultant RPF and the positive z axis, while Θ_{bd} is formed by the beam propagation direction and the positive z axis.

Thus, we can conclude that the RPF value does not keep constant for the different incidence angles. Neither does its direction, as can be found in Fig. 2.22b: except for their equalities for the end-on or side-on incidences of the beam ($\Theta_{bd}=0^\circ$ or 90°), the angle formed by the direction of the RPF and the z axis, θ_{RPF} , is always larger than incidence angle of the beam, Θ_{bd} . As evidenced by other numerical results not demonstrated in the present thesis, we comment that

the more a spheroid deviates from the sphere, the more the RPCS curve is influenced by the incidence and polarization angles.

Next, we study the influence of the polarization angle on the result of RPCS for the same particle and beam. With incidence angles 0° , 22.5° , 45° , 67.5° and 90° , the polarization of the incident wave changes from the TM mode ($\Phi_{bd} = 0^\circ$) to the TE mode ($\Phi_{bd} = -90^\circ$). In such a process, the RPCS curves of $C_{pr,z}$, $C_{pr,x}$, and $C_{pr,y}$ versus the polarization angles are illustrated in Fig. 2.23a, b and c, respectively. Evidently, when $\Theta_{bd} = 0^\circ$, $C_{pr,z}$ keeps constant for all polarization angles, due to the rotational symmetry of the spheroid around its semimajor axis. $C_{pr,z}$ becomes zero when the beam is tilted to the incidence angle 90° , since in this case the beam propagates along the x axis in the Cartesian coordinates of the spheroid. For the incidence angle $\Theta_{bd} = 22.5^\circ$, $C_{pr,z}$ shows a monotone increasing relationship with the growth of the polarization angle Φ_{bd} . Such a tendency of increasing slows down for $\Theta_{bd} = 45^\circ$. When $\Theta_{bd} = 67.5^\circ$, the $C_{pr,z}$ curve versus Φ_{bd} becomes monotone decreasing. As to $C_{pr,x}$, it grows gradually with the increase of Φ_{bd} for all incidence angles except when $\Theta_{bd} = 0^\circ$, which corresponds to the end-on incidence of the beam when no transverse forces exist. Interestingly enough, the $C_{pr,y}$ - Φ_{bd} curve presents a parabolic shape for the incidence angles $\Theta_{bd} = 22.5^\circ$, 45° , and 67.5° . The maximum of $C_{pr,y}$ locates stably at $\Phi_{bd} = -45^\circ$, as can be found in Fig. 2.23c. But for the end-on incidence ($\Theta_{bd} = 0^\circ$) or side-on incidence ($\Theta_{bd} = 90^\circ$), $C_{pr,y}$ is equal to zero at all polarization angles. Considering the ray optics viewpoint, this is because the two geometrical rays at the same polarization plane and symmetrical about the beam axis have symmetrical trajectories inside the particle so that they produce no forces in the y direction. For other incidence angles, $C_{pr,y}$ still keeps zero at the polarization angles $\Phi_{bd} = 0^\circ$ and -90° , since in these cases two symmetrical incident rays respectively located at the left and right sides of O_P - xz plane can still be found propagating symmetrically inside the spheroid so that eventually no forces are produced in the y direction. However, for a given incidence angle $0^\circ < \Theta_{bd} < 90^\circ$ and at the other polarization angles $-90^\circ < \Phi_{bd} < 0^\circ$, such a symmetrical propagation does not exist any longer, therefore $C_{pr,y}$ happens to be non-zero.

Note should be paid to the fact that the RPCS for $0^\circ \leq \Phi_{bd} \leq 90^\circ$ is identical to its counterpart corresponding to $-\Phi_{bd}$. Also, the RPCS for $90^\circ \leq \Phi_{bd} \leq 180^\circ$ and $-180^\circ \leq \Phi_{bd} \leq -90^\circ$ is identical to its

counterpart corresponding to $-\Phi_{bd}$.

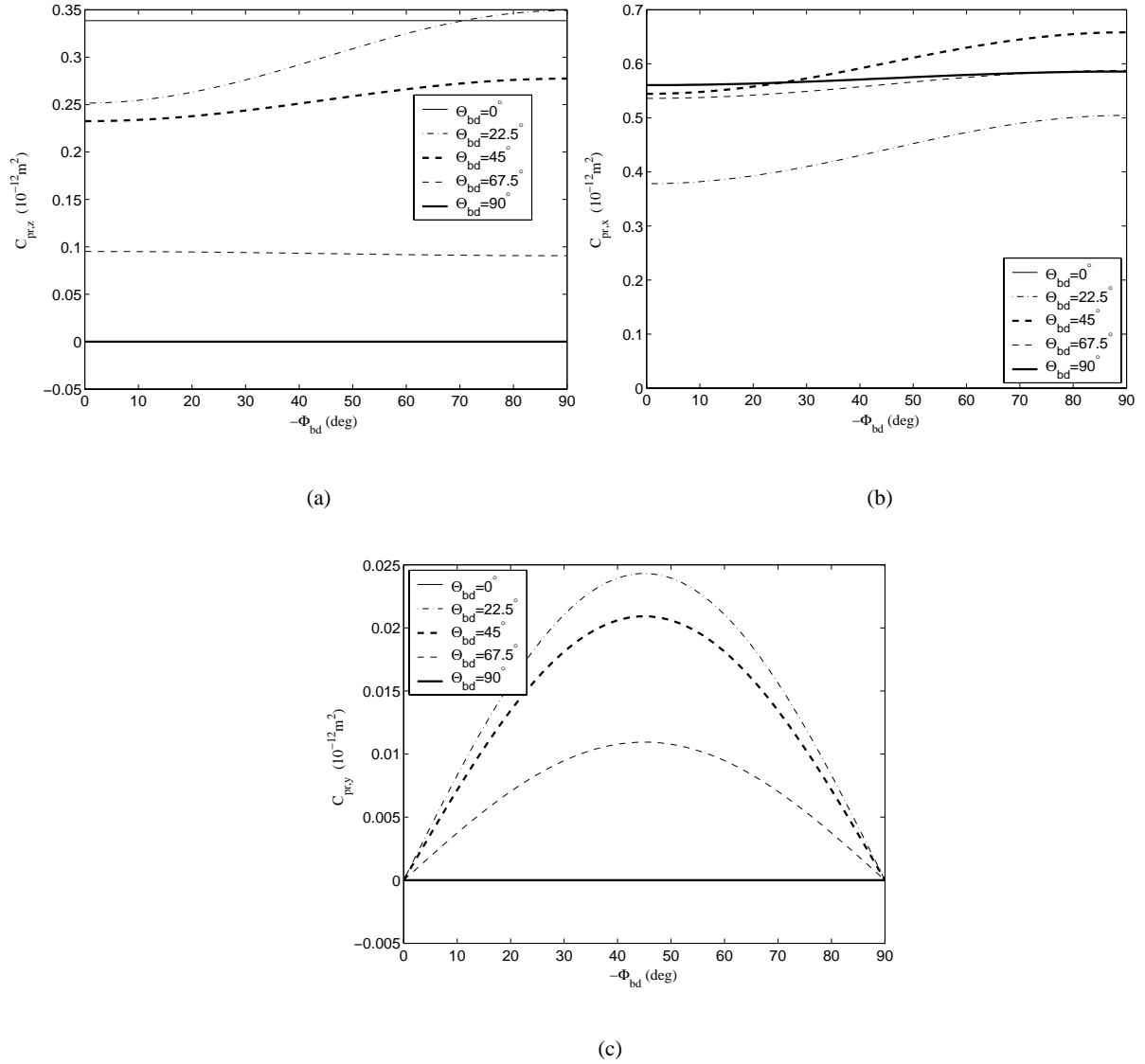


Fig. 2.23 RPCS versus the polarization angle Φ_{bd} for 5 incidence angles $\Theta_{bd}=0^\circ$, 22.5° , 45° , 67.5° and 90° . The beam and the spheroid are the same as in Fig. 2.22. In Fig. 2.23(a), (b) and (c) are plotted the curves of $C_{pr,z}$, $C_{pr,x}$ and $C_{pr,y}$ versus Φ_{bd} , respectively. For $\Theta_{bd}=0^\circ$, $C_{pr,x}$ and $C_{pr,y}$ are zero and therefore their curves are not explicitly found in the figures.

2.4.3.4 Radiation pressure force versus beam center location

For on-axis location of the spheroid, under the action of the longitudinal RPF the spheroid is attracted toward the beam center. In such a process, we need to explore the influence of beam

center location $O_B(x_0, y_0, z_0)$ on the RPCS. First, we discuss the case of end-on incidence of the beam. In this case, the beam center O_B is located on the z axis so that $x_0=y_0=0 \mu\text{m}$. We consider a Rayleigh particle ($r \ll \lambda$) of $r=0.01 \mu\text{m}$ as an example, which is representative of RPCS prediction for Rayleigh particles. For both spherical and spheroidal particles of the same projection radius r and illuminated by an end-on incident circular Gaussian beam of waist radius $\omega_0=\lambda$ and its electric field polarized in $O_P\text{-}xz$ plane, the $C_{pr,z}$ curves versus z_0 show a symmetrical shape about the point with $z_0=0 \mu\text{m}$ and $C_{pr,z}$ is almost zero, as can be found in Fig. 2.24. Meanwhile, the absolute value of longitudinal RPCS ($|C_{pr,z}|$) of the oblate/prolate spheroid is smaller/larger than that of the sphere and increases/decreases with the growth of the axis ratio from 1.0 to 1.2. These axis ratios can be considered caused by an ‘‘Optical Stretcher’’, which is discussed in Subsection 2.4.3.2. Such a phenomenon is observed for very small particles within the Rayleigh size range. However, the discrepancy becomes evident for the particles of the size beyond the Rayleigh region. For example, when $r=1.0 \mu\text{m}$, $|C_{pr,z}|$ at almost all z_0 decreases with the growth of the axis ratios from 1.0 to 1.10, as indicated by Fig. 2.25. Also, at relatively far location of the beam center O_B from the particle center O_P (say, $|z_0| > 20 \mu\text{m}$), the curvatures of the beam wavefronts at $+|z_0|$ and $-|z_0|$, which correspond to the particle located at the converging or diverging parts of the beam, respectively, are weak enough to be looked on as being identical. Therefore the $C_{pr,z}$ curve is found symmetrical with respect to the axis $z_0=0 \mu\text{m}$.

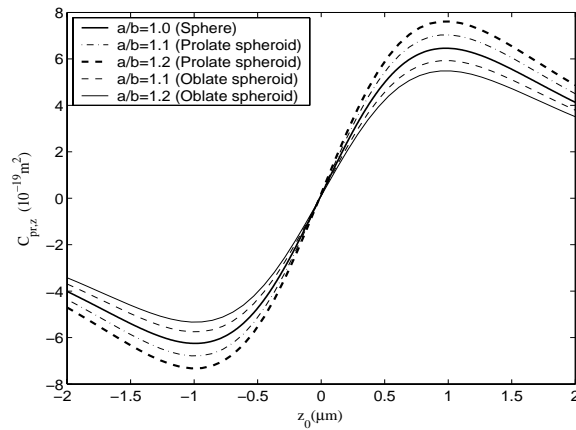


Fig. 2.24 Longitudinal RPCS versus the location of Rayleigh particle along the z axis. The circular Gaussian beam has a waist radius $w_0=\lambda$. The spheroids have the relative refractive index $\hat{m}=1.5$ but different axis ratios $a/b=1.1$ and 1.2 respectively. The projection radius of the particles is assumed to be $r=0.01 \mu\text{m}$ so that we have $r=b$ for the prolate spheroid and $r=a$ for the oblate one. The incidence and polarization angles of the beams are $\Theta_{bd}=\Phi_{bd}=0$.

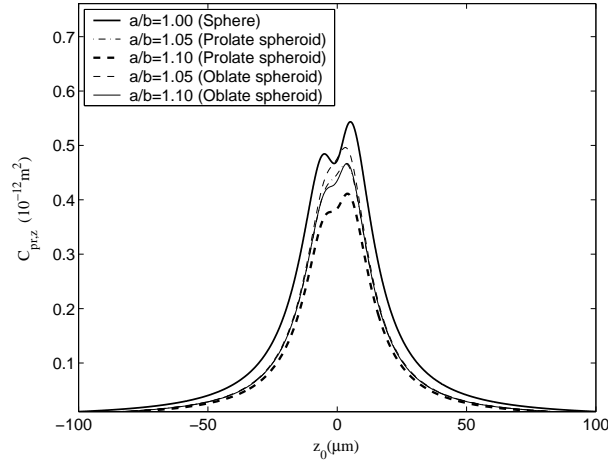


Fig. 2.25 Longitudinal RPCS versus particle location along the z axis. The circular Gaussian beam has a waist radius $w_0=2\lambda$. The spheroids have the same relative refractive index $\hat{m}=1.5$ but the different axis ratios $a/b=1.05$ and 1.10 , respectively. The projection radius of the particles is assumed to be $r=1.0 \mu\text{m}$ so that we have $r=b$ for the prolate spheroid and $r=a$ for the oblate one. The incidence and polarization angles of the beams are $\Theta_{\text{bd}}=\Phi_{\text{bd}}=0$.

Next, we discuss the case of off-axis incidence of a beam on a spheroid. The beam center O_B is at the plane $z_0=0$, but it does not coincide with the particle center O_P , namely $x_0 \neq 0$ or $y_0 \neq 0$. A circular Gaussian beam of waist radius $w_0=2\lambda$, with the incidence and polarization angles $\Theta_{\text{bd}} = \Phi_{\text{bd}} = 0$ illuminates spheroids of the same projection radius $r=1.0 \mu\text{m}$ but the different axis ratios $a/b=1.00, 1.01, \text{ and } 1.10$. Since the beam center is located along the x axis, we have $y_0=z_0=0 \mu\text{m}$. In this case, the longitudinal and the transverse RPCS curves, $C_{\text{pr},z}$ and $C_{\text{pr},x}$ versus x_0 , are plotted in Fig. 2.26a and Fig. 2.26b respectively. Also, for the beam center located along the y axis ($x_0=z_0=0 \mu\text{m}$), results of $C_{\text{pr},z}$ and $C_{\text{pr},y}$ are plotted in Fig. 2.27a and Fig. 2.27b. We can find from Fig. 2.26a and Fig. 2.27a that, for the same projection radius $r=1.0 \mu\text{m}$ the longitudinal pressures exerted on the spheroids of axis ratio $a/b \leq 1.1$ are less than those exerted on the sphere when the beam center O_B is not close enough to the particle center O_P , say $x_0 \geq 0.32 \mu\text{m}$ for $C_{\text{pr},x}$ and $y_0 \geq 0.40 \mu\text{m}$ for $C_{\text{pr},y}$. Meanwhile, as indicated by Fig. 2.26b and Fig. 2.27b, the transverse pressures exerted on the spheroids are less than those exerted on the sphere once the beam center does not locate far enough from the particle center, say $0 \leq x_0 \leq 1.75 \mu\text{m}$ for $C_{\text{pr},x}$ and $0 \leq y_0 \leq 1.65 \mu\text{m}$ for $C_{\text{pr},y}$.

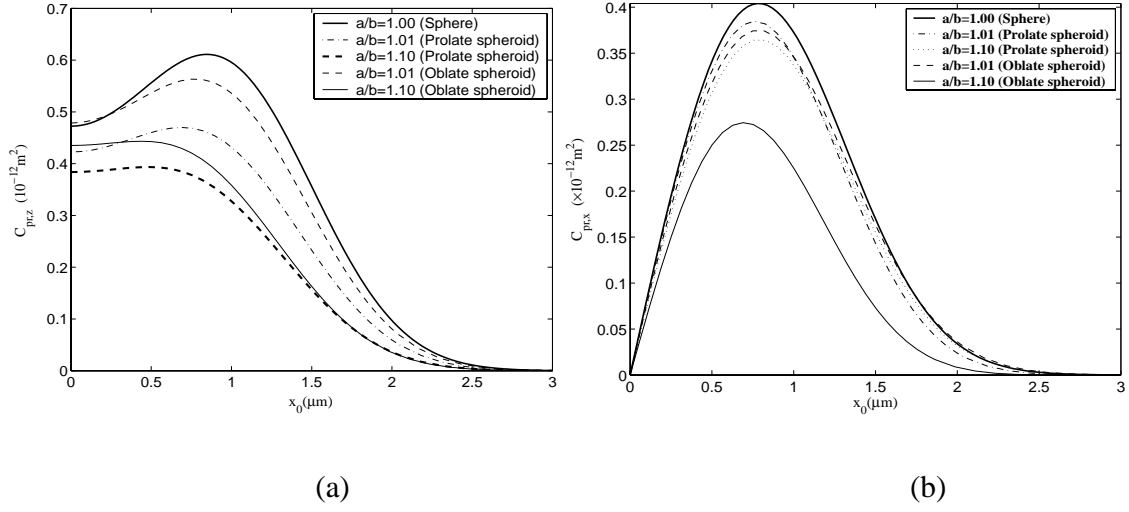


Fig. 2.26 Transverse RPCS $C_{pr,x}$ versus the beam center location along the positive x axis. The circular Gaussian beam of a waist radius $w_0=2\lambda$ is assumed to be incident on spheroids of same relative refractive index $\hat{n}=1.5$ but with different axis ratios $a/b=1.00, 1.01,$ and 1.10 respectively. The beam center locates on the x axis so that $y_0=z_0=0 \mu\text{m}$. The incidence and polarization angles of the beam are $\Theta_{bd}=\Phi_{bd}=0$. The projection radius of the particle is $r=1.0 \mu\text{m}$. (1): Fig. 2.26(a) is for the longitudinal RPCS $C_{pr,z}$ versus x_0 ; and (2): Fig. 2.26(b) is for the transverse RPCS $C_{pr,x}$ versus x_0 . Attention should be paid to the fact that, in the current case, another transverse RPCS, $C_{pr,y}$, is zero and its curve is not plotted.

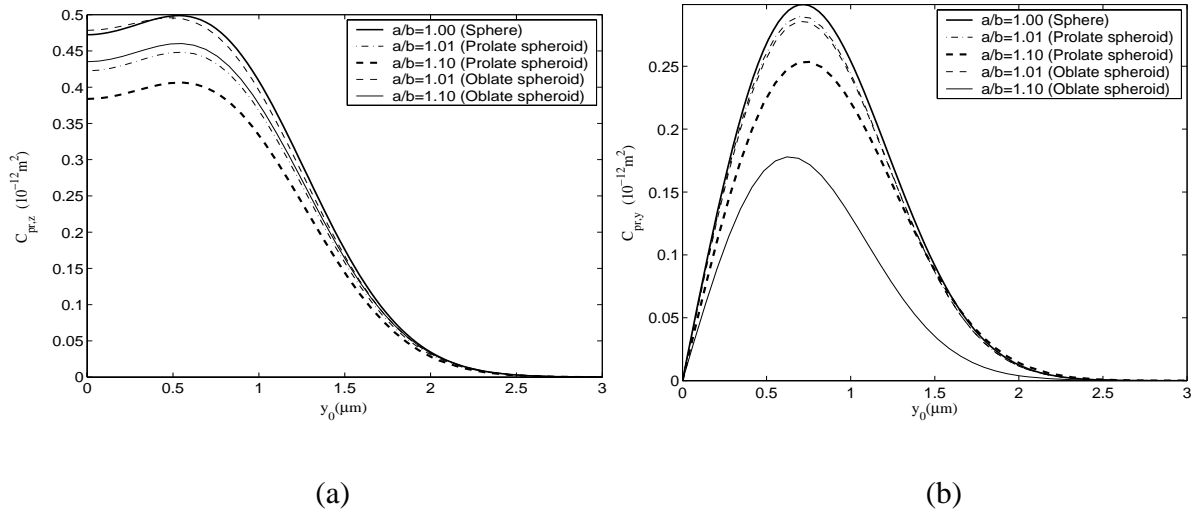


Fig. 2.27 Same as Fig. 2.26 but for the transverse RPCS $C_{pr,y}$ versus the beam center location along the positive y axis. The beam center O_B locates on the positive y axis so that $x_0=z_0=0 \mu\text{m}$. (1): Fig. 2.27(a) is for the longitudinal RPCS $C_{pr,z}$ versus y_0 ; and (2): Fig. 2.27(b) is for the transverse RPCS $C_{pr,y}$ versus y_0 . Attention should be paid to the fact that, in the current case, another transverse RPCS, $C_{pr,x}$, is zero and its curve is not plotted.

When the volatile oil is polluted or contains some impurities, the refractive index might have a non-zero imaginary part. In this case, the influence of the refractive index on RPCS should be examined. We use an astigmatic elliptical Gaussian beam (Xu et al., 2006a) of waist radii along u and v directions being λ and 10λ respectively ($w_{0u}=\lambda$ and $w_{0v}=10\lambda$). The locations of the waist radii along the u and v axes are $-0.5 \mu\text{m}$ and $0.5 \mu\text{m}$, respectively ($w_u=-0.5 \mu\text{m}$ and $w_v=0.5 \mu\text{m}$). The beam is assumed to be incident on a prolate spheroid of axis ratio $a/b=1.5$ and semiminor axis length $b=1.0 \mu\text{m}$. The real part of the refractive index of the prolate spheroids is 1.5 ($\text{Re}(\hat{m})=1.5$) and its imaginary part $\text{Im}(\hat{m})$ increases from 0 to 0.1 by steps. For these parameters, we observe a gradual increase of $C_{pr,z}$ in Fig. 2.28. However, when $\text{Im}(\hat{m})$ further grows to 1.0, a decrease is observed. Since the influence of the imaginary part of the refractive index on the behavior of the RPCS curves versus z_0 has been found similar to the one for the C_{abs} curves, the explanation can be as follows: when more (less) energy is absorbed by the particle, more (less) angular momentum is transferred to the particle so that the longitudinal RPCS becomes larger (smaller).

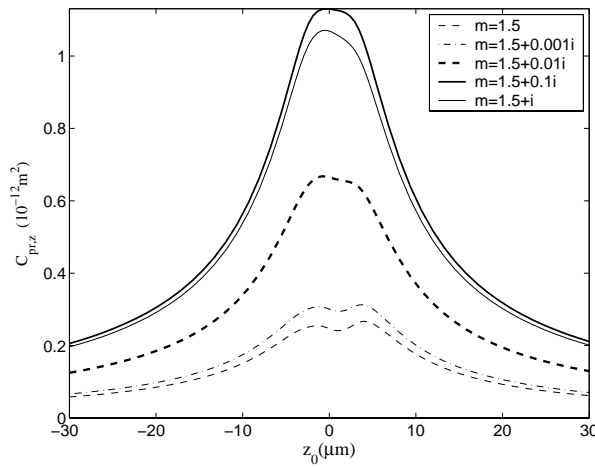


Fig. 2.28 Longitudinal RPCS versus z_0 for a prolate spheroid of axis ratio $a/b=1.5$ and semiminor axis length $b=1.0 \mu\text{m}$ illuminated by an astigmatic elliptical Gaussian beam of waist radii along u and v directions being λ and 10λ , respectively ($w_{0u}=\lambda$ and $w_{0v}=10\lambda$). The locations of the waist radii w_{0u} and w_{0v} are $-0.5 \mu\text{m}$ and $0.5 \mu\text{m}$, respectively ($w_u=-0.5 \mu\text{m}$ and $w_v=0.5 \mu\text{m}$). The incidence and polarization angles of the beam are $\Theta_{bd}=\Phi_{bd}=0$. The five curves in Fig. 2.28 correspond to spheroids of different refractive indices $\hat{m}=1.5, 1.5+0.001i, 1.5+0.01i, 1.5+0.1i$, and $1.5+i$.

2.5 Conclusion

By solving the equations obtained from the boundary conditions, the unknown coefficients for scattered and internal fields are determined. Analytical expressions for the calculation of extinction, scattering and radiation pressure crosssections are obtained and demonstration calculations are made. Two special cases, plane wave scattering by a spheroid and shaped beam scattering by a sphere are proved recoverable from the present theory.

Through coordinate transformation, the beam description in its own Cartesian coordinates can be converted to that in the coordinates of the spheroid. Afterward the arbitrarily oriented and shaped beam is successfully expanded in terms of spheroidal vector wave functions multiplied by a set of spheroidal BSCs. However, these BSCs have to be evaluated by the quadrature method instead of the localized principle once the coordinates of the beam and the particle are not parallel to each other. The spheroidal BSCs calculated by our method are comparable to those obtained by Asano and Yamamoto for the case of plane wave incidence. For the special case of the beam coordinates parallel to those of the particle, all the symmetry relationships for spherical BSCs also stand for spheroidal ones. On the basis of beam expansion, arbitrarily oriented shaped beam scattering by a spheroid are studied.

To our particular interest might be the numerical calculations of RPF performed for both prolate and oblate spheroids illuminated by plane wave or circular/elliptical Gaussian beam. When studying the influence of particle shape on the RPF, we compare the results of RPCS of the spheroids to those of the spheres. For the plane wave incidence, the RPCS curve versus the particle size for a prolate spheroid is found to have a back- and downward shift when compared to the RPCS curve for a sphere. Such a shift becomes up- and forward for an oblate spheroid of the same axis ratio as that of the prolate one. Moreover, the resonance strength of the oblate/prolate spheroid is stronger/weaker than that of the sphere. Also, when the particle is located on the beam axis, the resultant RPF exerted on the spheroid, unlike on the sphere, is not always along the beam propagation direction denoted by the incidence angle Θ_{bd} . Furthermore, its value does not remain constant. In addition, altering the polarization angle can also bring changes to the RPF for a beam of oblique incidence ($\Theta_{bd} \neq 0^\circ$). By use of the present theory, our numerical simulation of the “Optical Stretcher” indicates that, during the deformation of a RBC

acted on by two extremely focused TEM_{00} beams with $w_0=0.5\lambda$ and given beam power, the longitudinal RPF exerted on the cell with its location in the beam characterized by $w/r=1.1$ linearly increases by 20% when it is deformed from a spherical particle to a spheroidal one having an axis ratio $a/b=1.23$.

Chapter 3. Geometrical Optics Approximation of Gaussian Beam Scattering by a Spheroid

In the preceding chapter, the generalized Lorenz-Mie theory (GLMT) has been developed to describe the interaction between a laser beam and a spheroid. It proves to be a complete and exact solution to Maxwell's equations and can serve as rigorous theoretical basis for optical particle characterization. However, as stated in Chapter 1, when the projection radius of the spheroid is larger than $\sim 5 \mu\text{m}$ ($r \geq \sim 5 \mu\text{m}$) or the axis ratio is larger than ~ 3 ($a/b \geq \sim 3$), such a theory can be hardly applied to practical calculations ascribed to the poor convergence of radial spheroidal functions of the second kind for large aspect ratio or large size. Furthermore, for a relatively large particle, to ensure the precision of calculation, a large but ill-conditioned coefficient matrix is required to determine the unknown coefficients from boundary conditions, which might invoke numerical instabilities in solving the linear equations. In the face of such a difficulty, geometrical optics (GO) is expected to work instead of the rigorous theory due to its advantages of more straightforward treating of scattering phenomenon and much higher efficiency in numerical calculations.

As a kind of shaped beam, the Gaussian beam of fundamental mode (TEM_{00}) found most applications in laser particle characterization. For its on-axis incidence on a sphere or a spheroid, the complex amplitude of its electric field is rotationally symmetric around the z -axis, which is also the rotationally symmetric axis of the sphere and the spheroid. In this case, mathematics for three-dimensional ray tracing inside them can be simplified to two-dimensional. In this chapter, we first study circular Gaussian beam scattering by a spherical particle and compare the results with GLMT's prediction for a sphere. On such a basis, GO approximation is further extended to the case of a spheroidal particle.

3.1 Gaussian beam scattering by a sphere

This subsection is devoted to the extension of the geometrical optics approximation to the light scattering of an on-axis Gaussian beam by a spherical particle. In this instance, the TE and TM polarizations always stay separate and there is no polarization mixing upon successive internal

reflections. It is an important basis for a further extension to the light scattering by a large spheroid, which is discussed in Subsection 3.2.

3.1.1 Extension of geometrical optics approximation

We consider that a TEM_{00} Gaussian beam, of waist radius w_0 , wavelength λ_0 in vacuum, and polarized in the x direction, propagates along the z axis. Its center O_G is located at $(0, 0, z_0)$ in the particle coordinate system O_P - xyz (see Fig. 3.1). The radius of the spherical particle is r and relative complex refractive index is $\hat{m} = m_r + m_i i$.

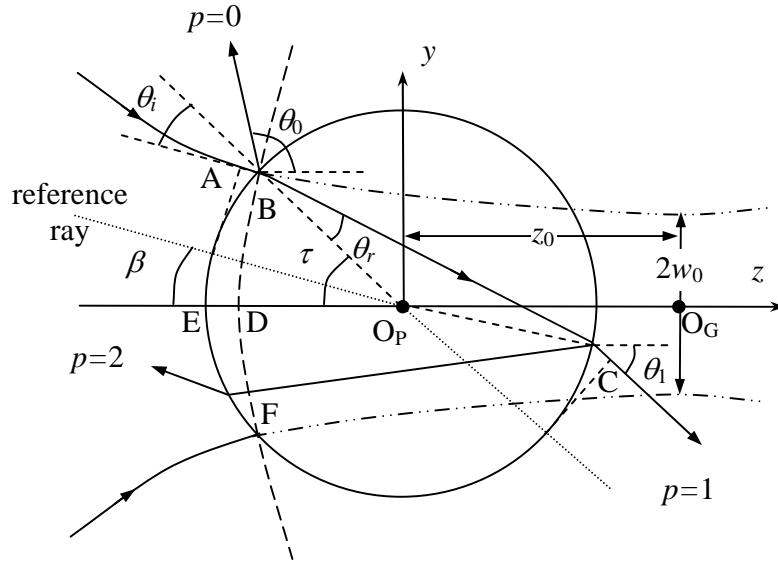


Fig. 3.1. Scheme of GO of a homogeneous sphere illuminated by a Gaussian beam. The particle is located on the z axis of the incident beam. (The points $B, D,$ and F are on an isophase of the beam).

In the first-order approximation, the complex amplitude of the electric field of the incident Gaussian beam (designated by the subscript G) S_G at any point $A(x, y, z)$ is described by (Siegman, 1986):

$$S_G(x, y, z) = |S_G| \exp(i\phi_i), \quad (3-1)$$

where $|S_G|$ and ϕ_i denote the amplitude and the phase of the Gaussian beam, which are given, respectively, by

$$|S_G| = \frac{w_0}{w} \exp\left(-\frac{x^2 + y^2}{w^2}\right) \quad (3-2)$$

and

$$\phi_i(x, y, z) = -k_1 \left[(z - z_0) + \frac{x^2 + y^2}{2R} \right] + \tan^{-1} \left(\frac{z - z_0}{z_R} \right), \quad (3-3)$$

where k_1 ($k_1=2\pi/\lambda_1$) is the wavenumber in the surrounding medium; the local beam radius w is related to the beam waist radius w_0 by $w = w_0 \left\{ 1 + [(z - z_0)/z_R]^2 \right\}^{1/2}$, the wavefront curvature radius R and the Rayleigh length z_R read, respectively, as $R = (z - z_0) \left\{ 1 + [z_R / (z - z_0)]^2 \right\}$ and $z_R = \pi w_0^2 / \lambda_1$.

Within the framework of GO, the scattered field S_j can be calculated by a superposition of the contributions of all modes of rays, including the specularly reflected rays, $S_{j,0}$, the refracted rays of order p , $S_{j,p}$, which undergo $p-1$ internal reflections as well as the diffracted field S_d , i.e.,

$$S_j = S_d + \sum_{p=0}^{\infty} S_{j,p}, \quad (3-4)$$

where the subscript j is 1 or 2, indicating, respectively, the component perpendicular ($\varphi=90^\circ$) or parallel ($\varphi=0^\circ$) to the scattering plane. The far-field scattering intensity I_j at an observation point with distance R_s from the particle center is calculated by:

$$I_j = \frac{I_0}{(k_1 R_s)^2} i_j(\theta) = \frac{I_0}{(k_1 R_s)^2} |S_j(\theta)|^2, \quad (3-5)$$

where I_0 is the intensity at the center of the Gaussian beam.

3.1.1.1 Diffraction of a Gaussian beam

To consider the diffraction effect, we use the model of Chevaillier et al. (1986, 1990) for Gaussian beam diffraction by a disk of radius r . On the basis of their work, the amplitude of the diffracted field by a spherical particle of size parameter $\alpha=k_1 r$ in far field can be obtained from

the following compact formula:

$$S_d = \frac{\alpha^2}{2\pi} \left(\frac{w_0}{w} \right) \int_0^{2\pi} d\varphi' \int_0^1 \exp(-At^2) \exp[i(Bt + Ct^2)] t dt, \quad (3-6)$$

where $A = \left(\frac{r}{w} \right)^2$, $B = -\alpha \tan \theta \cos(\varphi - \varphi')$ and $C = \frac{\alpha^2}{2k_1 R}$. When A is small, i.e., the radius of the particle is smaller than the local beam waist radius ($r \leq w$), the integral equation in Eq.(3-6) can be evaluated analytically through using Legendre polynomial approximation (Chevaillier et al., 1986). However, in our calculation, the integral of Eq.(3-6) is directly evaluated numerically to remove the limitation of $r \leq w$.

3.1.1.2 Propagation of the rays of Gaussian beam

Within the framework of GO, the Gaussian beam is considered as a combination of bundles of rays, each of them propagates in the direction \vec{F} normal to the local wavefront surface of the incident beam. With the aid of the phase function ϕ_i described by Eq.(3-3), \vec{F} can be represented by the partial derivatives F_x , F_y , and F_z of ϕ_i : $\vec{F} = F_x \vec{i} + F_y \vec{j} + F_z \vec{k}$. For the special case of on-axis incidence, due to the axial symmetry of the Gaussian beam, the propagation direction of the rays at any point on the O_P - yz plane can be simplified to (F_y, F_z) , and the incidence angle θ_i on the sphere (Fig. 3.1) is then obtained by

$$\cos \theta_i = \frac{|yF_y + zF_z|}{\sqrt{(y^2 + z^2)(F_y^2 + F_z^2)}}, \quad (3-7)$$

where F_y and F_z read as:

$$F_y = \frac{\partial \phi_i}{\partial y} = -\frac{2z_R y (z - z_0)}{w_0^2 [z_R^2 + (z - z_0)^2]}, \quad (3-8)$$

$$F_z = \frac{\partial \phi_i}{\partial z} = \frac{z_R}{z_R^2 + (z - z_0)^2} - \frac{z_R y^2 [z_R^2 - (z - z_0)^2]}{w_0^2 \left\{ z_R^2 + [z_R^2 - (z - z_0)^2]^2 \right\}} - k_1. \quad (3-9)$$

The angle β between the z axis and the propagating direction of the ray incident on point A is

then determined by $\beta = \tan^{-1} \left(\frac{F_y}{F_z} \right)$. The total deviation of a ray of order p from the z axis can be evaluated by

$$\theta'_p = 2p\theta_r - 2\tau - (p-1)\pi + \beta, \quad (3-10)$$

where θ_r is the refraction angle and can be related to the incidence angle θ_i by Snell's law, while τ is the angle between vector $\overline{BO_p}$ and the z axis. So we have the relation $\tau = \beta + \theta_i$. All these angles are illustrated in Fig. 3.1. Obviously, when beam waist radius w_0 tends to infinity (the angle β tends to 0 and $\theta_i = \tau$) the special case of plane wave incidence is recovered.

The scattering angle for a ray of order p , θ_p , is related to the total deviation angle θ'_p by

$$\theta'_p = 2\pi k_p + q_p \theta_p, \quad (3-11)$$

where k_p is an integer and q_p is equal to 1 or -1 . The values of k_p should be properly chosen so that the scattering angle θ_p is well restricted within the range $[0, \pi]$.

3.1.1.3 Phase shifts

Within the framework of GO approximation of the plane wave scattering by a spherical particle, two kinds of phase shifts should be taken into account: the phase shift due to the optical path $\phi_{p,PH}$ and the phase shift due to the focal lines (inside and outside the sphere) $\phi_{p,FL}$. Thus the final combined phase shift ϕ_p can be expressed as (van de Hulst, 1957):

$$\phi_{p,pl} = \frac{\pi}{2} + \phi_{p,PH} + \phi_{p,FL}, \quad (3-12)$$

where the first term $\pi/2$ in Eq. (3-12) is added only for the sake of convenience in the expression of the scattered wave and it has no effect on the scattered field.

The phase due to the optical path $\phi_{p,PH}$ relative to the reference for an incident ray (see Fig. 3.1) is given by

$$\phi_{p,PH} = 2k_1 r (\cos \theta_i - p m_r \cos \theta_r). \quad (3-13)$$

Following van de Hulst's discussion (van de Hulst, 1957), the phase advances by $\pi/2$ after each passage of a focal line, which is formed by intersections of adjacent rays. And for the plane wave incidence, the phase shift due to the focal lines reads as

$$\phi_{p,FL} = \frac{\pi}{2} (p - 2k_p + \frac{1}{2}s - \frac{1}{2}q_p), \quad (3-14)$$

where the definitions of k_p and q_p are the same as in Eq.(3-11) and $s = -\text{sgn}(d\theta'_p / d\theta_i)$.

However, for a Gaussian beam illumination, the phase shift due to the curvature of the wavefront, ϕ_G , should be taken into account. The phase differences between the phase on the front curvature ϕ_i and the reference points D and E are, respectively, $\phi_{AB} = k_1 r (1 - \cos \theta_i)$ and $\phi_{ED} = k_1 (r + z_0) - \phi_i$ (The points B , D , and F in Fig. 3.1 are on an isophase of the beam). Thus the phase shift due to the curvature of the Gaussian wavefront is then:

$$\phi_G = \phi_{AB} - \phi_{ED} = \phi_i - k_1 (z_0 + r \cos \theta_i). \quad (3-15)$$

Hence for Gaussian beam illumination, we have the following expression for phase shift calculation:

$$\phi_p = \frac{\pi}{2} + \phi_{p,PH} + \phi_{p,FL} + \phi_G. \quad (3-16)$$

We may find that when w_0 tends to infinity, ϕ_i tends to be $k_1 (z_0 - z)$ and $z = -r \cos \theta_i$. Then ϕ_G is equal to zero. Hence the case of plane wave incidence is recovered.

But in the case of Gaussian beam illumination, we find it difficult to deduce an analytical expression for $\phi_{p,FL}$ to count the number of focal lines the ray encounters during its travel inside and outside the sphere. Nevertheless, as pointed out by van de Hulst (1957), the intersection of two adjacent rays produce a focal point and their foci form the focal lines. Such a criterion also holds for Gaussian beam scattering. Therefore a procedure is designed to numerically determine the intersections of adjacent rays which produce focal points, both inside and outside the particle.

3.1.1.4 Amplitude of scattered field

When a bundle of rays arrives at the surface of a particle, it is reflected and refracted each time it encounters the surface of the sphere, diverged or converged due to the local curvature of the surface and the refractive index, and attenuated if the particle is absorbing.

The factor of the amplitude attenuation due to the reflection and/or the refraction for the emergent ray of order p is given by

$$\varepsilon_{j,p} = \begin{cases} r_j, & \text{for } p = 0 \\ (1 - r_j^2)r_j^{(p-1)}, & \text{for } p \geq 1 \end{cases}, \quad (3-17)$$

where r_j is the Fresnel reflection coefficients calculated by

$$r_1 = \frac{\cos \theta_i - m_r \cos \theta_r}{\cos \theta_i + m_r \cos \theta_r}, \quad (3-18)$$

$$r_2 = \frac{m_r \cos \theta_i - \cos \theta_r}{m_r \cos \theta_i + \cos \theta_r}. \quad (3-19)$$

The divergence factor due to the local curvature of the particle is given by

$$D_G = \frac{\cos \theta_i \sin \tau}{\sin \theta_p \left| \frac{d\theta'_p}{d\tau} \right|}. \quad (3-20)$$

When a sphere is illuminated by a plane wave, a simple analytical expression of $\frac{d\theta'_p}{d\tau}$ can be obtained (Glantschnig and Chen, 1980) since, for plane wave incidence ($\beta=0$), θ'_p has an explicit relation with τ and θ_i , as indicated by Eq. (3-10). For Gaussian beam illumination, however, $\beta \neq 0$. Moreover, β depends not only on the incident point (defined by τ) but also on the focalization of the beam. Therefore it is difficult to obtain the analytical expression for $\frac{d\theta'_p}{d\tau}$.

Instead, $\frac{d\theta'_p}{d\tau}$ is numerically evaluated by the following expression for the l th ray:

$$\left| \frac{d\theta'_p}{d\tau} \right|_l = \left| \frac{\theta_{p,l+1} - \theta_{p,l-1}}{\tau_{l+1} - \tau_{l-1}} \right|. \quad (3-21)$$

When the particle is absorbing, the amplitude is attenuated during the ray's propagation inside the particle. Since the total optical path inside the particle for a ray of order p is $2pr \cos \theta_r$, the attenuation factor ξ_p can be evaluated by

$$\xi_p = \exp(-2k_1 r m_i p \cos \theta_r). \quad (3-22)$$

Taking into account all of these factors, we have the following amplitude of the scattered field for a ray of order p at the scattering angle θ :

$$S_{j,p}(\theta) = k_1 r |S_G| \varepsilon_{j,p} \xi_p D_G^{1/2} \exp(i\phi_p). \quad (3-23)$$

It should be noted that the total scattering amplitude at an observation point is the contribution of all emergent rays. Because the incident rays of each order p have their own set of scattering angles, to make a final superposition of amplitudes of all orders of the rays at the same scattering angles, which is described by Eq.(3-4), one-dimensional piecewise cubic interpolation is adopted for unification.

3.1.2 Numerical results and discussion

On the basis of the approach described in the preceding Subsection 3.1.1, a code is written in MATLAB and has been run on a PC. To validate the method and the code we compare the scattering diagrams for a transparent and absorbing sphere calculated by the extended geometrical-optics approximation (EGOA) with those by the GLMT and by the Debye series; the latter permits to verify the contributions of each order of the rays. The relative deviation from the GLMT is quantified for different angle ranges.

It's noteworthy that for all the demonstration calculations, to improve the calculation efficiency but not lose the approximation precision, the maximum order of rays p_{\max} is chosen to be 20, i.e., the refracted rays which undergo less than 20 internal reflections are considered. In addition, the incident rays on the surface of upper hemisphere are linearly spaced and their number is chosen to be 2500. Such a number gives the same results as done by 5000 rays do and therefore is

considered sufficient.

3.1.2.1 Comparison to the generalized Lorenz-Mie theory

The EGOA is an approximate method based on ray theory. It permits us to identify the contribution of all orders of rays. The GLMT, on the other hand, is an exact solution to the scattering of a linearly polarized shaped beam by a dielectric sphere. By comparing the results of the two methods, the validation range of the EGOA can be clarified.

The scattered diagrams for a transparent water droplet located at the centre of a Gaussian beam are shown in Fig. 3.2-Fig. 3.4. The refractive index of the particle is assumed to be 1.333 ($\hat{m}=1.333$) and the wavelength of the incident beam is $0.6328 \mu\text{m}$ ($\lambda_0=0.6328 \mu\text{m}$). For clarity in the graphic presentation, a relatively small particle of radius $r=25 \mu\text{m}$ is chosen for calculation. But we can anticipate the conclusion that the EGOA better predicts the scattered field for a larger particle than for a small one. Attention should be paid to that at Descartes rainbow angles, the intensity should be infinite due to the stationary deflection of the emergent rays. However, this is not apparent in the figures since numerically the emergent rays' change of deviation angle $d\theta'_p$ at the vicinity of rainbow is small enough but not zero.

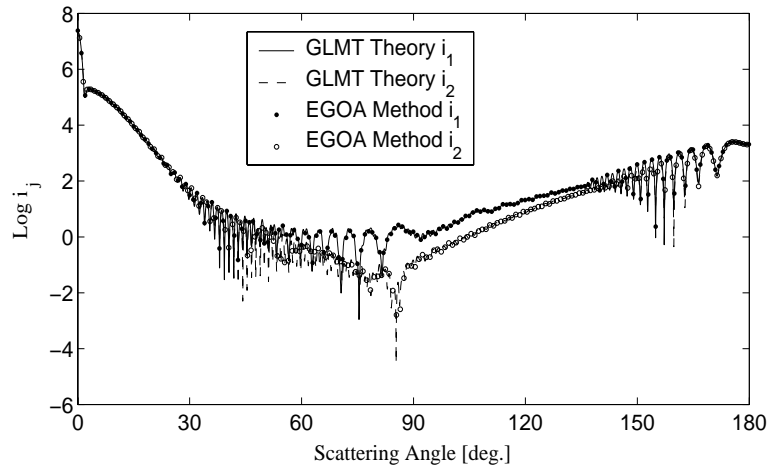


Fig. 3.2. Comparison of the scattering intensities calculated by the GLMT and the EGOA for a pure water droplet of refractive index $\hat{m}=1.333$ and radius $r=25 \mu\text{m}$ illuminated by a Gaussian beam of waist radius $w_0=10 \mu\text{m}$ and wavelength $\lambda_0=0.6328 \mu\text{m}$. The particle is located at the center of the beam ($z_0=0 \mu\text{m}$).

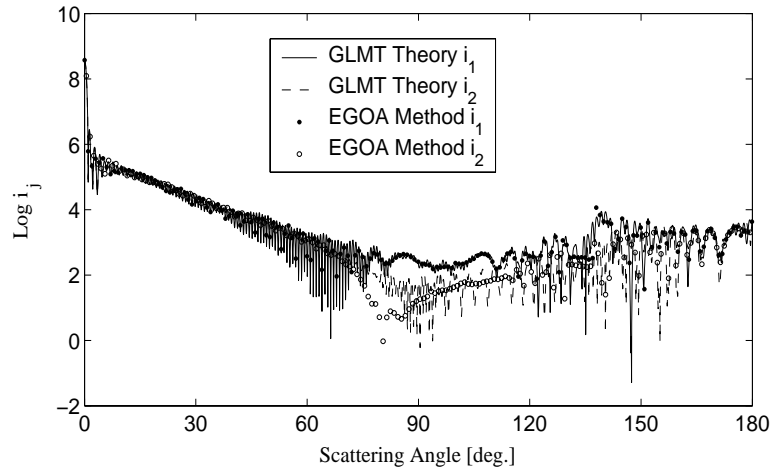
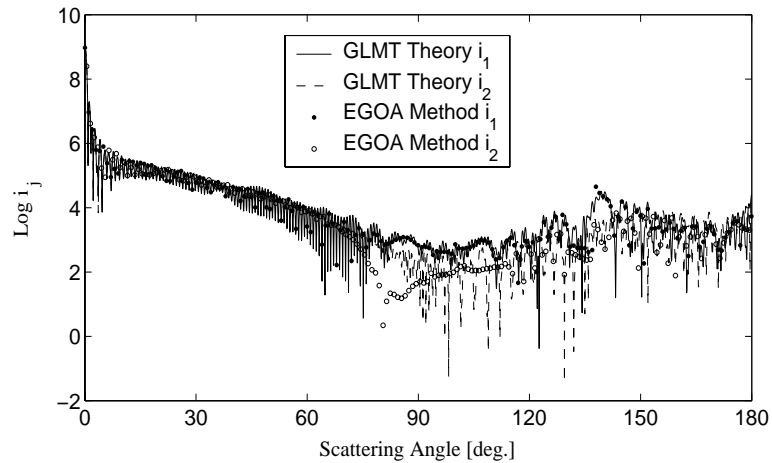

 Fig. 3.3. Same parameters as Fig. 3.2 but with the beam waist radius $w_0=25 \mu\text{m}$.

 Fig. 3.4. Same parameters as Fig. 3.2 but with the beam waist radius $w_0 \rightarrow \infty$.

Fig. 3.2 shows that when the radius is small compared with the beam waist radius, the agreement of the EGOA and the GLMT is satisfactory in all the directions from 0° to 180° . When the radius of the particle is as large as (Fig. 3.3) or greater than (Fig. 3.4) the beam waist radius the discrepancy between the two methods appears. The discrepancy at the angles around the rainbow and the angles at the vicinity of 90° increases as the ratio of the waist radius to the particle radius grows. Such a phenomenon can be explained by the fact that when the beam radius is smaller than the radius of the particle, the intensity of the rays corresponding to the lower-order rainbows is very weak. Meanwhile, the intensity of the rays adjacent to the edge of

the particle and associated with surface wave is also weak. Thus the effect of surface wave is also negligible. Therefore, the EGOA predicts the scattering intensity well. But when the beam waist increases to be comparable or larger than the particle radius, the intensity of the rays responsible for the rainbows and the surface wave has more important contribution to the scattered fields. In such a situation, the EGOA can not predict the scattering intensity well at relevant angles.

The EGOA is also valid for slightly absorbing particles. In Fig. 3.5 to Fig. 3.6 we show respectively the scattered diagrams of a polluted water droplet ($\hat{m}=1.333+0.01i$) and an urban aerosol particle ($\hat{m}=1.55+0.09i$) (Shettle and Fenn, 1979). In order to compare with the results in Fig. 3.2, the radii of the beam waist and the particle are taken to be the same as those in Fig. 3.2. Good agreement between the EGOA and the GLMT is found except for small difference at the Brewster angle for the urban aerosol sphere. It is worth noting that the oscillation of the scattering pattern at large angles is much flattened in these diagrams since the intensities of high order rays are attenuated by the absorption of the particle, thus the effect of interference between the externally reflected rays and the rays of other orders is very weak. An example in the regime of anomalous diffraction is also given in Fig. 3.7, where the refractive index of the particle \hat{m} is 1.02 while other parameters are same as those in Fig. 3.2. The coincidence between the results of the GLMT and the EGOA are still found satisfactory.

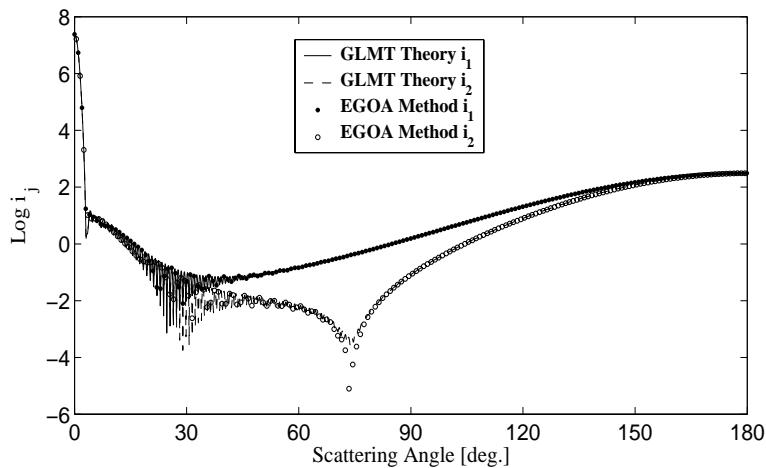
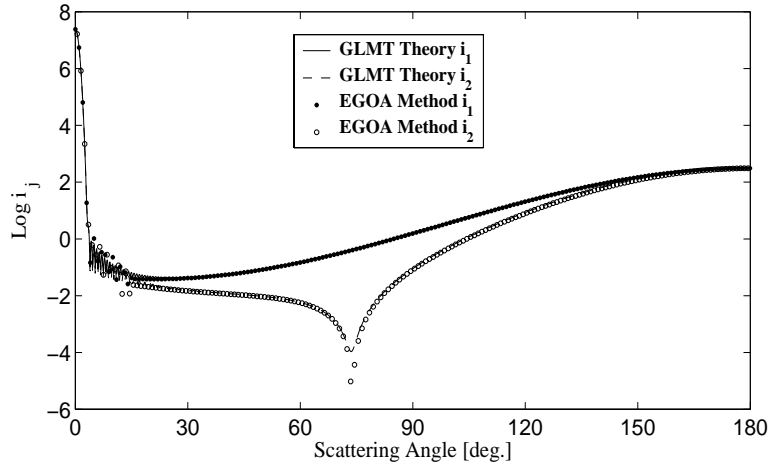
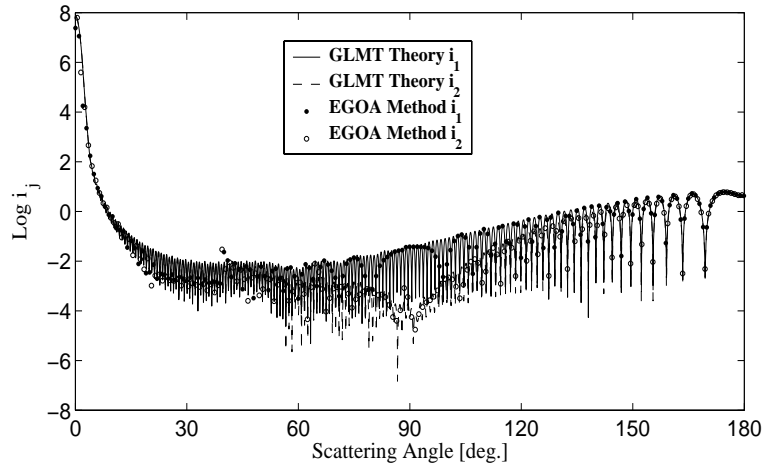


Fig. 3.5. Same parameters as Fig. 3.2, but with $\hat{m}=1.333+0.01i$.


 Fig. 3.6. Same parameters as Fig. 3.2, but with $\hat{m}=1.55+0.09i$.

 Fig. 3.7. Same parameters as Fig. 3.2, but with $\hat{m}=1.02$.

To qualify the validity range of the EGOA in different parameter set of (r, w_0, z_0, \hat{m}) , we compare the energy flux calculated by the EGOA with that by the GLMT within different scattering angular ranges for transparent particles and absorbing ones. To this end, we define the relative deviation δ_r of the EGOA to the GLMT as the ratio of discrepancy of the flux calculated by the two methods in the same angular interval $[\theta_1, \theta_2]$ to the flux calculated by the GLMT in this interval:

$$\delta_r = \left| \frac{\Phi_{\text{GLMT}} - \Phi_{\text{EGOA}}}{\Phi_{\text{GLMT}}} \right| \times 100\% . \quad (3-24)$$

We define the absolute deviation δ_a as the discrepancy of the flux calculated by the two methods for a given angular interval $[\theta_1, \theta_2]$ relative to the total scattered flux:

$$\delta_a = \left| \frac{\Phi_{\text{GLMT}} - \Phi_{\text{EGOA}}}{\Phi_{\text{total}}} \right| \times 100\% , \quad (3-25)$$

where Φ indicates the energy flux of the unpolarized light and is calculated by

$$\Phi = \frac{\lambda_0^2 I_0}{4\pi} \int_{\theta_1}^{\theta_2} [i_1(\theta) + i_2(\theta)] \sin \theta d\theta , \quad (3-26)$$

and Φ_{total} indicates the total flux from 0° to 180° .

The absolute and the relative discrepancies between EGOA and GLMT for a water droplet located at the centre of a Gaussian beam of wavelength $\lambda_0=0.6328 \mu\text{m}$ are presented in Table 3.1-Table 3.2. The first remark made by us is that the absolute discrepancy is very small except in the near forward direction because $\sim 90\%$ of scattered energy is concentrated in the forward angular range from 0 to $200/\alpha$ degrees for a particle of radius approximately more than five times the wavelength. Therefore, the relative discrepancy should be used to evaluate the deviation of the EGOA from the GLMT. Comparing Table 3.1 with Table 3.2, we can find that the deviation between EGOA and GLMT is smaller for a larger particle in most angular intervals except the near forward region (0° - 20°). This means that, generally, for the same radius ratio w_0/r , a better approximation is achieved by the EGOA for a larger particle than for a smaller one. Meanwhile, for a transparent particle, the best agreement can be found when the beam waist radius is nearly half of the particle radius. The disagreement becomes obvious in the rainbow region or at angles around 90° . Such a deviation is mainly caused by two well-known reasons: The geometrical rays shut down near the rainbow angle and the so-called surface wave is not within the capability of ray optics for the description of scattering and has not been taken into account in our calculation. Its influence will be further analyzed in the next section. However, when the particle is absorbing, the deviations in the middle and backward regions of (60° - 180°) are not evident, as indicated by comparing Table 3.2 with Table 3.3. In these two

tables the imaginary parts of the refractive indices of the 100 μm particle are 0 and 0.005, respectively. We can also find that for absorbing particles, better approximation within $[0^\circ, 20^\circ]$ can be achieved since it corresponds better to the opaque disk model used in the diffraction calculation.

Table 3.1 Absolute and relative discrepancies δ_a and δ_r (expressed in percentage) between EGOA and GLMT for a pure water droplet of $\hat{m}=1.333$, $r=25 \mu\text{m}$, $z_0=0 \mu\text{m}$, and $\lambda_0=0.6328 \mu\text{m}$.

Beam waist	Absolute Discrepancy δ_a						relative discrepancy δ_r					
	0°-20°	20°-60°	60°-90°	90°-120°	120°-150°	150°-180°	0°-20°	20°-60°	60°-90°	90°-120°	120°-150°	150°-180°
$w_0=r/4$	5.34	0.00	0.00	0.00	0.01	0.07	5.52	3.76	15.69	4.80	4.02	2.23
$w_0=r/2$	4.21	0.01	0.00	0.00	0.03	0.00	4.43	0.29	2.35	0.28	5.32	0.04
$w_0=r$	1.69	0.16	0.12	0.02	0.13	0.05	2.17	0.87	15.50	6.99	9.10	6.38
$w_0=2r$	1.47	0.36	0.29	0.06	0.16	0.12	2.10	1.42	20.20	16.30	8.37	19.02
$w_0 \rightarrow \infty$	1.54	0.46	0.38	0.08	0.17	0.16	2.29	1.66	21.71	21.00	7.58	25.15

Table 3.2 Same as Table 3.1, but with $r=100 \mu\text{m}$.

Beam waist	Absolute Discrepancy δ_a						relative discrepancy δ_r					
	0°-20°	20°-60°	60°-90°	90°-120°	120°-150°	150°-180°	0°-20°	20°-60°	60°-90°	90°-120°	120°-150°	150°-180°
$w_0=r/4$	9.27	0.00	0.00	0.00	0.00	0.00	9.48	0.16	1.06	0.14	0.23	0.16
$w_0=r/2$	4.42	0.00	0.00	0.00	0.00	0.00	4.65	0.01	1.29	0.01	0.44	0.01
$w_0=r$	4.05	0.03	0.05	0.01	0.10	0.02	5.26	0.16	7.32	3.01	7.40	3.26
$w_0=2r$	2.47	0.06	0.12	0.02	0.16	0.05	3.48	0.23	9.38	7.31	8.79	9.81
$w_0 \rightarrow \infty$	3.23	0.07	0.15	0.03	0.19	0.07	4.71	0.26	10.04	9.60	8.91	13.18

Table 3.3 Same as Table 3.2, but with $\hat{m}=1.333+0.005i$.

Beam waist	Absolute Discrepancy δ_a						relative discrepancy δ_r					
	0°-20°	20°-60°	60°-90°	90°-120°	120°-150°	150°-180°	0°-20°	20°-60°	60°-90°	90°-120°	120°-150°	150°-180°
$w_0=r/4$	0.21	0.00	0.00	0.00	0.00	0.00	0.21	1.05	0.26	0.30	0.25	0.21
$w_0=r/2$	3.57	0.00	0.00	0.00	0.00	0.00	3.64	0.40	0.03	0.03	0.03	0.03
$w_0=r$	3.33	0.01	0.00	0.00	0.00	0.00	3.44	0.75	0.02	0.02	0.02	0.02
$w_0=2r$	0.86	0.02	0.00	0.00	0.00	0.00	0.90	0.86	0.02	0.02	0.02	0.02
$w_0 \rightarrow \infty$	2.52	0.02	0.00	0.00	0.00	0.00	2.65	0.89	0.02	0.02	0.02	0.02

Attention should be paid to the fact that when the radii ratio w/a is small, typically less than one fourth, the deviation between the EGOA and the GLMT becomes significant for a relatively small particle (Table 3.1). This is caused by two reasons. With respect to GLMT, when the beam is tightly focused, its profile described by GLMT that one is no longer same as the original profile. Some discrepancies appear between the non-Maxwellian description of the incident field by Davis's first-order approximation (Davis, 1979) and the reconstructed Maxwellian field from the beam-shape coefficients evaluated by the localization approximation, which might leads to some discrepancy between the reconstructed field and the given Gaussian beam field (Gouesbet and Lock, 1994; Lock and Gouesbet, 1994). With respect to the EGOA, ray theory is not quantitatively accurate for small particles and the assumption of a three-dimensional sphere to a two-dimensional disk in diffraction theory (Chevaillier et al., 1986, 1990) and non-inclusion of the surface wave rays, tunneling rays as well as the complex rays also bring in some errors to the scattering calculation. In addition, to facilitate ray tracing, we use straight trajectory approximation for all the rays, both inside and outside the sphere. But factually, the rays of the beam incident on the spheroid are curved, so they should still have curved trajectories inside the sphere. Therefore such an approximation also causes some errors for the incidence of a strongly focused beam.

To show the effect of the surface wave for different sizes of particle, we show in Fig. 3.8 and Fig. 3.9 the scattering intensities in a reduced angular range of $[80^\circ, 100^\circ]$ for a water droplet of radii 10 and 100um, respectively, and illuminated by the plane wave. We find that the general

agreement between the GLMT and the EGOA is better for a large particle than for a small one owing to a reduced influence of the surface wave. But attention should be paid to the discrepancy that still existing at rainbow angles. This is because for large particles, the rainbow of wave theory has finite intensity, whereas the rainbow of ray theory has infinite intensity mathematically.

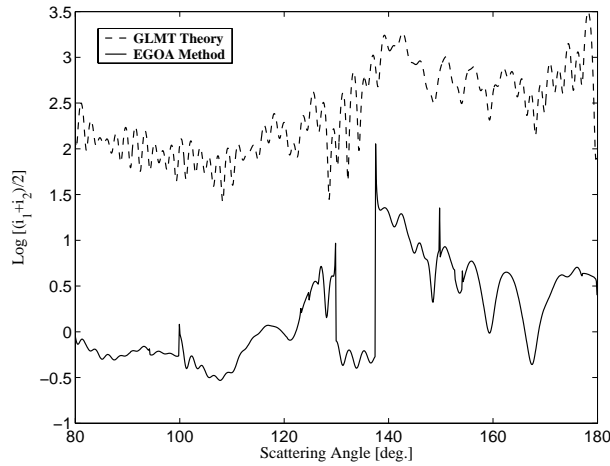


Fig. 3.8. Comparison of scattered intensities computed by the GLMT and the EGOA for plane wave scattered by a water droplet of $\hat{m}=1.333$ and $r=10 \mu\text{m}$. The parameters of the beam are $w_0 \rightarrow \infty$, $\lambda_0=0.6328 \mu\text{m}$ and $z_0=0 \mu\text{m}$. The EGOA's result has been offset by a factor of 10^2 for clarity.

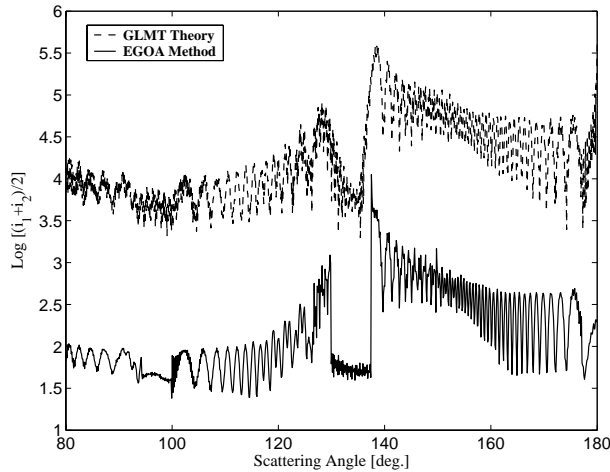


Fig. 3.9. Same parameters as Fig. 3.8, but with $r=100 \mu\text{m}$.

3.1.2.2 Comparison to Debye series

The EGOA permits us to decompose the contribution of different orders of rays that gives a clear physical picture of the mechanism of light scattering. This is one of the most attractive aspects of the GO. On the other hand, by writing the Mie coefficients into Debye series, we can also identify the contribution of each term, which clarifies the physical origin of many effects occurring in the light scattering. Even though the theoretical origins of the terms in the EGOA and in the Debye series are not exactly the same, their physical significations are identical.

Fig. 3.10 shows the contributions of each order of rays as well as the total scattering intensities of a homogeneous sphere located at the center of a Gaussian beam computed by the EGOA and Fig. 3.11 is for the same case but calculated by Debye series. Comparison of the two figures indicates that the agreement is satisfactory for different orders of rays, except at rainbow angles and in the zones where geometrical rays tend to disappear or disappear.

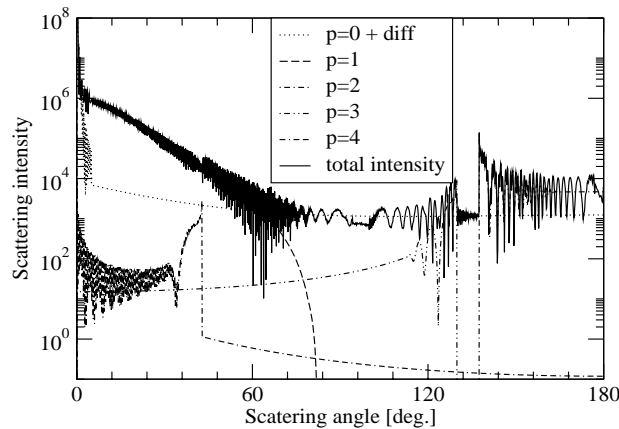


Fig. 3.10. Scattering intensities calculated by the EGOA for a sphere ($r=50\ \mu\text{m}$, $\hat{m}=1.333$) illuminated by a Gaussian beam ($w_0=50\ \mu\text{m}$, $\lambda_0=0.6328\ \mu\text{m}$). For clarity, the maximum intensity in the figure is taken to 10^8 instead of the maximum of 6×10^{10} at 0° .

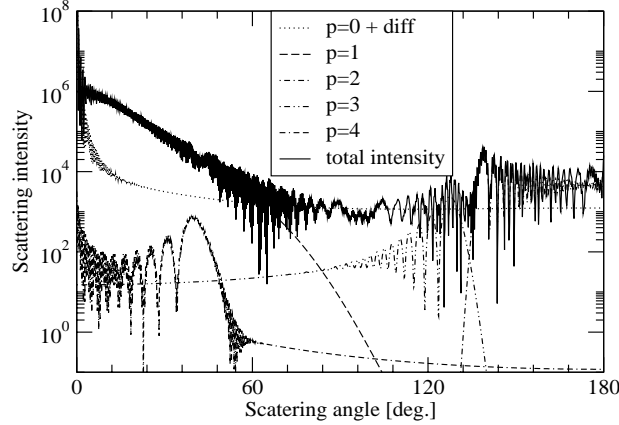


Fig. 3.11. Same parameters as Fig. 3.10, but Debye series are used.

3.1.3 Evaluation of surface wave influence

Within the framework of GO, the surface wave rays, tunneling rays and complex rays are not taken into account. We are more concerned about the surface wave because of its more important contribution to the scattering (Hovenac and Lock, 1992). As referred to in Subsection 3.1.2, the surface wave plays an important role at scattering angles around 90° .

According to van de Hulst's localization principle (van de Hulst, 1957), for a particle of size parameter $\alpha \gg 1$, l th partial wave can be associated with a geometrical light ray with the incidence angle θ_i which satisfies $\sin \theta_i \approx l/\alpha = l/k_1 r$.

By introducing two parameters, $l_{\pm} = x \pm c\alpha^{1/3}$ ($c \geq 3$) (Nussenzveig, 1969), the partial waves characterized by $0 \leq l \leq l_-$ can be related with the contribution from diffracted field and reflected and refracted rays calculated by GO; those characterized by $l \geq l_+$ are negligible due to the fast damping by centrifugal barrier. Thus our main concern is the partial waves characterized by $l_- \leq l \leq l_+$ at the edge region of the sphere. Such a region can be interpreted as where the grazing rays ($[l_-, \alpha]$) and the tunneling rays ($[\alpha, l_+]$) dominate. It gives rise to the so-called surface wave and tunneling rays which play a role of smoothing the lit and shadow region (Lock, 2003). For a plane wave incident on a spherical particle, through Nussenzveig's modified Watson transformation, their angular distribution and interference with other orders of rays can be

well estimated (Hovenac, 1991; Nussenzevig, 1969). In the case of a Gaussian beam, however, the problem becomes more complicated, ascribed to the non-uniform intensity profile and a varying centre and radius of curvature of wavefront during its propagation. Although we have tried to combine numerically the surface wave with the geometrical rays, so far we have not been successful.

Nevertheless, we can still give a qualitative analysis of the surface wave effect since its contribution depends on the incident flux contained in the surface wave zone. The more the energy that is contained in the surface wave zone, the more contribution is made by the surface wave. Therefore it is reasonable for us to evaluate the influence of surface by introducing a flux ratio index (FRI) F , which compares the flux contained in the surface wave zone $A \rightarrow C \rightarrow B$ to that in the non surface wave zone $S \rightarrow A$, as illustrated in Fig. 3.12.

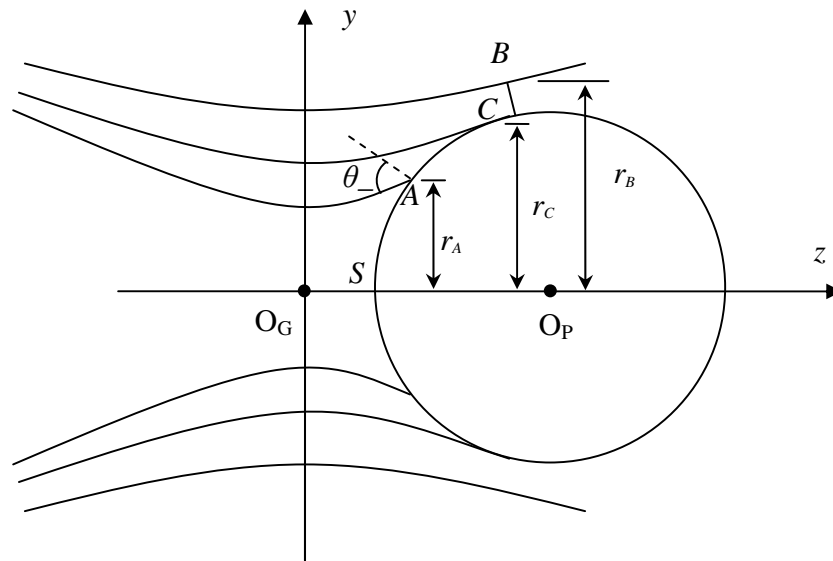


Fig. 3.12. Figure of the surface wave zone $A \rightarrow B$, in which the near-grazing incidence zone $A \rightarrow C$ corresponding to $[\theta_-, \pi/2]$ and $C \rightarrow B$ is the region for both surface wave rays and tunneling rays.

The region between the two points A and C corresponds to the near-grazing incidence where $\theta_i \in [\theta_-, \pi/2]$, θ_- is the same as that of plane wave incidence, and the region $C \rightarrow B$ corresponds to the zone of both surface wave rays and tunneling rays, where \overline{CB} has the length of $c\alpha^{1/3}$. Thus we have

$$F = \frac{\Phi_{A \rightarrow C} + \Phi_{C \rightarrow B}}{\Phi_{S \rightarrow A}} \times 100\% , \quad (3-27)$$

where $\Phi_{A \rightarrow C}$, $\Phi_{C \rightarrow B}$, and $\Phi_{S \rightarrow A}$ designate the flux contained in the regions $A \rightarrow C$, $C \rightarrow B$, and $S \rightarrow A$, respectively. The flux $\Phi_{A \rightarrow C}$ and $\Phi_{C \rightarrow B}$ can be calculated by

$$\Phi_{A \rightarrow C} = \Phi_{S \rightarrow C} - \Phi_{S \rightarrow A} , \quad (3-28)$$

$$\Phi_{C \rightarrow B} = \Phi_{S \rightarrow B} - \Phi_{S \rightarrow C} . \quad (3-29)$$

Using r_A , r_B , and r_C to designate the vertical distances, respectively, from the points A , B , and C to the x axis, we have

$$\Phi_{S \rightarrow A} = 2\pi \int_0^{r_A} I_G \cos(\bar{F}, \bar{z}) r dr , \quad (3-30)$$

$$\Phi_{S \rightarrow B} = 2\pi \int_0^{r_B} I_G \cos(\bar{F}, \bar{z}) r dr , \quad (3-31)$$

$$\Phi_{S \rightarrow C} = 2\pi \int_0^{r_C} I_G \cos(\bar{F}, \bar{z}) r dr . \quad (3-32)$$

As an example, F is calculated for the particles of radii 25, 50, 100, and 200 μm versus beam waist radius. The results are illustrated in Fig. 3.13. With the growth of the beam waist radius, the FRI increases to a constant for each particle size, which means more proportion of flux is contained by surface wave and it has a gradually remarkable effect to the scattering behavior. For a pure droplet of radius $r=25$, 100, and 250 μm , to control the deviation error of the GLMT from the EGOA within 5%, we find that the local beam waist should be less than 13 μm , 75 μm , and 280 μm , respectively. Hence, once the beam waist is small enough, the surface wave effect can be greatly suppressed.

FRI also depends on the particle size. As illustrated by Fig. 3.13, for a same value of w_0 , the surface wave effect is more significant for a small particle than for a large one. This is because, compared with the geometrical rays, the surface wave has a decreasing area proportion for an increasing particle size. For the extreme case of plane wave incidence, comparison of FRI can be more straightforward made through calculating the projection area ratio of the surface wave zone (Δs_{sw}) and the nonsurface wave zone (Δs_{n-sw}) since $I_G=I_0=\text{const}$ in this case. Then we have $[\Delta s_{sw} / \Delta s_{n-sw}]_{w_0 \rightarrow \infty} = 4c / [(k_1 r)^{1/3} - c(k_1 r)^{-1/3}]^2$, which means that better results can be achieved by

the EGOA for larger particles than for small ones. Especially when the beam waist tends to infinity and r is large enough, F is inversely proportional to $\alpha^{2/3}$.

Thus, we end this subsection by the comment that EGOA gives better results for a larger particle illuminated by a relatively focused Gaussian beam.

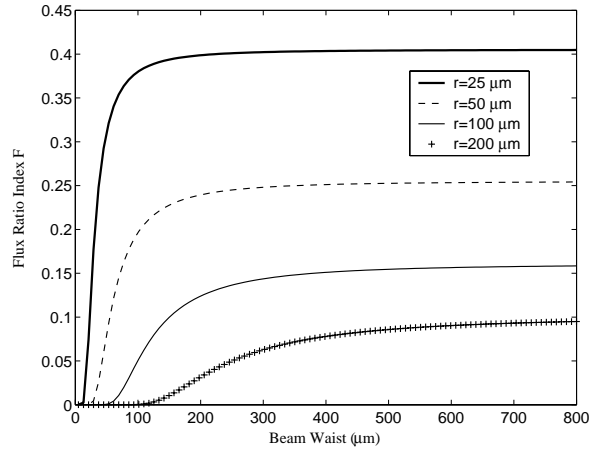
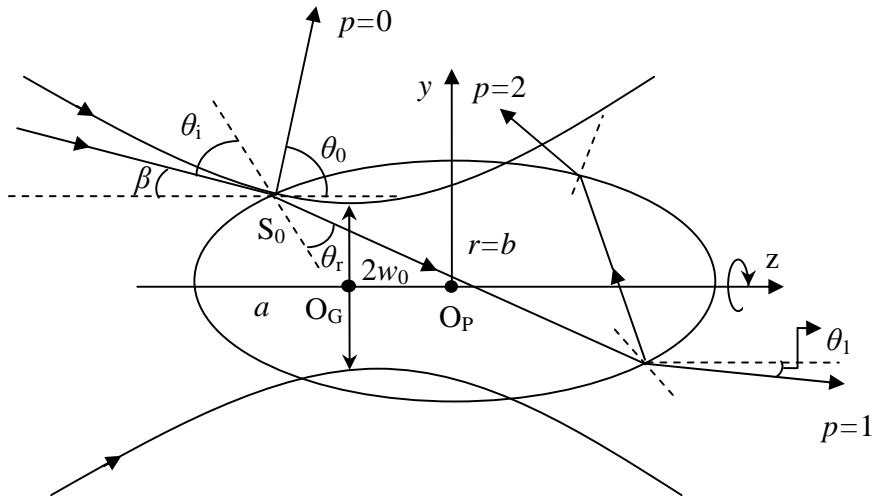


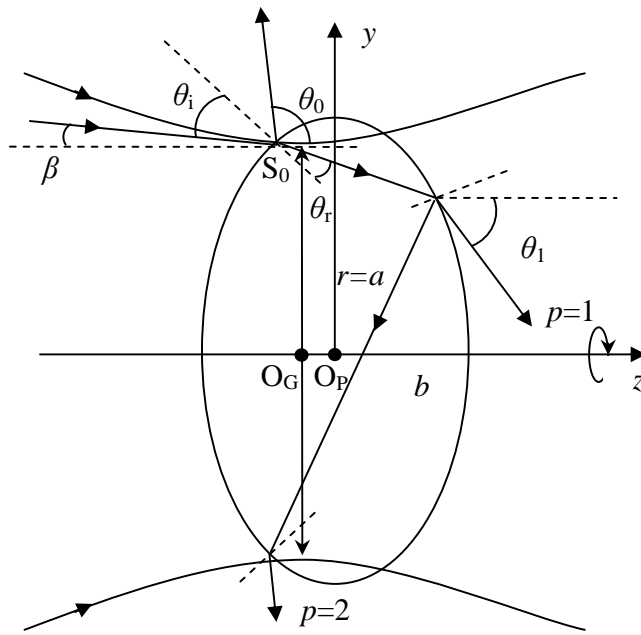
Fig. 3.13. FRI F of the surface wave for particles of radii 25, 50, 100, and 200 μm . ($c=4$, $z_0=0$, $\hat{m}=1.333$).

3.2 Gaussian beam scattering by a spheroid

In this subsection, the far-field scattering of a spheroidal particle illuminated by a Gaussian beam is discussed. The prolate and oblate spheroids are formed by rotating an ellipse around its major axis of length $2a$ and the minor one of length $2b$, respectively, as illustrated in Fig. 3.14. Since the beam propagates along the rotational axis of the spheroid, the situation of end-on incidence is brought in and the incident and scattered rays are all symmetric to the scattering plane. In this case, the TE and TM polarizations always stay separate and the mathematical handling can be simplified. For any other orientation of the spheroid or off axis incidence, there is no longer such symmetry; the plane of incidence changes at every interaction of a ray with the spheroid surface, leading to TE-TM polarization mixing that is difficult to unravel. As was done for spherical particle in Subsection 3.1, we still use the straight trajectory approximation for all the rays, both inside and outside the sphere.



(a)



(b)

Fig. 3.14. Scheme of ray tracing in a homogeneous spheroid which is located on z -axis of the incident Gaussian beam. Rotation axis of the spheroid is z -axis. (a) Prolate spheroid; (b) Oblate spheroid.

3.2.1 Description of the method

A TEM₀₀ Gaussian beam of waist radius w_0 , wavelength λ_0 in vacuum, and polarized in the x direction is assumed to propagate along the z axis, on which is located a spheroid of relative refractive index $\hat{m} = m_r + m_i i$. The center of the particle O_P is located at the origin of the coordinate system and the center of the beam O_G at $(0, 0, z_0)$. The aspect ratio κ of the spheroid is defined as the ratio of its semiaxis along the symmetric axis (z direction) and the semiaxis in the transverse direction (in O_P - xy plane), so $\kappa > 1$ for a prolate spheroid and $\kappa < 1$ for an oblate one. For convenience, we use a and b to denote the semimajor and semiminor axes of the spheroid, respectively, and r to denote the projection radius of the spheroid in O_P - xy plane. Therefore we have $r = a$ for the oblate spheroid and $r = b$ for the prolate one.

As for the spherical particle, the scattered field is also considered as a superposition of contributions of all the orders of rays, including specularly reflected rays, $S_{j,0}$, refracted rays of order p , $S_{j,p}$, which undergo $p-1$ internal reflections as well as the diffraction field S_d . The scattered field is then calculated by the summation of the complex amplitude of the diffracted field, reflected ray and all orders of refracted rays, as indicated by Eq. (3-4). And the far-field scattering intensity I_j at an observation point with distance R_s from the particle center is calculated by Eq. (3-5).

Calculation of the diffraction and description of the propagation of the Gaussian beam remain the same as for the spherical particle. We neglect also the so-called climbing wave (James, 1976) in geometrical diffraction theory for simplicity and treat the three-dimensional spheroid as a two-dimensional disk with radius r (Chevaillier et al., 1986, 1990). The externally reflected and refracted rays can be treated in the same manner as that for spherical particle, but we have no longer analytical expressions for deviation angle evaluation, the phase shifts and the number of focal lines passed by the rays. Therefore a sophisticated numerical algorithm is developed to predict the scattering intensity according to definition of the phase shift, the divergent and the attenuation factors.

Since van de Hulst's definition of the focal points (van de Hulst, 1957) still holds for the Gaussian beam scattering by the rotationally symmetric spheroid, the phase shift due to the focal

lines $\phi_{p,FL}$, is still numerically determined by the number of intersections both inside and outside of the spheroid, as done for the sphere. However, it is worth noting that for a spheroid, both the refractive index m_r and the aspect ratio κ decide the number of the focal line a ray encounters, while for a sphere, only the refractive index m_r takes effect.

3.2.1.1 Phase shift due to optical path

For a spherical particle, once the incidence angle is known, the incidence angle of the ray inside the sphere always stays same and the length of each optical path between two successive internal reflection points keeps constant. For a spheroid, however, each time the ray hits the boundary of the spheroid, the incidence angle changes and the length of the optical path inside the spheroid varies. No analytical expression is found for them. Then we evaluate the path numerically step by step.

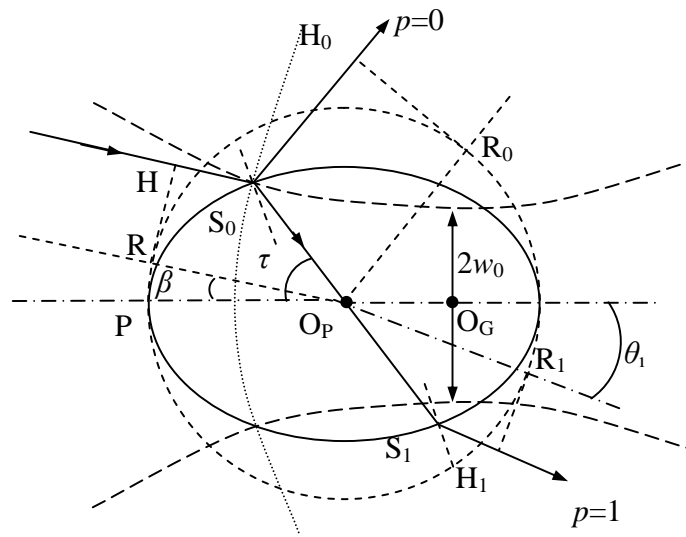


Fig. 3.15. Scheme for the calculation of phase shifts.

We consider a prolate spheroid illuminated by a Gaussian beam as shown in Fig. 3.15. The center of the beam is located at O_G with a distance $|z_0|$ from the center of the particle O_P . First, similar to the case of a sphere, three kinds of phase shifts are taken into account: the phase shift due to the optical path $\phi_{p,PH}$, the phase shift due to the focal lines (inside and outside of the

sphere) $\phi_{p,FL}$, and that due to the wavefront curvature of the Gaussian beam ϕ_G :

$$\phi_p = \frac{\pi}{2} + \phi_{p,PH} + \phi_{p,FL} + \phi_G. \quad (3-33)$$

We take the ray passing by the centre of the particle O_p with the same direction as the incident and the emergent rays as reference, i.e., RO_pR_1 , where R, R_1 are the intersection points between the radii and the reference circle, which has the same radius as the semimajor axis a . Then the phase shift of the reflected ray is

$$\phi_{0,PH} = k_1 \left(\overline{RO_p} - \overline{HS_0} + \overline{O_pR_0} - \overline{S_0H_0} \right). \quad (3-34)$$

The phase shift for the directly transmitted ray without any internal reflection can be evaluated by (see Fig. 3.15)

$$\phi_{1,PH} = k_1 \left[\left(\overline{RO_p} - \overline{HS_0} \right) - m_r \overline{S_0S_1} + \left(\overline{O_pR_1} - \overline{S_1H_1} \right) \right]. \quad (3-35)$$

Similarly, the phase shift for the ray undergoing $p-1$ internal reflections is determined by

$$\phi_{p,PH} = k_1 \left[\left(\overline{RO_p} - \overline{HS_0} \right) - m_r L_p + \left(\overline{O_pR_p} - \overline{S_pH_p} \right) \right], \quad (3-36)$$

where the total path in the spheroid $L_p = \sum_{i=1}^p \overline{S_{i-1}S_i}$ is evaluated numerically. For all orders of p , $\overline{O_pR_p} - \overline{S_pH_p}$ is calculated from the coordinate of the incident point of the ray on the surface of the particle and the deviation angle θ_p :

$$\overline{O_pR_p} - \overline{S_pH_p} = \sqrt{z_{i,p}^2 + y_{i,p}^2 - \overline{H_pR_p}^2} = \sqrt{z_{i,p}^2 + y_{i,p}^2 - \frac{(y_{i,p} - z_{i,p} \tan \theta_p)^2}{\tan^2 \theta_p + 1}}, \quad (3-37)$$

where $(y_{i,p}, z_{i,p})$ is the intersection point of the incident ray and particle surface. And for $\overline{RO_p} - \overline{HS_0}$, we have

$$\overline{RO_p} - \overline{HS_0} = \sqrt{z_{i,0}^2 + y_{i,0}^2 - \frac{(y_{i,0} - z_{i,0} \tan \beta)^2}{\tan^2 \beta + 1}}. \quad (3-38)$$

Then phase shift due to the curvature of the wavefront should be taken into account. As for the case of spherical particle, it is defined by

$$\phi_G = \phi_{HS_0} - \phi_{PQ} = \phi_{HS_0} - [k(z_0 + a) - \phi_i] = k_1 \left(a - \sqrt{z_{i,0}^2 + y_{i,0}^2 - \frac{(y_{i,0} - z_{i,0} \tan \beta)^2}{\tan^2 \beta + 1}} \right) - [k(z_0 + a) - \phi_i]. \quad (3-39)$$

The phase shift of the externally reflected ray is then given by

$$\phi_{0,PH} = k_1 \sqrt{z_{i,0}^2 + y_{i,0}^2 - \frac{(y_{i,0} - z_{i,0} \tan \beta)^2}{\tan^2 \beta + 1}} + k_1 \sqrt{z_{i,0}^2 + y_{i,0}^2 - \frac{(y_{i,0} - z_{i,0} \tan \theta_0)^2}{\tan^2 \theta_0 + 1}}, \quad (3-40)$$

and the phase for the refracted ray is given by

$$\phi_{p,PH} = \sqrt{z_{i,0}^2 + y_{i,0}^2 - \frac{(y_{i,0} - z_{i,0} \tan \beta)^2}{\tan^2 \beta + 1}} - k_1 m_r L_p + k_1 \left[\sqrt{z_{i,p}^2 + y_{i,p}^2 - \frac{(y_{i,p} - z_{i,p} \tan \theta_p)^2}{\tan^2 \theta_p + 1}} \right], \quad (3-41)$$

where β is the angle between incident ray HS_0 and the z axis and θ_p is the scattering angle of the emergent ray. θ_p , L_p , and $(y_{i,p}, z_{i,p})$ are determined from the ray tracing program similar to that in an elliptical cross section (Marcuse, 1974). It is proved that when $\kappa \rightarrow 1$,

$$L_p = 2pr \cos \theta_r, \quad (3-42)$$

$$k_1 \sqrt{z_{i,0}^2 + y_{i,0}^2 - \frac{(y_{i,0} - z_{i,0} \tan \beta)^2}{\tan^2 \beta + 1}} = k_1 r \cos \theta_i, \quad (3-43)$$

$$k_1 \sqrt{z_{i,p}^2 + y_{i,p}^2 - \frac{(y_{i,p} - z_{i,p} \tan \theta_p)^2}{\tan^2 \theta_p + 1}} = k_1 r \cos \theta_i. \quad (3-44)$$

Namely Eqs.(3-39)-(3-41) recover to the corresponding expressions of the spherical particle scattering.

3.2.1.2 Phase shift due to total reflection

Particularly for the ray tracing in a spheroid, the total reflection may be encountered and it should be taken into account carefully, since it results in two effects. One is absence of the

emergent rays beyond the critical angle θ_c , the other is additional phase shifts $\Delta\phi_{p,T,j}$, where the subscript $j=1$ or 2 stands for the perpendicular or parallel component. Then we have (Ghatak, 1977)

$$\Delta\phi_{p,T,1} = 2 \tan^{-1} \left[\frac{(\sin^2 \theta_{i,p} - 1/m_r^2)^{1/2}}{\cos \theta_{i,p}} \right], \quad (3-45)$$

$$\Delta\phi_{p,T,2} = 2 \tan^{-1} \left[\frac{m_r^2 (\sin^2 \theta_{i,p} - 1/m_r^2)^{1/2}}{\cos \theta_{i,p}} \right]. \quad (3-46)$$

Although such a phase change can be incorporated into a complex number expression of reflection coefficients, Eqs.(3-45)-(3-46) are more convenient for later superposition (Xu et al., 2004a) of amplitude and phase separately. Accounting all these effects, the final expression of phase shift should be revised as

$$\phi_{p,j} = \frac{\pi}{2} + \phi_G + \phi_{p,PH} + \phi_{p,FL} + \Delta\phi_{p,T,j}. \quad (3-47)$$

The above equations for a prolate spheroid are all valid for an oblate one.

3.2.1.3 Amplitude of scattered field

After $p-1$ internal reflections, the amplitude of an incident ray, $\varepsilon_{j,p}$, can be calculated by

$$\varepsilon_{j,p} = \begin{cases} r_{j,p} & \text{for } p = 0 \\ (1 - r_{j,0}^2)^{1/2} (1 - r_{j,p}^2)^{1/2} \prod_{n=1}^{p-1} (-r_{j,n}) & \text{for } p \geq 1 \end{cases}, \quad (3-48)$$

where $r_{j,p}$ is Fresnel coefficients calculated by

$$r_{1,p} = \frac{\cos \theta_{i,p} - m_r \cos \theta_{r,p}}{\cos \theta_{i,p} + m_r \cos \theta_{r,p}}, \quad (3-49)$$

$$r_{2,p} = \frac{m_r \cos \theta_{i,p} - \cos \theta_{r,p}}{m_r \cos \theta_{i,p} + \cos \theta_{r,p}}. \quad (3-50)$$

On the other hand, when a bundle of rays arrive at a surface, it is diverged or converged

according to the local curvature of the surface. As for the spherical particle scattering, the divergence factor D_G is defined by

$$D_G = \frac{\cos \theta_i \sin \tau}{\sin \theta_p \left| \frac{d\theta'_p}{d\tau} \right|}, \quad (3-51)$$

where τ is the position angle between vector $\overline{S_0 O_p}$ and the z axis. It can be calculated by

$$\tau = \tan^{-1} \left(\frac{y_{i,0}}{z_{i,0}} \right). \quad (3-52)$$

Similar to the spherical particle scattering, the divergence factor $\left| \frac{d\theta'_p}{d\tau} \right|$ for the spheroid is approximated numerically by

$$\left| \frac{d\theta'_p}{d\tau} \right| = \frac{|\theta'_{p,l+1} - \theta'_{p,l-1}|}{\left[\frac{r_{l-1}^2 + r_{l+1}^2 - 2r_{l-1}r_{l+1} \cos(\tau_{l+1} - \tau_{l-1})}{r_l^2} \right]^{1/2}}, \quad (3-53)$$

where θ'_p is the deviation angle of the emergent ray and the subscripts $l-1$ and $l+1$ designate the two incident rays adjacent to the l th one. r_l is the distance from the intersection point $S_0(y_{i,0}, z_{i,0})$ of the l th incident ray and particle surface incident to the particle centre $O_p(0, 0)$, namely,

$$r_l = (y_{i,0,l}^2 + z_{i,0,l}^2)^{1/2}. \quad (3-54)$$

For an absorbing spheroid, an attenuation factor should also be taken into account. When the path inside a spheroid L_p is known, the attenuation factor ξ_p can be easily obtained from

$$\xi_p = \exp(-k_1 m_i L_p). \quad (3-55)$$

Through energy balance identity (Hovenac. 1991), the amplitude of an emergent ray can then be calculated by

$$S_{j,p} = k_1 r |S_G| \varepsilon_{j,p} D_G^{1/2} \xi_p \exp(i\phi_p), \quad (3-56)$$

where S_G is the amplitude of the Gaussian beam at the intersection point of the incident Gaussian ray and the surface of the spheroid.

3.2.2 Numerical results and discussion

According to the method presented in Subsection 3.2.1, in this subsection we predict the scattered intensities of a prolate or oblate spheroid illuminated by a Gaussian beam. The particle can be transparent or absorbing. As done for the spherical particle, the diffraction of the spheroid is approximated by a simple disk of the same projection section as that of the spheroid in the plane perpendicular to the incident beam. The surface wave has not been taken into account. However, its potential influence on a scattering is also analyzed through evaluating FRI which gives a qualitative analysis of the surface wave effect.

3.2.2.1 Scattering diagrams of a spheroid

For all the numerical calculations presented, the number of internal reflections, p_{\max} , is taken to be 20. And 2000 equidistant incident rays are adopted to carry out the ray tracing in the spheroid. These values are found enough to ensure the precision of the final interpolation and the convergence of amplitudes summation.

To check our algorithm and verify the code, the calculation is carried out for a prolate and an oblate spheroid with an aspect ratio approaching 1. The result is compared with that predicted by using the GLMT. In Fig. 3.16 and Fig. 3.17, the scattering intensities of a transparent water droplet ($\hat{m}=1.333$) and a slightly absorbing one ($\hat{m}=1.333+0.001i$) with a projection radius $r=100\ \mu\text{m}$ illuminated by a Gaussian beam are compared with those of a sphere predicted by the GLMT. We find that when the aspect ratio κ approaches 1, the scattering diagrams tend to those predicted by the GLMT and EGOA for the sphere. We also calculate the forward scattering intensities of a prolate spheroid of semimajor axis $a=15\ \mu\text{m}$ and semiminor axis $b=10\ \mu\text{m}$ illuminated by a plane wave (Fig. 3.18) and compare with the result obtained by Hovenac (1991). Same intensity profiles are found.

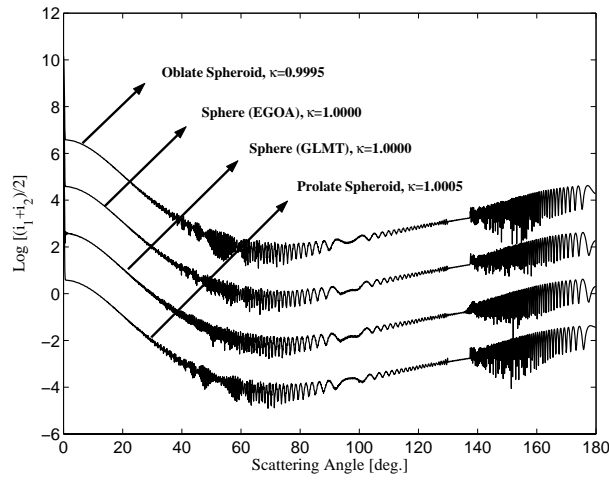


Fig. 3.16. Comparison of the scattering intensity calculated by the GLMT for a sphere and by the EGOA for a spherical, prolate ($\kappa=1.0005$) and oblate ($\kappa=0.9995$) spheroid. The projection radius of the spheroid r is equal to the radius of the sphere ($r=a=100 \mu\text{m}$). The particle of refractive index $\hat{m}=1.333$ is located at the center of a Gaussian beam of waist radius $w_0=50 \mu\text{m}$ and wavelength $\lambda_0=0.6328 \mu\text{m}$. The curves of the EGOA have been, respectively, offset by the factors of 10^2 , 10^4 , and 10^6 for clarity.

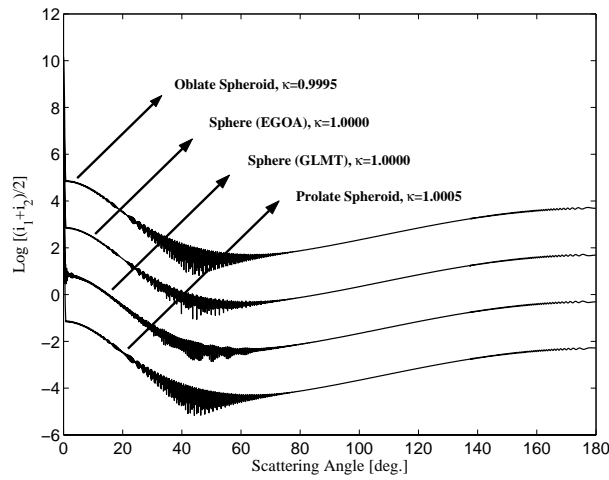


Fig. 3.17. Same parameters as Fig.3 but with $\hat{m}=1.333+0.001i$.

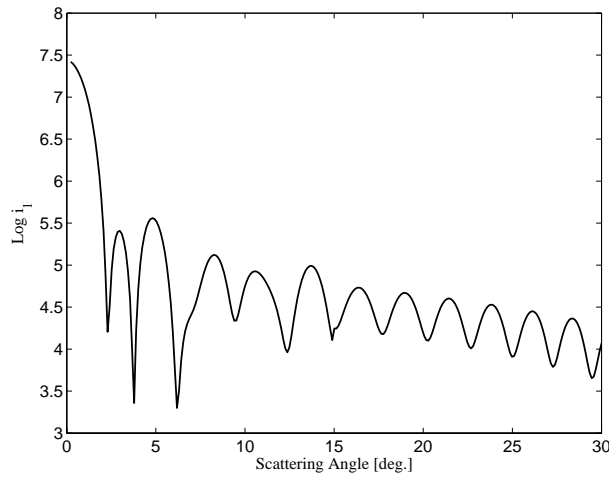


Fig. 3.18. Forward-scattering intensity of a spheroidal droplet of projection radius $r=b=10\ \mu\text{m}$ and aspect ratio $\kappa=1.5$ illuminated by a plane wave. The scattering pattern is the same as that given by Hovenac (1991) in Fig. 8.

Then the dependence of the scattering pattern on aspect ratio of the spheroid is shown in Fig. 3.19 and Fig. 3.20. A water droplet of refractive index $\hat{m}=1.333$ is assumed to be illuminated by a Gaussian beam of waist radius $w_0=50\ \mu\text{m}$. The projection radius r of the particle remains $100\ \mu\text{m}$ in all the calculations. With the increase of the aspect ratio, a remarkable backward movement of the primary rainbow position is observed except for $\kappa=2$ for which neither primary- nor higher-order rainbows are clearly observable. It's noteworthy that, for the aspect ratio $\kappa=0.5$, as illustrated in Fig. 3.19, both primary- and third-order rainbows are remarkable and they locate at 100° and 70° , respectively. The secondary-order rainbow, however, is hardly perceivable. The dependence of the rainbow position on the aspect ratio and the focalization of the beam as well as the particle location will be examined in Subsection 3.2.2.2.

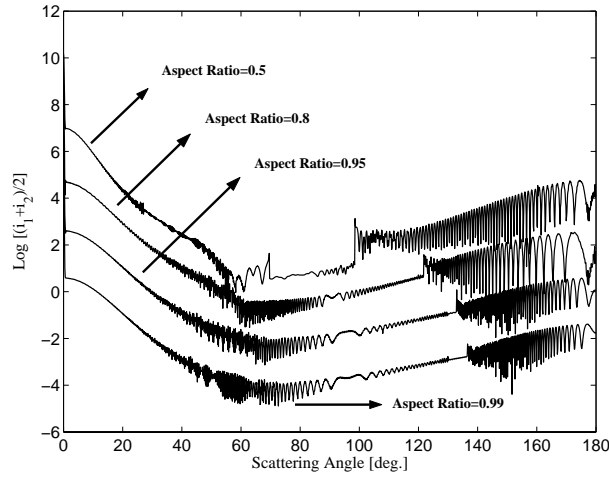


Fig. 3.19. Scattering intensity calculated by the EGOA for an oblate droplet of projection radius $r=100\ \mu\text{m}$, different aspect ratios, and located at the center of a Gaussian beam of $w_0=50\ \mu\text{m}$, $\lambda_0=0.6328\ \mu\text{m}$. The results of the cases $\kappa=0.8, 0.95,$ and 0.99 have been respectively offset by the factors of $10^2, 10^4,$ and 10^6 for clarity.

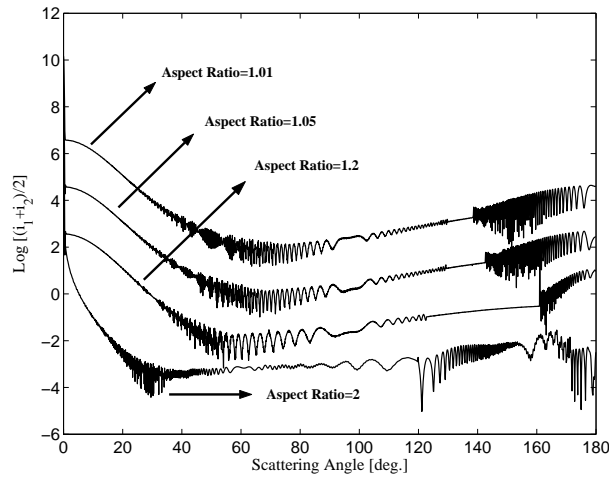


Fig. 3.20. Scattering intensity calculated by the EGOA for a prolate droplet of projection radius $r=100\ \mu\text{m}$, different aspect ratios, and located at the center of a Gaussian beam of $w_0=50\ \mu\text{m}$, $\lambda_0=0.6328\ \mu\text{m}$. The results of the cases $\kappa=1.05, 1.2,$ and 2.0 have been, respectively, offset by the factors of $10^2, 10^4,$ and 10^6 for clarity.

In a spheroid, the way of propagation for the surface wave rays might be different from that in a sphere because the surface curvature of the spheroid varies from place to place and the incidence angle changes each time the ray hits the surface of the spheroid. Up to now, we have not been able to develop a numerical or theoretical approach to evaluate quantitatively the surface wave effect in our calculation. However, in this thesis we try discussing qualitatively the surface wave effect from the viewpoint of the energy incident on the surface at near-grazing

angle and neglect the concrete propagation behavior of surface wave inside the particle as well as the newly created surface wave by internal near-grazing incidence. Such a simplification permits a similar flux analysis of the surface wave, as given in Subsection 3.1.3, by using the FRI F , which reveals to some extent the potential influence of the surface wave on the scattering. For the spheroid, we use the same definition of the flux ratio index F as for the sphere.

In Fig. 3.21 are plotted the F curves versus the aspect ratio for a Gaussian beam ($w_0=50\ \mu\text{m}$) and quasi plane wave ($w_0=10\ \text{cm}$ in the calculation). The refractive index and the projection radius of the spheroid are 1.333 and $100\ \mu\text{m}$, respectively ($\hat{m}=1.333$ and $r=100\ \mu\text{m}$). It is evident that for the same aspect ratio κ , the FRI for the beam of waist half of the projection radius of the spheroid is much smaller than that for the plane wave because the incident intensity in the surface wave zone is so weak that can be neglected. This means the surface wave has a limited potential influence to the scattering when the ratio of beam waist radius w_0 to the projection radius of the spheroid r is small.

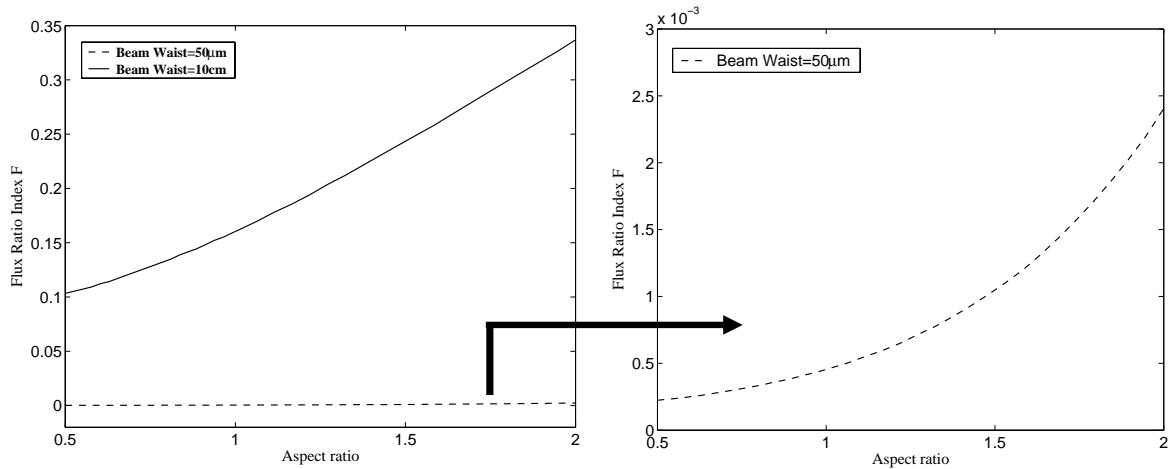


Fig. 3.21. Impact factor as a function of aspect ratio calculated for a spheroid of projection radius $r=100\ \mu\text{m}$ illuminated by a Gaussian beam of waist radius $w_0=50\ \mu\text{m}$ (dashed curve) and quasi-plane wave of $w_0=10\ \text{cm}$ (solid curve).

Meanwhile, Fig. 3.21 shows that the FRI increases with the aspect ratio. This reveals the fact that the surface wave has more remarkable influence on the scattering of a prolate spheroid than on the scattering of an oblate one.

Combined with the discussions for the spherical particle in Subsection 3.1, we end the section

with the following comments.

1. The surface wave effect depends on the ratio of the size of the particle to the beam waist radius; the smaller the ratio is, the less the effect is important. As found for the sphere, the flux ratio index F is inversely proportional to $x^{2/3}$ for a plane wave incident on a large sphere.
2. The surface wave effect depends on the local curvature of the surface of the particle, the aspect ratio, and the propagation directions of the incident Gaussian rays, or the focalization of the beam. These parameters decide the size of surface wave zone. For example, a prolate spheroid has a larger surface wave zone than an oblate one for the same projection radius r . Same effect can be achieved by a spheroid located before or behind the beam waist.

3.2.2.2 Geometric rainbow angle of primary order

The surface wave rays, tunneling rays, as well as the complex rays are not included in our GO approximation, which brings in some inaccuracies to scattering calculation. However, the prediction of the rainbow position θ_{rg} for a Gaussian beam incident on a spheroid can still be achieved within the framework of GO, as done by Moebius (1910) for plane wave incidence. We are especially interested in the angular location of the primary rainbow of a spheroid, due to its more practical applications in thermometry and particle sizing technologies (van Beeck and Riethmuller, 1996; Yildiz et al., 2002).

From the viewpoint of GO, the stationary deflection of the emergent rays experiencing one internal reflection with respect to the variation of position angles, i.e., $d\theta_2/d\tau \rightarrow 0$, produces the start point of the primary geometrical rainbow. On the basis of such a definition, rainbow positions versus beam waist radius, the aspect ratio, the refractive index, and the particle location in the beam can be predicted accordingly.

As pointed out in Subsection 3.2.2.1, the surface wave effect increases with the aspect ratio of the spheroid. GO might not be accurate enough for large aspect ratios and its validity needs further verification. However, with the decrease of aspect ratio, the rays impinge on a flatter surface and the observed backscatter in experiment is also quite different from the prediction of the GO (Hovenac, 1991). Therefore in the present subsection, we only discuss the rainbow of a

spheroid not greatly deformed from the sphere, i.e., $0.5 \leq \kappa \leq 2.0$.

a. Rainbow position versus aspect ratio and comparison with Moebius's results

The geometric rainbow is found to be sensitive to the aspect ratio. As illustrated in Fig. 3.22, when a spheroid water droplet of refractive index $\hat{m}=1.333$ and projection radius $r=100 \mu\text{m}$ is located at the centre of the beam, the geometric angular position of the rainbow θ_{rg} moves backward from 98.7° for $\kappa=0.5$ to 180° for $\kappa=1.42$. The rainbow disappears for the aspect ratio between 1.42 and 1.58, then reappears and moves to the forward until 152° for $\kappa=2$. Such a result is obtained for all the four beam waists radii $25 \mu\text{m}$, $75 \mu\text{m}$, $200 \mu\text{m}$, and $3000 \mu\text{m}$.

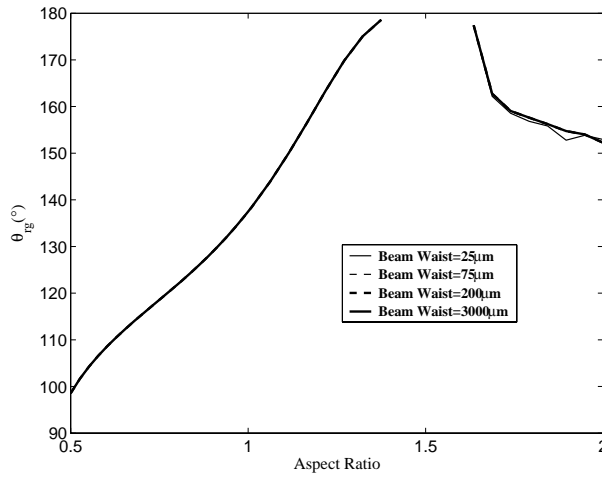


Fig. 3.22. Primary-order rainbow position versus aspect ratio, predicted by the EGOA for a spheroidal droplet of projection radius $r=100 \mu\text{m}$ and illuminated by the Gaussian beam of waist radii $w_0=25, 75, 200,$ and $3000 \mu\text{m}$, respectively.

To explore the rainbow phenomenon for a spheroid of different aspect ratios, we perform ray tracing for a prolate spheroid of aspect ratios $\kappa=1.35$ (case $\kappa < 1.42$), $\kappa=1.5$ (case $1.42 \leq \kappa \leq 1.58$), and $\kappa=1.65$ (case $\kappa > 1.58$), with same projection radius $r=100 \mu\text{m}$. Three parallel incident rays, labeled by a, b and c are used for ray tracing. They correspond to the emergent rays $a', b',$ and c' , respectively. As illustrated in Fig. 3.23, after experiencing one internal reflection, the emergent ray b' corresponds to the rainbow angle of $\theta_{\text{rg}}=177.1^\circ$ and 175.5° , respectively, for a spheroid of $\kappa=1.35$ and $\kappa=1.65$, and the other two emergent rays a' and c' locate at the same side of ray b' , which indicates that there is a turning angle for the emergent rays at the geometrical rainbow angle. For the spheroid of aspect ratio $\kappa=1.5$ the turning angle does

not exist; therefore there is no rainbow phenomenon. This can also be seen clearly from the variation of the deviation angle θ_p' of emergent rays versus the incidence angle in Fig. 3.24. It is noteworthy that for all these three aspect ratios, after experiencing one internal reflection, all the incident rays are refracted out from the spheroid.

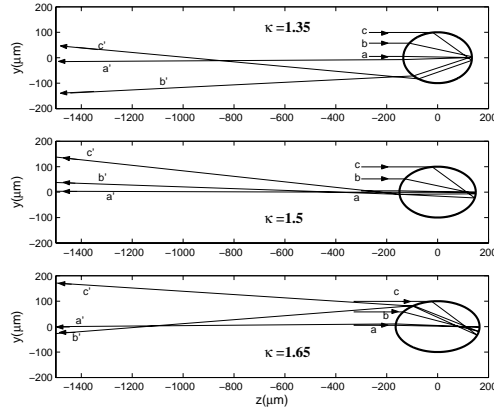


Fig. 3.23. Ray tracing in three prolate spheroids with the same projection radius $r=100 \mu\text{m}$ but different aspect ratios $\kappa=1.35$, $\kappa=1.50$, and $\kappa=1.65$, respectively. The three incident rays are parallel to the z axis.

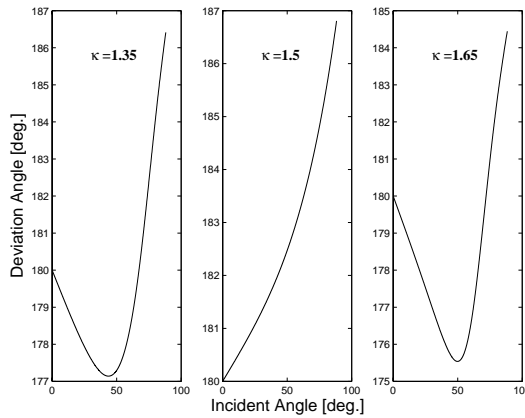


Fig. 3.24. Deviation angle θ_p' of the emergent rays ($p=2$) from three prolate spheroids with the same projection radius $r=100 \mu\text{m}$, but with aspect ratios $\kappa=1.35$, $\kappa=1.5$, and $\kappa=1.65$, respectively (2000 equidistant incident rays are used).

In Fig. 3.25 can we find that, for the beam of waist radii $w_0=25$ and $75 \mu\text{m}$, the intensity magnitude of the incident rays associated with the rainbow angle grows drastically when the aspect ratio increases. This reveals that the rays causing primary-order rainbows move from the

edge region of the particle toward the beam axis. Such a comment is confirmed by adopting 2000 equidistant rays to perform the ray tracing in a prolate droplet of projection radius $r=100 \mu\text{m}$ and refractive index $\hat{m}=1.333$, and illuminated by a plane wave. When κ increases from 1.01 to 1.25 and then to 1.40, the rays at $y_{1652} = 826 \mu\text{m}$, $y_{1471} = 735.5 \mu\text{m}$, and $y_{642} = 321 \mu\text{m}$ are found associated with $d\theta_2 / d\tau = 0$, respectively.

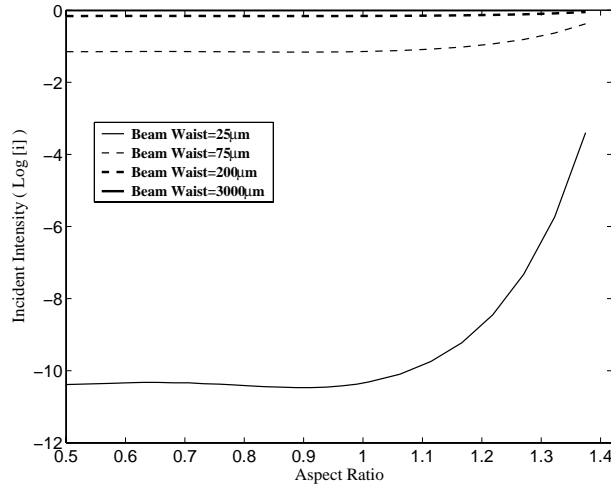


Fig. 3.25. Intensity of the incident ray associated with the rainbow position θ_{rg} in Fig. 3.22.

Next, we compare Moebius's prediction of the primary rainbow to that of EGOA method. Moebius (1910) found the following simple formula for the deviation of geometrical rainbow, $\Delta\theta_{\text{rg}}$ for the case of plane incident on a prolate or oblate spheroid:

$$\Delta\theta_{\text{rg}} = 16 \left(\frac{b-a}{b+a} \right) \frac{\cos \tau_{\text{rg},o}}{m_r} \sin^3 \left[\arccos \left(\frac{\cos \tau_{\text{rg},o}}{m_r} \right) \right] \cos(\theta_{\text{rg},o} - 2\Theta_{\text{pl}}), \quad (3-57)$$

where Θ_{pl} is the angle between the incoming plane wave and the z -axis (here $\Theta_{\text{pl}}=0^\circ$ for end-on incidence), the incidence angle corresponding to rainbow angle, $\tau_{\text{rg},o}$ for a sphere (the subscript "o" designate the sphere) is calculated by

$$\sin \tau_{\text{rg},o} = \left[(m_r^2 - 1) / 3 \right]^{1/2}, \quad (3-58)$$

and $\theta_{\text{rg},o}$ is the geometrical rainbow angle for a sphere and can be related to $\tau_{\text{rg},o}$ by

$$\theta_{\text{rg},o} = -2\tau_{\text{rg},o} + 4\tau'_{\text{rg},o}, \quad (3-59)$$

where the refraction angle $\tau'_{\text{rg},o}$ is obtained from the incidence angle $\tau_{\text{rg},o}$ by using Snell's law:

$$\cos(\tau'_{\text{rg},o}) = \frac{\cos(\tau_{\text{rg},o})}{m_r}, \quad (3-60)$$

The droplet with refractive index $\hat{m} = 1.333$ is illuminated by a plane wave of wavelength $\lambda_0 = 0.6328 \mu\text{m}$. The calculation is made for spheroids of aspect ratio κ between 0.8 and 1.2. The results are illustrated in Fig. 3.26. We find that the discrepancy of Moebius's result with that of the EGOA is less than 0.5° for $|\kappa - 1| \leq 0.05$ and less than 2° for $|\kappa - 1| \leq 0.11$. The more the aspect ratio differs from 1, the more the discrepancy. This is because Moebius theory is only an $O(\kappa)$ approximation to the exact ray tracing, which can be applied only for the aspect ratio quite near unity.

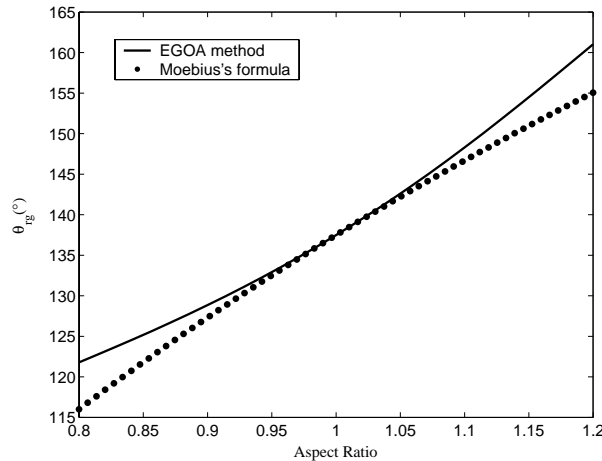


Fig. 3.26. Comparison of primary-order rainbow position (versus aspect ratio) predicted by the EGOA and the Moebius's formula when a spheroidal droplet of projection radius $r = 100 \mu\text{m}$ is illuminated by a plane wave.

It's noteworthy that according to the definition of rainbow, the emergent rays of $p=2$ might have more than one stationary deflection angle if the spheroid deviates much from the sphere, e.g., $\kappa < 0.89$ or $\kappa > 1.68$. Within the framework of GO, this means that there exist several revolutions of the emergent rays corresponding to more than one primary rainbow. However, in Fig. 3.22, the first stationary deflection angle is looked on as the occurrence position of the primary rainbow.

3.2.2.3 Rainbow position versus waist radius

Except for some tiny differences when κ approaches 2.0, nearly the same primary rainbow positions are predicted for the different beam waist radii, as shown in Fig. 3.22. The difference of θ_{rg} between $w_0=25$ and $3000 \mu\text{m}$ is found to be less than 0.06° when κ is between 0.5 and 1.42. This is because the divergence angle is very small, less than 0.46° for the beam of waist radius $w_0>25 \mu\text{m}$ and wavelength $\lambda_0=0.6328 \mu\text{m}$.

3.2.2.4 Rainbow position versus refractive index

The primary rainbow position is sensitive to the refractive index. A relationship of geometric rainbow position θ_{rg} versus the refractive index m_r is shown in Fig. 3.27, when a prolate spheroid of the same projection radius $r=100 \mu\text{m}$ illuminated by a plane wave ($w_0 \rightarrow \infty$) of wavelength $\lambda_0=0.6328 \mu\text{m}$. We find that for all the κ values, the rainbow position moves backward when the refractive index increases, until 180° . This is consistent with the phenomenon in Fig. 3.19 and Fig. 3.20, in which the position of the primary rainbow exhibits a backward moving phenomenon, from nearly 98.7° ($\kappa=0.5$) to 161° ($\kappa=1.2$) and then disappears ($\kappa=2$).

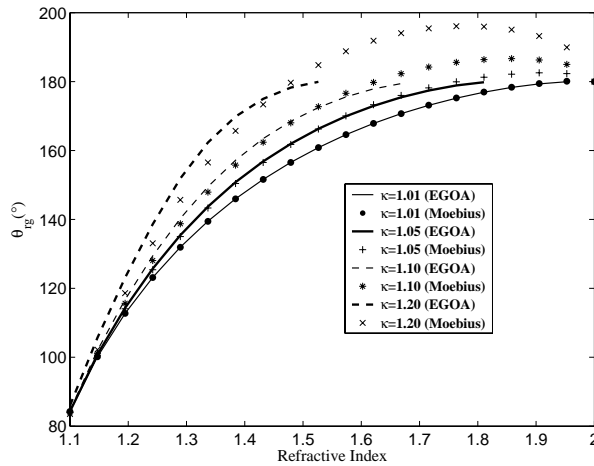


Fig. 3.27. Geometric rainbow position versus refractive index for a prolate spheroid illuminated by a plane wave. The results indicated by the curves are calculated by the EGOA and those indicated by symbols are calculated by the Moebius's formula.

3.2.2.5 Rainbow position versus particle location

The preceding discussions are based on the assumption that the particle is located at the center of the beam. Actually, when the beam is not too much focused, the dependency of θ_{rg} on the particle's location in the beam is not quite remarkable. For example, when $w_0=r=100\ \mu\text{m}$ and the prolate droplet of $\kappa=1.1$ and $\hat{m}=1.333$ moves along the z axis, the primary rainbow position varies slightly at the vicinity of 148.2936° (see Fig. 3.28), which corresponds to plane wave incidence.

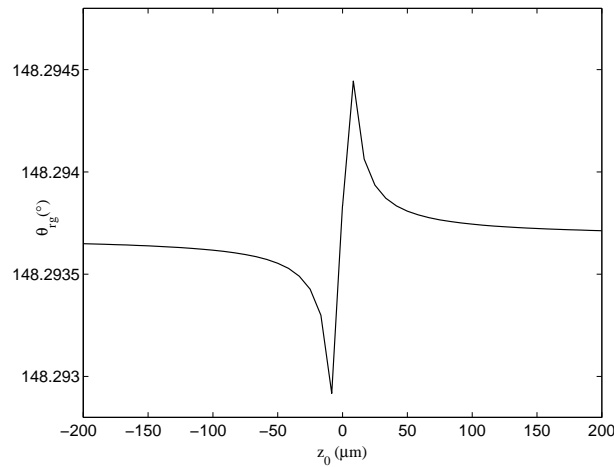


Fig. 3.28. Geometric rainbow position θ_{rg} versus particle position z_0 for a prolate droplet of aspect ratio $\kappa=1.1$, projection radius $r=100\ \mu\text{m}$ and illuminated by a Gaussian beam of waist radius $w_0=100\ \mu\text{m}$.

3.3 Conclusion

The GO approximation has been extended to describe light scattering by a transparent or absorbing sphere and spheroid for on-axis illumination of Gaussian beam. To explore the EGOA's validity range, a comparison is made to the GLMT for a sphere. It is found that when the particle radius is much larger than the wavelength the agreement between the EGOA and GLMT is good. The relative discrepancy is normally less than 5% when the beam waist radius is smaller than the particle radius. But such a discrepancy becomes more remarkable if the beam waist radius is larger than the radius of the sphere, since in this situation ray theory have some inaccuracies at angles where surface wave plays an important role.

For an absorbing sphere the agreement between the results of EGOA and those of GLMT is

fairly good in all angular directions. However, for a relatively small particle (say the radius of the particle is less than 50 times the wavelength), when the ratio of the beam waist radius and the particle radius is smaller than one fourth, the discrepancy between the two theories becomes remarkable.

On the basis of these works for a spherical particle, the EGOA is extended to the studies of the Gaussian beam scattered by a large spheroid. The position of the primary order rainbow angle is theoretically predicted and compared with that predicted by Moebius's formula. It shows a high dependence on the aspect ratio of the spheroid and its refractive index, but little on the beam waist radius as well as particle location in the beam when it is not extremely focused. Our EGOA permits to predict the rainbow position for a spheroid of any aspect ratio. The limitation of Moebius formula for rainbow prediction for the spheroids of aspect ratio near to unity is overcome. A nonrainbow region is identified for the droplet when its aspect ratio κ is within [1.42, 1.58].

By introducing the flux ratio factor F , the surface wave effect is qualitatively analyzed. It is found to have less influence on the scattering of a large particle illuminated by a relatively focused beam. Moreover, its effect depends not only on the refractive index, the size, and the surface curvature of the spheroid, but also on the focalization of the beam and the position of the particle in the beam.

Part II.

Online Wet Steam Measurement by Using Spectral Light Extinction Method

Chapter 4. Introduction

Particle size and concentration analysis is a fundamental topic of aerosol science, biomedical science and many industrial processes. The last several decades have seen more and more optical means applied in particle and particle system characterization because of their advantages of non-intrusive measurement and rapid data processing.

Compared with other optical particle sizing methods, such as the laser diffraction method (Allen, 1997), the angular scattering method (Holve and Self., 1979a, b), and the photo correlation spectroscopy (Berne and Pecora, 1976), etc., the light extinction method (LEM) (van Dongen et al., 1994; Wang et al., 1994) has several outstanding features: a more simpler optical layout, no strict requirements on photoelectric detecting system and ease in operation. Theoretical and experimental studies have indicated that the LEM can be applied to the measure the particles of diameter in [0.1-5.0] μm by using the visible wavelength range of a light source. Such a range is between the lower limit of laser diffraction method and the upper limit of photo correlation spectroscopy.

Abundant references can be found during the development of the LEM in the past several decades. The main contributions to this method in history will be reviewed in this chapter. They can be classified roughly into the following three aspects to be discussed in detail in the upcoming subsections: 1. development of light extinction method; 2. Influence of some factors; 3. Inversion algorithms.

4.1 Development of light extinction method

Generally speaking, the LEM includes two-wavelength method (Uthe, 1982), three-wavelength method (Teorell, 1931; Cashdollar et al., 1977; Wittig et al., 1981; Kourti et al., 1987), picture-matching method (Walters et al., 1980), and spectral light extinction method (SLEM) (van Dongen et al., 1994; Wang et al., 1994). Except the SLEM, all the methods aim at the evaluation of the average size as well as the concentration of a particle system. For example, the two-wavelength method (Uthe, 1982) is based on the monotonic relationship between the extinction coefficient ratio of two wavelengths R_Q ($R_Q=Q_{\text{ext}}(\hat{m}, d, \lambda_1)/Q_{\text{ext}}(\hat{m}, d, \lambda_2)$) for particle (relative

refractive index \hat{m}) of mean diameter d less than a certain value d_{\max} ($d < d_{\max}$).

However, in the whole range of d , there exist oscillations with the $Q_{\text{ext}}-d$ curve for lossless and weakly absorbing particles so that the particle diameter d has multi-valued dependency on a same extinction coefficient ratio R_Q . In this case at least two extinction coefficient ratios, or three wavelengths, are needed to determine the average diameter and the concentration (Teorell, 1931; Cashdollar et al., 1977; Wittig et al., 1981).

A critical improvement of LEM is the usage of a series of extinction ratios selected from a spectrum generated by a light source with a certain bandwidth. Since in this case much more information about the particle system can be collected, and the inversion of particle size distribution instead of a mean value, e.g., D_{32} , becomes possible. Such an improvement also brings out the SLEM used in this thesis to measure the polystyrene particles and the wet steam in a turbine.

Because of the aforementioned characteristics and advantages of the LEM and SLEM, they have found many applications in aerosol science and technology. For example, Walters and Skingley (1979) used the LEM to measure the droplets contained in the wet steam flow; Crawley et al. (1997) developed the SLEM system for online crystallization measurement. Recently, urban aerosol measurements by using the SLEM have been conducted by Kocifaj and Horvath (2005). In addition, the SLEM have also been used for measurement of fresh undiluted cigarette smoke, soot particles contained in the combustion flame, and the flue gas of the diesel engine (Dittmann et al., 1994; Widmann et al., 2003). To date, the LEM has also been successfully combined with other measurement techniques, e.g., the forward scattering method (Nefedov et al., 1997), light fluctuation method (Wessely, 1999), etc., to meet higher requirement of measurement.

4.2 Influence of some factors

In the development of the LEM, influence of some factors on the measurement precision, such as the refractive index, the multiple scattering, the particle nonsphericity, and the forwarding scattering effect have been discussed. They are to be briefly reviewed in the upcoming subsections.

4.2.1 Refractive index

Influence of inaccurate estimation of refractive index on the inverse results has been systematically studied by Wang et al. (1996). It is found that small inaccuracy involved in refractive index of the particle of ~ 0.05 ($\Delta\hat{m}_p=0.05$) might bring in a maximum deviation of 5~6% to the inversed mean diameter. When water is used as the surrounding medium, it can be considered as transparent and has an average refractive index 1.333 ($\hat{m}_1=1.333$) at common temperature and pressure, though in the strict sense its real value changes slightly with the wavelength. Taking advantage of the sensibility extinction ratio on the refractive index, Xu et al. (2005) explore the feasibility of measuring the refractive index of the particle by using SLEM. It was found that when the monodispersity of the particle system is high enough, the SLEM is applicable.

4.2.2 Multiple scattering and forward scattering

A useful parameter for characterization of the scattering regimes is the optical thickness ζ , which is calculated by the turbidity τ multiplied with the distance L the light traverses through the measurement zone ($\zeta=\tau L$). As suggested by Swanson et al. (1999), we use the optical thickness ζ as the parameter to distinguish three scattering regimes: the single scattering regime characterized by $\zeta < 1$, the multiple scattering regime characterized by $1 < \zeta < 10$, and diffusion regime characterized by $\zeta \geq 10$.

Since the extinction method is based on the measurement of the directly transmitted light intensities, the detected signal should not contain any component of the scattering intensities. However, the detector used in the SLEM system has a definite size corresponding to a certain forward angular range, so that in theory the detector receives the scattered intensities more or less. When the detector used in the SLEM system is large, corresponding to a larger collection angle, the influence of forward scattering effect should be carefully considered, even for the single scattering regime (Deepak and Box, 1978a, b).

Most researchers restrict the application of Beer-Lambert law to the situation of single scattering regime, so that the influence of multiple scattering can be neglected. However, Swanson et al.'s

research indicates that the validity range of Beer-Lambert law used by the LEM and the SLEM could cover completely the single scattering and multiple scattering regimes ($\xi < 10$) as long as the maximum half collection angle of the detector ($\Delta\theta_{1/2}$) is less than one tenth of the first angular minimum in the Fraunhofer diffraction pattern of a disk with the same projection area as that of the spherical particle (Swanson et al., 1999). Namely,

$$\Delta\theta_{1/2} \leq \frac{1}{10} \Delta\theta = 0.122 \frac{\lambda}{\hat{m}_1 d}, \quad (4-1)$$

where λ is the wavelength of incident light in the medium and d is the diameter of the particle. This means that to measure the polystyrene particle of diameter $d=10 \mu\text{m}$, refractive index 1.590 ($\hat{m}_{\text{II}}=1.590$) and suspended in water ($\hat{m}_1=1.333$), the collection angle should be less than 0.26° for the wavelength of 488 nm and the optical thickness ξ as large as 10.

For a larger collection angle of the detector, multiple scattering effect should be taken into account even for small optical thickness. Studies on this subject have been carried out by Schnablegger and Glatter (1995) via solving the radiative transfer equation (RTE). Through incorporation of the first-order approximation of multiple scattering into PSD inversion (Schnablegger and Glatter, 1995), the requirement on light transmittance is claimed to be reduced from $(I/I_0) > 95\%$ to $(I/I_0) > 70\%$. Similar work is also carried out by Hireleman (1988, 1991) and Kokhanovsky and Weichert (2001). Their work concentrates on the calculation of the scattered intensities in the regime of multiple scattering. And the incident wave is assumed to be planar.

In comparison with the RTE method, the Monte Carlo method is more flexible and has no special requirements on the incident profile of the beam, neither on the dimension, the shape, or the location of the detector. Therefore it finds more applications in direct numerical simulations of particle sizing in multiple scattering regime. By using the Monte Carlo method, influence of multiple scattering on the transmitted intensities reaching a detector of certain shape and dimension has been carried out by Bruscaioni et al. (1987), Briton et al. (1992), and Czerwinski et al (2001a, b). Such a method is also to be employed by us to evaluate the multiple scattering effect for our optical system.

As to the diffusion regime at a much higher particle concentration ($\xi \geq 10$), it is not be concerned in this thesis since it is rarely encountered in wet steam measurement.

4.2.3 Non-sphericity of the particle

For non-spherical particle sizing, a popular way is to use the volume equivalent sphere for coefficient matrix calculation by applying the Mie theory. In this case, however, errors unavoidably appear with the inversed PSD and the amount of large particles is generally underestimated (Kocifag and Horvath, 2005). In multi-angle scattering experiments, the influence of particle's non-sphericity on the inverse results has been studied by Heintzenburg (1978). To improve the measurement results, Liu et al. (1998) use both anomalous diffraction theory and T-matrix method to study the overall extinction efficiency of the randomly oriented circular cylinders of different diameter-to-length ratios (D/L). The extinction spectrum for the spheroids of randomly orientation is also studied by Asano and Sato (1980). It is found that the employment of T-matrix method and rigorous theory in non-spherical particles measurements can improve much the inverse results (Liu et al., 1999).

4.3 Inversion algorithms

Inverse problem is an important aspect of optical particle sizing. Although most optical means developed for particle system characterization, e.g., laser diffraction method (Allen, 1997), global rainbow method (van Beeck, 2001), and transmission fluctuation method (Shen et al., 2005) obtain the final PSD through discretizing the integral equations into matrix form and then solving it, the inverse problem in the SLEM seems more difficult than those in most of others. This is mainly due to the serious oscillation of the kernel function Q_{ext} versus particle size.

To date, the inversion algorithms can be roughly classified into two types: dependent model and independent model. The dependent model algorithm assumes that the particle system conforms to a given unimodal size distribution, e.g., the Rosin-Rammler distribution and the logarithmic normal distribution (Stevensen et al., 1961; Kerker, 1969; Barth, 1984). Most of them can be characterized by two parameters: one is for the characterization of a special diameter, e.g., the diameter representing the peak value of PSD, while the other is for the restriction of the distribution width. These pre-assumed PSDs can be applied in some special industrial

processes where the size distribution of the particles can be empirically known. For example, the Rosin-Rammler function can be employed to model the particles generated in the grinding process; the logarithmic normal distribution can be used to represent most of colloidal populations frequently skewed. In these cases, the inversion becomes to determine the optimized values of these parameters leading to the best fitting of the reconstructed spectrum to the measured one. As dependent model algorithms, simplex iteration, quasi-Newton method and Powell algorithm, etc. (Adby and Demster, 1974) have the drawback that optimization might be trapped into the local optimized solutions instead that the global one is found (Xu et al., 2004b). Moreover, in most situations it is difficult for us to get any prior knowledge about the PSD shapes of the particles produced in most industrial processes.

Thus, we turn to the independent model algorithm which does not make any assumption of the PSD in advance. The particle size solution is obtained directly by solving the Fredholm integral equations discretized into matrix form. A critical review of independent model algorithm has been given by Kandlikar and Ramachandran (1999). Among all the independent model algorithms, the Phillips-Twomey algorithm (Twomey, 1979) has been widely used. Its application in practical particle size analysis by using the SLEM has been done by Walters et al. (1980). To ensure the positive solution of the volume or number fraction in each size interval, the Phillips-Twomey method can be combined with the non-negative least square (NNLS) method (Lawson and Hanson, 1974) so that the Phillips-Twomey-NNLS algorithm is formed (Niemann and Weichert, 1995). However, the difficulty of the Phillips-Twomey-NNLS algorithm lies in the choosing of an optimized Lagrange multiplier γ which serves as an equilibration point ensuring both the smoothness of the PSD solution and the fitting of the reconstructed extinction spectrum to the measured one (King, 1982). To find such a point, the Generalized Cross-Validation (GCV) criterion (Golub et al., 1979) and the L-curve method (Hanson, 1992) are developed. According to the GCV criterion, the optimized value of the Lagrange multiplier corresponds to the minimum of an objective function with respect to γ . According to the L-curve method, however, the optimized value of the Lagrange multiplier locates at the corner of the objective function (presenting L-curve shape). Such a corner is characterized by the maximum curvature. The drawback of the GCV criterion is that the objective function might have a flat minimum, so it is difficult for us to find the best solution.

Moreover, the GCV criterion can not be applied to the occasions that correlated measurement errors exist. Though in the later situation L-curve method can be applied, it is not convergent for highly multimodal distributions (Hanke, 1996). As another effective independent model algorithm of great availability in optical particle sizing, the optimized regularization technique (ORT) is developed by Schnablegger and Glatter (1991). In such a method, a set of basic cubic Splines are introduced, each spline representing a basic size distribution function within a certain size window. Thus the inversion becomes to determine the weight coefficients multiplied with the basic PSDs. To ensure the positive solution, the NNLS method is used to determine these weight coefficients. To smooth the solution, the minimum of the first derivative of the coefficients is to be found. In the end, the optimization also becomes to find the best Lagrange multiplier balancing both the smoothness of solution and the fitting of the reconstructed spectrum to the measured one (Schnablegger and Glatter, 1995).

Compared to the Phillips-Twomey-NNLS and the ORT algorithms, the genetic algorithm (Lienert et al., 2001, 2003; Li and Wilkinson, 2001) has no need to find the optimized regularization parameter. Within the framework of standard genetic algorithm, each value in the variable range of a parameter is assigned a sequence of binary digits (or gene) 0 and 1. The length of the sequence l depends on the required precision. For instance, to minimize the object function $f(x_1, x_2)$ with constrains $1 \leq x_1 \leq 5$, $100 \leq x_2 \leq 150$, l_1 has to be set as 12 for the precision of x_1 being 0.001 and l_2 has to be set as 9 for the precision of x_2 being 0.1 ($2^{11} \leq (5-1)/0.001 \leq 2^{12}$ and $2^8 \leq (150-100)/0.1 \leq 2^9$). The chromosome is a simple connection of the two arrays of the binary codes for x_1 and x_2 , which leads to the whole length of the chromosome being $l=l_1+l_2$. With a random creation of the initial chromosome population, e.g., 50, the optimization begins and the performance of these individuals is judged by the evaluation function. Through an appropriate selection function, individuals with higher evaluation result have more chances to survive and be selected out to make crossover with each other. There are several schemes for such a selection process. As to the mutation, it is a simple flip from original “0” to “1” or inversely, “1” to “0” at a certain bit of the chromosome. With the passage of generation, GA converges to the optimum solution in the end. The convergence of GA has been proved mathematically and described as “Schema Theorem” (Michelewicz, 1996). However, GA is quite time-consuming: the requirement on high precision of results and the increase of size

intervals drastically increase the CPU time for inversion. Therefore so far it has not been widely applied in optical particle sizing.

In addition to all these algorithms, the Chahine iterative algorithm (Ferri, 1989), the successive overrelaxation Method (Hageman and Young, 1981), the hybrid regularization method (Böckmann, 2001), etc., are also developed for different optical means of particle sizing because of their special advantages and characteristics. Since they do not have excellent performance in PSD inversion in the SLEM, here they are not introduced in detail.

4.4 Organization of Part II

The second part of the present thesis is organized into 4 chapters: Chapter 5 is contributed to the general statement of SLEM, including the basic principle and the inversion algorithms. Chapter 6 is contributed to the sensibility and stability test of the SLEM system and evaluation of measurement error by standard polystyrene particle sizing. Chapter 7 is contributed to online measurement of wet steam generated by an experimental turbine in R&D EDF. Finally, Chapter 8 is contributed to the theoretical and experimental exploration of the applicability of the current system in measuring the wet steam of high concentration.

Chapter 5. Spectral Light Extinction Method

In this chapter, we introduce the principle of the spectral light extinction method (SLEM) as well as the two independent model algorithms, the Phillips-Twomey-NNLS algorithm (Twomey algorithm) and the optimized regularization technique (ORT).

5.1 Basic principle

We consider an electromagnetic plane wave of wavelength λ in the medium and incidence intensities $I_0(\lambda)$. After traversing a distance Z through the homogeneous particulate medium, the transmitted intensities $I(\lambda)$ can be calculated by the following Beer-Lambert law:

$$I(\lambda) = I_0(\lambda) \exp[-\xi(\lambda)], \quad (5-1)$$

where the optical thickness ξ can be calculated from the turbidity τ by

$$\xi = \tau Z. \quad (5-2)$$

When the particle concentration is low, the overall extinction can be considered as the superposition of the contribution by all single particles, so that for the monodisperse particles of the unique diameter D and the number concentration C_n (per unit volume), the turbidity τ is calculated by

$$\tau = C_n \frac{\pi D^2}{4} Q_{\text{ext}}(\hat{m}, D, \lambda), \quad (5-3)$$

where Q_{ext} is the extinction coefficient of a single spherical particle and \hat{m} is the relative refractive index used for extinction coefficient calculation defined by

$$\hat{m} = \hat{m}_{\text{II}} / \hat{m}_{\text{I}} = m_r + m_i i, \quad (5-4)$$

where \hat{m}_{I} and \hat{m}_{II} designate the refractive indices of the medium and the particle, respectively, and the subscripts r and i designate the real and imaginary parts, respectively.

For polydisperse particles characterized by the normalized number frequency distribution $n(D)$,

the turbidity τ is calculated by

$$\tau(\lambda) = \frac{C_n \pi}{4} \int_0^\infty Q_{\text{ext}}(\hat{m}, D, \lambda) n(D) D^2 dD. \quad (5-5)$$

Incorporating Eq.(5-5) into Eq.(5-2) and then utilizing Eq. (5-1), we obtain

$$\ln(I/I_0) = -\frac{C_n \pi}{4} Z \int_0^\infty Q_{\text{ext}}(\hat{m}, D, \lambda) n(D) D^2 dD. \quad (5-6)$$

Via the following relationship between the normalized volume frequency distribution $v(D)$ and the normalized number frequency distribution $n(D)$:

$$C_v v(D) = \frac{\pi D^3}{6} C_n n(D). \quad (5-7)$$

Eq. (5-6) is equivalent to

$$\ln(I/I_0) = -\frac{3}{2} C_v Z \int_0^\infty Q_{\text{ext}}(\hat{m}, D, \lambda) v(D) / D dD, \quad (5-8)$$

where C_v is volume concentration of the particles in the medium. Since $n(D)$ and $v(D)$ are normalized, their integral over D from zero to infinity tends to unity, namely:

$$\int_0^\infty n(D) dD = 1, \quad (5-9)$$

$$\int_0^\infty v(D) dD = 1. \quad (5-10)$$

On the basis of Eq. (5-8), for a series of wavelengths selected from the spectrum corresponding to a light source of given bandwidth, we have

$$\left\{ \begin{array}{l} \ln(I/I_0)_{\lambda_1} = -\frac{3Z}{2} \int_0^\infty V(D) Q_{\text{ext}}(\hat{m}, D, \lambda_1) / D dD \\ \ln(I/I_0)_{\lambda_2} = -\frac{3Z}{2} \int_0^\infty V(D) Q_{\text{ext}}(\hat{m}, D, \lambda_2) / D dD \\ \dots \quad \dots \quad \dots \\ \ln(I/I_0)_{\lambda_m} = -\frac{3Z}{2} \int_0^\infty V(D) Q_{\text{ext}}(\hat{m}, D, \lambda_m) / D dD \end{array} \right., \quad (5-11)$$

where the volume frequency distribution (VFD) $V(D)$ can be obtained from its normalized form

$v(D)$ and the volume concentration C_v via the following relation:

$$V(D) = C_v v(D). \quad (5-12)$$

Provide that the size range is discretized into n intervals, and we have $(n+1)$ nodes designated by $D_0, D_1, D_2, \dots, D_n$. Assuming that the volume frequency V_j to be constant in each size interval $[D_{j-1}, D_j]$, through discretization we have

$$\int_0^\infty \frac{1}{D} Q_{\text{ext}}(\lambda_i, \hat{m}, D) V(D) dD = \sum_{j=1}^n A_{i,j} V_j, \quad (5-13)$$

where each element in the coefficient matrix $A(m \times n)$ can be evaluated by

$$A_{i,j} = \int_{D_{j-1}}^{D_j} Q_{\text{ext}}(\lambda_i, \hat{m}, D) / D dD. \quad (5-14)$$

Finally, a linear equation set in matrix form can be established as follows:

$$W = E / C = AV, \quad (5-15)$$

where $C = -3Z/2$ and the extinction spectrum vector $E = [E_1, E_2, \dots, E_m]^T$, where m is the number of wavelengths and each element E_i can be calculated by

$$E_i = \ln(I / I_0)_{\lambda_i}. \quad (5-16)$$

Because of the oscillation of the $Q_{\text{ext}}-D$ curve, the Fredholm integrals of the first kind contained in Eq. (5-11) bring in a seriously ill-posed coefficient matrix A characterized by a large condition number. Various optimization methods have been developed in the past several decades. Two of them, the Twomey algorithm and the ORT, are very effective for data inversion in SLEM and will be introduced in Subsection 5.2.

When the solution vector V is known, the volume fraction of particle in each interval, ΔV_j , can be calculated by

$$\Delta V_j = V_j \Delta D_j. \quad (5-17)$$

Thereafter, the volume concentration of the particle can be obtained through the following

calculation:

$$C_v = \sum_{j=1}^n (\Delta V_j), \quad (5-18)$$

and the normalized VFD can be obtained by

$$v_j = V_j / C_v. \quad (5-19)$$

The particle number in each size interval ΔN_j can be obtained from its counterpart V_j :

$$N_j = V_j / \left[\frac{\pi}{6} \left(\frac{D_{j-1} + D_j}{2} \right)^3 \right], \quad (5-20)$$

And the number concentration C_n and the normalized number frequency n_j can be obtained, respectively, by

$$C_n = \sum_{j=1}^n \left[\Delta V_j / \left[\frac{\pi}{6} \left(\frac{D_{j-1} + D_j}{2} \right)^3 \right] \right] \quad (5-21)$$

and

$$n_j = N_j / C_n. \quad (5-22)$$

In some situations, we also need to know the Sauter mean diameter (SMD), D_{32} , which is defined by

$$D_{32} = \frac{\int_0^{\infty} D^3 N(D) dD}{\int_0^{\infty} D^3 N(D) dD}. \quad (5-23)$$

Moreover, the volume and number mean diameters, $D_{v_{50}}$ and $D_{n_{50}}$, are the two parameters defined for characterization of the mean diameter of the PSD. The volume/number portions occupied by the particles with diameters below and over $D_{v_{50}} / D_{n_{50}}$ are identical. To sufficiently characterize the PSD, more parameters $D_{v_{03}} / D_{n_{03}}$, $D_{v_{10}} / D_{n_{10}}$, and $D_{v_{97}} / D_{n_{97}}$ are also used to characterize the PSD in some cases. This means that the volume/number portions occupied by

the particles with diameters below and over D_{v_x}/D_{n_x} are $x\%$ and $(100-x)\%$, respectively.

5.2 Inversion algorithms

As discussed in Chapter 4, two types of algorithms, dependent and independent models can be distinguished to handle the inverse problem. It has been found that (Xu et al., 2004b), the drawback of the dependent model algorithm is that the particle size distribution (PSD) should be assumed to conform to a certain function shape which is generally characterized by two parameters e.g., the Rosin-Rammler (*R-R*) distribution (to be introduced in Subsection 5.4.1). Then the inversion becomes to determine their optimized values which minimize the deviation of the reconstructed extinction spectrum from the measured one, namely:

$$\begin{cases} F = \max(|W - AV|) \\ V \geq 0 \end{cases} \quad (5-24)$$

Generally, the objective function presents a multimodal distribution when measurement error exists. And for most dependent model algorithms, the optimization process which begins from a start point might be trapped into a local optimized solution. Fig. 5.1 gives a contour of the objective function F , with 2% random error added to the extinction spectrum generated from a preassumed *R-R* PSD with parameters $\bar{D}=2.0 \mu\text{m}$ and $K=4$ through direct calculation via Eq. (5-11). The aim of our algorithms is to search the minimum of F . An inappropriate start point might lead to finding of the local optimized values indicated by the text in normal font instead that of the global optimized value indicated by the text in bold font. Although presetting several start points can reduce the adventure of finding the local optimized values, it is still difficult to know the potential locations of the global optimized parameters when random measurement errors exist. In addition, the dependent model algorithm can not handle the multimodal PSD inversion, which is characterized by more parameters.

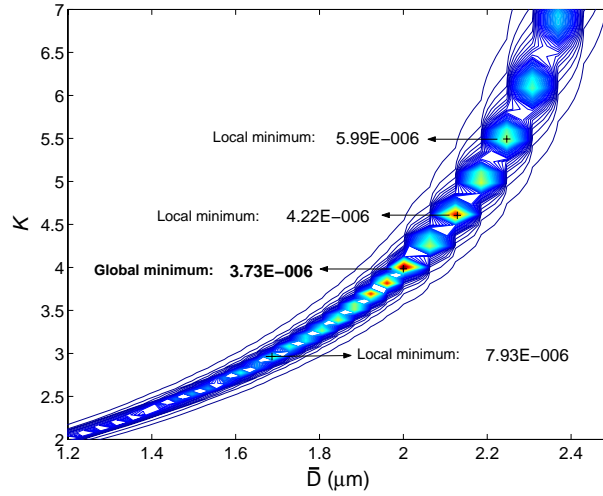


Fig. 5.1 Contour of deviation evaluation function F . The extinction spectrum generated from a given R - R PSD ($\bar{D}=2.0 \mu\text{m}$, $K=4$) of polystyrene particles dispersed in the pure water ($\hat{m}=1.590/1.333$) is used as measured data, with random error 2% added. For dependent model algorithm, the task is to find the global minimum (indicated by the text in bold font). However, an inappropriate start point might lead to the finding of local minima (indicated by the text in normal font).

To overcome the drawback of the dependent model algorithm, the independent model algorithm is used to directly inverse the PSD from the measured data of extinction spectrum. Both Twomey algorithm and ORT are employed because of their excellent performance in handling the data measured by SLEM.

5.2.1 Phillips-Twomey-NNLS algorithm

Due to the extremely large condition number of coefficient matrix A , Eq. (5-15) can not be straightforward solved via the mathematical operation $V=A^{-1}W$. To reduce the condition number of the matrix, Twomey introduces a smoothing matrix H multiplied by a Lagrange factor γ so that following equation is brought in (Twomey, 1979; Markowski, 1987):

$$(A^T A + \gamma H)V = A^T W, \quad (5-25)$$

where

$$H = \begin{bmatrix} 1 & -2 & 1 & 0 & 0 & \dots & 0 \\ -2 & 5 & -4 & 1 & 0 & 0 & \dots \\ 1 & -4 & 6 & -4 & 1 & 0 & \dots \\ \dots & \dots & \dots & \dots & \dots & \dots & \dots \\ 0 & \dots & 1 & -4 & 6 & -4 & 1 \end{bmatrix}. \quad (5-26)$$

Thus the inversion becomes the minimization of Eq. (5-25), namely,

$$\min \left[\left\| (A^T A + \gamma H)V - A^T W \right\| \right], \quad (5-27)$$

To ensure the positive solution of V ($V \geq 0$), the non-negative least square (NNLS) algorithm is used to solve Eq. (5-25) (Lawson and Hanson, 1974).

It is noteworthy that an appropriate choice of the Lagrange factor γ is significant for ensuring the quality of inversion, since a too small γ leads to the oscillation of PSD while a too large one makes an obvious disagreement of the measured spectrum and the reconstructed one from the inversed concentration and PSD. To find a balance between the two extreme situations, the ‘‘Generalized Cross-Validation (GCV) method’’ is proposed (Golub et al., 1979). According to the GCV method, the balance point can be found through minimizing the following function U with respect to γ :

$$U(\gamma) = k \frac{\left\| \left[I - A(AA^T + \gamma H)^{-1} A^T \right] W \right\|^2}{Tr \left\{ \left[I - A(AA^T + \gamma H)^{-1} A^T \right] \right\}}, \quad (5-28)$$

where k is the order of the matrix and I is the identity matrix. ‘‘ $\|\dots\|$ ’’ represents the norm of a matrix and ‘‘ Tr ’’ represents the trace of the matrix.

However, as discussed in Chapter 4, the drawback of GCV is that the objective function $U(\gamma)$ might have a flat minimum so that it is difficult for us to find the best solution. Moreover, GCV cannot be applied in the occasions when correlated measurement errors exist. Therefore in our inversion process, the optimized Lagrange factor γ is empirically determined.

5.2.2 Optimized regularization technique

The optimized regularization technique (ORT) is first introduced by Schnablegger and Glatter

(1995). Its basic idea is the assumption of PSD to be the superposition of a series of B -splines. Each spline has its own size window $[D_j, D_{j,j+k}]$ for j th spline (k is the order of the spline). Then the inversion becomes to determine the weight coefficients multiplied with these splines.

5.2.2.1 B -splines

A well-conditioned basis of the B -splines $B=\{ N_{0,k}, N_{1,k}, N_{2,k}, \dots, N_{n,k} \}$ can be obtained by the recursion formulas as follows:

$$N_{j,1}(D) = \begin{cases} 1 & D_j \leq D \leq D_{j+1} \\ 0 & \text{otherwise} \end{cases}, \quad (5-29)$$

$$N_{j,k}(D) = \frac{D - D_j}{D_{j+k-1} - D_j} N_{j,k-1}(D) + \frac{D_{j+k} - D}{D_{j+k} - D_{j+1}} N_{j+1,k-1}(D), \quad (5-30)$$

where D_j are the knots, with $j=0, 1, 2, \dots, n+k$ as well as $D_0 \leq D_1 \leq D_2 \leq \dots \leq D_{n+k}$. $N_{j,k}(D)$ are the B -spline of order k with bearing interval $[D_j, D_{j+k}]$. Fig. 5.2 gives an example of the B -splines of $k=4$ and $n=6$.

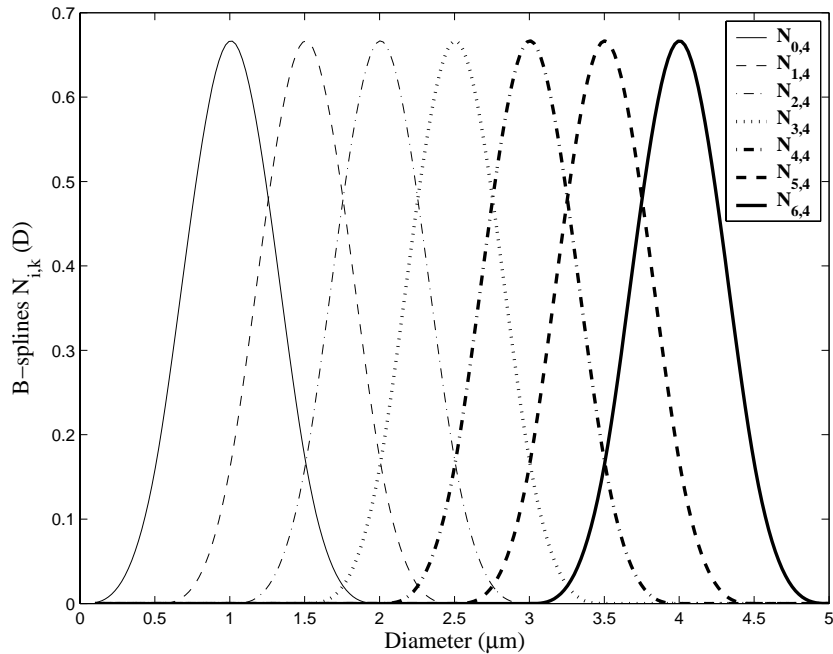


Fig. 5.2 B -splines used for PSD construction, in the figure are plotted seven B -splines of order 4 ($k=4$).

5.2.2.2 Matrix construction

The particle size distribution can then be expressed in terms of B -splines multiplied by a set of weight coefficients c_j :

$$V(D) = \sum_{j=0}^n c_j N_{j,k}(D). \quad (5-31)$$

Thus, Eq. (5-8) can be written into the following form:

$$\ln(I/I_0) = -\frac{3Z}{2} \sum_{j=0}^n c_j \int_{D_j}^{D_{j+k}} Q_{\text{ext}}(\hat{m}, D, \lambda) N_{j,k}(D) / D dD, \quad (5-32)$$

Then the matrix form of the equation set can be written as

$$W = Ac, \quad (5-33)$$

where

$$A_{i,j} = \int_{D_j}^{D_{j+k}} Q_{\text{ext}}(\lambda_i, \hat{m}, D) N_{j,k}(D) / D dD. \quad (5-34)$$

Through solving Eq. (5-33) by Twomey algorithm introduced in Subsection 5.2.1, the weight coefficients c_j are obtained. Then the VFD and the volume concentration can be obtained by Eq. (5-31) and Eq. (5-18), respectively. The NFD and the number concentration can be obtained accordingly from Eq. (5-20) and Eq. (5-21), respectively.

5.3 Presentation of the software TURACE 5.0

To meet the requirement of current studies, the software TURACE has been designed and developed by the author from the version 1.0 to version 5.0 in the past three years. At present it has following functions:

A. Direct calculation of the extinction spectrum from a given droplet distribution and the corresponding inversion with/without random error, which permits us to evaluate the sensibility of the algorithms to the random errors generated in practical measurements;

- B. Online particle size and concentration analysis;
- C. Demonstration of the extinction coefficient curve for a given refractive index of the particle;
- D. Continuous acquisition of spectra from single or dual channels with regulable time interval;
- E. Online statistical analysis of the instabilities of the intensity spectrum as well as extinction spectrum;
- F. Post processing of the saved spectra, e.g., calculation of the standard deviation of extinction spectra, and statistical analysis of the measured results to obtain the mean SMD, volume and number concentration of the particle system.

Function A is used in the current chapter. Function B is used in Chapter 7 for online wet steam measurement. Functions D-F are used in Chapter 6 for sensibility and stability test of the SLEM system. A brief presentation of the software can be found in Appendix F.

5.4 Numerical investigation of inversion algorithms

In this section we test the resistance of the inversion algorithm to the random measurement error by numerical simulation. The process can be briefly introduced as follows: first, a particle system with given PSD and concentration is assumed so that a series of extinction spectrum is generated by direct calculation indicated by Eq. (5-11). Next, the random error is added to the spectrum and such a spectrum is used as the “measured” data for inversion. Finally, the inversion results of PSD and concentration are compared to the given ones to evaluate the performance of the inversion algorithms.

5.4.1 Rosin-Rammler distribution

We use the *R-R* distribution to construct the unimodal, bimodal and multimodal PSD. The volume accumulation function of a unimodal *R-R* distribution can be described by

$$V_a(D) = C_v \left\{ 1 - \exp \left[- \left(D / \bar{D} \right)^K \right] \right\}, \quad (5-35)$$

where C_v is the volume concentration of the particles, \bar{D} is the characteristic diameter

corresponding to the maximum value of volume frequency distribution to be indicated by Eq. (5-36), and K is the distribution factor. For a given unimodal distribution, the smaller K is, the wider the PSD becomes. Via differential processing of Eq. (5-35), the volume frequency distribution function can be yielded as follows:

$$V(D) = \frac{dV_a}{dD} = C_v \left\{ K / \bar{D} (D / \bar{D})^{K-1} \exp \left[- (D / \bar{D})^K \right] \right\}. \quad (5-36)$$

On the basis of the unimodal R - R distribution, we have the following expression for the volume accumulation function of N -modal PSD:

$$V_a(D) = \sum_{i=1}^N C_{v,i} \left\{ 1 - \exp \left[- (D / \bar{D}_i)^{K_i} \right] \right\}. \quad (5-37)$$

When $N=1$, the unimodal PSD is recovered. When $N=2$, the bimodal PSD is recovered. $C_{v,i}$ is the volume concentration of the particle population i . Then the total volume concentration is

$$C_v = \lim_{D \rightarrow \infty} V(D) = \sum_{i=1}^N C_{v,i}. \quad (5-38)$$

And the normalized VFD is

$$v(D) = dV(D) / dD = \sum_{i=1}^N (C_{v,i} / C_v) (K_i / \bar{D}_i) (D / \bar{D}_i)^{K_i-1} \exp \left[- (D / \bar{D}_i)^{K_i} \right]. \quad (5-39)$$

The corresponding NFD is

$$n(D) = \frac{dN(D)}{dD} = 6 / \pi D^3 \sum_{i=1}^N (C_{v,i} / C_v) (K_i / \bar{D}_i) (D / \bar{D}_i)^{K_i-1} \exp \left[- (D / \bar{D}_i)^{K_i} \right]. \quad (5-40)$$

5.4.2 Inversion without measurement errors

5.4.2.1 Inversion of unimodal particle size distribution

First, a unimodal R - R PSD of the spherical water droplets ($\hat{m}=1.333$) with a given set of distribution parameters is used for generating the basic extinction spectrum, which is then used for inversion. The particle diameter range $[0.01, 5.00] \mu\text{m}$ is discretized into 101 intervals. The extinction spectrum is calculated for 100 equidistant points within the visible wavelength range

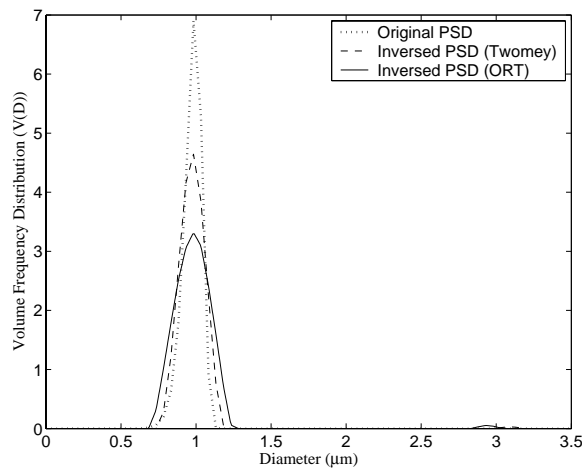
[0.40, 0.95] μm . The parameters used for numerical calculations are listed in Table 5.1. The inversed results of the SMDs D_{32} and volume concentrations C_v , as well as their deviations from the pre-assumed values are listed in 0. The original and inversed PSDs are presented in Fig. 5.3a (for PSD1) and Fig. 5.4a (for PSD2). Comparison of the original and reconstructed spectra can be found in Fig. 5.3b (for PSD1) and Fig. 5.4b (for PSD2). For both PSD1 and PSD2, the agreement between the initial and reconstructed spectra is found satisfactory. And for both narrow (PSD1) and wide (PSD2) size distributions the absolute errors with both SMDs and volume concentrations are weak (less than $\sim 1.0\%$ for D_{32} and 0.6% for C_v).

Table 5.1 Parameters used for simulation of unimodal PSD inversion

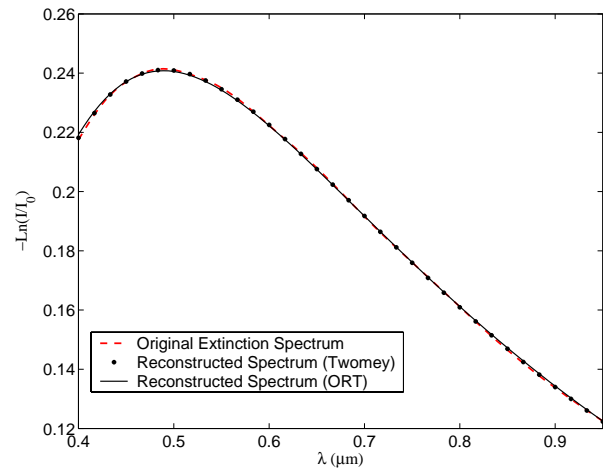
PSD	PSD1	PSD2	Parameters for inversion	
C_v	1×10^{-6}		Wavelength range	[0.40-0.95] μm (100 equidistant points)
(\bar{D}, K)	$\bar{D}=1.0 \mu\text{m},$ $K=20$	$\bar{D}=1.0 \mu\text{m},$ $K=4$	$[D_{\min}, D_{\max}]$	[0.01-5.0] μm (100 intervals)
D_{32}	0.969 μm	0.816 μm	Lagrange Multiplier	Twomey: $\gamma=0.01$
				ORT: $\gamma=0.05$ ($n=98$)

Table 5.2 Comparison of the given and inversed SMDs and volume concentrations

		PSD1	PSD2
D_{32} given (μm)		0.969	0.816
D_{32} inversed (μm)	Twomey	0.970	0.815
	ORT	0.967	0.824
Error of D_{32} (%)	Twomey	+0.050	-0.128
	ORT	-0.277	+1.014
C_v given ($E-6$)		1.000	1.000
C_v inversed ($E-6$)	Twomey	1.006	0.998
	ORT	1.015	1.076
Error of C_v (%)	Twomey	+0.577	-0.225
	ORT	+0.154	-0.108



(a)



(b)

Fig. 5.3 Inversed results for unimodal distribution PSD1. (a): Original and inversed PSDs; (b): Original and reconstructed extinction spectra.

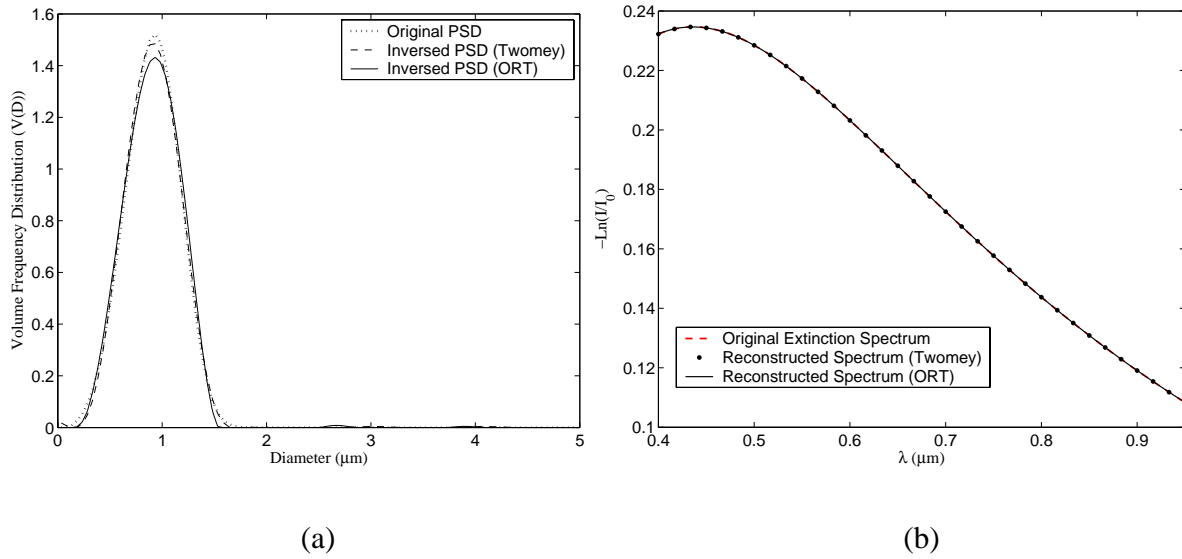


Fig. 5.4 Inversed results for unimodal distribution PSD2. (a): Original and inversed PSDs; (b): Original and reconstructed extinction spectra.

5.4.2.2 Inversion of bimodal particle size distribution

In the same way, the bimodal distribution is assumed to generate the basic extinction spectrum for inversion. The bimodal droplet system is composed of two subunimodal PSDs of equal volume quotients and with distribution parameters (\bar{D}, K) being $(1.0 \mu\text{m}, 4.0)$ and $(2.5 \mu\text{m}, 8.0)$, respectively. The inversion parameters are set same as those for unimodal PSD (see Table 5.1). Comparison of the given and inversed PSD and spectra is illustrated in Fig. 5.5, indicating that both algorithms can retrieve the two main peaks existing with the pre-assumed PSD, though a redundant peak appears at the vicinity of $D=3.7 \mu\text{m}$. The inversed SMDs D_{32} and volume concentrations C_v are listed in Table 5.3, from which we can find that for both algorithms the deviations of the inversed SMDs D_{32} from the given value are less than $\sim 5.0\%$ and the deviations of the inversed volume concentrations C_v from the given value are less than $\sim 10.0\%$. These deviations are more obvious than their counterparts for unimodal distribution, which means that the accuracies reduce when we measure the bimodal PSD.

Table 5.3 Comparison of the given and inversed SMDs and volume concentrations

		PSD2+PSD3
(\bar{D}, K)		PSD2: (1.0 μm , 4.0)+PSD3: (2.5 μm , 8.0)
Volume Percentage		50%, 50%
D_{32} given (μm)		1.203
D_{32} inversed (μm)	Twomey	1.165
	ORT	1.142
Error of D_{32} (%)	Twomey	-3.226
	ORT	-5.079
C_v given (E-6)		1.000
C_v inversed (E-6)	Twomey	1.053
	ORT	1.101
Error of C_v (%)	Twomey	5.255
	ORT	10.080

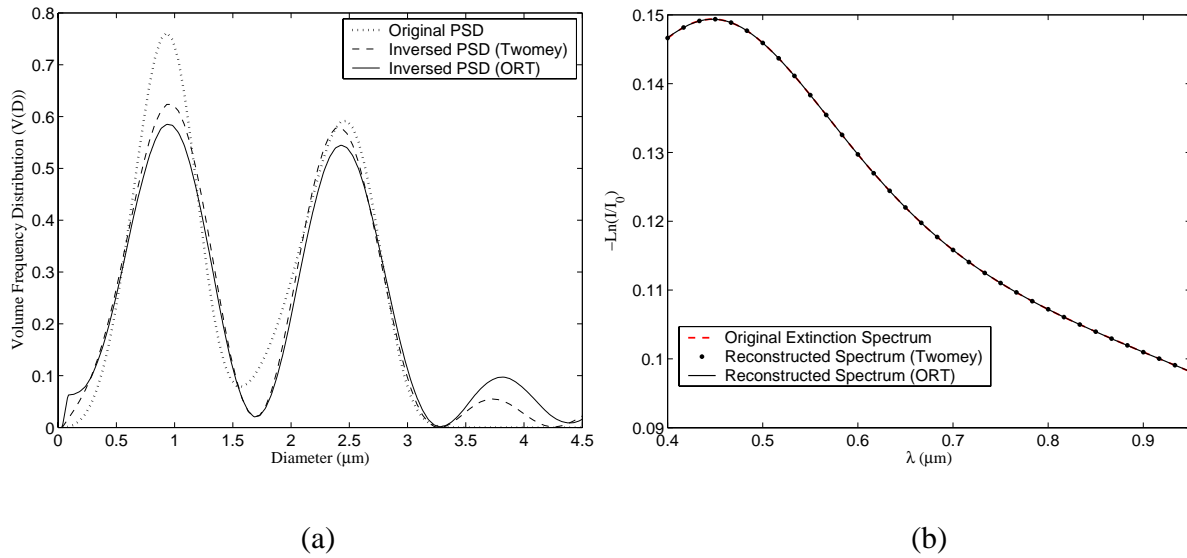


Fig. 5.5 Inversed results for bimodal particle size distribution. The droplet size distribution is composed of two subunimodal PSDs of equal volume quotients and with distribution parameters (\bar{D}, K) being $(1.0 \mu\text{m}, 4.0)$ and $(2.5 \mu\text{m}, 8.0)$, respectively. (a): Original and inversed PSDs; (b): Original and reconstructed extinction spectra.

5.4.3 Inversion with measurement errors

In the preceding subsection, inversions are made for the ideal situation when no measurement errors exist. However, in realistic situation, measurement errors are unavoidable. Therefore in this subsection, we evaluate the resistance of the two inversion algorithms to these errors.

5.4.3.1 Inversion of unimodal particle size distribution

The parameters for the two inversion algorithms are the same as those used for unimodal PSD inversion (see Table 5.1), but random errors of level 0.1% and 1.0% are added to the basic extinction spectrum generated from PSD2 with distribution parameters (\bar{D}, K) set as $(1.0 \mu\text{m}, 8.0)$. One hundred simulated extinction spectra are used to obtain the mean inversed SMD \bar{D}_{32} and volume concentration \bar{C}_v , which are listed in Table 5.4. It is indicated that when the measurement error level increases from 0.1% to 1.0%, the absolute error of the mean inversed SMD \bar{D}_{32} increases from $\sim 0.3\%$ to $\sim 5.7\%$ for Twomey algorithm and from $\sim 1.2\%$ to $\sim 7.6\%$ for ORT, and the absolute error of the mean inversed volume concentration \bar{C}_v increases from $\sim 0.8\%$ to $\sim 8.8\%$ for Twomey algorithm and from $\sim 0.3\%$ to $\sim 5.2\%$ for ORT.

Table 5.4 Comparison of the given and the averaged results of the inversed SMDs D_{32} and volume concentrations C_v (100 spectrum samples used)

		PSD2 (0.1% error)	PSD2 (1.0% error)
D_{32} given (μm)		0.816	
\bar{D}_{32} inversed (μm)	Twomey	0.818	0.769
	ORT	0.826	0.878
Error of \bar{D}_{32} (%)	Twomey	0.321	-5.746
	ORT	1.220	7.646
C_v given (E-6)		1.000	
\bar{C}_v inversed (E-6)	Twomey	1.008	1.088
	ORT	1.003	1.052
Error of \bar{C}_v (%)	Twomey	0.817	8.828
	ORT	0.257	5.156

In Fig. 5.6a-Fig. 5.7a are listed the inversed results of PSD from one of the 100 extinction spectra. It is found from the inversed PSD that the main peak existing with the original PSD can be retrieved by both algorithms. For the same particle size distribution (PSD2), comparison of Fig. 5.4a with Fig. 5.6a indicates that the error level of 0.1% has little influence on the measurement results. However, for the error level of 1.0%, a redundant peak appears at the vicinity of $D=3.5 \mu\text{m}$, as can be found in Fig. 5.7a. The appearance of the redundant peak indicates that the inverse results become more inaccurate with the increase of measurement errors, though the agreements between the reconstructed spectra and the given ones are still found excellent for all these error levels, as indicated by Fig. 5.6b-Fig. 5.7b.

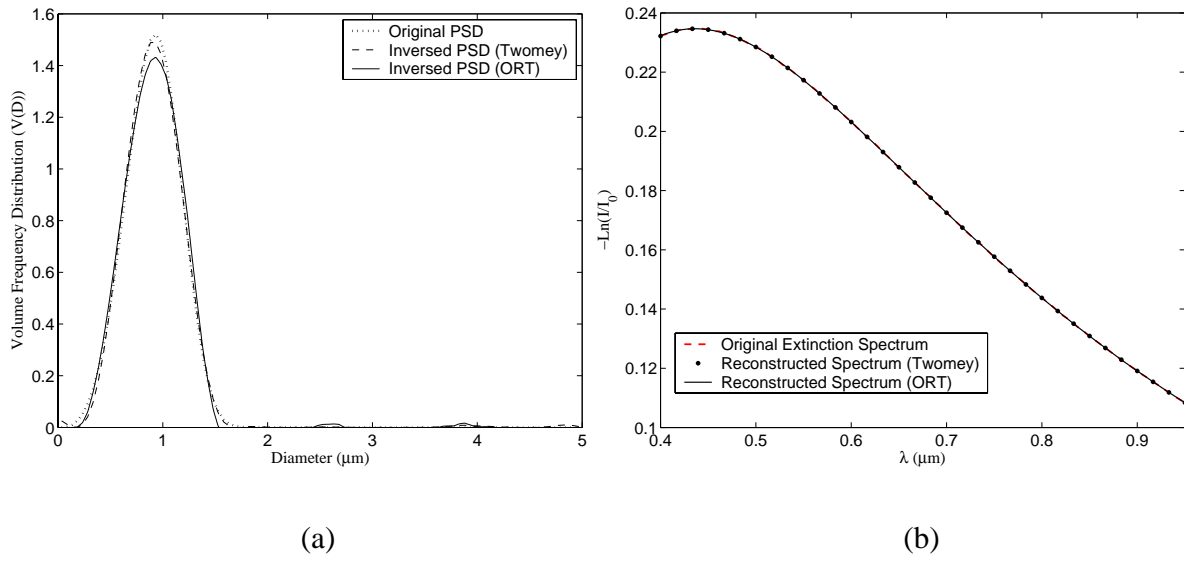


Fig. 5.6 Comparisons of the inversed results and the given ones (0.1% random error added). (a) Given and inversed PSDs; (b) Given and reconstructed spectra.

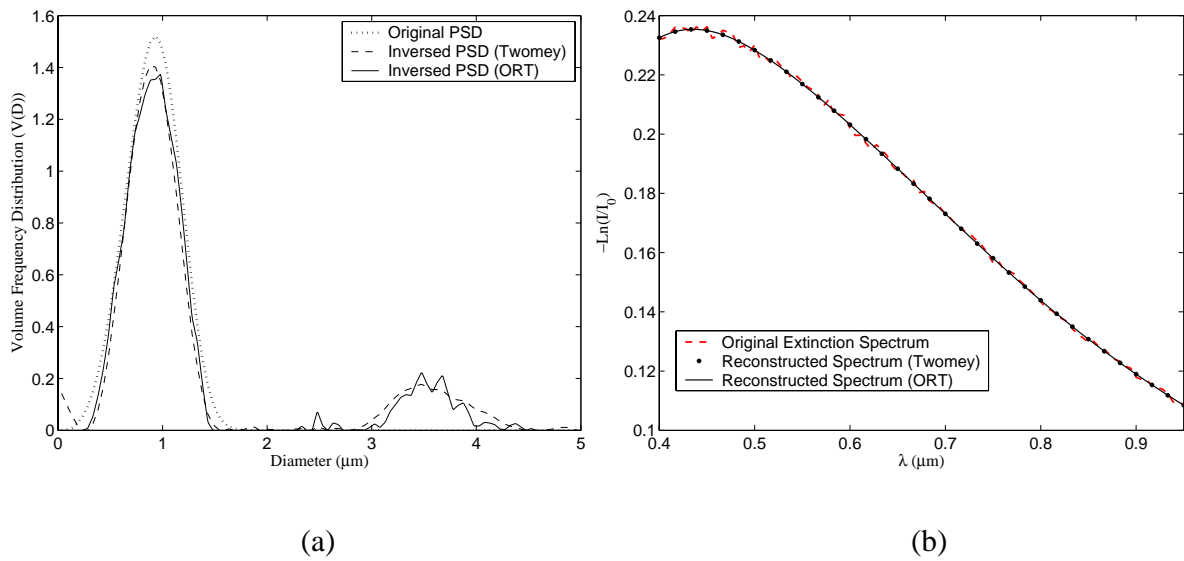


Fig. 5.7 Comparisons of the inversed results and the given ones (1.0% random error added). (a) Given and inversed PSDs; (b) Given and reconstructed spectra.

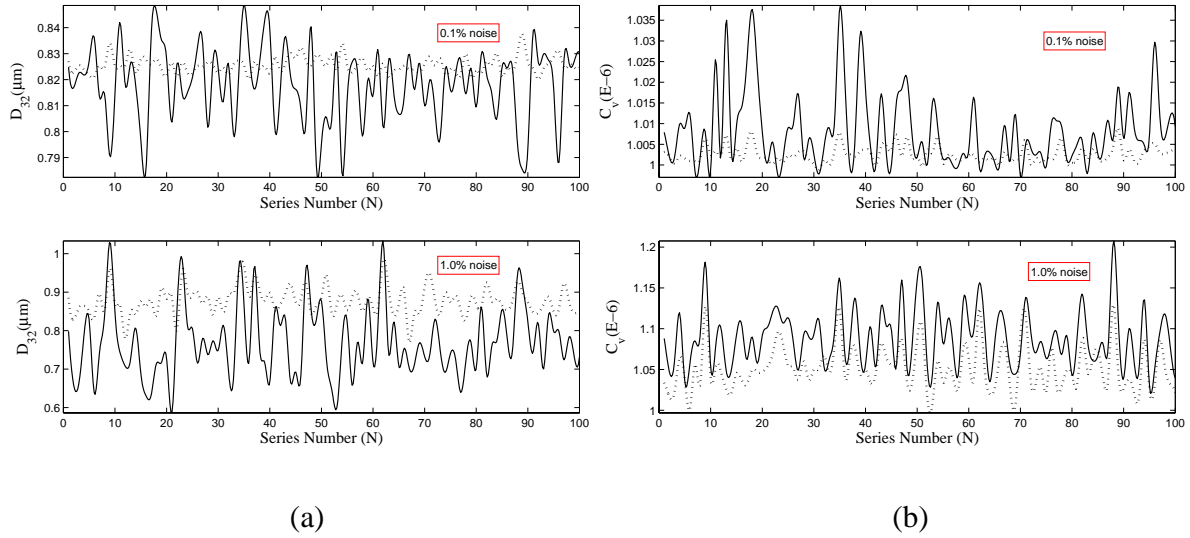


Fig. 5.8 The SMDs D_{32} and volume concentrations C_v for 100 samples of extinction spectra with error levels 0.1% and 1.0%. The solid curve represents the results calculated by the Twomey algorithm and the dotted curve represents the results calculated by the ORT. (a): SMDs D_{32} ; (b) Volume concentrations C_v .

In Fig. 5.8 is plotted the SMDs D_{32} and the volume concentrations C_v for all the 100 simulated extinction spectra, from which average result of D_{32} and C_v are calculated and listed in Table 5.4. Fluctuations of the D_{32} and C_v curves corresponding to the Twomey algorithm are found more drastic than those corresponding to the ORT, which indicates that the ORT is a more stable algorithm in data inversion. But for both algorithms, these fluctuations become more obvious with the increase of error level.

5.4.3.2 Inversion of bimodal particle size distribution

The basic extinction spectrum is calculated from an assumed PSD composed of two R - R subunimodal distributions of equal volume quotients and with parameters (\bar{D}, K) being $(1.0 \mu\text{m}, 4.0)$ and $(2.5 \mu\text{m}, 8.0)$, respectively. The errors of levels 0.1% and 1.0% are added to the basic extinction spectrum, respectively. The parameters for the two inversion algorithms are set same as those for unimodal PSD inversion (see Table 5.1). Also, one hundred spectra are generated for a given error level. Then the mean inversed SMDs \bar{D}_{32} and mean volume concentrations \bar{C}_v are calculated and listed in Table 5.5. It is indicated that when the measurement error level increases from 0.1% to 1.0%, the absolute error of the mean inversed SMD \bar{D}_{32} increases from $\sim 2.4\%$ to $\sim 20.1\%$ for Twomey algorithm and from $\sim 4.0\%$ to $\sim 14.5\%$ for ORT, and the absolute

error of the mean inversed volume concentration \bar{C}_v increases from ~6.2% to ~18.4% for Twomey algorithm and from ~11.3% to ~20.3% for ORT.

Table 5.5 Comparison of the given and the averaged results of the inversed SMDs D_{32} and volume concentrations C_v (100 spectrum samples used)

		PSD2+PSD3 (0.1% error)	PSD2+PSD3 (1.0% error)
(\bar{D}, K)		PSD2: (1.0 μm , 4.0) + PSD3: (2.5 μm , 8.0)	
Volume Percentage		50%, 50%	
D_{32} given (μm)		1.203	
\bar{D}_{32} inversed (μm)	Twomey	1.174	0.961
	ORT	1.155	1.029
Error of \bar{D}_{32} (%)	Twomey	-2.410	-20.116
	ORT	-3.990	-14.464
C_v given (E-6)		1.000	
\bar{C}_v inversed (E-6)	Twomey	1.062	1.184
	ORT	1.113	1.203
Error of \bar{C}_v (%)	Twomey	6.211	18.427
	ORT	11.340	20.315

The inversed PSDs as well as the comparisons of the given spectra with the reconstructed ones are illustrated in Fig. 5.9-Fig. 5.10. As can be found in Fig. 5.9a, when 0.1% error is added, the two main peaks of the inversed PSDs are essentially same as the those existing with the given PSD, though a redundant peak appears at the vicinity of $D=3.7 \mu\text{m}$. Such a result is nearly same as that inversed in the situation of no measurement error existing (see Fig. 5.5a). When the error level increases to 1.0%, the two peaks can still be recognized (see Fig. 5.10a), but the redundant distribution also becomes more obvious. We can not affirm that the appearance of the redundant

peaks is due to the drawback of algorithm, since the PSDs with spoiled peaks also lead to a satisfactory agreement of the reconstructed and given spectra, as indicated by Fig. 5.10b-Fig. 5.11b. When we compare the reconstructed spectra associated with the random errors of all the levels in a same figure, very little difference among them can be distinguished (see Fig. 5.11). Numerical simulations show that for a further larger error level (e.g., $\geq 2.0\%$), several essentially different PSDs might correspond to a nearly same extinction spectrum. Such a phenomenon is found more obvious when multimodal PSD is concerned. It is mainly caused by the oscillation nature of $Q_{\text{ext}}-D$ curve and the multiple value relation between Q_{ext} and D . In this case, PSD inversion becomes more difficult or even impossible.

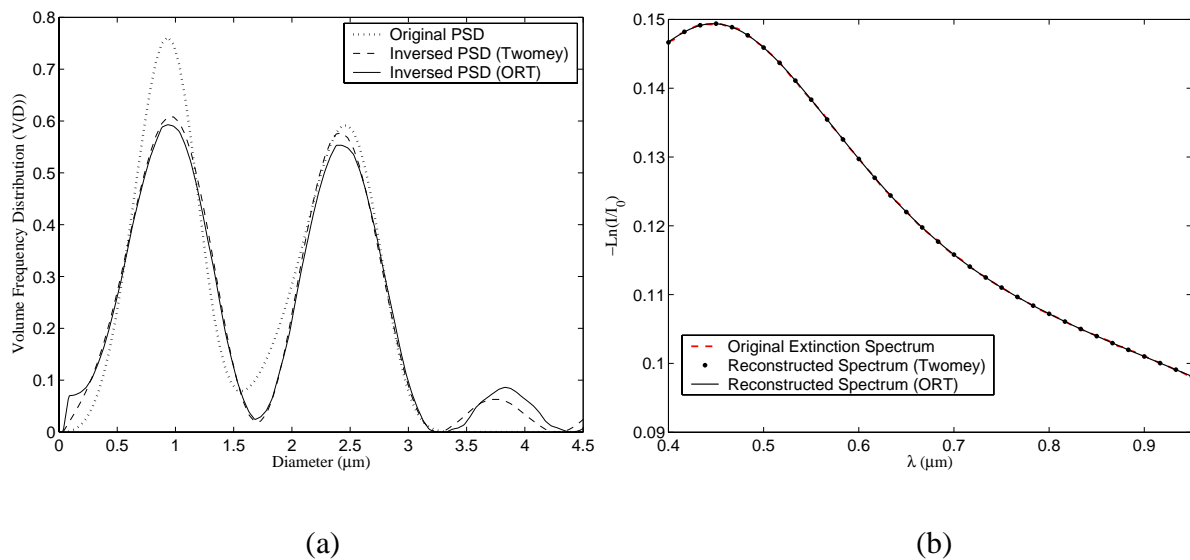


Fig. 5.9 Comparison of the inverted results and the given ones (0.1% random error added). (a) Given and inverted PSDs; (b) Given and reconstructed spectra.

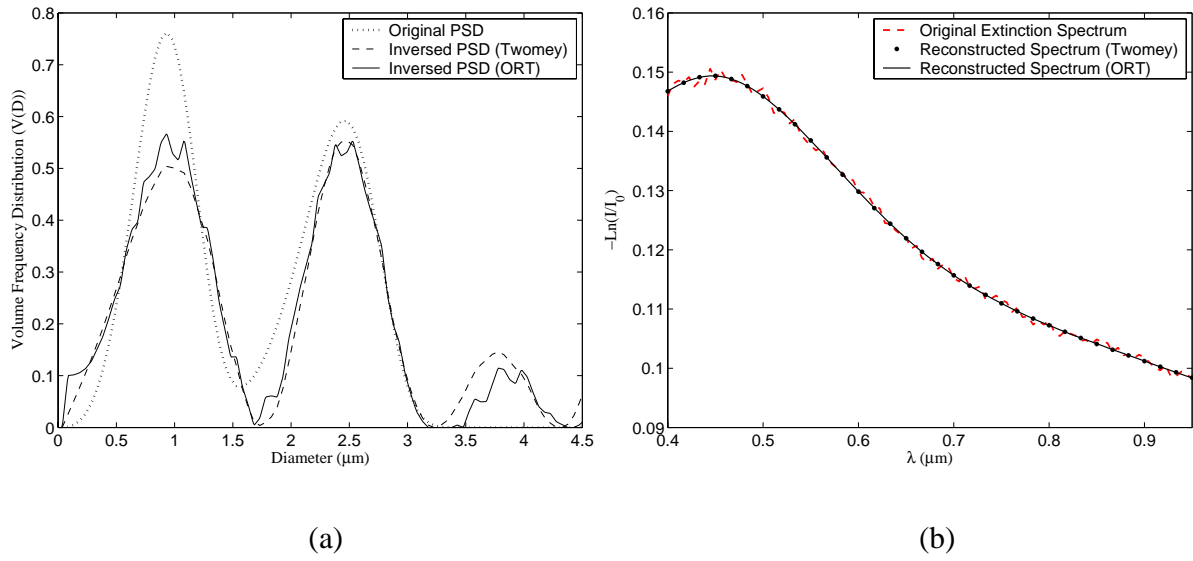


Fig. 5.10 Comparison of the inverted results and the given ones (1.0% random error added). (a) Given and inverted PSDs; (b) Given and reconstructed spectra.

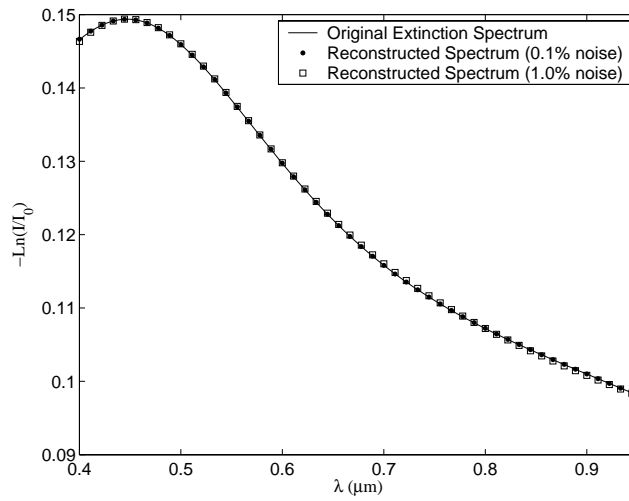


Fig. 5.11 Comparison of the reconstructed spectra corresponding to the error levels 0.1% and 1.0%.

In Fig. 5.12 are plotted the SMDs D_{32} and volume concentrations C_v for 100 spectrum samples, from which their average values are obtained and listed in Table 5.5. For the same error level, the fluctuations of both the SMDs D_{32} and the volume concentrations C_v inverted by the Twomey algorithm and the ORT are found to be nearly on the same level.

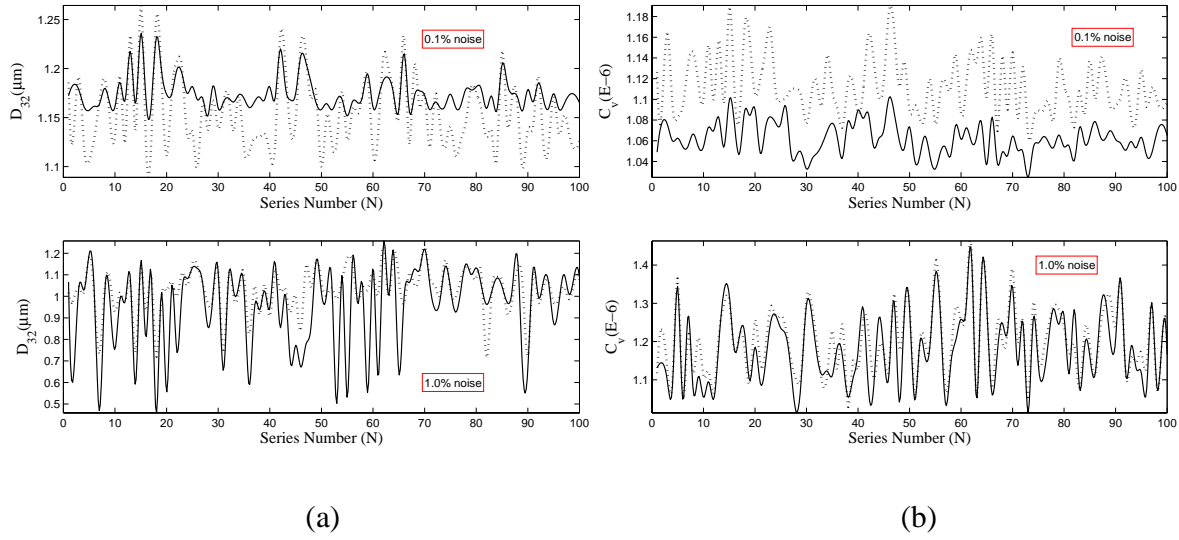


Fig. 5.12 The SMDs D_{32} and volume concentrations C_v for 100 samples of extinction spectra with error levels 0.1% and 1.0%. The solid curve represents the results calculated by the Twomey algorithm and the dotted curve represents the results calculated by the ORT. (a): SMDs D_{32} ; (b) Volume concentrations C_v .

5.5 Conclusion

The principle of SLEM is introduced in this chapter. By numerical simulation, performance of the Twomey algorithm and the ORT is investigated. We found both algorithms are capable of handling unimodal and bimodal PSD inversion. Numerical simulation indicates that the ORT is more stable than the Twomey algorithm in the existence of measurement error. The deviations of the inversed SMDs and volume concentrations from the given ones become more obvious with the increase of error level. For unimodal PSD inversion by ORT, for example, when the error level increases from 0.1% to 1.0%, the absolute error of the inversed SMD \bar{D}_{32} increases from $\sim 1.2\%$ to $\sim 7.6\%$, and the absolute error of the inversed volume concentration \bar{C}_v increases from $\sim 0.3\%$ to $\sim 5.2\%$. For bimodal PSD inversion, the resistance of both algorithms to the random error is reduced. To improve the precision of the measurement results, the measurement should be as exact as possible and the monodispersity of the particle system should be as high as possible.

Chapter 6. Sensibility and Stability of Measurement System

In this chapter, we carry out the experimental studies of the stability and sensibility of the measurement system, which might cause error to the measurement results of particle size and concentration. The test is mainly for the light source and the spectrometer. On such a basis, the sensibility of the SLEM system to the slight variation of the particle concentration is explored. Finally, we apply the spectral light extinction method in experimental standard polystyrene particle sizing to explore the applicability of the developed optical system.

6.1 Stability of the light source

This study includes obtaining the spectra emitted by a halogen lamp and a deuterium + halogen lamp (DH 2000) to analyze the level of spectral fluctuation in time domain. The typical usable wavelength range of a halogen lamp (HL 2000) is 0.35-1.00 μm . And the usable wavelength range of the DH 2000 is 0.23-1.10 μm . The main characteristics of these light sources provided by the manufacturer can be found in the Appendix G. The light sources are illustrated in Fig. 6.1.

Two types of spectrometers are prepared for the measurements, SD 2000 (Ocean Optics), with two channels, maximum acquisition frequency of 200 Hz, and detectable wavelength range [0.35-1.1] μm , and HR 2000+ (Ocean Optics), with one channel, maximum acquisition frequency of 1000 Hz, and the detectable wavelength range is 0.20-1.1 μm . Both of them are based on the CCD of 2048 pixels, corresponding to 2048 wavelength. The two spectrometers are illustrated in Fig. 6.2. More detail on the characteristics of the spectrometers given by the manufacturer can be found in Appendix H. The advantages of these spectrometers include

1. Simultaneous acquisition of signals of all wavelengths;
2. Easy operation;
3. Acquisition subroutine incorporable into the data processing software with a friendly interface to users.

Since the temperature change or mechanical vibration might cause wavelength shift to the

spectrometer, the spectral lamps, Hg and Cd lamps (see Fig. 6.1) with given spectral lines of emission are used for wavelength calibration.

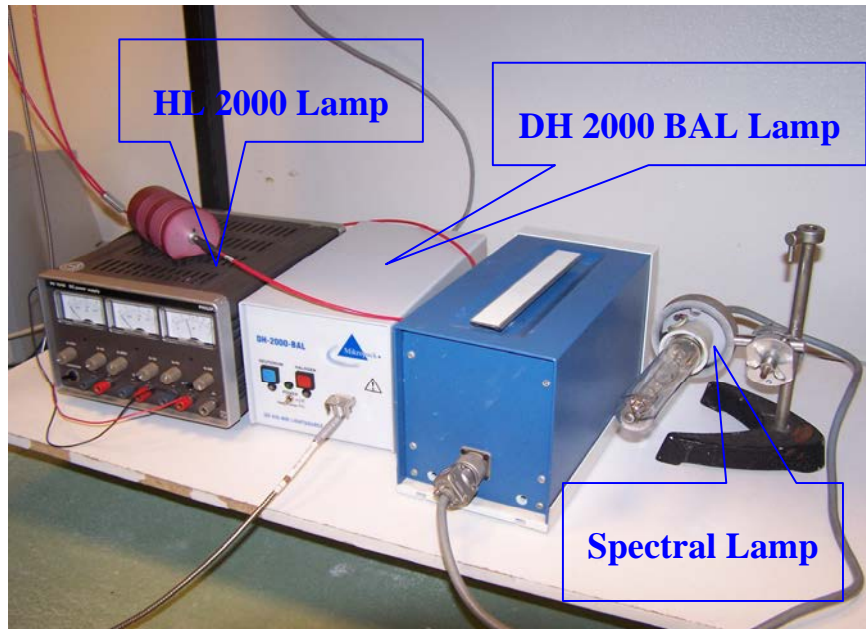


Fig. 6.1 Light sources used in the experiments.



Fig. 6.2 Spectrometer SD 2000 and HR 2000+ used in SLEM system.

The stability of the light source depends on the following several factors:

1. The stability of the electric current;
2. The fluctuation of the temperature;
3. The mechanical stability of the experimental setup.

Before carrying out the experimental studies on fluctuation studies, we discuss the calibration of the SLEM system and the two statistical parameters for characterizing the standard deviation of the intensity.

6.1.1 Calibration of the system

The detection and elimination of the white noise is a necessary step before practical measurement. It is done in the following way: we turn off the light source and save a series of noise spectra acquired by the two channels. Then two averaged noise spectra, corresponding to the two channels of the spectrometer, are calculated and recorded. They will be subtracted from the later measured intensity spectra automatically. Fig. 6.3 gives a plot of two typical white noise spectra detected by the two channels in a dark room.

When SD 2000 is used for online particle sizing, the intensity measured by its channel Master $I_{0,ori}(\lambda)$ and that measured by channel Slave, $I_0(\lambda)$ must be calibrated before the entering of the particles. This is because the sensibility of the two detectors in these channels is different and the optical paths from the light source to them are not identical. The calibration, i.e. determination of the intensity ratio coefficients $C_0(\lambda)=I_0(\lambda)/I_{0,ori}(\lambda)$ for all the wavelengths detected by the two channels is necessary before carrying out particle sizing. Once $C_0(\lambda)$ is obtained, I_0 can be obtained by $I_0(\lambda)=C_0(\lambda)I_{0,ori}(\lambda)$ during the measurement process. Fig. 6.4 gives a typical plot of intensity ratio coefficients versus wavelength. It shows clearly that the “sensibility” of the two channels varies much with the wavelength. After the calibration the spectra acquired from the two channels when no absorbing medium exists are nearly identical, as indicated by Fig. 6.5. In the existence of the particles or other absorbing media, the intensities of transmitted light $I(\lambda)$ which are smaller than the incidence intensities $I_0(\lambda)$ and detected by the channel Slave are measured so that the transmittance ratios $T(\lambda)$ and the extinction ratio $E(\lambda)$ can be obtained.

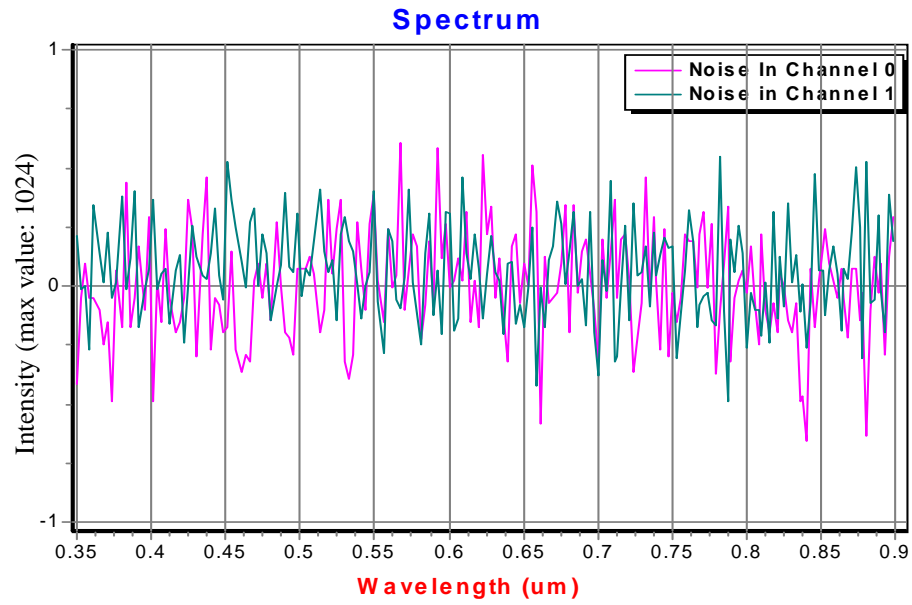


Fig. 6.3 White noise.

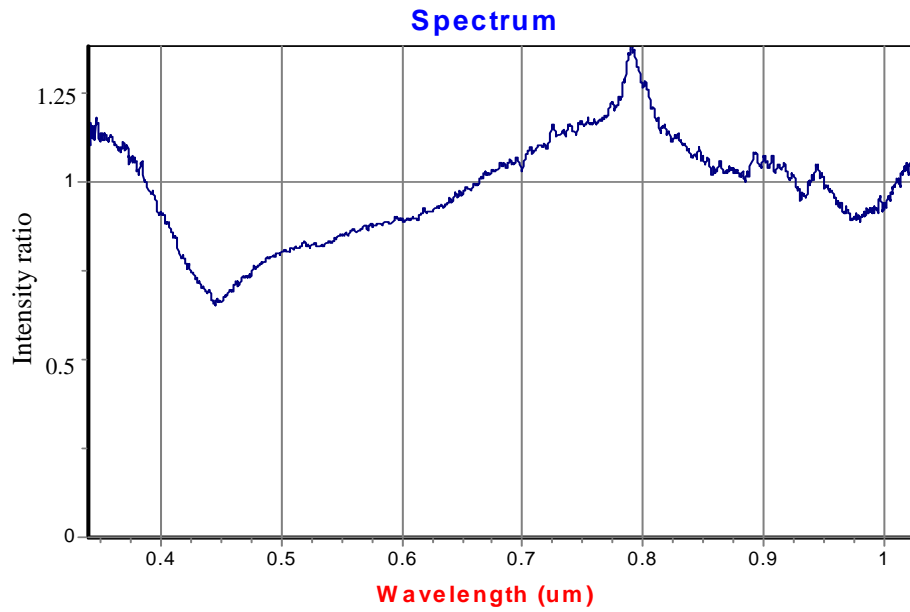


Fig. 6.4 Intensity ratio coefficients $C_0(\lambda)$.

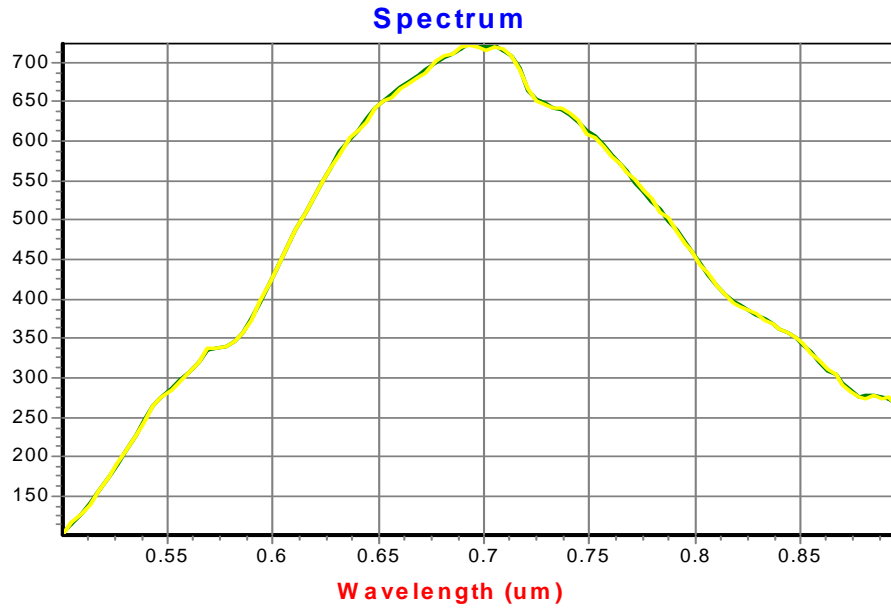


Fig. 6.5 Spectra acquired from the two channels after intensity calibration and noise elimination.

6.1.2 Mean standard deviation of intensity

The fluctuations of the light source are characterized by two types of statistical parameters: the mean standard deviation of the average intensity, σ , and the mean standard deviation of intensity with respect to the wavelength, σ_λ , which is to be discussed in the following subsections.

a) Mean standard deviation of the average intensity

For each spectrum, we calculate the mean intensity for a selected range of wavelength, corresponding to a given number (N) of wavelengths among the original 2048 ones. The average intensities $I(\lambda)$ is calculated by

$$\bar{I} = \frac{\sum_{i=1}^N I(\lambda_i)}{N}. \quad (6-1)$$

For a series of M spectra, the mean intensity is calculated by

$$\bar{I}_1 = \frac{\sum_{j=1}^M \bar{I}_j}{M}. \quad (6-2)$$

And the mean standard deviation (MSD) of the average intensity is calculated by

$$\sigma = \sqrt{\frac{\sum_{j=1}^M (\bar{I}_j - \bar{I}_1)^2}{M}}. \quad (6-3)$$

Such a standard deviation (SD) characterizes the instabilities for a wavelength range. In addition, we define the following relative MSD of the average intensity:

$$\sigma_r = \frac{\sigma}{\bar{I}_1}. \quad (6-4)$$

b) Mean standard deviation of intensity with respect to the wavelength

The MSD defined in the preceding subsection does not sufficiently reflect the intensity fluctuation for a given wavelength. In order to characterize the fluctuation of intensity for each wavelength, we define the MSD of intensity with respect to the wavelength as follows:

$$\sigma_\lambda = \frac{\sum_{i=1}^N \sigma_i}{N}, \quad (6-5)$$

where the SD of intensity with respect to each wavelength, σ_i , is calculated from M spectra for a same wavelength:

$$\sigma_i = \sqrt{\frac{\sum_{j=1}^M [I_j(\lambda_i) - \bar{I}(\lambda_i)]^2}{M}}, \quad (6-6)$$

where $\bar{I}(\lambda_i)$ is the mean intensity of M measured spectra corresponding to the same wavelength λ_i :

$$\bar{I}(\lambda_i) = \frac{\sum_{j=1}^M I_j(\lambda_i)}{M}. \quad (6-7)$$

In addition, we define the relative MSD of intensity with respect to the wavelength as follows:

$$\sigma_{\lambda,r} = \frac{\sigma_{\lambda}}{\bar{I}}. \quad (6-8)$$

The two standard definitions defined in the present subsection are for the incidence intensities $I_0(\lambda)$ and the transmitted ones $I(\lambda)$. Since the spectra from both channels can be simultaneously acquired by the spectrometer SD 2000 for online particle sizing, the two standard definitions for transmission ratios, $T=I(\lambda)/I_0(\lambda)$, are defined in the same way as that for $I_0(\lambda)$ and $I(\lambda)$. In the measurements, $I(\lambda)$ is detected by channel Slave and $I_0(\lambda)$ is detected by channel Master so that we have $T= I_s(\lambda)/I_M(\lambda)$. When no absorbing medium exists, T should be unity for all wavelengths.

6.1.3 Measurement results

To get stable intensity, the lamp is turned on at least 15 minutes before the measurement. Fig. 6.6 shows an example of typical evolution of the mean intensities detected by the two channels of the spectrometer for the lamp DH 2000. Statistics are made for the wavelength range [0.35, 1.0] μm . The relative MSD of the average intensity detected by channels Master and Slave are 0.014% (0.065/476.04) and 0.012% (0.058/475.86), respectively. And the relative MSD of the average transmission ratio is 0.017% (0.00017/0.99962). Fig. 6.7 gives an example of the evolution of SD of intensity with respect to the wavelength. For the wavelengths within [0.35, 1.0], its mean value is 0.056% (0.268/476.04) for Channel Master and 0.056% (0.265/475.86) for Channel Slave. And the maximum value is ~0.084% (0.4/476), corresponding to the wavelength at the vicinities of 0.65 and 0.90 μm . The MSD of the transmission ratio with respect to the wavelength detected by the two channels is 0.10%.

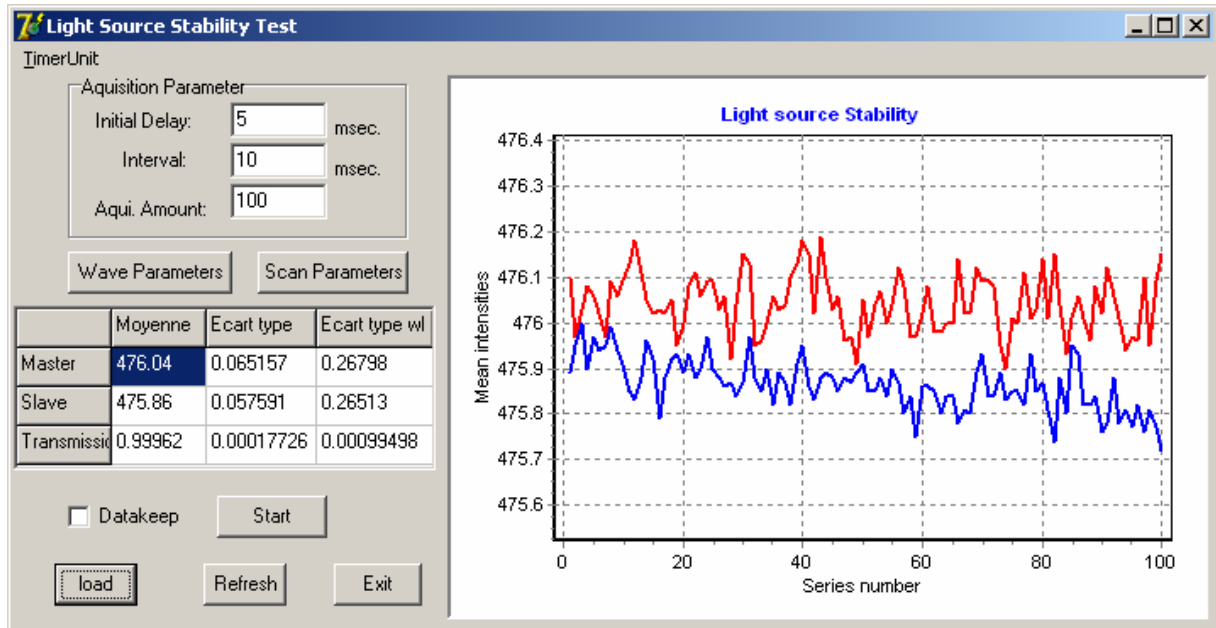


Fig. 6.6 Typical mean intensity acquired by the two channels of SD 2000.

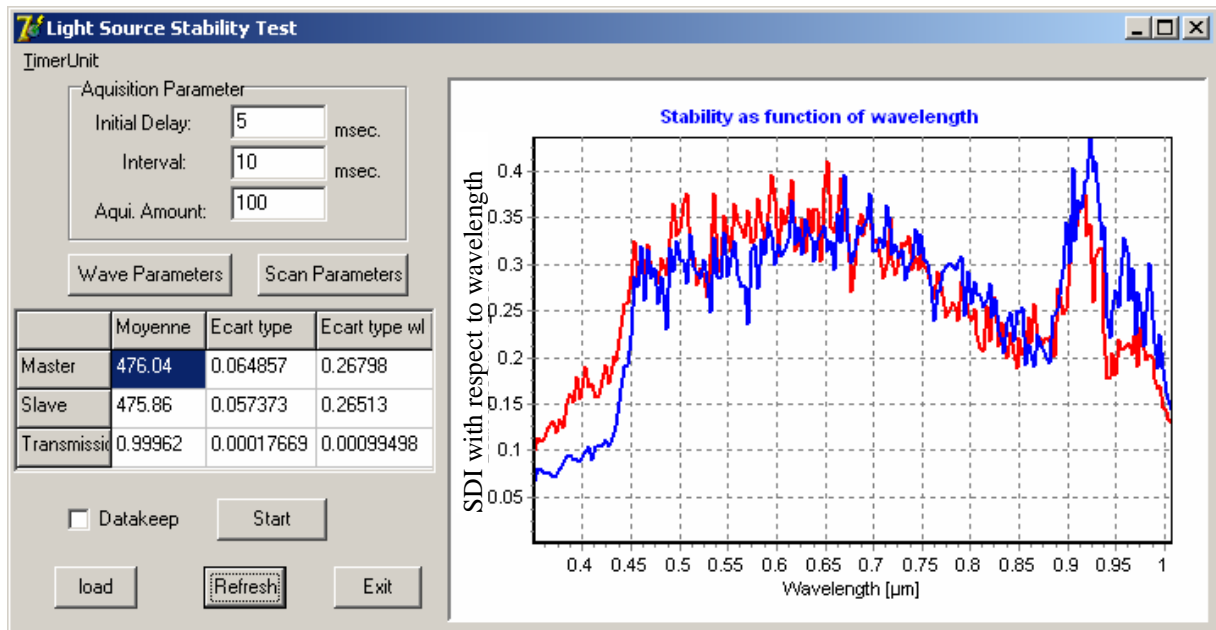


Fig. 6.7 Typical SD of intensity with respect to the wavelength (the red and blue curves represent the SDs of I_M and I_S measured from channel Master and channel Slave, respectively).

We use “Integration time T_I ”, “Sample number S_n ”, and “Boxcar of wavelength B_w ” as three main parameters for spectrum acquisition. More integration time T_I is used, more light flux is collected. The spectrometer acquires S_n spectra, calculates the mean intensities for each

wavelength λ_i and transfers them to the computer. In addition, for each wavelength λ_i , the spectrometer factually exports an average value of the intensities detected by B_w pixels (boxcar of wavelength) corresponding to the B_w wavelengths in the vicinity of λ_i .

In addition to these parameters, “Number of wavelength (N_w)” is defined as the number of wavelength re-selected by in the software TURACE 5.0 for inversion as well as the “Time interval of acquisition (ΔT)” indicating the pause time between two continuous spectral acquisitions. And to make the statistics, a series of N_s spectra are measured for mean incidence and transmitted intensities calculation for each wavelength.

In order to characterize the fluctuation of the intensities of the light source, several series of spectra have been acquired with different values of these parameters, e.g., the time interval of acquisition ΔT , the sample number S_n , and the boxcar of wavelength B_w . For each acquisition, the SDs defined in Subsection 6.1.2 are calculated for the intensities detected by both channels (I_M and I_S) as well as the transmission ratios (I_S/I_M).

Results of the two types of statistical parameters of the fluctuations measured from the light sources HL 2000 and DH 2000 are listed in Table 6.1-Table 6.2. The relative MSD of the average intensity ratio and the relative MSD of intensity ratio with respect to the wavelength are in bold font.

Through analyzing the data listed in Table 6.1-Table 6.2, we comment that the MSD of the average intensity ratio (transmittance ratio, I_S/I_M) is very weak in all the cases studied. Relative to the mean intensity ratio, its value is between 0.021% and 0.060% for the light source HL 2000 and between 0.018% and 0.028% for the light source DH 2000. The MSD is also small for I_M and I_S , the intensities measured from channel Master and channel Slave, respectively. These values do not show high dependence on the integration time T_I , the boxcar of wavelength B_w , or the sample number S_n for each spectrum. Although the fluctuation could be further weakened by increasing their values, it is not suggested for online particle sizing. Relative to the mean intensity ratio, the MSD of intensity ratio with respect to the wavelength is less than 0.21% for HL 2000 and 0.1% for DH 2000. Numerical simulation indicates that such a noise level is weak enough to have negligible influence on the measurement results. Thus the stability of the light

sources HL 2000 and DH 2000 is confirmed.

Table 6.1 Test of the stability of the light source HL 2000 (The spectrometer SD 2000 is used and I_M denotes the intensity detected by channel Master and I_S denotes the intensity detected by channel Slave).

Integration time (T_I , ms)	5	5	5	5
Sample number (for averaging, S_n)	5	5	5	50
Boxcar of wavelength (B_w)	1	5	5	5
Selected range of wavelength (μm)	0.35-0.95	0.35-0.95	0.35-0.95	0.35-0.95
Number of wavelength (N_w)	200	200	200	200
Time interval of acquisition (ΔT , ms)	10	1	10	10
Number of spectra (N_s)	100	100	100	100
Mean intensity (Master, I_M)	433.11	433.91	434.71	434.98
Mean intensity (Slave, I_S)	438.17	436.92	435.97	435.01
Mean intensity ratio (I_S/I_M)	1.0117	1.0069	1.0029	1.0001
MSD of average intensity I_M	0.0721	0.2386	0.0634	0.1015
MSD of average intensity I_S	0.1220	0.1995	0.0603	0.1241
MSD of average intensity ratio I_S/I_M	0.000369	0.00060	0.00021	0.00034
Relative MSD of average intensity ratio I_S/I_M (%)	0.037	0.060	0.021	0.034
MSD of intensity I_M with respect to λ	0.5296	0.3359	0.2803	0.1273
MSD of intensity I_S with respect to λ	0.5435	0.3687	0.2998	0.1514
MSD of intensity ratio I_S/I_M with respect to λ	0.0021	0.0013	0.0011	0.00049
Relative MSD of intensity ratio I_S/I_M with respect to λ (%)	0.21	0.12	0.11	0.05

Table 6.2 Test of the stability of the light source DH 2000 (The spectrometer SD 2000 is used and I_M denotes the intensity detected by channel Master and I_S denotes the intensity detected by channel Slave).

Integration time (T_I , ms)	20	20	20	20
Sample number (for averaging, S_n)	5	10	10	10
Boxcar of wavelength (B_w)	5	5	10	10
Selected range of wavelength (μm)	0.35-0.95	0.35-0.95	0.35-0.95	0.35-0.95
Number of wavelength (N_w)	200	200	200	200
Time interval of acquisition (ΔT , ms)	10	10	1	1000
Number of spectra (N_s)	100	100	100	100
Mean intensity (I_M)	476.04	476.16	477.64	478.83
Mean intensity (I_S)	475.86	475.78	477.51	478.81
Mean intensity ratio (I_S/I_M)	0.99962	0.99920	0.99951	0.99996
MSD of average intensity I_M	0.0648	0.0934	0.0734	0.1236
MSD of average intensity I_S	0.0574	0.0556	0.0386	0.0570
MSD of average intensity ratio I_S/I_M	0.00018	0.00026	0.00017	0.000282
Relative MSD of average intensity ratio I_S/I_M (%)	0.018	0.026	0.017	0.028
MSD of intensity I_M with respect to λ	0.2680	0.2150	0.1545	0.2028
MSD of intensity I_S with respect to λ	0.2651	0.2080	0.1464	0.1568
MSD of intensity ratio I_S/I_M with respect to λ	0.00099	0.00080	0.00057	0.00068
Relative MSD of intensity ratio I_S/I_M with respect to λ (%)	0.099	0.080	0.057	0.068

6.2 Sensibility of extinction spectrum to variation of concentration

Online measurements of the spectra directly from the light source and those have transmitted through the absorbing medium permits us reduce the potential error caused by the instabilities of the light source. And the light source is stable so that the fluctuation of the spectrum is found small enough to be ignored. On such a basis, we further explore the sensibility of the SLEM system to the variation of the particle concentration of absorbing medium, which can be the water and milk emulsion or the polystyrene particle suspension.

6.2.1 Measurement of spectrum variation of water and milk emulsion

We design and carry out the extinction measurement of the water and milk emulsion. The milk used in the measurement is half degreased. It is a colloidal medium containing a number of protein macromolecules. They can be considered as irregular particles of sizes from about 1.0 nm to 1.0 μm . By adding the milk into the water, we can manually control and change the transmittance ratio very precisely of the light through the medium.

6.2.1.1 Measurement conditions

Measurement conditions used in our measurements are listed in Table 6.3. The optical setup can be found in Fig. 6.8.

Table 6.3 Conditions for the water and milk measurements.

Light source Type	HL 2000
Spectrometer Type	SD 2000
Integration time (T_I , ms)	20
Sampling number (S_n)	5
Boxcar of wavelength (B_w)	2
Number of spectra (N_s)	100
Range of wavelength (μm)	0.35-0.95
Time interval of acquisition (ΔT , μs)	10

A beaker of the labeled volume 300 ml is filled with water mixed with the milk. Such a mixture is adjusted to have an initial extinction ratio I/I_0 of $\sim 50\%$ in the SLEM system. By adding 1.5 ml water into the beaker, each time we can obtain a change of extinction ratio of $\sim 0.5\%$. The measurements have been done by using the light source HL 2000. The integration time T_1 is set as 20 ms, the sampling number S_n is set as 5 and the boxcar of wavelength B_w is set as 10. For each concentration, three series of measurements have been made and each series contains 100 spectra ($N_s=100$). Before the measurements, the water and milk emulsion are sufficiently agitated to obtain a sufficient mixture.

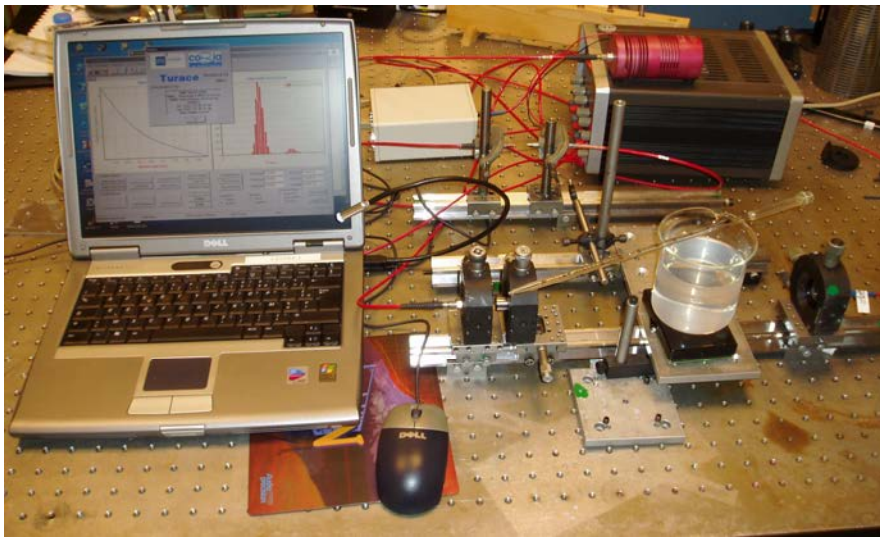


Fig. 6.8 Optical setup for the water and milk emulsion measurement.

6.2.1.2 Transmission and extinction spectrum

The transmittance and extinction spectra versus the wavelength at the beginning of the measurement are shown in Fig. 6.9.

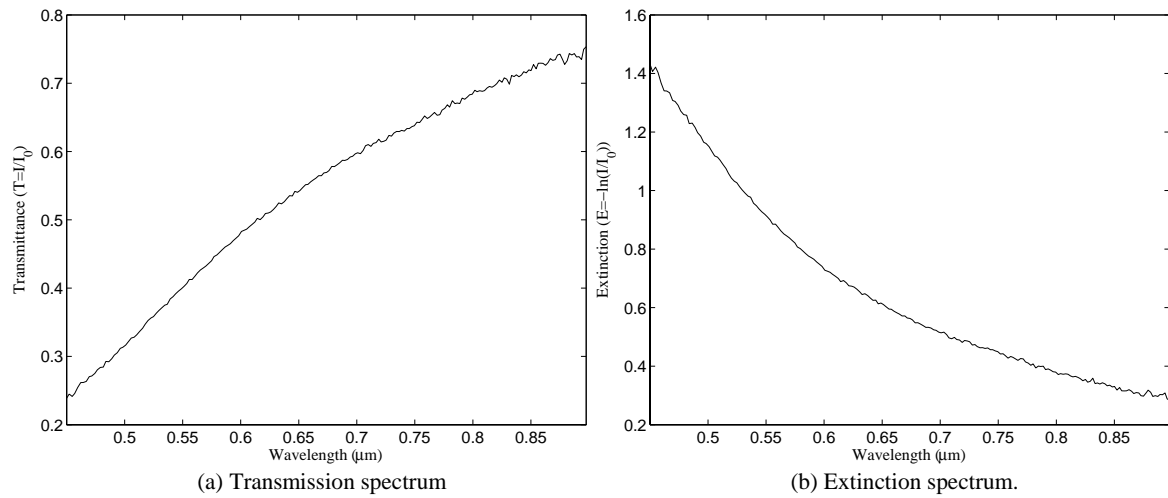


Fig. 6.9 Transmittance and extinction spectra of water and milk emulsion.

In order to know the fluctuation of the transmittance and extinction spectra versus the wavelength, the MSD of intensity with respect to the wavelength is calculated for each series of measurement. As indicated by Fig. 6.10, such an evaluation has been made for 100 spectra within the wavelength range $[0.45, 0.90] \mu\text{m}$.

Obviously, the relative MSDs of incident and transmitted intensities with respect to the wavelength are very small, being 0.08% ($0.395/487.5$) for channel Master and 0.15% ($0.389/264.3$) for channel Slave, corresponding to the relative MSD of the transmission spectrum 0.12% ($0.000635/0.542$). For particles of size $0.1 \leq D \leq 5.0 \mu\text{m}$, such a deviation corresponds to the random error level less than $\sim 0.04\%$, which is too small to bring in any influence on the inversed results of PSD and volume concentration. Thus the current system can be considered stable enough for measurement.

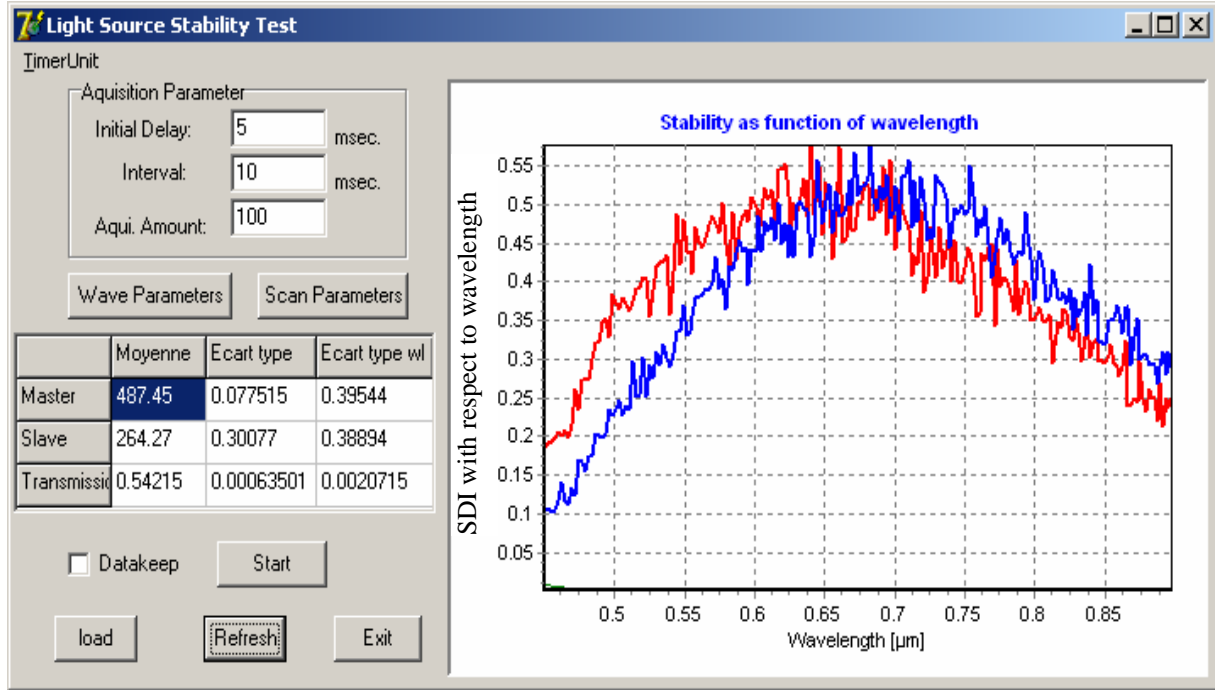


Fig. 6.10 SD with respect to the wavelength (the red and blue curves represent the SDs of I_M and I_S , respectively).

6.2.1.3 Results

The mean incident intensities and the mean transmitted intensities for each wavelength have been calculated from a series of 100 measured spectra. The mean transmitted intensities \bar{T}_{meas} versus the concentration are given in Table 6.4. The theoretical transmittance ratio versus the quantity of the water added is calculated by using the Beer-Lambert's law, which can be written as function of the volume concentration. According to the Beer-Lambert's law, the transmittance ratio depends on the volume ratio of protein molecules to the emulsion, v_m/v_0 multiplied by a constant term a . Namely,

$$T = e^{\frac{-av_m}{v_0}}. \quad (6-9)$$

If we use T_0 to denote the initial transmittance ratio of the water and milk emulsion, after adding a small volume of water Δv , the transmittance ratio of the mixture becomes

$$T = e^{\frac{-av_m}{v_0 + \Delta v}} = e^{\frac{-av_m}{v_0} \left(\frac{1}{1 + \Delta v/v_0} \right)} = T_0^{\frac{1}{1 + \Delta v/v_0}}. \quad (6-10)$$

The transmittance ratio calculated from this relationship is given in the sixth column of Table 6.4. It can be found that for the water and milk emulsion, the relative error of transmission \bar{T} is less than 0.04% and that of extinction \bar{E} is less than 0.06%. These results indicate that the transmission and extinction spectra are very sensible to the concentration change of milk molecules. A slight change of the mean transmission 0.5% is measurable by the current system. The comparison between the measured and calculated transmittance ratios is given in Fig. 6.11.

Table 6.4 Transmission and extinction ratios of the water and milk emulsion.

Δv (ml)	$\bar{T}_{\text{meas.,1}}$	$\bar{T}_{\text{meas.,2}}$	$\bar{T}_{\text{meas.,3}}$	\bar{T}_{mean}	$\bar{T}_{\text{calcul.}}$	Variation of measured \bar{T} (%)	Relative error of $\bar{T}_{\text{meas.}}$ (%)	$\bar{E}_{\text{meas.}}$	Variation of measured \bar{E} (%)	Relative error of $\bar{E}_{\text{meas.}}$ (%)
0	0.5370	0.53733	0.53751	0.53728	0.53728	Ref.	Ref.	0.62124	Ref.	Ref.
1.5	0.53882	0.53906	0.53907	0.53898	0.53903	0.170	-0.009	0.61808	-0.511	0.015
3	0.54053	0.54104	0.54097	0.54085	0.54077	0.357	0.015	0.61461	-1.078	-0.024
4.5	0.54226	0.54251	0.54284	0.54254	0.54249	0.526	0.009	0.61149	-1.593	-0.015
6	0.54389	0.54404	0.54413	0.54402	0.54421	0.674	-0.035	0.60877	-2.048	0.057
7.5	0.54564	0.54555	0.54576	0.54565	0.54591	0.837	-0.048	0.60578	-2.552	0.079
9	0.54748	0.54757	0.54768	0.54758	0.54760	1.030	-0.004	0.60225	-3.153	0.006

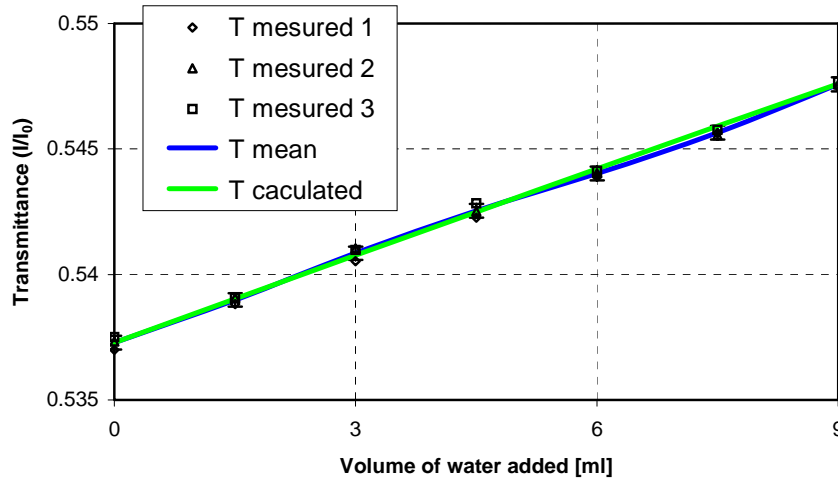


Fig. 6.11 Measurement results of the transmittance ratio of the water and milk emulsion.

6.2.2 Measurement of concentration variation of standard polystyrene particles

Our system is developed to measure the particle size distribution. Therefore the most straightforward way for validation is by the usage of standard particles. In this subsection, experimental examination of the sensibility of the SLEM system to the small concentration variation of the standard polystyrene particle suspensions is carried out. The optical setup is same as that for water and milk measurement system, except that the beaker is replaced by a sampling cell of the length $L=40$ mm. The standard polystyrene particles used for the test have the refractive index $\hat{m}_n=1.590$ at the wavelength $\lambda=589$ nm. The manufacturer of the standard polystyrene particles is Duck Scientific, Inc. They are dispersed by the pure mineral water of refractive index $\hat{m}_1=1.333$ at common temperature and pressure.

6.2.2.1 Measurement conditions

The measurements have been carried out for two kinds of standard polystyrene particles, with labeled diameters $0.5 \mu\text{m}$ and $1.0 \mu\text{m}$, respectively, and suspended in the distilled water in a sampling cell of dimension $10\text{mm}\times 40\text{mm}\times 40\text{mm}$. Before measurement, we manually agitate the suspension carefully with a syringe in order to make the particles in the suspension dispersed sufficiently.

For each concentration, five series of spectra are measured. Each series of spectra contains 100 spectra, from which we calculate the mean intensity for each wavelength. All the parameters used in the data acquisition are given in Table 6.5. As to be stated later in Chapter 7, the optimized regularization technique (ORT) is found more effective in practical PSD inversion. Therefore it is used in this subsection to study the sensibility of the system to the variation of volume concentration of the particles. The parameters used for inversion are given in Table 6.6.

Table 6.5 Parameters for acquisition used in the polystyrene particle measurements.

Labeled diameter (D , μm)	0.5	1.0
Integration time (T_I , ms)	20	20
Boxcar of wavelength (B_w)	5	5
Sample number (S_n)	5	5
Number of spectra (N_s)	100	100

Table 6.6 The parameters used for inversion in polystyrene particles measurements.

Range of wavelength (μm)	0.40-0.95
Number of wavelength	100
Particle size range (μm)	0.1-5.0
Number of size intervals	100
Algorithm	ORT ($\gamma=1.0\text{E-}4$, $n=98$)

6.2.2.2 Results

In order to know the sensibility of the SLEM system to the variation of volume concentration of particles, we use C_{v_0} to designate the initial volume concentration. After adding the water of volume Δv into the beaker, the volume concentration C_v is

$$C_v = \frac{v}{v_0 + \Delta v} = \frac{v}{v_0} \frac{1}{1 + \Delta v / v_0} = C_{v_0} \frac{1}{1 + \Delta v / v_0}, \quad (6-11)$$

where v_0 is the initial volume of the suspension and v is the total volume of particles.

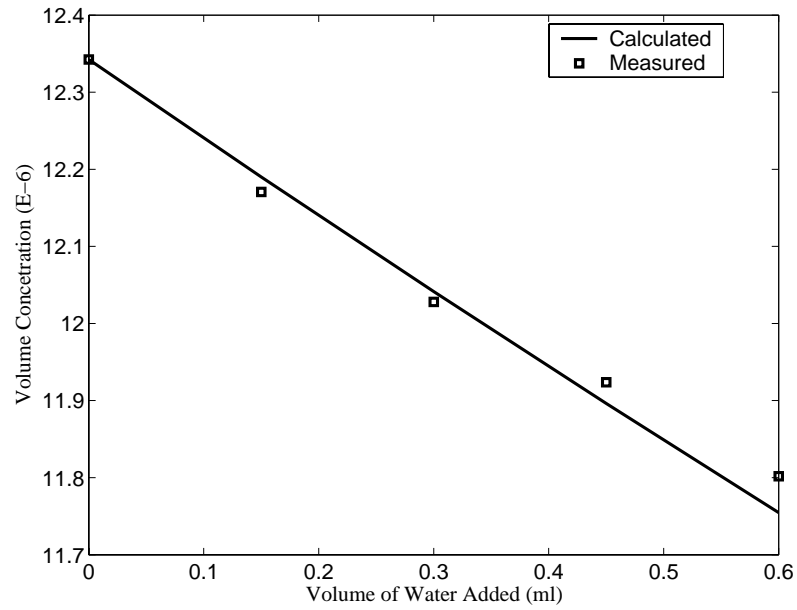
The inversed results of the volume concentration of the polystyrene particles of the diameters $D=0.5 \mu\text{m}$ and $1.0 \mu\text{m}$ are compiled in Table 6.7 and Table 6.8, respectively. The volume concentration C_v calculated by Eq.(6-11) is also given in these tables. Comparison of the theoretical and measured volume concentrations is presented in the Fig. 6.12 and Fig. 6.13.

At the beginning, the quantity of the polystyrene particles dispersed in water is adjusted so that the transmittance ratio is $\sim 50\%$. Then each time, a certain volume of water is added into the sampling cell to achieve a volume concentration change of $\sim 0.5\%$.

for the particles of diameters $0.5 \mu\text{m}$ and $1.0 \mu\text{m}$, the initial diluted polystyrene particle suspensions in the beaker has the heights 30.0 mm and 28.0 mm , respectively, which corresponding to the volume 12 ml and 11.2 ml . The minimum graduation of the syringe used for water addition is 0.05 ml . The precision of the volume of water added into the sampling cell is estimated to be 0.025 ml , so that the error of the volume concentration is less than $\sim 0.2\%$. From the relative errors listed in the last column of Table 6.7-Table 6.8, we can evaluate that the present system permits to measure the variation of volume concentration of 0.5% with uncertainty less than $\sim 0.4\%$. Additionally, the calculated SMDs for these standard particles are $0.5275 \mu\text{m}$ and $1.0780 \mu\text{m}$, with deviation errors being 5.5% and 7.8% , respectively.

Table 6.7 Measured and predicted volume concentration $v/v_0 (\times 10^{-6})$ for the polystyrene particles of diameter $0.5 \mu\text{m}$ ($v_0=12 \text{ ml}$).

Δv (ml)	Meas. 1	Meas. 2	Meas. 3	Meas. 4	Meas. 5	\bar{C}_v	$\Delta C_v / C_{v_0}$ (%)	C_v (calcul.)	$\frac{\bar{C}_v - C_v}{C_v}$ (%)
0	12.353	12.348	12.329	12.338	12.344	12.342	0 (Ref.)	12.342	Ref.
0.15	12.154	12.167	12.182	12.174	12.178	12.171	-1.392	12.190	-0.160
0.30	12.033	11.998	12.031	12.045	12.034	12.029	-2.547	12.041	-0.111
0.45	11.902	11.926	11.928	11.925	11.937	11.902	-3.392	11.896	0.231
0.6	11.792	11.813	11.802	11.869	11.733	11.802	-4.379	11.755	0.402

Fig. 6.12 Calculated and measured volume concentration (0.5 μm).Table 6.8 Measured and predicted volume concentration v/v_0 ($\times 10^{-6}$) for the polystyrene particles of diameter 1.0 μm ($v_0=11.2$ ml).

Δv (ml)	Meas. 1	Meas. 2	Meas. 3	Meas. 4	Meas. 5	\bar{C}_v	$\Delta C_v / C_{v_0}$ (%)	C_v (calcul.)	$\frac{\bar{C}_v - C_v}{C_v}$ (%)
0.00	5.315	5.317	5.336	5.332	5.357	5.331	0 (Ref.)	5.331	Ref.
0.15	5.250	5.2575	5.296	5.283	5.283	5.274	-1.083	5.261	0.242
0.30	5.180	5.182	5.184	5.200	5.191	5.180	-2.700	5.192	-0.093
0.45	5.134	5.130	5.150	5.146	5.135	5.139	-3.612	5.126	0.260
0.60	5.070	5.047	5.057	5.067	5.055	5.059	-5.104	5.060	0.020

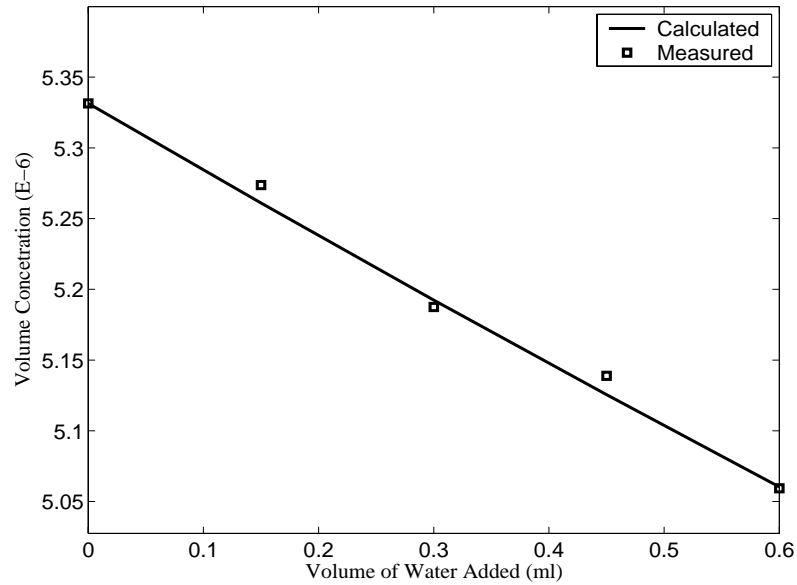


Fig. 6.13 Calculated and measured volume concentration ($1.0 \mu\text{m}$).

6.3 Size and concentration measurement of standard polystyrene particles

To explore the applicability of the developed optical system and evaluate the measurement error, we apply the spectral light extinction method to measure the size and concentration of the standard polystyrene particles in this section. The standard polystyrene particles of labeled diameters 0.3 , 0.5 , 1.0 , and $3.0 \mu\text{m}$ are measured.

6.3.1 Experimental setup

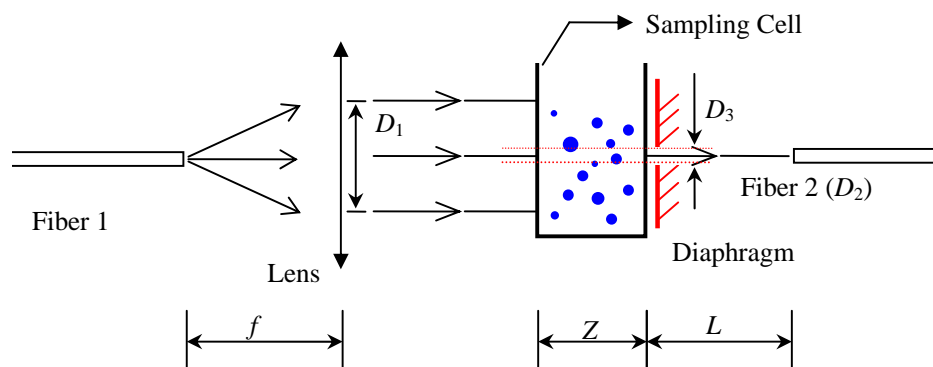


Fig. 6.14 Schematic diagram of the optical setup.

The schematic diagram of the optical setup is illustrated in Fig. 6.14. A multimodal fiber (Fiber

1) is used as the launching fiber, with one of its end connected to the light source and the other one fixed at the focal point of the lens so that the incident light wave is collimated to the diameter of ~ 8 mm ($D_1=8$ mm). When the light traverses the sampling cell, it is partly scattered and absorbed by the particles suspended in the sampling cell. A diaphragm is put close enough at the back of the sampling cell. It is utilized to prevent the scattered intensities by the particles at the edge zones from reaching the detecting fiber (Fiber 2). In our experiments, the diaphragm is adjusted to the opening diameter of 2.0 mm ($D_3=2.0$ mm). The diameter of the Fiber 2 is quite small ($D_2=0.4$ mm) and it is located 150 mm away from the sampling cell ($L=150$ mm), leading to the half collection angle of the receiver being $\sim 0.08^\circ$. In addition, the transparent sampling cell has the dimension of 40mm \times 40mm \times 10mm so that the length of the measurement zone is 40 mm ($Z=40$ mm). As to be verified in Chapter 8, for such an optical configuration the scattered intensities reaching the detecting fiber is small enough to be neglected for single and multiple scattering regimes ($\xi \leq 10$) even when the diaphragm is removed. Therefore all the intensities detected by Fiber 2 can be looked on as the contribution of the transmitted light.

The measurement is performed by the software TURACE 5.0 developed by us for the SLEM system, which has a friendly interface for easy operation. In TURACE 5.0, the data acquisition mode is alternative: single channel or double channel. In the current experiments, double channel mode is chosen so that the original intensity I_0 and transmitted intensities I can be obtained simultaneously. Such a mode is also adopted for online wet steam measurement.

6.3.2 Measurements

The halogen lamp HL 2000 is used as the light source. There are 2048 wavelengths ranging from 0.3400 μm to 1.0255 μm detected by the spectrometer. The intensities corresponding to the wavelengths within [0.4, 0.95] μm are found strong enough. Two hundred of them are selected out and each of them is calculated from the mean value of the intensities corresponding to 10 adjacent wavelengths ($B_w=10$). All the parameters used for data acquisition and inversion are listed in Table 6.9.

Table 6.9 The parameters used for acquisition and inversion.

Integration time (T_I , ms)	100
Boxcar of wavelength (B_w)	10
Sample number (S_n)	5
Number of spectra (N_s)	100
Range of wavelength (μm)	0.40-0.95
Number of wavelength (N_w)	200
Particle size range (μm)	0.1-5.0
Number of size intervals (N_i)	100
Algorithm	ORT ($\gamma=1.0\text{E}-4$, $n=98$)

6.3.2.1 Unimodal distribution

First, we perform the measurement for each particle diameter. The inversed results of SMD D_{32} and volume concentration C_v are listed in Table 6.10. In Fig. 6.15-Fig. 6.18 are plotted the inversed PSD and the comparison of the reconstructed spectrum with the original one.

Table 6.10 Inversed Sauter diameter (D_{32}) and volume concentration (C_v) of the standard polystyrene particles.

		PSD 1	PSD 2	PSD 3	PSD 4
D_{32} given (μm)		0.3	0.5	1.0	3.0
D_{32} inversed (μm)	Twomey	0.066	0.415	1.086	2.934
	ORT	0.319	0.526	1.082	3.011
Error of D_{32} (%)	Twomey	-78.0	-17.0	8.6	-2.2
	ORT	6.4	5.2	8.2	0.37
C_v inversed	Twomey	2.863E-5	3.503E-5	4.827E-6	2.910E-6
	ORT	6.435E-6	2.627E-5	4.740E-6	3.066E-6

As can be found from Table 6.10, ORT's inversed results of SMD are close to the labeled values of the standard particles, with deviations less than 10%. The Twomey algorithm, however, leads to more obvious deviations. Especially for the standard particle of $D=0.3 \mu\text{m}$, the inversed result of SMD is $0.066 \mu\text{m}$, with the error being -78.0% . Moreover, the PSD obtained by the Twomey algorithm presents a gradually decreasing shape for $0 \leq D \leq 0.5 \mu\text{m}$, which is evidently unbelievable.

Comparison of the two algorithms indicates that the ORT has a better performance in practical particle sizing than the Twomey algorithm does, though the reconstructed spectra from Twomey's PSDs might agree better with the measured ones than the ORT's results do, which can be found in Fig. 6.15b-Fig. 6.17b.

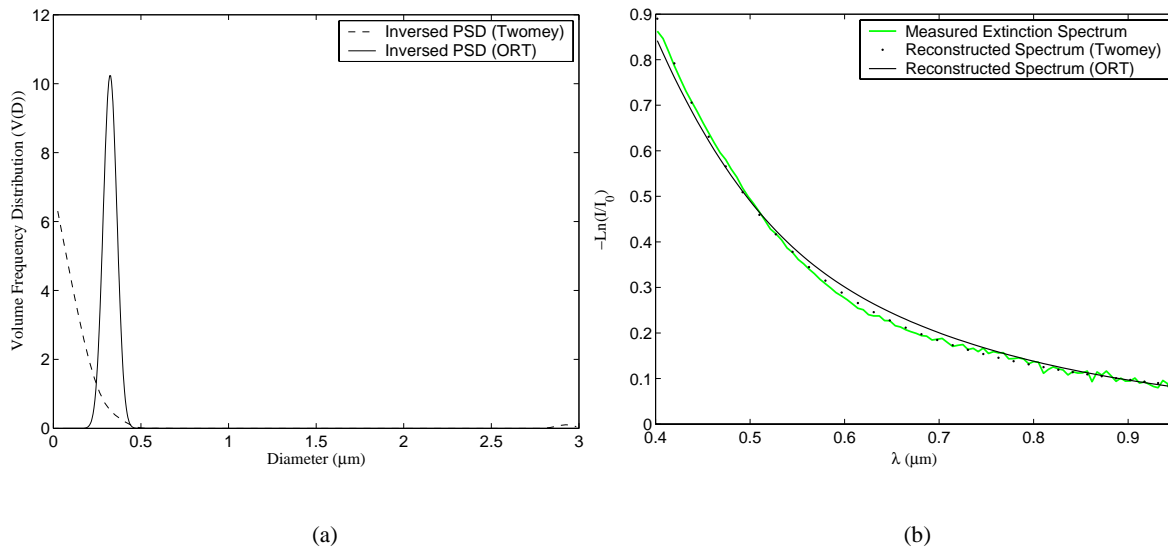


Fig. 6.15 Inverse results of PSD ($D=0.3 \mu\text{m}$) and comparison of the original and reconstructed spectra. (a) Inversed PSD; (b) Comparison of the original and reconstructed spectra.

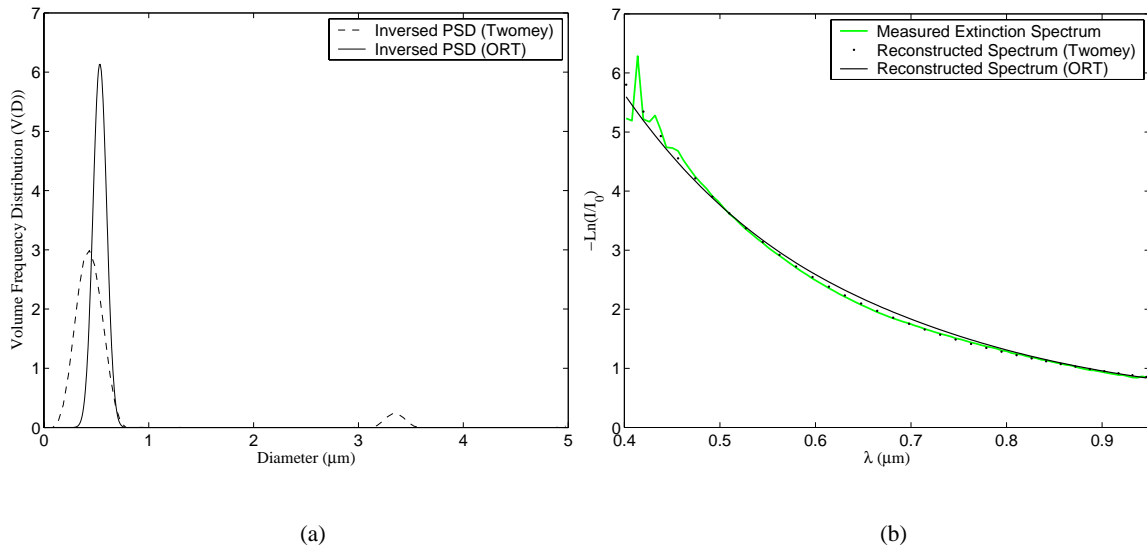


Fig. 6.16 Inverse results of PSD ($D=0.5 \mu\text{m}$) and comparison of the original and reconstructed spectra. (a) Inversed PSD; (b) Comparison of the original and reconstructed spectra.

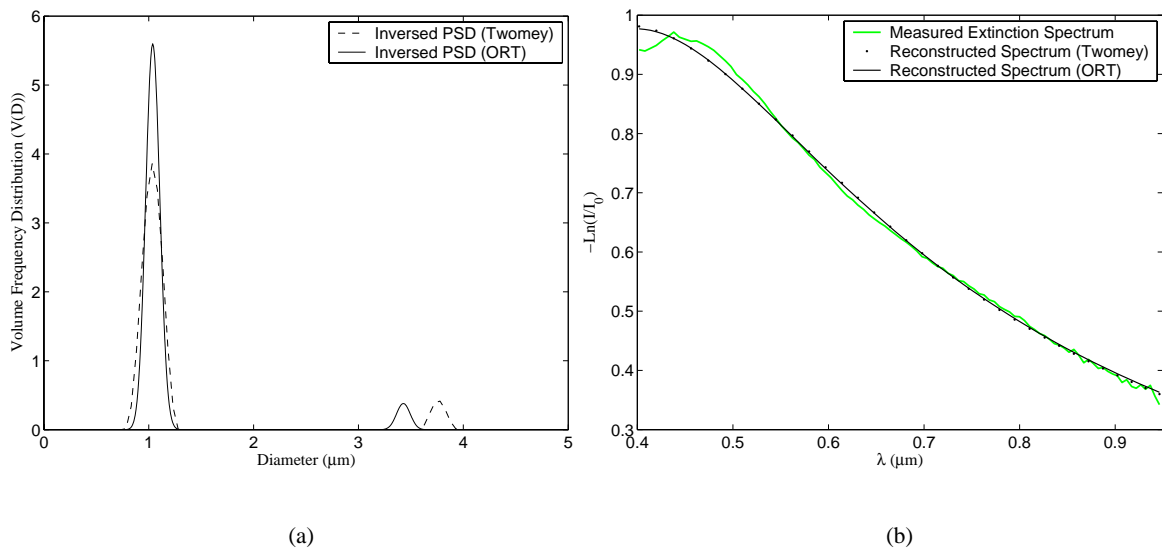


Fig. 6.17 Inverse results of PSD ($D=1.0 \mu\text{m}$) and comparison of the original and reconstructed spectra. (a) Inversed PSD; (b) Comparison of the original and reconstructed spectra.

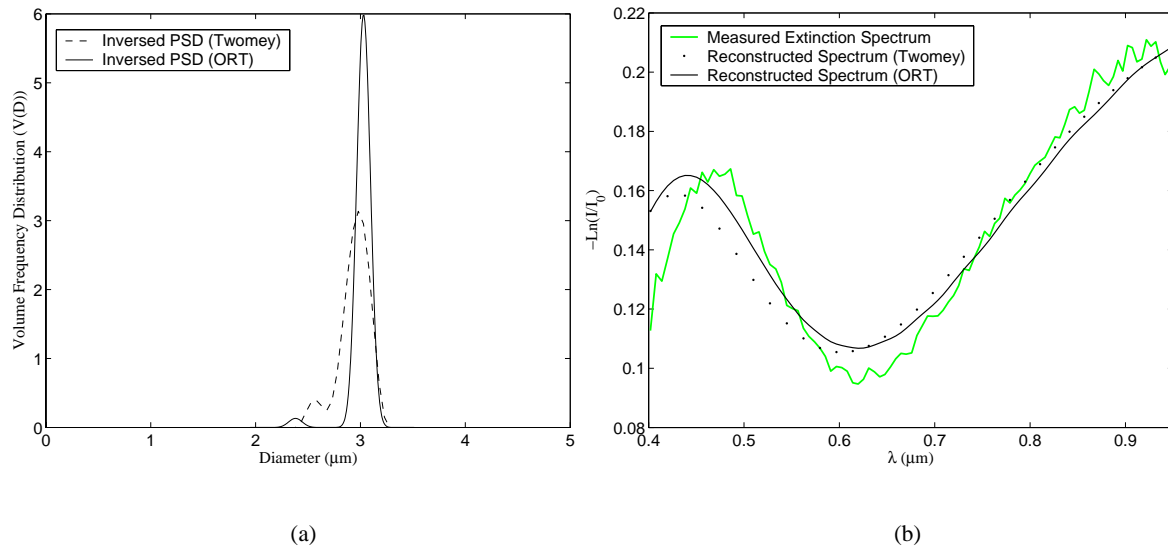


Fig. 6.18 Inverse results of PSD ($D=3.0 \mu\text{m}$) and comparison of the original and reconstructed spectra. (a) Inversed PSD; (b) Comparison of the original and reconstructed spectra.

6.3.2.2 Bimodal and multimodal distribution

In this subsection we discuss the measurement of the mixture of particles of different diameters. Two or three of the standard polystyrene particles of diameters $D=0.5$, 1.0 , and $3.0 \mu\text{m}$ are selected and mixed together to produce a bimodal or multimodal PSD.

In Fig. 6.19 is plotted the inversed PSD and the reconstructed spectrum of the mixture of PSD2 and PSD3. The observed peaks existing with the ORT's results locate at $D=0.54$ and $1.08 \mu\text{m}$, corresponding to the deviations of $\sim 8.0\%$ and $\sim 8.0\%$, respectively, from the labeled mean diameters of PSD2 and PSD3. As to the results of the Twomey algorithm, the two main peaks locate at $0.55 \mu\text{m}$ and $1.15 \mu\text{m}$, corresponding to the deviations of $\sim 10.0\%$ and $\sim 15.0\%$, respectively, from the labeled values.

In Fig. 6.20 is plotted the inversed PSD result and reconstructed spectrum of the mixture of PSD2 and PSD4. The observed peaks existing with the ORT's results locate at $D=0.56$ and $3.11 \mu\text{m}$, corresponding to the deviations of about 12.0% and 3.7% , respectively, from the labeled values. As to the results of the Twomey algorithm, the two main peaks locate at $D=0.35$ and $3.17 \mu\text{m}$, corresponding to the deviations of about $\sim 30.0\%$ and $\sim 5.7\%$, respectively, from the labeled values. In addition, there exists a split distribution at the vicinity of $D=4.8 \mu\text{m}$.

In Fig. 6.21 is plotted the inversed PSD result and reconstructed spectrum of the mixture of PSD3 and PSD4. The observed peaks existing with the ORT's results locate at $D=1.18$ and 3.17 μm , corresponding to the deviations of $\sim 18.0\%$ and $\sim 5.7\%$, respectively, from the labeled values. As to the results of the Twomey algorithm, the two main peaks are at 1.13 and 3.25 μm , corresponding to the deviations of $\sim 13.0\%$ and $\sim 8.33\%$, respectively, from the labeled values. In addition, a split distribution is still found at the vicinity of $D=4.8$ μm .

In Fig. 6.22 is plotted the inversed PSD result and reconstructed spectrum of the mixture of PSD2, PSD3, and PSD4. The observed three main peaks existing with the ORT's PSD results locate at $D=0.58$, 1.08 , and 3.14 μm , corresponding to the deviations of $\sim 8.0\%$, $\sim 8.0\%$, and $\sim 4.7\%$, respectively, from the labeled values. However, the Twomey algorithm merges the first two peaks of PSD2 and PSD3 so that only two main peaks can be recognized at the vicinities of $D=0.68$ and 3.12 μm .

From these measurements, we are persuaded again that in most cases, the ORT is more sophisticated than the Twomey algorithm in the practical bimodal or even multimodal PSD inversion, though both algorithms lead to a perfect agreement of the reconstructed and the original spectra.

To make the measurement system more approximate to that designed for wet steam measurement, after each measurement the diaphragm is removed and the spectrum is recorded again. However, little difference has been found between the spectrum measured with and without the diaphragm. This means that for the current SLEM system, the scattering intensities from the particles at the edge zones, which is characterized by $D_2/2 \leq D \leq D_1/2$ (see Fig. 6.14), have no essential influence on the extinction spectrum. The reason will be explored in the next chapter.

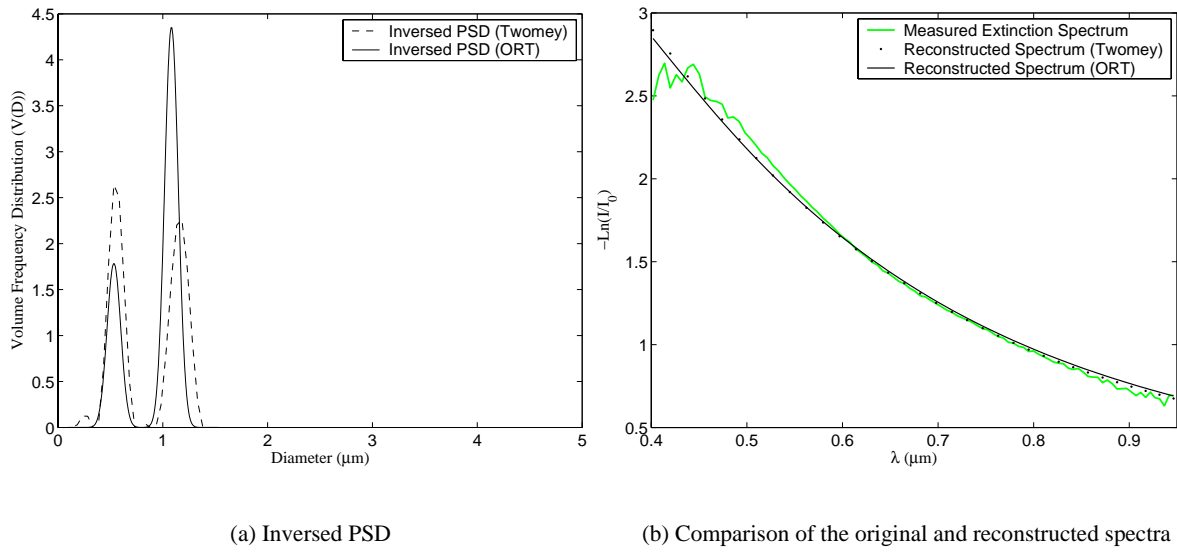


Fig. 6.19 Inversed PSD of the mixture of PSD2 and PSD3 and comparison of the original and reconstructed spectra. The inversed SMDs by using the Twomey algorithm and the ORT are 0.729 μm and 0.826 μm, respectively.

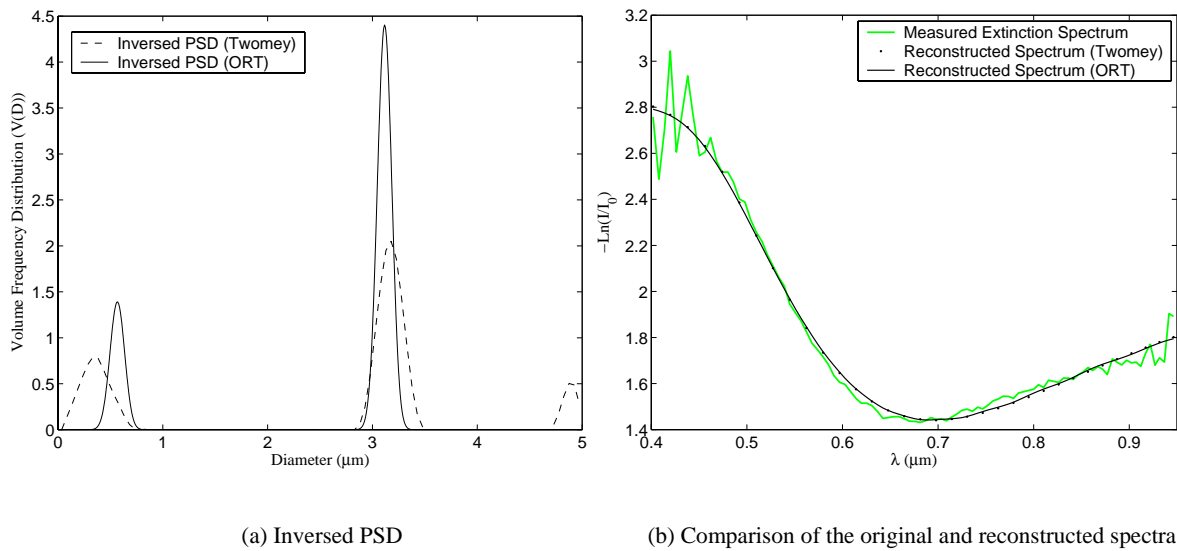


Fig. 6.20 Inversed result of mixture of PSD2 and PSD4 and comparison of the original and reconstructed spectra. The inversed SMDs by using the Twomey algorithm and the ORT are 0.846 μm and 1.476 μm, respectively.

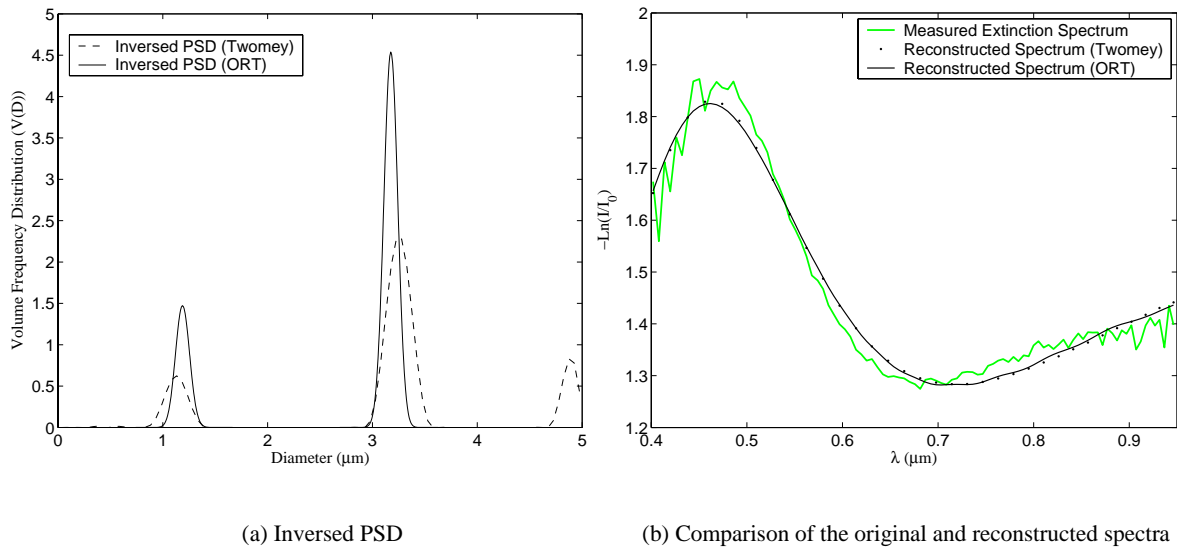


Fig. 6.21 Inversed PSD of the mixture of PSD 3 and PSD 4 and comparison of the original and reconstructed spectra. The SMDs by using the Twomey algorithm and the ORT are 2.536 μm and 2.243 μm, respectively.

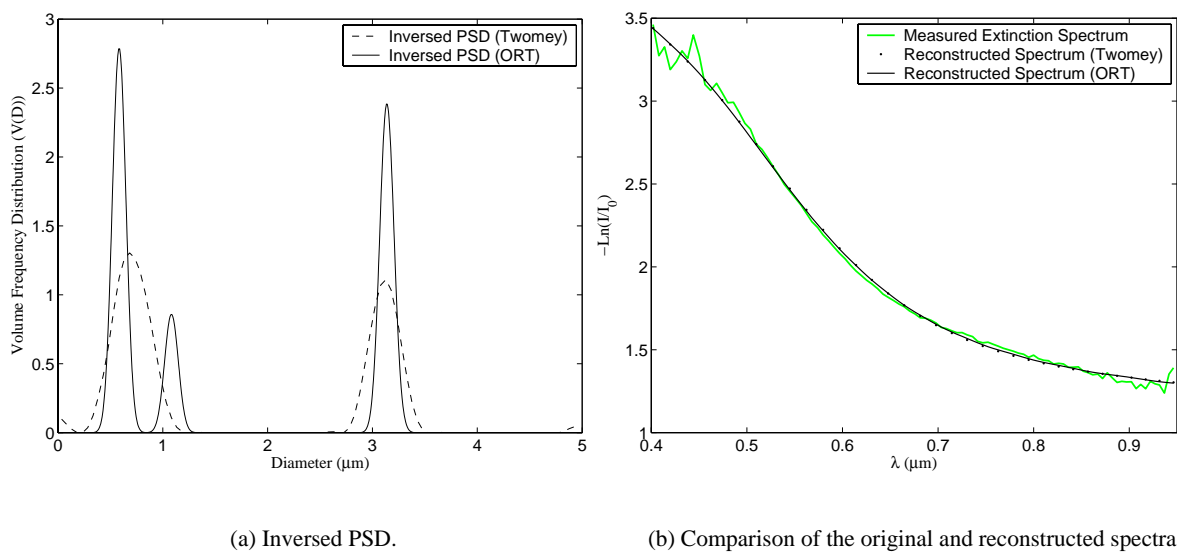


Fig. 6.22 Inversed PSD of the mixture of PSD 2, PSD 3, and PSD 4 and comparison of the original and reconstructed spectra. The inversed SMDs by using the Twomey algorithm and the ORT are 0.835 μm and 0.955 μm, respectively.

6.4 Conclusion

To characterize the stability of the light source, the MSD of the average intensity and the MSD of intensity with respect to the wavelength are examined experimentally. These SDs show some dependence on the acquisition parameters. The relative MSD of the average intensity ratio is

found less than 0.06% and 0.028% for light sources HL 2000 and DH 2000, respectively, when the integration time is less than 20 ms ($T_1 \leq 20$ ms), the sampling number S_n is 5 ($S_n=5$), the boxcar of wavelength is 2 ($B_w=2$), and the number of spectra is 100 ($N_s=100$). The relative MSD of the intensity ratio with respect to the wavelength is less than 0.21% and 0.1% for the light sources HL 2000 and DH 2000, respectively. The fluctuation of spectra with such a SD has little influence on the measurement results.

On such a basis, we further study the sensibility of the SLEM system to the small change of the transmission spectrum. Using the water and milk emulsion, we have shown experimentally that a small variation of the mean transmission of 0.5% is measurable by the current system. Using the standard polystyrene particles of diameters 0.5 and 1.0 μm , we find the small change of particle volume concentration of 0.5% is measurable. Then experimental application of SLEM in standard polystyrene particle is carried out in this chapter. The ORT is found more effective than the Twomey algorithm in practical experimental data inversion. The errors of the measured SMDs of the standard polystyrene particles are found less than $\sim 10\%$. These experiments lead to the conclusion that although the absolute measurement of D_{32} is not highly accurate (with errors less than 10%), the measurement of volume concentration variation ΔC_v (relative measurement) by the current system is high enough, with errors less than $\sim 0.4\%$ for $\Delta C_v=0.5\%$.

Chapter 7. Wet Steam Measurement

The measurement of standard polystyrene particles in the preceding chapter assures us that the current system designed on the basis of spectral light extinction method (SLEM) has the measurement errors less than ~10% when optimized regularization technique (ORT) is chosen for data inversion. In this chapter, we further apply the same system in online wet steam measurement, including droplet size distribution and wetness measurement. Before carrying out the measurement, we give the relation between the wetness and the particle concentration.

7.1 Wetness

The measured wetness of the two-phase flow, denoted by the sign Y_M , is obtained from the volume concentration of the droplets contained in the flow, C_v , the density of the vapor phase of the water, ρ_g , and the density of the liquid phase of water, ρ_f , as follows:

$$Y_M = \frac{m_f}{m_f + m_g} = \frac{C_v \rho_f}{C_v \rho_f + (1 - C_v) \rho_g}, \quad (7-1)$$

where m_f and m_g are the mass of the liquid and vapor phase of water, respectively. And ρ_f and ρ_g are the liquid and vapor phase densities, respectively. Since the volume of droplets contained in the flow occupies a very small proportion, namely $C_v \ll 1$, Eq.(7-1) can be simplified to the following form:

$$Y_M = \frac{m_f}{m_f + m_g} = \frac{C_v}{C_v + \rho_r}, \quad (7-2)$$

where the expression of the density ratio of the two phases of the water, ρ_r , is calculated by

$$\rho_r = \rho_g / \rho_f. \quad (7-3)$$

The density of vapor and liquid phased are decided by the pressure of the saturated steam at the measurement point from the saturated steam chart.

7.2 Experimental setup

In this subsection, we apply the SLEM system, which is described in Section 6.3 of Chapter 6, in the measurement of the wet steam generated by an experimental turbine installed on platform PAT (Plate-forme Aérodynamique et Thermodynamique) in EDF (Dorey et al., 2006). The scheme of the facility and the photo for realistic measurements are shown in Fig. 7.1 and Fig. 7.2. The overheated steam is cooled by water spraying and then conducted to a turbine. Such a turbine system is designed to produce the wet steam with a very good stability and a very fine adjustment of turbine inlet temperature and pressure so that the concentration of droplets corresponds to the wetness that prevails at the exit of low pressure cylinder.

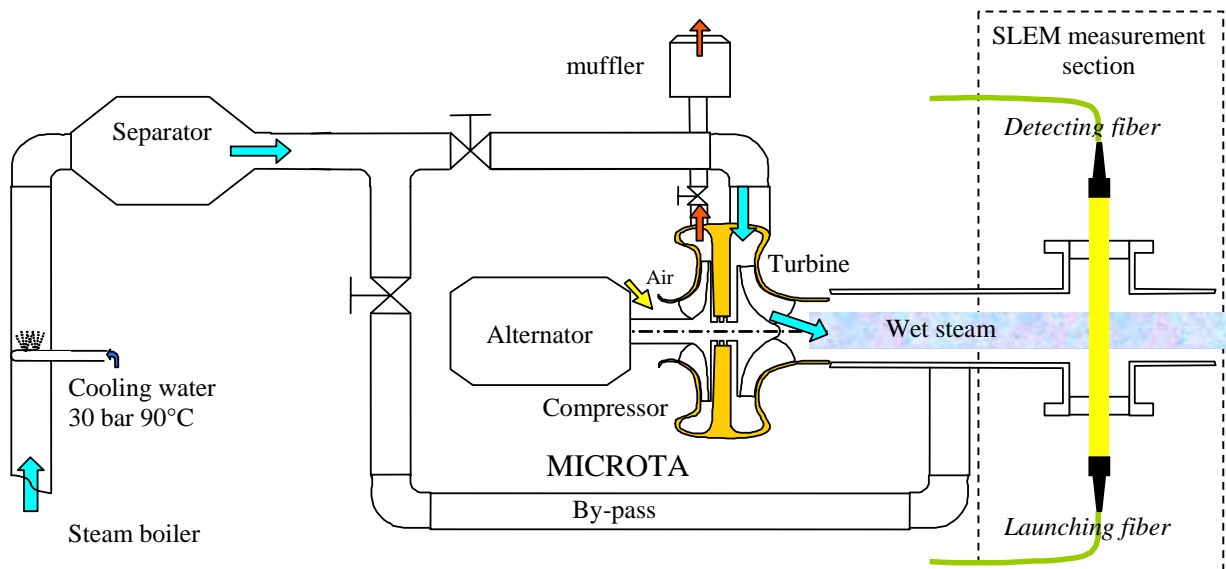
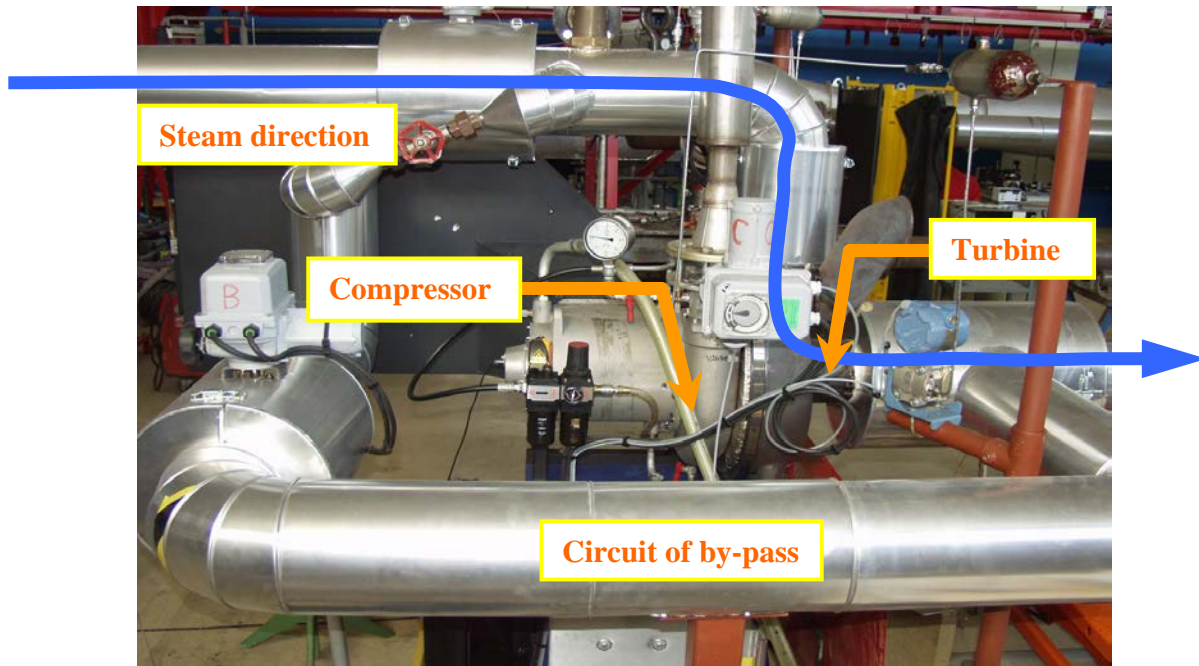
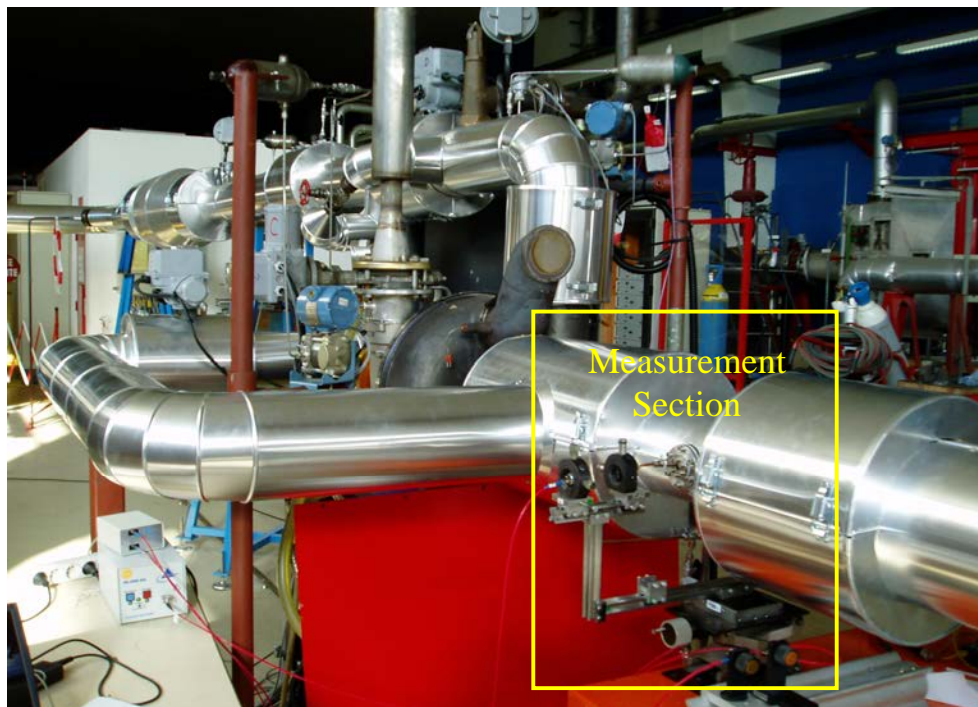


Fig. 7.1 Scheme of installation plat-form.



(a) Turbine system



(b) SLEM measurement system installed on the turbine

Fig. 7.2 Realistic photos of the turbine system and the optical measurement system installed on the plat-form PAT.

7.3 Measurements

The measurement of the wetness and the size distribution has been done in a series of conditions of inlet temperature with a step of $\sim 0.5^\circ\text{C}$. We show hereafter an example of such a measurement. The upstream and downstream pressures are 1.034 bar and 0.552 bar, respectively. The turbine inlet temperature at downstream is varied from 127.5°C to 130°C . The rotational speed of the turbine is 38 750 tr/min.

By using the parameters listed in Table 7.1 for data acquisition and inversion, the inversed result of volume frequency distribution of the droplets, which is calculated from a spectrum averaged from one series of 100 continuously spectra, are plotted in Fig. 7.3a, from which we found that the PSD is quasi monodisperse. A small part of volume is found occupied by the particles of diameters $\sim 2.7 \mu\text{m}$. However, their absolute number is not remarkable, as indicated by the number frequency distribution in Fig. 7.3b. The reconstructed spectrum is compared with the measured one in Fig. 7.4, leading to a perfect agreement.

Table 7.1 The parameters used for acquisition and inversion.

Integration time (T_I , ms)	100
Boxcar of wavelength (B_w)	10
Sample number (S_n)	5
Number of spectra (N_s)	100
Range of wavelength (μm)	0.40-0.95
Number of wavelength (N_w)	200
Particle size range (μm)	0.1-5.0
Number of size intervals (N_I)	100
Algorithm	ORT ($\gamma=1.0\text{E-}4$, $n=98$)

Since the measurement is online, the SLEM system permits to obtain rapid temporal evolution of SMD of the droplets and wetness, as indicated in Fig. 7.5 and Fig. 7.6. They

correspond to a series of 100 spectra acquired within 10 seconds. We can find from Fig. 7.5 that in such a time period, the Sauter mean diameter D_{32} varies within the range $[0.6, 0.9] \mu\text{m}$ and the wetness varies within $[0.59\%, 0.68\%]$. It is interesting to find that from 2.0s to 2.5s, there appears a jump of SMD of about $0.05 \mu\text{m}$. The reason for such a phenomenon remains to be examined.

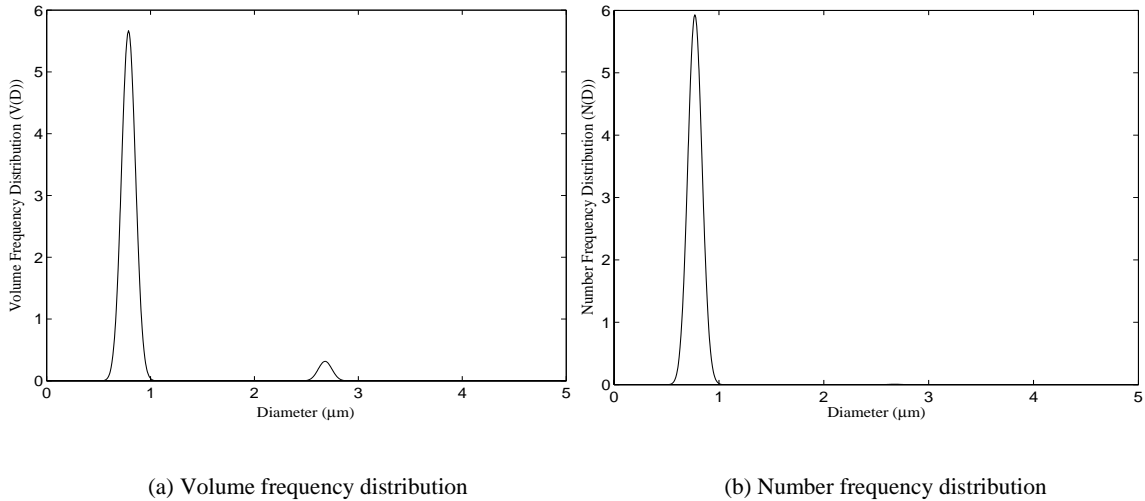


Fig. 7.3 Volume and number frequency PSD of the droplets in wet steam.

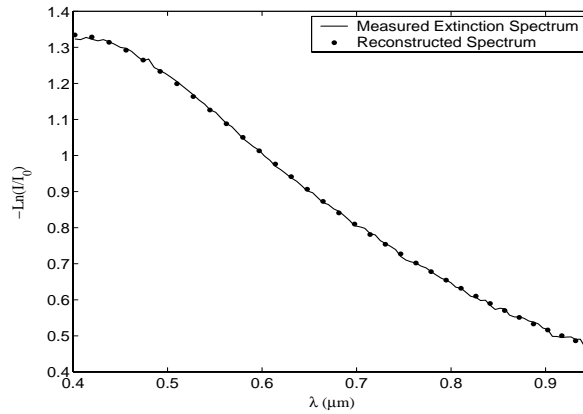


Fig. 7.4 Comparison of the reconstructed spectrum to the measured one, which is averaged from 100 continuously acquired spectra.

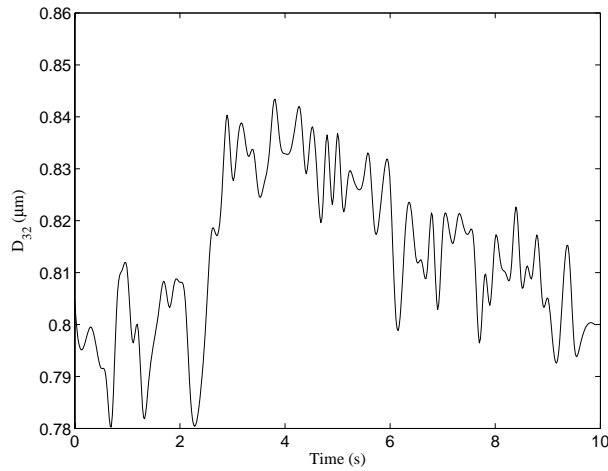


Fig. 7.5 Temporal evolution of the Sauter mean diameter D_{32} .

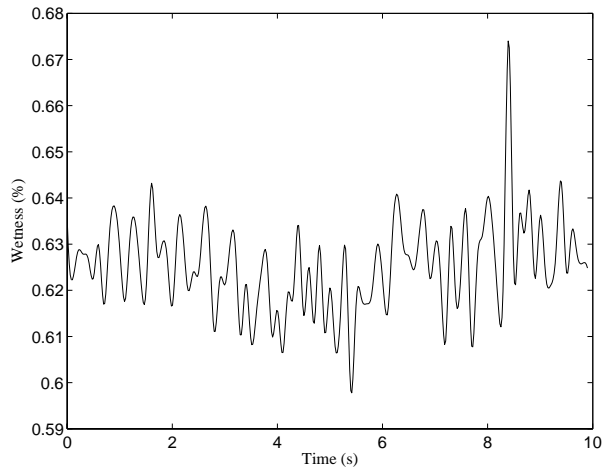


Fig. 7.6 Temporal evolution of the measured steam wetness Y_M .

The measured wetness, Y_M , can be compared with the theoretically predicted one, Y_T , which is inferred from the inlet conditions and the efficiency of the turbine (previously measured without cooling) at a certain measurement section. The calculation is formulized in IAPWS (1997). Fig. 7.7 gives a comparison of the theoretical and measured wetness (Dorey et al., 2006). The measured wetness shown here is the mean value calculated from the 100 measured spectra and the theoretical wetness are predicted according to the pressures and the temperatures at the upstream and the downstream, and the gain of the turbine. The discrete data are fitted by a linear regression line. We find that the deviation of the measured wetness from the theoretical one is within [1.6%, 4.5%] for $0.6% < Y_T < 0.8%$. Wetness measurements are also carried out for other

pressure and temperature conditions. The results are shown in Fig. 7.8-Fig. 7.11 (Dorey et al., 2006).

Remarkable difference between the theoretically calculated and measured wetness can be found in Fig. 7.8 and Fig. 7.10, corresponding to the deviations of the measured wetness from the theoretical one being within [7%, 90%], [22%, 28%], and [23%, 33%], respectively. This might be due to the fact that low theoretical wetness is influenced a lot by the turbine efficiency experimentally determined. In other words, small measurement errors of turbine efficiency bring in remarkable variations of the theoretically predicted wetness.

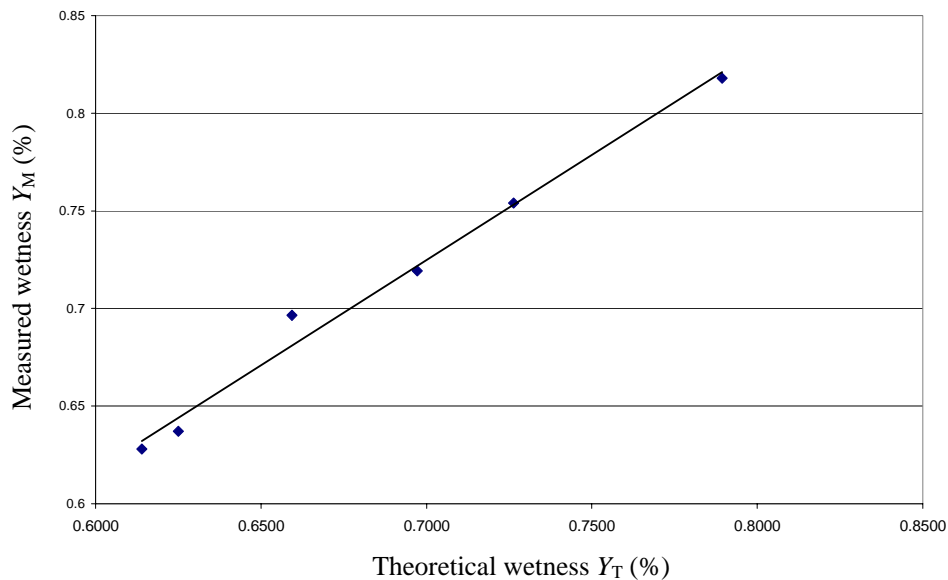


Fig. 7.7 Comparison of the theoretical and measured wetness of the wet steam. The upstream and downstream pressures are 1.03 bar and 0.55 bar, respectively. The turbine inlet temperature at downstream is varied from 127.5°C to 130°C. The length of the measurement zone is 86 mm ($Z=86$ mm). The deviation of the measured wetness from the theoretical one is within [1.6%, 4.5%].

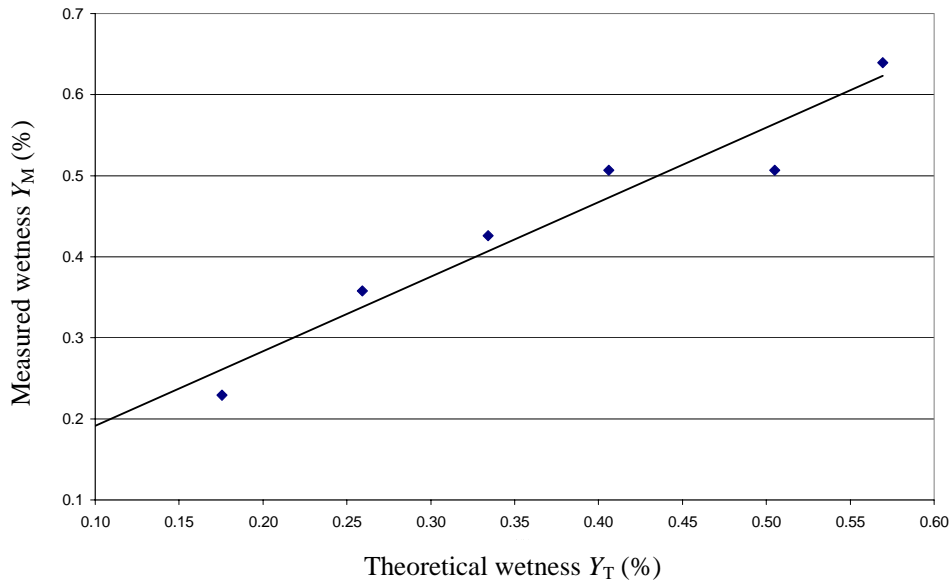


Fig. 7.8 Comparison of the theoretical and measured wetness of the wet steam. The upstream and downstream pressures are 1.28 bar and 0.67 bar, respectively. The turbine inlet temperature at downstream is varied from 135°C to 140°C. The length of the measurement zone is 71 mm ($Z=71$ mm). The deviation of the measured wetness from the theoretical one is within [7%, 90%].

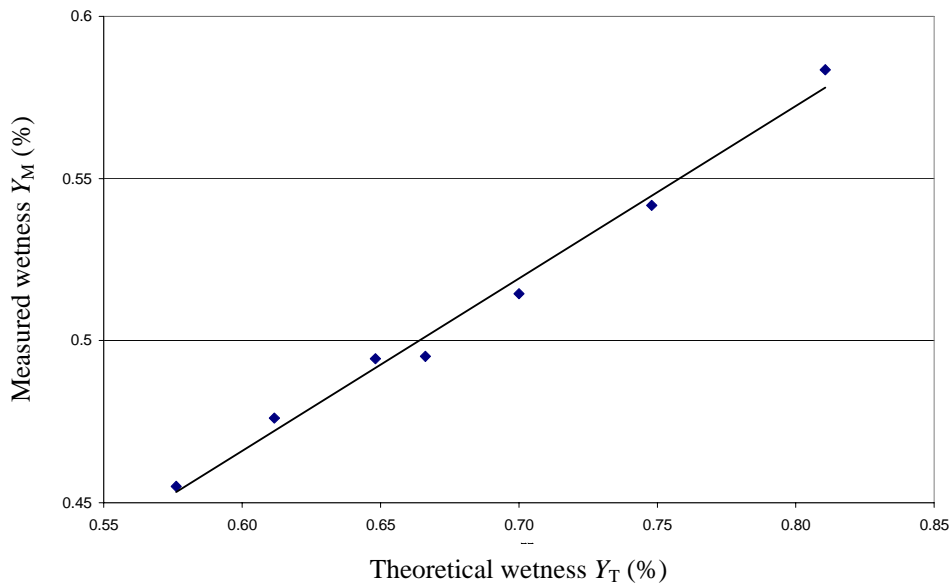


Fig. 7.9 Comparison of the theoretical and measured wetness of the wet steam. The upstream and downstream pressures are 1.28 bar and 0.67 bar, respectively. The turbine inlet temperature at downstream is varied from 130°C to 134°C. The length of the measurement zone is 71 mm ($Z=71$ mm). The deviation of the measured wetness from the theoretical one is within [22%, 28%].

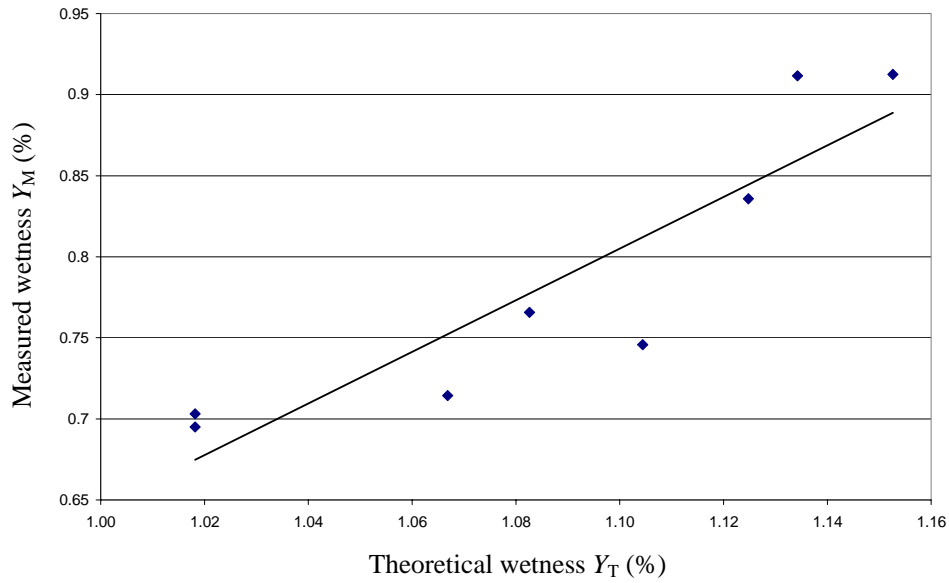


Fig. 7.10 Comparison of the theoretical and measured wetness of the wet steam. The upstream and downstream pressures are 1.28 bar and 0.67 bar, respectively. The turbine inlet temperature at downstream is varied from 126°C to 129°C. The length of the measurement zone is 71 mm ($Z=71$ mm). The deviation of the measured wetness from the theoretical one is within [23%, 33%].

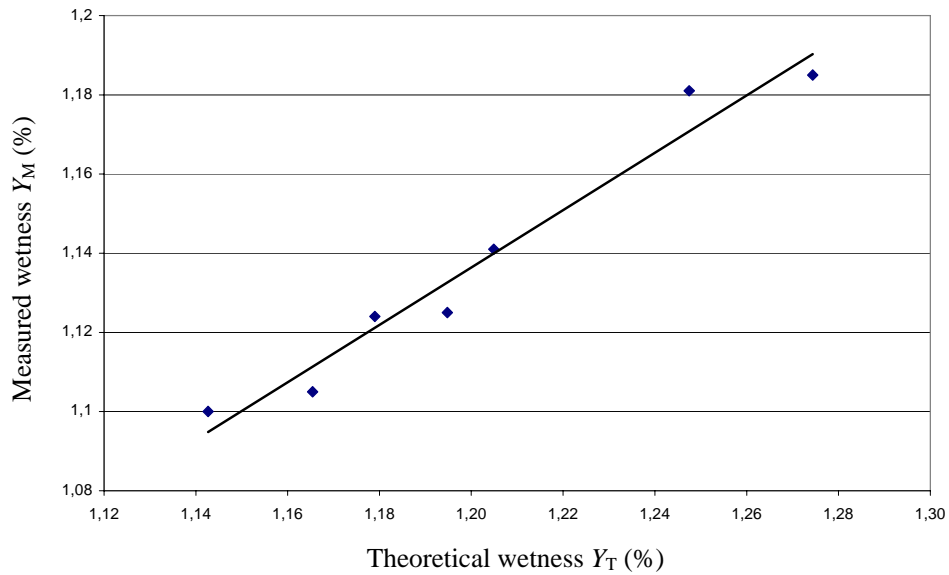


Fig. 7.11 Comparison of the theoretical and measured wetness of the wet steam. The upstream and downstream pressures are 1.03 bar and 0.55 bar, respectively. The turbine inlet temperature at downstream is varied from 127.5°C to 130.5°C. The length of the measurement zone is 86 mm ($Z=86$ mm). The deviation of the measured wetness from the theoretical one is within [4%, 7%].

7.4 Conclusion

The current system can be successfully applied in online wet steam measurement. Temporal evolution of SMD D_{32} and wet steam wetness Y_M is obtained. It provides an effective index for the water erosion diagnosis and the turbine efficiency studies. For the working condition of upstream and downstream pressures are 1.03 bar and 0.55 bar, respectively, the deviation of the measured wetness from the theoretical one is within [1.6%, 4.5%] for $0.6\% < Y_T < 0.8\%$ when the turbine inlet temperature at downstream is varied from 127.5°C to 130°C. However, the deviation increases for other working conditions, which might be caused by the measurement errors of turbine efficiency.

Chapter 8. Particle Sizing in High Concentration

In the preceding chapters, the theoretical and experimental studies on spectral light extinction method (SLEM) have been carried out, including algorithm verification, sensibility test, standard polystyrene particle and wet steam measurement. Nevertheless, we have assumed that the light intensity detected by the receiving fiber is simply the contribution of the transmitted light. In practice, the fiber possesses a finite size, which forms a solid angle to collect the scattered intensities. We might get curious about their contribution to the final detected signals especially when the numerical aperture of the fiber is great and the opening diameter of the diaphragm (D_3) is larger than that of the detector (D_2), since in this case there exists a large edge zone characterized by $D_2/2 \leq D \leq D_3/2$ (see Fig. 8.1) and the scattered intensities by more particles are collected by the detector. Moreover, in the situation of high concentration multiple scattering happens, which must be considered carefully in experiments. In this chapter, the influences of all these factors on the extinction spectrum are studied by numerical simulation based on Monte Carlo method.

8.1 Monte Carlo method

The central idea of the Monte Carlo method is the simulation of the light scattering phenomenon by using density probabilities. We assume a light beam incident on the particle system containing N particles, whose optical thickness $\xi = NQ_{\text{ext}}Z$, where Q_{ext} is the extinction efficiency factor of a single spherical particle of diameter d . In Monte Carlo method, the light is discretized into a number of “photons”, which are scattered or absorbed when interacting with the particles. The path length of a photon between two successive interactions, denoted by l , can be described by a random number q_1 ranging in $[0, 1]$ through the following equation:

$$l = -\ln q_1 / Q_{\text{ext}}. \quad (8-1)$$

To decide whether the photon is absorbed by the particle during the interaction, another random number q_2 is introduced and compared to the albedo factor a defined by the ratio of the scattering efficiency and the extinction efficiency as follows:

$$a = Q_{\text{sca}} / Q_{\text{ext}}. \quad (8-2)$$

For $q_2 \geq a$, the photon is absorbed, otherwise it is scattered. The new direction of a scattered photon can be determined by the phase function, which accounts for the probability of scattering in a given direction characterized by the scattering angle θ . In the present study, the following Henyey-Greenstein phase function P_{HG} , which is discussed by van de Hulst (1957) is employed to take such a role:

$$P_{\text{HG}}(\cos \theta) = \frac{a(1-g^2)}{(1+g^2-2g \cos \theta)^{3/2}}, \quad (8-3)$$

where the asymmetry parameter g is defined as the cosine-weighted average of the phase function. For a spherical particle of dimensionless size parameter a and Mie coefficients a_n and b_n , the analytical expression of asymmetry parameter g can be calculated by

$$g = \frac{4}{\alpha^2 Q_{\text{sca}}} \sum_{n=1}^{\infty} \left[\frac{n(n+2)}{n+1} \text{Re}(a_n a_{n+1}^* + b_n b_{n+1}^*) + \frac{2n+1}{n(n+1)} \text{Re}(a_n + b_n) \right]. \quad (8-4)$$

On the basis of these basic parameters, two-dimension and three-dimension Monte Carlo method for particle sizing simulation by using light extinction method has been developed by Briton et al. (1992), Brusaglioni et al. (1987), Su et al. (2004), etc. When enough photons are adopted, the results agree well with the experimental results of the extinction method (Brusaglioni et al., 1987). The code employed for our simulation is developed by Briton et al. (1992) and Su et al. (2004). For the realistic measurement system of SLEM schemed in Fig. 8.1, the surviving photons escaping from the measurement zone at a certain angle after experiencing numerous interactions with the particles are counted. Their acceptance by the detector depends on the geometry of the detecting system, including the distance from the diaphragm to the detecting fiber L , the length of measurement zone Z , the diameter of detector D_2 , etc. Together with the diameter of the incident beam D_1 , these parameters determine the scattering behavior of the particles suspending or passing through the measurement zone.

8.2 Numerical studies

8.2.1 Evaluation of multiple scattering

The measurement system in current studies is shown in Fig. 8.1. In such a system, a

collimated beam of diameter D_1 traverses the measurement zone of length Z , in which are suspended the particles to be measured. L is the distance from the detecting fiber to the right side of the measurement zone. D_3 is the opening diameter of the diaphragm. Without loss of generality for all kinds of detectors, the numerical aperture of the detecting fiber in simulation is assumed to be 1.0 so that all the light intensities reaching the fiber can be detected.

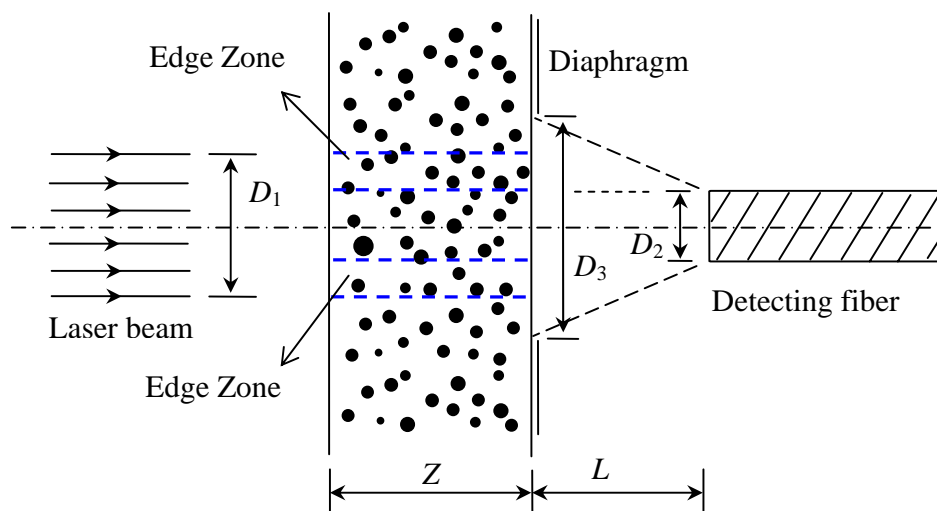


Fig. 8.1 Schematic diagram of the measurement system for Monte Carlo simulation.

8.2.2 Influence of scattering from particles in edge zone

The Monte Carlo method has the advantage of being able to simulate the realistic measurement situation. Our numerical simulation is based on the system described in the preceding subsection. The beam is collimated to the diameter of ~ 8 mm ($D_1=8$ mm). The receiving fiber has the diameter of 0.4 mm ($D_2=0.4$ mm). Since in practical wet steam measurement, the diaphragm is removed for the convenience of optical system construction and optical alignment, its opening diameter can be looked on as infinite ($D_3 \rightarrow \infty$) for numerical simulation in this case. On the basis of these parameters, we aim to find out an optimized distance from the measurement zone to the fiber, L , which makes the influence of intensities scattered by the particles in the edge zones negligible.

Since the diameter of the transmitted light bundle D_1 ($D_1=8$ mm) is larger than that of the detecting fiber D_2 ($D_2=0.4$ mm), theoretically there exists a part of scattered intensities received

by the detecting fiber, especially when $D_3 \gg D_2$, as indicated by Fig. 8.2. To evaluate their influence on the extinction spectrum, numerical simulations are firstly made for single scattering regime, which is characterized by the optical thickness less than 1.0 ($\xi < 1.0$). The number of photons used for simulation is 4,000,000. And 23 equidistant wavelengths within the wavelength range $[0.40, 0.95] \mu\text{m}$ are used for the extinction spectrum calculation ($N_w = 23$), with the step length being $0.25 \mu\text{m}$ ($\Delta\lambda = 0.25 \mu\text{m}$).

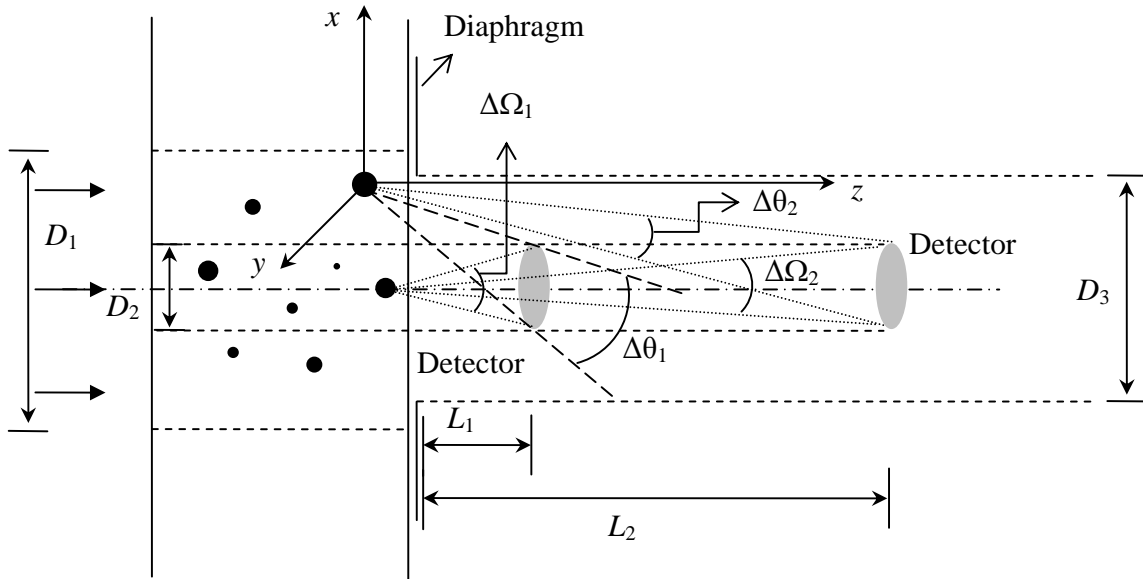


Fig. 8.2 Scattered intensities detected by the fiber.

Some basic conceptions should be clarified before numerical simulation. In Monte Carlo method, the transmitted intensities detected by the fiber are composed of parts: the directly transmitted intensities ($I_{\text{trans.}}$) which are not affected by the multiple scattering and the diffracted intensities ($\Delta I_{\text{diff.}}$) which are affected by the multiple scattering, namely:

$$I = I_{\text{trans.}} + \Delta I_{\text{diff.}} \quad (8-5)$$

Divided by the incidence intensities I_0 , the extinction ratio E_M in Monte Carlo model can be written in the following form:

$$E_M = \ln\left(\frac{I}{I_0}\right) = \ln\left(\frac{I_{\text{trans.}} + \Delta I_{\text{diff.}}}{I_0}\right) \quad (8-6)$$

However, the ideal extinction ratio is defined on the assumption that all the scattered intensities are excluded, namely $\Delta I_{\text{diff.}} \rightarrow 0$. Therefore in such an ideal model, the extinction ratio is defined by the ratio of the purely transmitted intensities $I_{\text{trans.}}$ and the incidence intensities I_0 , namely

$$E_1 = \ln \left(\frac{I}{I_0} \right) = \ln \left(\frac{I_{\text{trans.}}}{I_0} \right). \quad (8-7)$$

Moreover, the contribution of the scattered intensities by the particles in the edge zone, which is characterized by $D_2/2 \leq D \leq D_3/2$, is neglected by the ideal model. This part, however, can be considered by the Monte Carlo simulation.

To characterize the deviation of extinction spectra calculated by the ideal model and the Monte Carlo model, the mean absolute deviation ($\delta_{a, \text{mean}}$) of the extinction spectrum is defined as follows:

$$\delta_{a, \text{mean}} = \frac{\sum_{j=1}^{N_w} |E_{1,j} - E_{M,j}| / E_{M,j}}{N_w}, \quad (8-8)$$

where N_w is the number of the wavelengths used in simulation.

On the basis of these conceptions, we firstly simulate the case of polystyrene particles measurement. The numerical calculation is made for the measurement zone of the lengths $Z=10$, 40, and 70 mm respectively, corresponding to the number concentrations (C_n) of the particles being $3.08\text{E}+13$, $7.70\text{E}+12$, and $4.40\text{E}+12/\text{m}^3$, respectively. For the monodisperse particles of diameter $D=1.0 \mu\text{m}$, the optical thicknesses ξ calculated by

$$\xi = \frac{\pi}{4} (C_n Z) D^2 Q_{\text{ext}} \quad (8-9)$$

are same for all these three cases. For each length of the measurement zone, calculations are made for the distances from near to the measurement zone to far from it: $L=5$, 10, 25, 100, and 500 mm, respectively. As illustrated in Fig. 8.3-Fig. 8.5, the numerical results are compared to the extinction spectra obtained by the ideal model through direct superposition of the extinction ratios of all the single particles (namely “direct calculation”, which is discussed in Chapter 5).

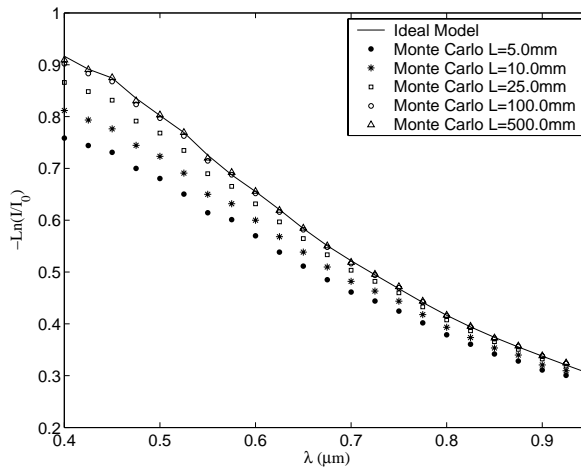


Fig. 8.3 Extinction spectra of the polystyrene particles of the diameter $D=1.0\ \mu\text{m}$ and the number concentration $C_n=3.08\text{E}+13/\text{m}^3$, and suspended in water. The length of the measurement zone is 10 mm ($Z=10\ \text{mm}$).

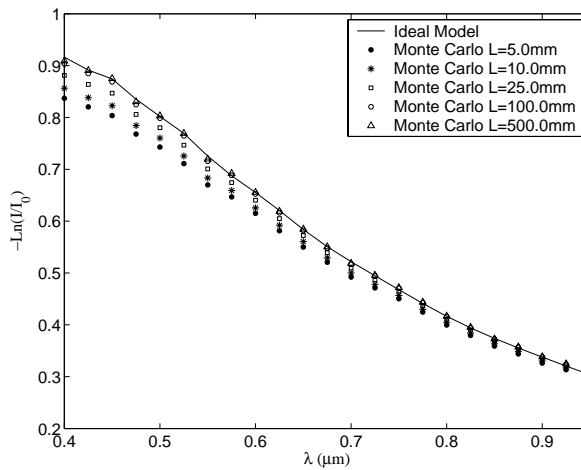


Fig. 8.4 Extinction spectra of the polystyrene particles of the diameter $D=1.0\ \mu\text{m}$ and the number concentration $C_n=7.70\text{E}+13/\text{m}^3$, and suspended in water. The length of the measurement zone is 40 mm ($Z=40\ \text{mm}$).

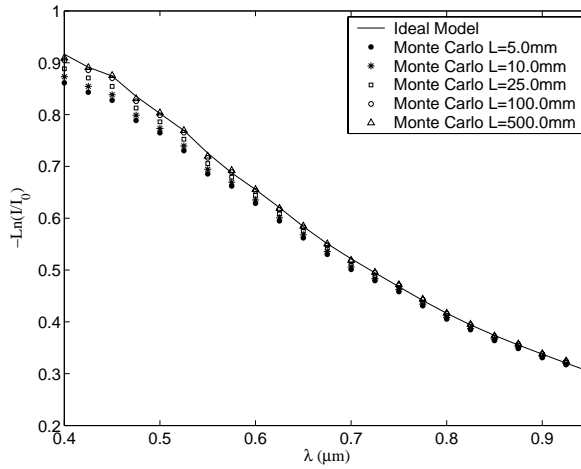


Fig. 8.5 Extinction spectra of the polystyrene particles of the diameter $D=1.0 \mu\text{m}$ and the number concentration $C_n=4.40\text{E}+12/\text{m}^3$, and suspended in water. The length of the measurement zone is 70 mm ($Z=70 \text{ mm}$).

Table 8.1 The mean absolute deviations ($\delta_{a, \text{mean}}$) for the polystyrene particles of the diameter $D=1.0 \mu\text{m}$.

Particle Type	D_3 (mm)	L (mm)	Z (mm)	$\delta_{a, \text{mean}}$ (%)
Polystyrene Particles	∞	25	40	2.03
Polystyrene particles	∞	100	40	0.56
Polystyrene particles	∞	150	40	0.46

From these figures, we find that the more a detecting fiber is away from the measurement zone, the more the detected extinction ratios $\ln(I/I_0)$ approach the ideal values $\ln(I_{\text{trans.}}/I_0)$. With the increase of distance from the measurement zone to the detecting fiber, the solid angle gradually decreases so that the scattered intensities become weaker till negligible ($\Delta I_{\text{diff.}} \rightarrow 0$).

A more straightforward proof is the mean absolute deviations ($\delta_{a, \text{mean}}$) of the extinction spectrum calculated for the distances $L=25, 100, \text{ and } 150 \text{ mm}$. The results illustrated in Table 8.1 indicate that for $Z=40 \text{ mm}$, $\delta_{a, \text{mean}}$ decreases from 2.03% to 0.46% when L increases from 25 mm to 150 mm.

In addition, through the comparison of the extinction spectra of the same distance L in Fig. 8.3- Fig. 8.5, we find that increasing the length of the measurement zone Z also reduces the influence of the scattered intensities. This is because for the same number of the particles (Same optical

thickness), the mean distance of the particles suspending in a measurement zone of long length (e.g., $C_n=4.40E+12/m^3$ and $Z=70$ mm) is longer than that of the same particles in a measurement zone of short length (e.g., $C_n=3.08E+13/m^3$, $Z=10$ mm), which generally brings in smaller solid angles for the detector to receive the scattered intensities.

Another observed phenomenon is that the deviation of the extinction ratio predicted by the ideal model from the Monte Carlo method that predicted by is larger at the smaller wavelength, which means the influence of scattered intensities on the extinction ratio corresponding to the smaller wavelength is more remarkable. This is due to the fact that smaller wavelength brings in larger size parameter so that the diffracted intensities contained in ΔI_{diff} are stronger in the near forward direction of the particle. According to Eqs.(8-6) and (8-7), such a deviation can be evaluated by ΔE as follows:

$$\Delta E = \ln\left(\frac{I_{trans.} + \Delta I_{diff.}}{I_0}\right) - \ln\left(\frac{I_{trans.}}{I_0}\right) = \ln\left(1 + \frac{\Delta I_{diff.}}{I_{trans.}}\right). \quad (8-10)$$

For large particles the absolute diffracted intensities contained in ΔI_{diff} are larger than those for the small ones and the transmitted intensities $I_{trans.}$ are smaller than those for the small ones. Therefore the deviation ΔE becomes larger.

Next, we simulate the case of water droplets (contained in wet steam). For the given lengths of measurement zone $Z=10, 40,$ and 70 mm, the number concentrations of water droplets of the diameter $D=1.0 \mu m$ and the refractive index $\hat{m}=1.333$ are set as $C_n=3.0E+13, 7.5E+12,$ and $4.3E+12/m^3$, respectively, so that the total number of the particles and the optical thickness is constant. For each length of the measurement zone, the calculations are made for the distances $L=5, 10, 25, 100,$ and 500 mm, respectively. As indicated by Fig. 8.6-Fig. 8.8, similar phenomena as that for the case of polystyrene particles can be found: when the distance from measurement zone to the detector or the length of the measurement zone increases, the influence of the scattered intensities on the extinction spectrum decreases and the scattered intensities by the particles in the edge zone have more obvious influence on the extinction ratio which corresponds to the smaller wavelength.

It is noteworthy that, for the measurement zone of length $Z=70$ mm, which is the

situation of realistic wet steam measurements, the influence of multiple scattering on the extinction is very little when the detecting fiber is 100 mm away from right side of the measurement zone ($L=100$ mm). As indicated by Table 8.2, the mean deviation $\delta_{a, \text{mean}}$ is less than 0.5% for the droplets of the diameter $D=1.0$ μm . Such a level can also be achieved in realistic polystyrene particle measurements by using the distance $L=150$ mm for the measurement zone of length 40 mm, as indicated in Table 8.1. According to our numerical simulation described in Chapter 5, such a deviation level brings in little influences on the inversed results.

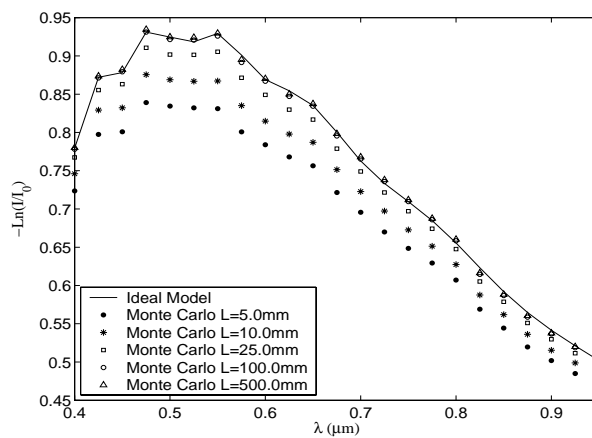


Fig. 8.6 Extinction spectra of the water droplets of the diameter $D=1.0$ μm and the number concentration $C_n=3.0E+13/\text{m}^3$. The length of the measurement zone is 10 mm ($Z=10$ mm).

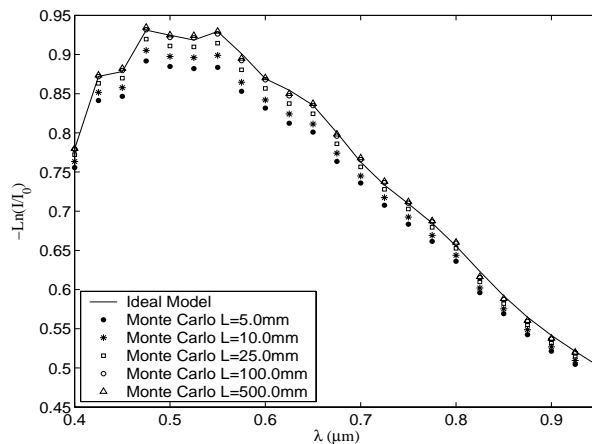


Fig. 8.7 Extinction spectra of the water droplets of the diameter $D=1.0$ μm and the number concentration $C_n=7.5E+12/\text{m}^3$. The length of the measurement zone is 40 mm ($Z=40$ mm).

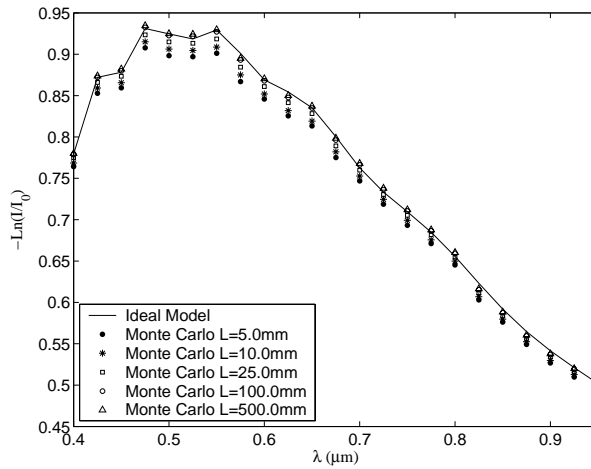


Fig. 8.8 Extinction spectra of the water droplets of the diameter $D=1.0 \mu\text{m}$ and the number concentration $C_n=4.3\text{E}+12/\text{m}^3$. The length of the measurement zone is 70 mm ($Z=70$ mm).

Table 8.2 The mean absolute deviations ($\delta_{a, \text{mean}}$) for water droplet of the diameter $D=1.0 \mu\text{m}$.

Water droplets	D_3 (mm)	L (mm)	Z (mm)	$\delta_{a, \text{mean}}$ (%)
Water droplets	∞	25	70	0.94
Water droplets	∞	50	70	0.60
Water droplets	∞	100	70	0.45

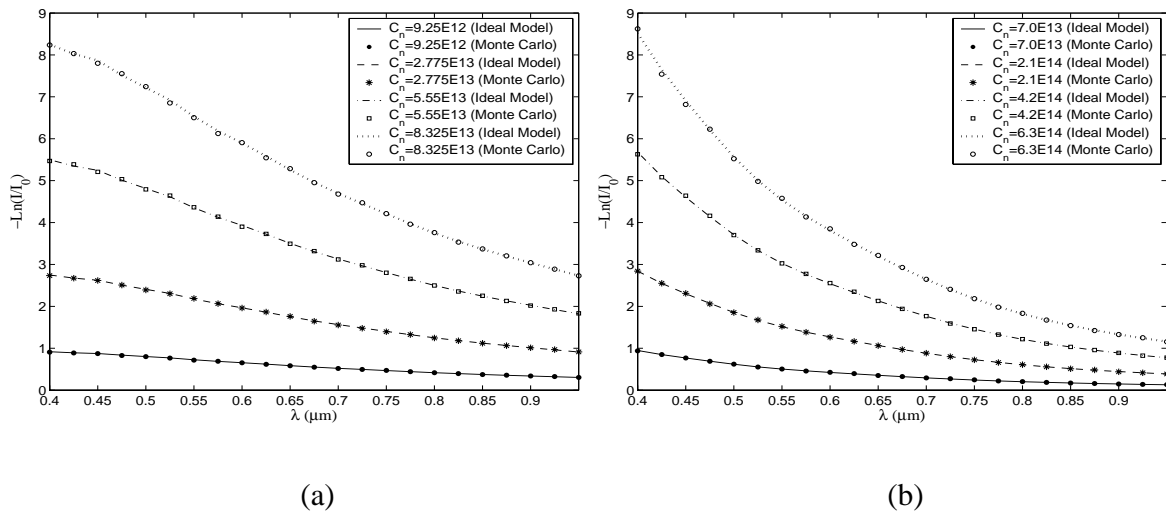
Persuaded by numerous simulations made for the particles of other diameters within $[0.1, 5.0] \mu\text{m}$, we recommend that for the current SLEM system the optimum distance L should be larger than 150 mm and 100 mm, respectively, for the lengths of measurement zone being 40 mm and 70 mm, which are adopted in realistic polystyrene particle and wet steam measurement, respectively (diaphragm is not used). Such a distance ensures the mean deviation of the spectra obtained by the ideal model (direct calculation used) from the realistic model (Monte Carlo method used) less than 0.5%, which leads to a negligible influence on the inversed results. In other words, the influence of scattering from particles in the edge zone can be neglected at these optimum distances.

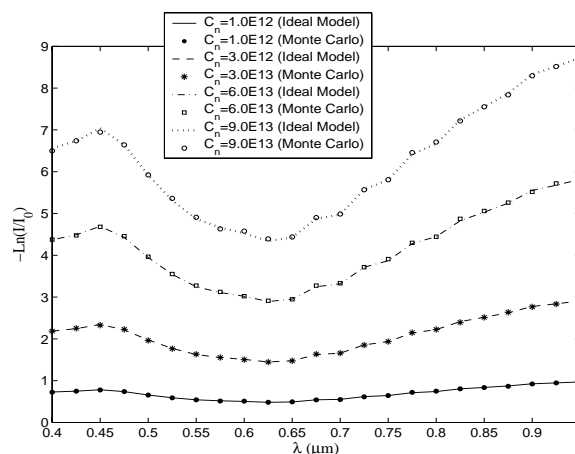
8.2.3 Influence of multiple scattering

We have demonstrated that for the current measurement system the scattered intensities from

the particles at the edge zone have little influences on the extinction spectra once the distance from the measurement zone to the detector is large enough. However, only single scattering regime is concerned in the preceding subsection. In this subsection, we further explore the influence of multiple scattering on the extinction spectrum. The proposed distances $L=150$ mm and 100 mm are used for the realistic polystyrene particles measurement system ($Z=40$ mm) and the wet steam measurement system ($Z=70$ mm). Through increasing the number concentration C_n , the influence of multiple scattering on the extinction spectrum is evaluated.

In numerical simulations, the diameters of the polystyrene particles are assumed to be 0.5 μm , 1.0 μm , and 3.0 μm respectively. As indicated by the numerical results illustrated in Fig. 8.9, when the maximum optical thickness of the polystyrene particles increases from less than 1.0 ($\xi_{\text{max}} < 1.0$) to larger than 8.0 ($\xi_{\text{max}} > 8.0$), excellent agreements are found between the extinction spectrum calculated from the ideal model and those predicted by Monte Carlo method. As listed in Table 8.3, the mean absolute deviation of spectrum of the ideal model keeps being less than 0.8% for all the number concentrations and diameters. Such a deviation level is found for all the polystyrene particles of the diameters within $[0.1, 5.0]$ μm . It is found to bring in little influence on the inversed results and hence negligible.





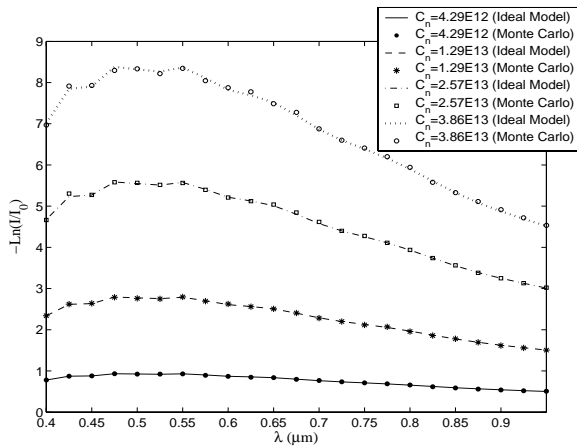
(c)

Fig. 8.9 Extinction spectrum of the polystyrene particles suspended in water. The distance from the measurement zone to the detector L is 150 mm. The length of measurement zone is $Z=40$ mm, which is the realistic situation of the standard particle measurement. (a) $D=1.0$ μm and C_n increases from $7.70\text{E}+12$ to $6.93\text{E}+13/\text{m}^3$; (b) $D=0.5$ μm and C_n increases from $7.00\text{E}+13$ to $2.25\text{E}+14/\text{m}^3$; c) $D=3.0$ μm and C_n increases from $1.00\text{E}+12$ to $9.00\text{E}+12/\text{m}^3$.

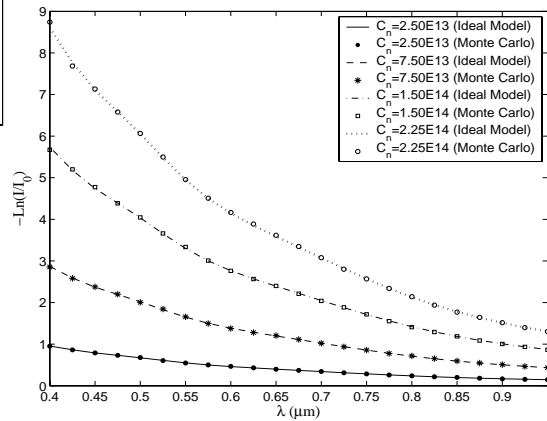
Table 8.3 Mean absolute deviation of spectrum of the ideal model for polystyrene particle measurement in the situation of high concentration ($Z=40$ mm and $L=150$ mm)

D (μm)	C_n	$\delta_{a, \text{mean}}$ (%)
0.5	$7.00\text{E}+13$	0.78
0.5	$2.10\text{E}+14$	0.39
0.5	$4.20\text{E}+14$	0.33
0.5	$6.30\text{E}+14$	0.54
1.0	$9.25\text{E}+12$	0.46
1.0	$2.78\text{E}+13$	0.35
1.0	$5.55\text{E}+13$	0.39
1.0	$8.33\text{E}+13$	0.37
3.0	$1.00\text{E}+12$	0.58
3.0	$3.00\text{E}+12$	0.31
3.0	$6.00\text{E}+12$	0.46
3.0	$9.00\text{E}+12$	0.48

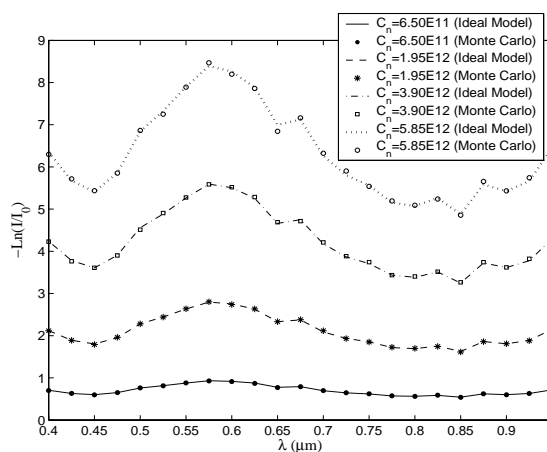
Similar studies have also been done for the water droplets of diameters $D=0.5, 1.0,$ and $3.0 \mu\text{m}$, respectively. As indicated by Fig. 8.10, the results of the ideal model also agree well with those predicted by Monte Carlo method for all concentrations corresponding to $0 < \xi < 9.0$. And we find from Table 8.4 that the mean absolute deviations of spectra obtained by ideal from those obtained by Monte Carlo method are less than 0.8% for all droplet sizes. And such a level of deviation has been found to have little influence on the inversed results. Such a conclusion is also supported by the numerous calculations performed for droplets of other diameters within $[0.1, 5.0] \mu\text{m}$. Therefore for the current optical configuration for wet steam measurement, influence of multiple scattering can be neglected. We comment that the negligible influence of multiple scattering is mainly due to the sufficiently small solid angle ensured by both small cross section of the detecting fiber ($\pi r^2 \approx 0.5 \text{ mm}^2$) and long distance from measurement zone to the detector.



(a)



(b)



(c)

Fig. 8.10 Extinction spectra of droplets with increasing number concentration. The distance from the measurement zone to the detector L is 100 mm. The length of measurement zone is $Z=70$ mm, which is the realistic situation of online wet steam measurement. (a) $D=1.0$ μm and C_n increases from $4.29\text{E}+12$ to $3.86\text{E}+13/\text{m}^3$; (b) $D=0.5$ μm and C_n increases from $2.50\text{E}+13$ to $2.25\text{E}+14/\text{m}^3$; c) $D=3.0$ μm and C_n increases from $6.50\text{E}+11$ to $5.85\text{E}+12/\text{m}^3$.

Table 8.4 Mean absolute deviation of spectrum of the ideal model for wet steam measurement in the situation of high concentration ($Z=70$ mm and $L=100$ mm).

D (μm)	C_n	$\delta_{a, \text{mean}}$ (%)
0.5	$2.50\text{E}+13$	0.64
0.5	$7.50\text{E}+13$	0.41
0.5	$1.50\text{E}+14$	0.40
0.5	$2.25\text{E}+14$	0.42
1.0	$4.29\text{E}+12$	0.45
1.0	$1.29\text{E}+13$	0.30
1.0	$2.57\text{E}+13$	0.29
1.0	$3.86\text{E}+13$	0.54
3.0	$6.50\text{E}+11$	0.44
3.0	$1.95\text{E}+12$	0.32
3.0	$3.90\text{E}+12$	0.43
3.0	$5.85\text{E}+12$	0.76

8.3 Experimental Studies

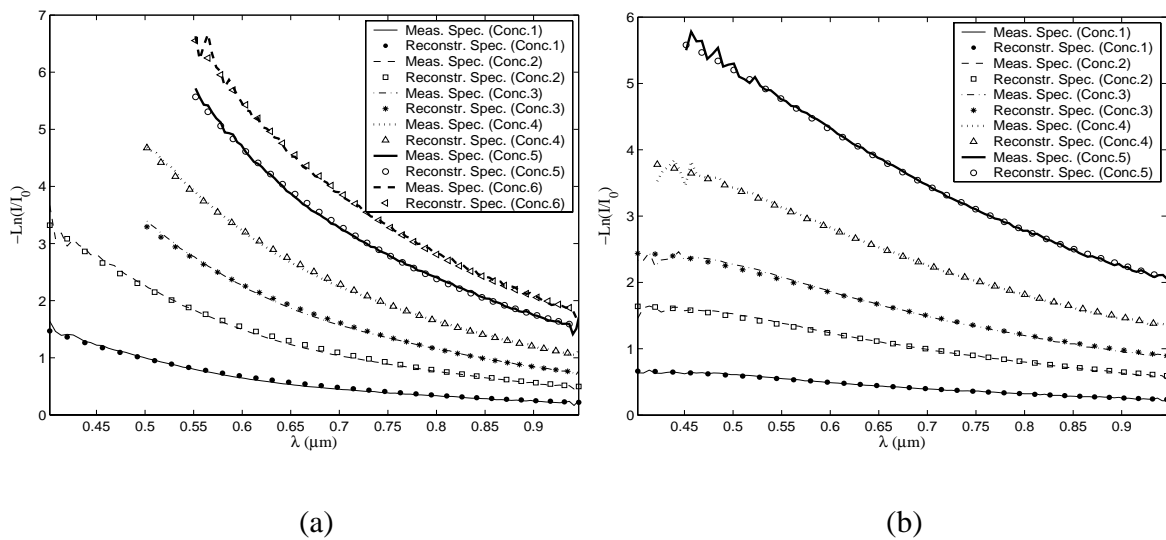
The experimental studies of particle sizing in the situation of high concentration is conducted in the present subsection to verify the conclusion obtained in the preceding subsection by numerical simulation stating that multiple scattering in the situation of high concentration can be neglected for the current optical configuration of the SLEM system. HL 2000 is used as the light source. The parameters used for data acquisition and inversion are listed in Table. 7.1 of Chapter 7.

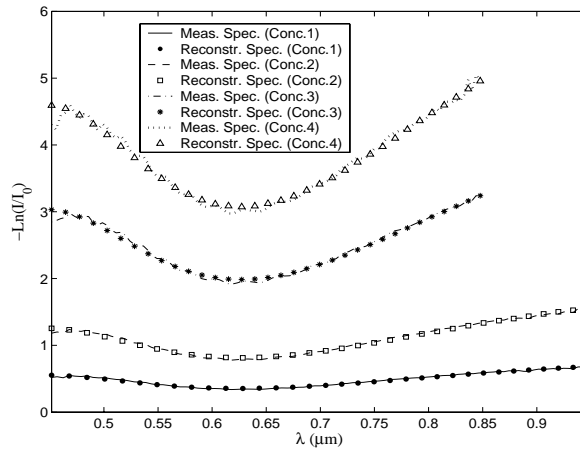
8.3.1 Polystyrene particles

Measurements are carried out for the polystyrene particles of diameters 0.5, 1.0, and 3.0 μm , respectively. For each concentration, a series of 100 continuous spectra are measured for averaging. The measurement zone has the length $Z=40$ mm. The detector is fixed 100 mm away from the measurement zone ($L=150$ mm). The measured and reconstructed spectra are illustrated in Fig. 8.11. We find that the mean optical thickness increases from $\bar{\xi}(\lambda) < 1.0$ (single scattering regime) to $\bar{\xi}(\lambda)_{\text{max}} \sim 4.0$ (multiple scattering regime), which corresponds to a mean transmission ratio \bar{T} being ~ 0.02 . Further increasing the number concentration C_n leads the transmitted intensities to be subjected more to the noises so that local oscillations of spectrum take place at the edge regions of the wavelength range. This is because for a halogen light source, the original intensities at the edge regions of the wavelength range are not as strong as those within the central zone. Moreover, for particles of the same diameter D less than 1.0 μm ($D \leq 1.0 \mu\text{m}$), light extinction at small wavelengths, which corresponding to relatively large size parameters, is more remarkable than that at large wavelengths. Therefore the transmitted intensities become even less so that they are more susceptible to be eroded by the noises. Considering all these effects, we use the spectra without drastic oscillation for inversion (see Fig. 8.11) and the inversed PSD are demonstrated in Fig. 8.12. The inversed results of SMDs D_{32} and volume concentrations C_v are illustrated in Fig. 8.13 and Fig. 8.14, respectively. For the polystyrene particles of diameter $D=0.5 \mu\text{m}$, very little differences among the inversed PSD curves can be recognized for different particle concentrations. For the polystyrene particle of the diameter $D=1.0 \mu\text{m}$, when compared to the solid PSD curve corresponding to the single

scattering regime the PSD curves corresponding to the multiple scattering regime have very slight leftward or rightward floating. As to the polystyrene particles of the diameter $D=3.0\ \mu\text{m}$, a spilt PSD appears at the vicinity of $D=2.4\ \mu\text{m}$ for concentration series 3 and 4. This might be caused by the lack of the extinction information at the near infrared region of wavelength $\lambda > 0.85\ \mu\text{m}$. However, the inversed SMDs D_{32} for these concentrations are nearly same, as indicated by Fig. 8.13 and Table 8.5. And the inversed volume concentrations show an incremental tendency (see Fig. 8.14 and Table 8.6), as it should be.

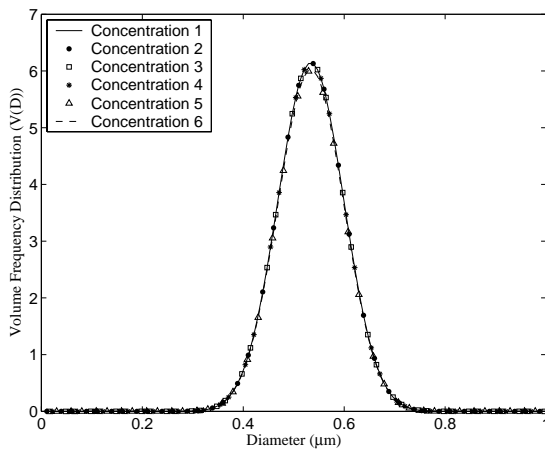
Through these measurements of polystyrene particles in the situation of high concentration, we have proved that for the current measurement system of SLEM, multiple scattering does not have little influence on the inversed results. Such a validation ensures the applicability of SLEM in wet steam measurement of high concentration, which is to be exemplified in the next subsection.



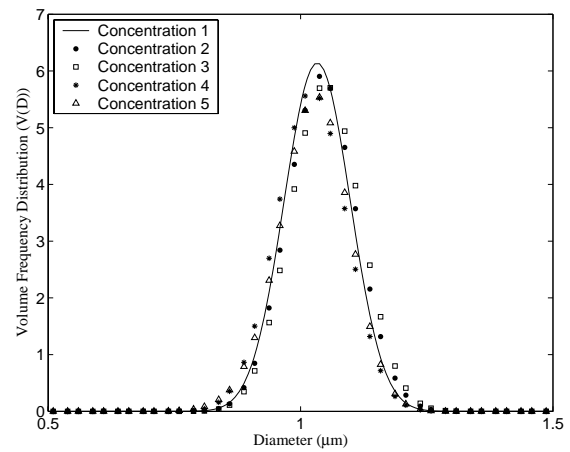


(c)

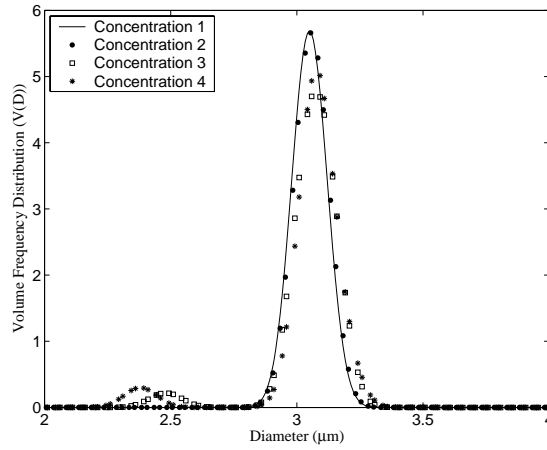
Fig. 8.11 Measured and reconstructed spectra of the standard polystyrene particles of the diameters: (a) $D=0.5 \mu\text{m}$; (b) $D=1.0 \mu\text{m}$; (c) $D=3.0 \mu\text{m}$.



(a)



(b)



(c)

Fig. 8.12 Inversed PSD for the standard polystyrene particles of the diameters: (a) $D=0.5 \mu\text{m}$; (b) $D=1.0 \mu\text{m}$; (c) $D=3.0 \mu\text{m}$.

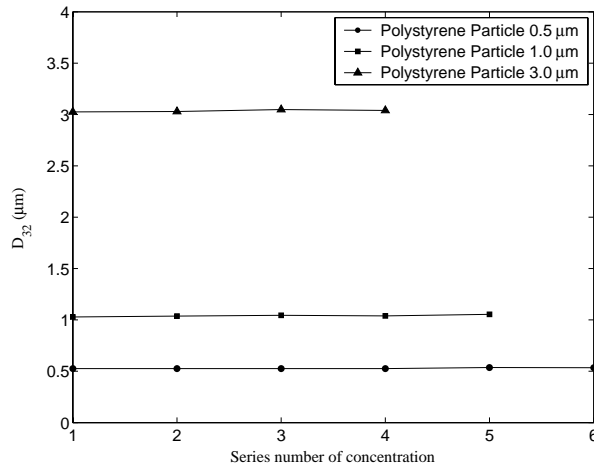


Fig. 8.13 Inversed SMDs (D_{32}) for the standard polystyrene particles of the diameters: (a) $D=0.5 \mu\text{m}$; (b) $D=1.0 \mu\text{m}$; (c) $D=3.0 \mu\text{m}$.

Table 8.5 Inversed Sauter mean diameters D_{32} at different concentrations (corresponding to Fig. 8.13).

D given (μm)	D_{32} inversed (μm)					
	Conc. 1	Conc. 2	Conc. 3	Conc. 4	Conc. 5	Conc. 6
0.5	0.526	0.526	0.526	0.526	0.536	0.535
1.0	1.029	1.037	1.045	1.039	1.055	—
3.0	3.026	3.029	3.048	3.040	—	—

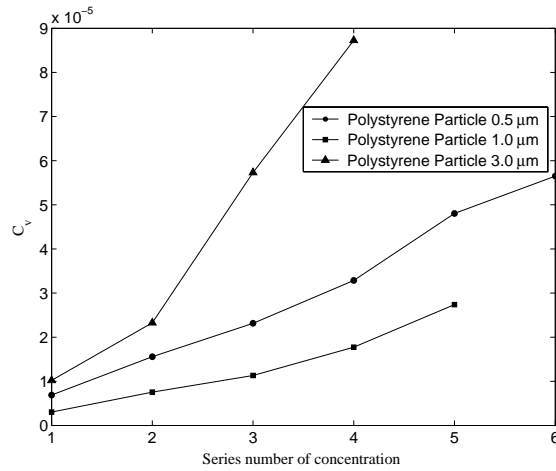


Fig. 8.14 Inversed volume concentrations (C_v) for the standard polystyrene particles of the diameters: (a) $D=0.5 \mu\text{m}$; (b) $D=1.0 \mu\text{m}$; (c) $D=3.0 \mu\text{m}$.

Table 8.6 Inversed volume concentrations C_v (corresponding to Fig. 8.14).

D given (μm)	C_v inversed (E-6)					
	Conc. 1	Conc. 2	Conc. 3	Conc. 4	Conc. 5	Conc. 6
0.5	6.8906	15.588	23.147	32.857	48.056	56.508
1.0	3.0266	7.557	11.323	17.740	27.388	—
3.0	10.209	23.271	57.314	87.270	—	—

8.3.2 Wet steam

In wet steam measurement, we might also meet the situation of high concentration. Numerical simulations by using the Monte Carlo method has indicated that for the current measurement system, multiple scattering happening for the optical thickness $1 < \xi < 10$ has little influence on the extinction spectrum when the detecting fiber locates more than 100 mm away from the measurement zone of length $Z=70$ mm. Such a conclusion is confirmed by the experimental studies performed in the preceding part for polystyrene particles. Thus in this subsection, we give some results of wet steam measurement in the situation of high concentration. The optical measurement system and the turbine system have been introduced in Chapter 7. In the measurement, the distance from the measurement zone to the detecting fiber is about 120 mm.

Fig. 8.15 presents an extinction spectrum averaged from a series of 100 continuously acquired

spectra within 10s for a certain working condition of pressure and temperature. The maximum optical thickness ($\xi_{\max} \sim 4.0$) is found locating at the wavelength $\lambda = 0.55 \mu\text{m}$, which corresponds to the multiple scattering regime with the transmission ratio (T) being ~ 0.02 . Corresponding to such a spectrum, Fig. 8.16 and Fig. 8.17 are the results of temporal evolutions of SMD D_{32} and the measured wetness Y_M , respectively. The mean values of D_{32} and wetness are $0.63 \mu\text{m}$ and 2.69% , respectively, around which slight fluctuations of the temporal results of D_{32} (Fig. 8.16) and Y_M (Fig. 8.17) are found. The maximum deviations of the fluctuations from the mean values are 2.72% and 3.89% for D_{32} and Y_M , respectively. This indicates that the flow is steady at the current working condition.

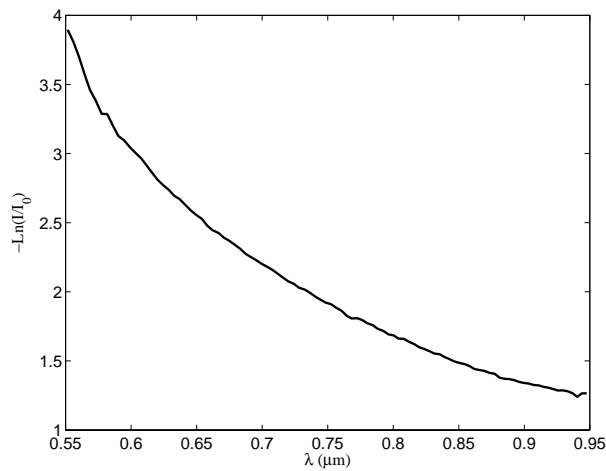


Fig. 8.15 Extinction spectrum averaged from a series of 100 continuously acquired spectra.

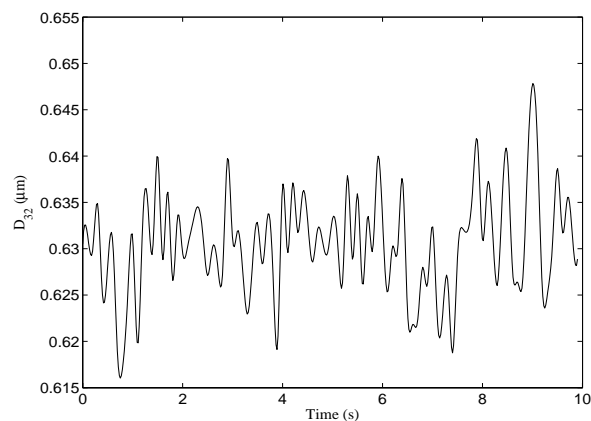


Fig. 8.16 Temporal evolution of Sauter mean diameter D_{32} measured at a certain pressure and temperature.

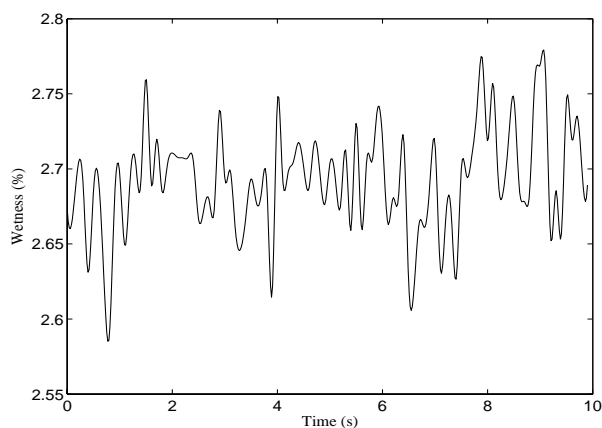


Fig. 8.17 Temporal evolution of measured wetness Y_M measured at a certain pressure and temperature.

8.4 Conclusion

By using Monte Carlo method, we evaluate the influence of the scattered intensities by the particles in the edge zone and the influence of the multiple scattering on the extinction spectrum obtained by the current SLEM system. It is found that for the polystyrene particle measurement by using the sampling cell of length $Z=40$ mm, the edge zone effect can be neglected once the detecting fiber located more than 150 mm away. And for the wet steam measurement of measurement zone $Z=70$ mm, the edge zone effect can be neglected once the detecting fiber is located more than 100 mm away. At these distances, the multiple scattering has little influences on the extinction spectrum for the optical thickness $1.0 \leq \xi \leq 10.0$, which are proved by the experiments.

Chapter 9. Conclusions and Perspectives

The present thesis is contributed to the development of the generalized Lorenz-Mie theory (GLMT) and the geometrical optics (GO) to describe the laser beam scattering by a homogeneous spheroid and the application of the spectral light extinction method in wet steam measurement. In this chapter we draw some conclusions from the work presented in the thesis and give a perspective on further studies.

9.1 Theory

On the basis of the GLMT for a sphere and plane wave scattering theory for a spheroid, which are proposed by Gouesbet and his colleagues since 1980's and Asano and Yamamoto in 1970's, respectively, arbitrary shaped beam scattering by a homogeneous spheroid is studied in this thesis. The beam is first expanded in the spheroidal coordinates so that the spheroidal beam shape coefficients ($G_{n,TE}^m, G_{n,TM}^m$) are obtained. In such a process, the classical localization principle is found inapplicable when the Cartesian coordinates of the particle and the beam are not parallel to each other. Instead, the integral method is employed. Next, the variable separation method is applied and the equations are established from the boundary conditions. Through solving these equations, the unknown coefficients multiplied with the spheroidal vector wave functions describing the scattered and internal fields are determined. Analytical expressions of the far-field scattering amplitudes, the scattering and extinction coefficients, and the radiation pressure force exerted on the spheroid are yielded. Numerical calculations are performed and indicate that the present theory can be used for arbitrary laser beam scattering by a spheroid, which can be prolate or oblate, transparent or absorbing. This work is potentially useful in laser particle characterization techniques for the non-spherical particles, including the phase Doppler anemometry, the laser diffraction method, and the rainbow thermometry, etc. The analytical expressions for rigorous radiation pressure force prediction are of particularly interests to optical trapping and manipulation of the spheroidal particles.

To make up for the disadvantages of the rigorous theory in far-field scattering calculation for the spheroids of large size, we extend the classical GO to describe shaped beam scattering by a

sphere and a spheroid. A complete GO solution is given for the circular Gaussian beam scattering by a sphere and a spheroid. Then our extended GO method is used for geometric rainbow prediction for spheroid of any aspect ratio. The requirement that the aspect ratio should be near to unity, which is premise of employing Moebius' method for geometric rainbow prediction, was removed.

On such a basis, more work remains to be done in the future. Relying on a robust ray tracing program and a generalized diffraction theory for shaped beam scattering by a spheroid, more shaped beams, e.g., the elliptical Gaussian beam and the higher-order Hermite-Gaussian beam of TEM_{mn} mode, can be used as the incident beams. And the current studies on end-on incidence of the laser beam are also expected to be extended to the case of oblique incidence or side-on incidence. A further extension of the GO to other non-spherical but regularly shaped particles remains to be done. Moreover, the efforts have only been made for the far-field scattering so far. In fact, GO's further application in radiation pressure force prediction for a spheroid is not a very difficult step, which is to be done in the future.

9.2 Experiment

The spectral light extinction method (SLEM) is applied in the development of an optical device for online wet steam measurement. Two algorithms, the Phillip-Twomey-NNLS algorithm (Twomey algorithm) and the optimized regularization technique (ORT) are used for inversion. The ORT proves to have a better performance in practical data inversion than Twomey algorithm does. The standard polystyrene particles and water and milk emulsion are used to evaluate the stability of the measurement system and its sensibility to the variation of particle concentration. Our experiments show that although the absolute measurement of D_{32} is not highly accurate (with errors less than 10%), the measurement of volume concentration variation ΔC_v (relative measurement) by the current system is high enough, with errors less than 0.4% for $\Delta C_v=0.5\%$.

Next, the wet steam measurements are carried out on an experimental turbine in Electricity of France (EDF). To evaluate the potential influences of the scattered intensities by the particles in the edge zone and the multiple scattering on the measurement results, the Monte Carlo method

is used for direct numerical simulation of the current system. The results show that once the distance between the measurement zone and detecting fiber is long enough, the scattered intensities by the particles in the edge zone have negligible influence on the extinction spectrum. Moreover, because the size of the detector is small enough (the diameter 0.4 mm), the multiple scattering has a negligible influence on the extinction spectrum. By using the SLEM system developed in the present thesis, further studies on wet steam measurement are expected to be made.

Appendix A

Computation of eigenvalues λ_{mn} and expansion coefficients d_r^{mn}

We adopt the method proposed by Hodge (1970) to calculate the eigenvalues λ_{mn} in prolate spheroidal coordinates. Substituting Eq. (2-83) into Eq. (2-4), we obtain the following recursion relation for expansion coefficients:

$$A_r^m(c)d_{r+2}^{mn}(c) + [B_r^{mn}(c) - \lambda_{mn}(c)]d_r^{mn}(c) + C_r^{mn}(c)d_{r-2}^{mn}(c) = 0, \quad (\text{A1})$$

where

$$A_r^m(c) = \frac{(2m+r+2)(2m+r+1)}{(2m+2r+5)(2m+2r+3)}c^2, \quad (\text{A2})$$

$$B_r^m(c) = (m+r)(m+r+1) + \frac{2(m+r)(m+r+1) - 2m^2 - 1}{(2m+2r+3)(2m+2r-1)}c^2, \quad (\text{A3})$$

and

$$C_r^m(c) = \frac{r(r-1)}{(2m+2r-3)(2m+2r-1)}c^2. \quad (\text{A4})$$

Eq.(A1) can be rewritten into the following detailed form:

$$A_0^m(c)d_2^{mn}(c) + [B_0^{mn}(c) - \lambda_{mn}(c)]d_0^{mn}(c) = 0, \quad (\text{A5})$$

$$A_1^m(c)d_3^{mn}(c) + [B_1^{mn}(c) - \lambda_{mn}(c)]d_1^{mn}(c) = 0, \quad (\text{A6})$$

$$A_2^m(c)d_4^{mn}(c) + [B_2^{mn}(c) - \lambda_{mn}(c)]d_2^{mn}(c) + C_2^{mn}(c)d_0^{mn}(c) = 0 \quad (\text{A7})$$

$$A_3^m(c)d_5^{mn}(c) + [B_3^{mn}(c) - \lambda_{mn}(c)]d_3^{mn}(c) + C_3^{mn}(c)d_1^{mn}(c) = 0 \quad (\text{A8})$$

$$\dots$$

$$A_r^m(c)d_{r+2}^{mn}(c) + [B_r^{mn}(c) - \lambda_{mn}(c)]d_r^{mn}(c) + C_r^{mn}(c)d_{r-2}^{mn}(c) = 0. \quad (\text{A9})$$

Then the eigenvalues can be calculated by solving the following matrix equation set in tridiagonal form (Han, 2001a):

Appendix B

Spheroidal vector wave functions

The spheroidal vector wave functions are defined as follows (Barton, 1995):

$$\mathbf{M}_{mn} = M_{mn,\xi} \mathbf{e}_\xi + M_{mn,\eta} \mathbf{e}_\eta + M_{mn,\phi} \mathbf{e}_\phi, \quad (\text{B1})$$

$$\mathbf{N}_{mn} = N_{mn,\xi} \mathbf{e}_\xi + N_{mn,\eta} \mathbf{e}_\eta + N_{mn,\phi} \mathbf{e}_\phi, \quad (\text{B2})$$

where

$$M_{mn,\xi} = \frac{\pm im\eta}{\sqrt{(\xi^2 \mp \eta^2)(\xi^2 \mp 1)}} R_{|m|n}^{(j)}(c, \xi) S_{|m|n}(c, \eta) \exp(im\phi), \quad (\text{B3})$$

$$M_{mn,\eta} = \frac{-im\xi}{\sqrt{(\xi^2 \mp \eta^2)(1-\eta^2)}} R_{|m|n}^{(j)}(c, \xi) S_{|m|n}(c, \eta) \exp(im\phi), \quad (\text{B4})$$

$$M_{mn,\phi} = \frac{\sqrt{(\xi^2 \mp 1)(1-\eta^2)}}{(\xi^2 \mp \eta^2)} \left[\xi R_{|m|n}^{(j)}(c, \xi) S'_{|m|n}(c, \eta) \mp \eta R'_{|m|n}{}^{(j)}(c, \xi) S_{|m|n}(c, \eta) \right] \exp(im\phi), \quad (\text{B5})$$

$$N_{mn,\xi} = \frac{(\xi^2 \mp 1)^{1/2}}{c(\xi^2 \mp \eta^2)^{3/2}} \left\{ \xi \left[\lambda_{|m|n} \mp c^2 \eta^2 \pm \frac{m^2}{\xi^2 - 1} \right] S_{|m|n}(c, \eta) R_{|m|n}^{(j)}(c, \xi) \mp \frac{2\xi\eta(1-\eta^2)}{\xi^2 \mp \eta^2} S'_{|m|n}(c, \eta) R_{|m|n}^{(j)}(c, \xi) \right. \\ \left. \pm \eta(1-\eta^2) S'_{|m|n}(c, \eta) R'_{|m|n}{}^{(j)}(c, \xi) \pm \left[\frac{\xi^2(1-3\eta^2) \pm \eta^2(\eta^2+1)}{\xi^2 \mp \eta^2} \right] S_{|m|n}(c, \eta) R'_{|m|n}{}^{(j)}(c, \xi) \right\} \exp(im\phi), \quad (\text{B6})$$

$$N_{mn,\eta} = \frac{\sqrt{1-\eta^2}}{c(\xi^2 \mp \eta^2)^{3/2}} \left[\xi(\xi^2 \mp 1) R'_{|m|n}{}^{(j)}(c, \xi) S'_{|m|n}(c, \eta) + \frac{\xi^2(\xi^2 \pm 1) + \eta^2(1 \mp 3\xi^2)}{(\xi^2 \mp \eta^2)} R_{|m|n}^{(j)}(c, \xi) S'_{|m|n}(c, \eta) \right. \\ \left. - \eta \left(\lambda_{|m|n} - c^2 \xi^2 - \frac{m^2}{1-\eta^2} \right) R_{|m|n}^{(j)}(c, \xi) S_{|m|n}(c, \eta) \pm \frac{2\xi\eta(\xi^2 \mp 1)}{(\xi^2 \mp \eta^2)} R'_{|m|n}{}^{(j)}(c, \xi) S_{|m|n}(c, \eta) \right] \exp(im\phi) \quad (\text{B7})$$

$$N_{mn,\phi} = \frac{im\sqrt{(\xi^2 \mp 1)(1-\eta^2)}}{c(\xi^2 \mp \eta^2)} \left[\pm \frac{\eta}{(\xi^2 \mp 1)} S'_{|m|n}(c, \eta) R_{|m|n}^{(j)}(c, \xi) + \frac{\xi}{1-\eta^2} R'_{|m|n}{}^{(j)}(c, \xi) S_{|m|n}(c, \eta) \right. \\ \left. + \frac{(\xi^2 \mp \eta^2)}{(\xi^2 \mp 1)(1-\eta^2)} S_{|m|n}(c, \eta) R_{|m|n}^{(j)}(c, \xi) \right] \exp(im\phi) \quad (\text{B8})$$

where $S'_{mn}(\cos\theta) = dS_{mn}(\cos\theta)/d(\cos\theta)$. In all pairs of signs in the above expressions, the upper signs pertain to the prolate functions and the lower ones pertain to the oblate functions. For a description of the incident and internal fields ($\mathbf{E}^{(i)}, \mathbf{H}^{(i)}$) and ($\mathbf{E}^{(t)}, \mathbf{H}^{(t)}$), the superscript j on

the radial function R_{mn} is 1, while for the description of the scattered fields ($\mathbf{E}^{(s)}$, $\mathbf{H}^{(s)}$), j is 3.

Or, the spheroidal vector wave functions can be written into the combination of odd and even items as followings:

$$\mathbf{M}_{mn} = \mathbf{M}_{emn} + i\mathbf{M}_{omn}, \quad (\text{B9})$$

$$\mathbf{N}_{mn} = \mathbf{N}_{emn} + i\mathbf{N}_{omn}, \quad (\text{B10})$$

where the subscripts o and e refer to the odd and even functions, respectively and

$$M_{e mn, \xi} = \frac{\mp m \eta}{\sqrt{(\xi^2 \mp \eta^2)(\xi^2 \mp 1)}} R_{|m|n}^{(j)}(c, \xi) S_{|m|n}(c, \eta) \Big|_{(-1)\cos(m\phi)}^{\sin(m\phi)}, \quad (\text{B11})$$

$$M_{e mn, \eta} = \frac{m \xi}{\sqrt{(\xi^2 \mp \eta^2)(1-\eta^2)}} R_{|m|n}^{(j)}(c, \xi) S_{|m|n}(c, \eta) \Big|_{(-1)\cos(m\phi)}^{\sin(m\phi)}, \quad (\text{B12})$$

$$M_{o mn, \phi} = \frac{\sqrt{(\xi^2 \mp 1)(1-\eta^2)}}{(\xi^2 \mp \eta^2)} \left[\xi R_{|m|n}^{(j)}(c, \xi) S'_{|m|n}(c, \eta) \mp \eta R_{|m|n}^{\prime(j)}(c, \xi) S_{|m|n}(c, \eta) \right] \Big|_{\sin(m\phi)}^{\cos(m\phi)}, \quad (\text{B13})$$

$$N_{e mn, \xi} = \frac{(\xi^2 \mp 1)^{1/2}}{c(\xi^2 \mp \eta^2)^{3/2}} \left\{ \xi \left[\lambda_{|m|n} \mp c^2 \eta^2 \pm \frac{m^2}{\xi^2 - 1} \right] S_{|m|n}(c, \eta) R_{|m|n}^{(j)}(c, \xi) \mp \frac{2\xi\eta(1-\eta^2)}{\xi^2 \mp \eta^2} S'_{|m|n}(c, \eta) R_{|m|n}^{(j)}(c, \xi) \right. \\ \left. \pm \eta(1-\eta^2) S'_{|m|n}(c, \eta) R_{|m|n}^{\prime(j)}(c, \xi) \pm \left[\frac{\xi^2(1-3\eta^2) \pm \eta^2(\eta^2+1)}{\xi^2 \mp \eta^2} \right] S_{|m|n}(c, \eta) R_{|m|n}^{\prime(j)}(c, \xi) \right\} \Big|_{\sin(m\phi)}^{\cos(m\phi)}, \quad (\text{B14})$$

$$N_{e mn, \eta} = \frac{\sqrt{1-\eta^2}}{c(\xi^2 \mp \eta^2)^{3/2}} \left[\xi(\xi^2 \mp 1) R_{|m|n}^{\prime(j)}(c, \xi) S'_{|m|n}(c, \eta) + \frac{\xi^2(\xi^2 \pm 1) + \eta^2(1 \mp 3\xi^2)}{(\xi^2 \mp \eta^2)} R_{|m|n}^{(j)}(c, \xi) S'_{|m|n}(c, \eta) \right. \\ \left. - \eta \left(\lambda_{|m|n} - c^2 \xi^2 - \frac{m^2}{1-\eta^2} \right) R_{|m|n}^{(j)}(c, \xi) S_{|m|n}(c, \eta) \pm \frac{2\xi\eta(\xi^2 \mp 1)}{(\xi^2 \mp \eta^2)} R_{|m|n}^{\prime(j)}(c, \xi) S_{|m|n}(c, \eta) \right] \Big|_{\sin(m\phi)}^{\cos(m\phi)}, \quad (\text{B15})$$

$$N_{o mn, \phi} = \frac{m\sqrt{(\xi^2 \mp 1)(1-\eta^2)}}{c(\xi^2 \mp \eta^2)} \left[\pm \frac{\eta}{(\xi^2 \mp 1)} S'_{|m|n}(c, \eta) R_{|m|n}^{(j)}(c, \xi) + \frac{\xi}{1-\eta^2} R_{|m|n}^{\prime(j)}(c, \xi) S_{|m|n}(c, \eta) \right. \\ \left. + \frac{(\xi^2 \mp \eta^2)}{(\xi^2 \mp 1)(1-\eta^2)} S_{|m|n}(c, \eta) R_{|m|n}^{(j)}(c, \xi) \right] \Big|_{-\cos(m\phi)}^{\sin(m\phi)}, \quad (\text{B16})$$

Appendix C

Orthogonality relations for some functions

The orthogonality relation for exponentials $\exp(ip\phi)$ is

$$\int_0^{2\pi} \exp[i(p-p')\phi] d\phi = 2\pi\delta_{pp'}. \quad (C1)$$

If we denote τ_n^m and π_n^m as the generalized Legendre functions of Ferrer's definition as follows:

$$\tau_n^p = \frac{dP_n^p(\cos\theta)}{d\theta}, \quad (C2)$$

$$\pi_n^p = \frac{P_n^p(\cos\theta)}{\sin\theta}, \quad (C3)$$

four orthogonality relations of them used in RPF calculation for a spherical particle have been found as follows (Gouesbet et al., 1988):

$$\begin{aligned} I_3 &= \int_0^\pi (\tau_n^{p|} \tau_{n'}^{p|} + p^2 \pi_n^{p|} \pi_{n'}^{p|}) \sin\theta \cos\theta d\theta \\ &= \frac{2(n-1)(n+1)(n+|p|)!}{(2n-1)(2n+1)(n-|p|-1)!} \delta_{n',n-1} + \frac{2(n'-1)(n'+1)(n'+|p|)!}{(2n'-1)(2n'+1)(n'-|p|-1)!} \delta_{n,n'-1}, \end{aligned} \quad (C4)$$

$$I_4 = \int_0^\pi (\tau_n^{p|} \pi_{n'}^{p|} + \tau_{n'}^{p|} \pi_n^{p|}) \sin\theta \cos\theta d\theta = \frac{2(n+|p|)!}{(2n+1)(n-|p|)!} \delta_{nn'}, \quad (C5)$$

$$\begin{aligned} I_5 &= \int_0^\pi (\tau_n^{p|} \tau_{n'}^{p+1|} + p(p+1) \pi_n^{p|} \pi_{n'}^{p+1|}) \sin^2\theta d\theta \\ &= \begin{cases} -\frac{2}{(2n+1)(2n'+1)} \frac{(n'+|p|+1)!}{(n'-|p|-1)!} [(n-1)(n+1)\delta_{n,n'+1} - (n'-1)(n'+1)\delta_{n',n+1}], & p \geq 0, \\ -\frac{2}{(2n+1)(2n'+1)} \frac{(n-|p|)!}{(n+|p|)!} [(n'-1)(n'+1)\delta_{n',n+1} - (n-1)(n+1)\delta_{n,n'+1}], & p < 0 \end{cases} \end{aligned} \quad (C6)$$

$$\begin{aligned} I_6 &= \int_0^\pi (p \pi_n^{p|} \tau_{n'}^{p+1|} + (p+1) \pi_{n'}^{p+1|} \tau_n^{p|}) \sin^2\theta d\theta \\ &= \begin{cases} -\frac{2}{(2n+1)} \frac{(n+|p|+1)!}{(n-|p|-1)!} \delta_{nn'}, & p \geq 0 \\ \frac{2}{(2n+1)} \frac{(n-|p|)!}{(n+|p|)!} \delta_{nn'}, & p < 0 \end{cases}. \end{aligned} \quad (C7)$$

Since the spheroidal angular functions $S_{pn}(c_1, \cos \theta)$ can be written as infinite series of the Legendre functions $P_n^p(\cos \theta)$ as follows:

$$S_{pn}(c_1, \cos \theta) = \sum_{r=0,1}^{\infty} d_r^{pn}(c_1) P_{|p|+r}^p(\cos \theta), \quad (\text{C8})$$

after some mathematical algebra, J_{mn}^p , K_{mn}^p , L_{mn}^p , and M_{mn}^p can be obtained by using the following orthogonality relations corresponding to I_3 , I_4 , I_5 , and I_6 , respectively but for S_{pn} and S'_{pn} :

$$J_{mn}^p = \int_0^\pi \left(\frac{dS_{|p|n}(c_1, \cos \theta)}{d\theta} \frac{dS_{|p|n'}(c_1, \cos \theta)}{d\theta} + p^2 \frac{S_{|p|n}(c_1, \cos \theta)}{\sin \theta} \frac{S_{|p|n'}(c_1, \cos \theta)}{\sin \theta} \right) \sin \theta \cos \theta d\theta$$

$$= \begin{cases} \sum_{r=2,1}^{\infty} r \frac{2(|p|+r-1)(|p|+r+1)}{(2|p|+2r-1)(2|p|+2r+1)} \frac{(2|p|+r)!}{(r-1)!} d_r^{|p|n} d_{r-1}^{|p|n'} + \\ \sum_{r=0,1}^{\infty} r \frac{2(|p|+r)(|p|+r+2)}{(2|p|+2r+1)(2|p|+2r+3)} \frac{(2|p|+r+1)!}{r!} d_r^{|p|n} d_{r+1}^{|p|n'}, & |n-n'| = \text{odd} \\ 0, & |n-n'| = \text{even} \end{cases}, \quad (\text{C9})$$

$$K_{mn}^p = \int_0^\pi \left[\frac{dS_{|p|n}(c_1, \cos \theta)}{d\theta} \frac{S_{|p|n'}(c_1, \cos \theta)}{\sin \theta} + \frac{dS_{|p|n'}(c_1, \cos \theta)}{d\theta} \frac{S_{|p|n}(c_1, \cos \theta)}{\sin \theta} \right] \sin \theta \cos \theta d\theta$$

$$= \begin{cases} 0, & |n-n'| = \text{odd} \\ \sum_{r=0,1}^{\infty} r \frac{2}{(2|p|+2r+1)} \frac{(2|p|+r)!}{r!} d_r^{|p|n} d_r^{|p|n'}, & |n-n'| = \text{even} \end{cases}, \quad (\text{C10})$$

$$\begin{aligned}
 L_{mn}^p &= \int_0^\pi \left(\frac{dS_{|p|n}(c_1, \cos \theta)}{d\theta} \frac{dS_{|p+1|n'}(c_1, \cos \theta)}{d\theta} + p(p+1) \frac{S_{|p|n}(c_1, \cos \theta)}{\sin \theta} \frac{S_{|p+1|n'}(c_1, \cos \theta)}{\sin \theta} \right) \sin^2 \theta d\theta \\
 &= \begin{cases} \left[- \sum_{r=2,3}^{\infty} \frac{2(|p|+r-1)(|p|+r+1)}{(2|p|+2r-1)(2|p|+2r+1)} \frac{(2|p|+r)!}{(r-2)!} d_r^{|p|n} d_{r-2}^{|p+1|n'} - \right. \\ \left. \sum_{r=0,1}^{\infty} \frac{2(|p|+r)(|p|+r+2)}{(2|p|+2r+1)(2|p|+2r+3)} \frac{(2|p|+r+2)!}{r!} d_r^{|p|n} d_r^{|p+1|n'} \right], & |n-n'| = \text{odd}, \quad p \geq 0, \\ \left[- \sum_{r=0,1}^{\infty} \frac{2(|p|+r)(|p|+r+2)}{(2|p|+2r+1)(2|p|+2r+3)} \frac{(2|p|+r)!}{r!} d_r^{|p|n} d_{r+2}^{|p-1|n'} - \right. \\ \left. \sum_{r=0,1}^{\infty} \frac{2(|p|+r-1)(|p|+r+1)}{(2|p|+2r-1)(2|p|+2r+1)} \frac{(2|p|+r)!}{r!} d_r^{|p|n} d_r^{|p-1|n'} \right], & |n-n'| = \text{odd}, \quad p < 0 \\ 0, & |n-n'| = \text{even} \end{cases}, \quad (C11)
 \end{aligned}$$

$$\begin{aligned}
 M_{mn}^p &= \int_0^\pi \left(p \frac{S_{|p|n}(c_1, \cos \theta)}{\sin \theta} \frac{dS_{|p+1|n'}(c_1, \cos \theta)}{d\theta} + (p+1) \frac{S_{|p+1|n'}(c_1, \cos \theta)}{\sin \theta} \frac{dS_{|p|n}(c_1, \cos \theta)}{d\theta} \right) \sin^2 \theta d\theta \\
 &= \begin{cases} 0, & |n-n'| = \text{odd} \\ \left[- \sum_{r=2,1}^{\infty} \frac{2}{2|p|+2r+1} \frac{(2|p|+r+1)!}{(r-1)!} d_r^{|p|n} d_{r-1}^{|p+1|n'}, & |n-n'| = \text{even}, \quad p \geq 0 \\ \sum_{r=0,1}^{\infty} \frac{2}{2|p|+2r+1} \frac{(2|p|+r)!}{r!} d_r^{|p|n} d_{r+1}^{|p-1|n'}, & |n-n'| = \text{even}, \quad p < 0 \end{cases}. \quad (C12)
 \end{aligned}$$

Appendix D

Spherical vector wave functions

The spherical vector wave functions are defined as follows (Stratton, 1941):

$$\mathbf{m}_{mn} = m_{mn,\theta} \mathbf{e}_\theta + m_{mn,\phi} \mathbf{e}_\phi, \quad (\text{D1})$$

$$\mathbf{n}_{mn} = n_{mn,r} \mathbf{e}_r + n_{mn,\theta} \mathbf{e}_\theta + n_{mn,\phi} \mathbf{e}_\phi, \quad (\text{D2})$$

where

$$m_{mn,\theta} = \frac{im}{\sin \theta} z_n(kr) P_{|m|n}(\cos \theta) \exp(im\phi), \quad (\text{D3})$$

$$m_{mn,\phi} = -z_n(kr) P'_{|m|n}(\cos \theta) \exp(im\phi), \quad (\text{D4})$$

$$n_{mn,r} = n(n+1) \frac{z_n(kr)}{kr} P_{|m|n}(\cos \theta) \exp(im\phi), \quad (\text{D5})$$

$$n_{mn,\theta} = \frac{1}{kr} \frac{\partial [rz_n(kr)]}{\partial r} P'_{|m|n}(\cos \theta) \exp(im\phi), \quad (\text{D6})$$

$$n_{mn,\phi} = \frac{im}{\sin \theta} \frac{\partial [rz_n(kr)]}{\partial r} P_{|m|n}(\cos \theta) \exp(im\phi). \quad (\text{D7})$$

where $P'_{mn}(\cos \theta) = (\partial / \partial \theta) P_n^m(\cos \theta)$. For the description of the incident and internal fields ($\mathbf{E}^{(i)}$, $\mathbf{H}^{(i)}$) and ($\mathbf{E}^{(t)}$, $\mathbf{H}^{(t)}$), $z_n(kr)$ is the n th-order spherical Bessel function, while for the description of the scattered field ($\mathbf{E}^{(s)}$, $\mathbf{H}^{(s)}$), $z_n(kr)$ is the n th-order Hankel function of the first kind.

Or, the spherical vector wave functions can be written into the combination of odd and even items as followings:

$$\mathbf{m}_{mn} = \mathbf{m}_{emn} + i\mathbf{m}_{omn}, \quad (\text{D8})$$

$$\mathbf{n}_{mn} = \mathbf{n}_{emn} + i\mathbf{n}_{omn}, \quad (\text{D9})$$

where the subscripts o and e refer to the odd and even functions, respectively and

$$m_{e_{omn}} = \mp \frac{m}{\sin \theta} z_n(kr) P_{|m|n}(\cos \theta) \frac{\sin m\phi}{\cos m\phi} \mathbf{e}_\theta - z_n(kr) P'_{|m|n}(\cos \theta) \frac{\cos m\phi}{\sin m\phi} \mathbf{e}_\phi, \quad (\text{D10})$$

$$\begin{aligned}
 n_{\epsilon_{mn}} &= n(n+1) \frac{z_n(kr)}{kr} P_{|m|n}(\cos \theta) \frac{\cos m\phi}{\sin m\phi} \mathbf{e}_r + \frac{1}{kr} \frac{\partial [rz_n(kr)]}{\partial r} P'_{|m|n}(\cos \theta) \frac{\cos m\phi}{\sin m\phi} \mathbf{e}_\theta \\
 &\mp \frac{m}{\sin \theta} \frac{\partial [rz_n(kr)]}{\partial r} P_{|m|n}(\cos \theta) \frac{\sin m\phi}{\cos m\phi} (m\phi) \mathbf{e}_\phi .
 \end{aligned} \tag{D11}$$

Appendix E

Electromagnetic fields of an astigmatic elliptical Gaussian beam

Following Davis's first order approximation (Davis, 1979), the laser sheet has the following description (Ren et al., 1994b, c; Siegman, 1986) in its own Cartesian coordinates O_B-uvw :

$$E_u = E_0 \psi_0^{sh} \exp(ikw), \quad (E1)$$

$$E_v = 0, \quad (E2)$$

$$E_w = -\frac{2Q_u u}{l_u} E_u, \quad (E3)$$

$$H_u = 0, \quad (E4)$$

$$H_v = H_0 \psi_0^{sh} \exp(ikw), \quad (E5)$$

$$H_w = -\frac{2Q_v v}{l_v} H_v, \quad (E6)$$

where

$$\psi_0^{sh} = -i\sqrt{Q_u Q_v} \exp\left[i\left(Q_u \frac{u^2}{w_{0u}^2} + Q_v \frac{v^2}{w_{0v}^2}\right)\right], \quad (E7)$$

as well as

$$Q_u = \frac{1}{-i + 2(w - w_u)/l_u}, \quad (E8)$$

$$Q_v = \frac{1}{-i + 2(w - w_v)/l_v}, \quad (E9)$$

$$l_u = kw_{0u}^2, \quad (E10)$$

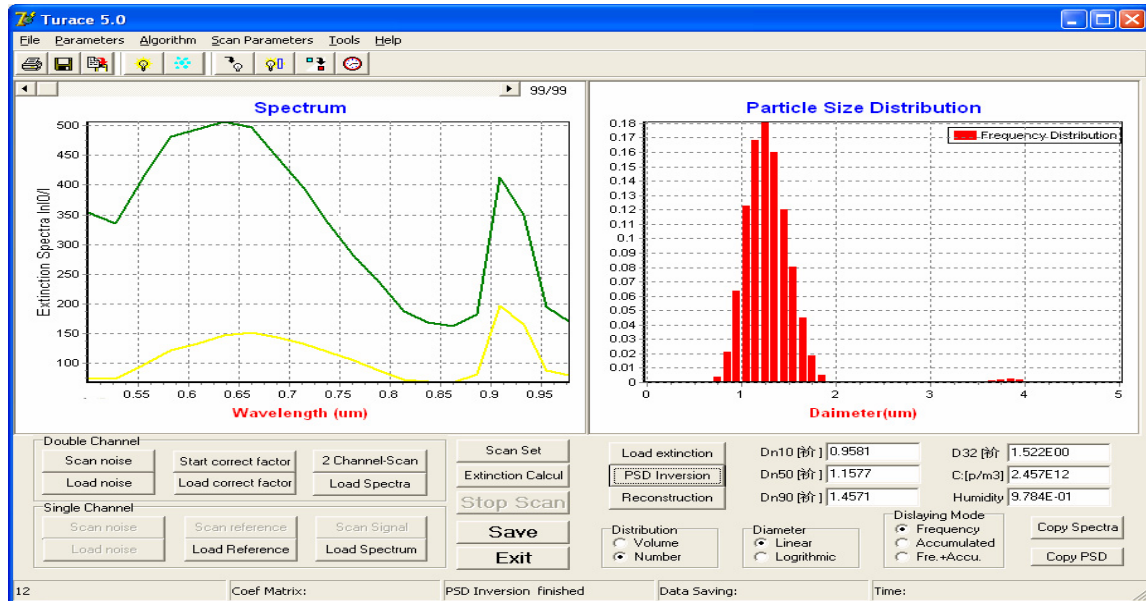
$$l_v = kw_{0v}^2, \quad (E11)$$

where w_{0u} and w_{0v} are the beam waist radii along the u and v axes respectively, as well as w_u and w_v are the locations of the beam waists along the u and v axes (w_{0u} and w_{0v}), respectively. When we set $w_u=w_v=0$, the common elliptical Gaussian beam with waist plane locating at $w=0$ will be recovered. When we further set $w_{0u}=w_{0v}$, the special case of circular Gaussian beam can be recovered.

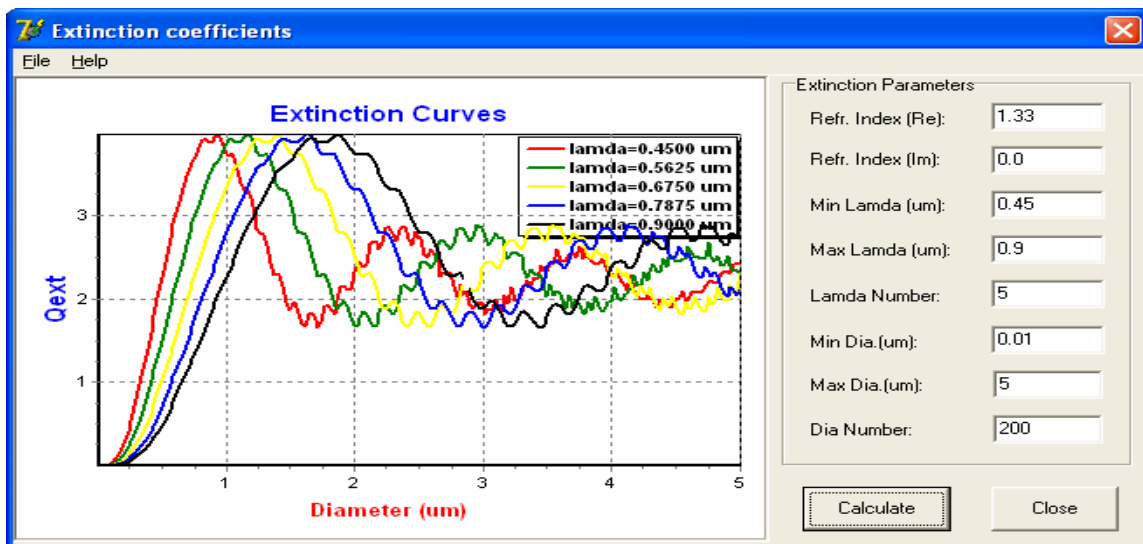
Appendix F

Presentation of the Software TURACE 5.0

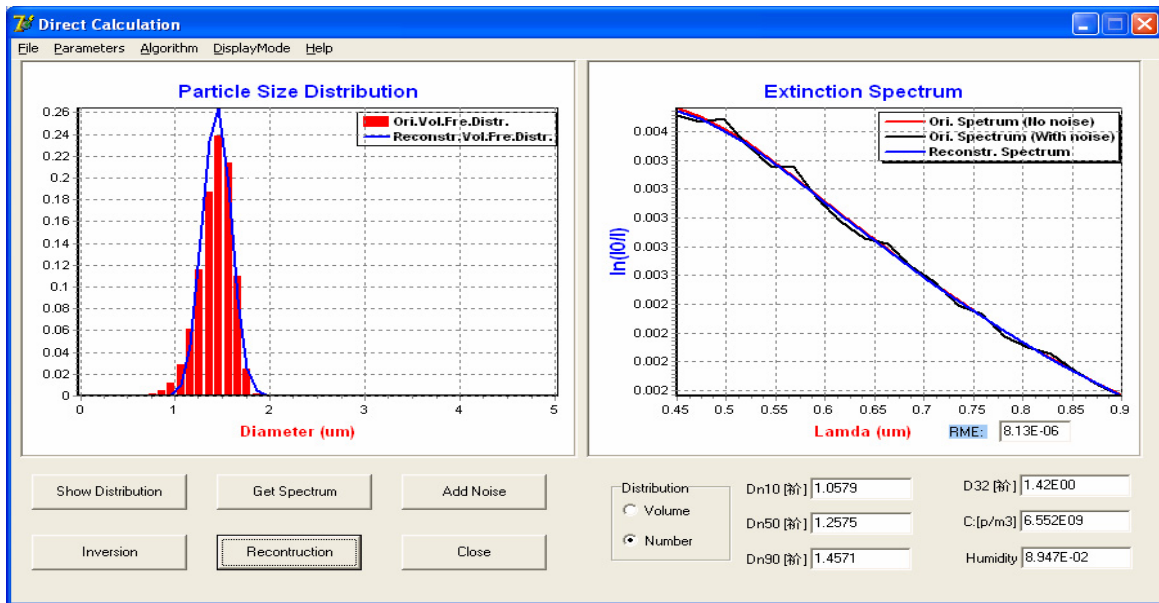
1). Interface for on-line and off-line particle sizing



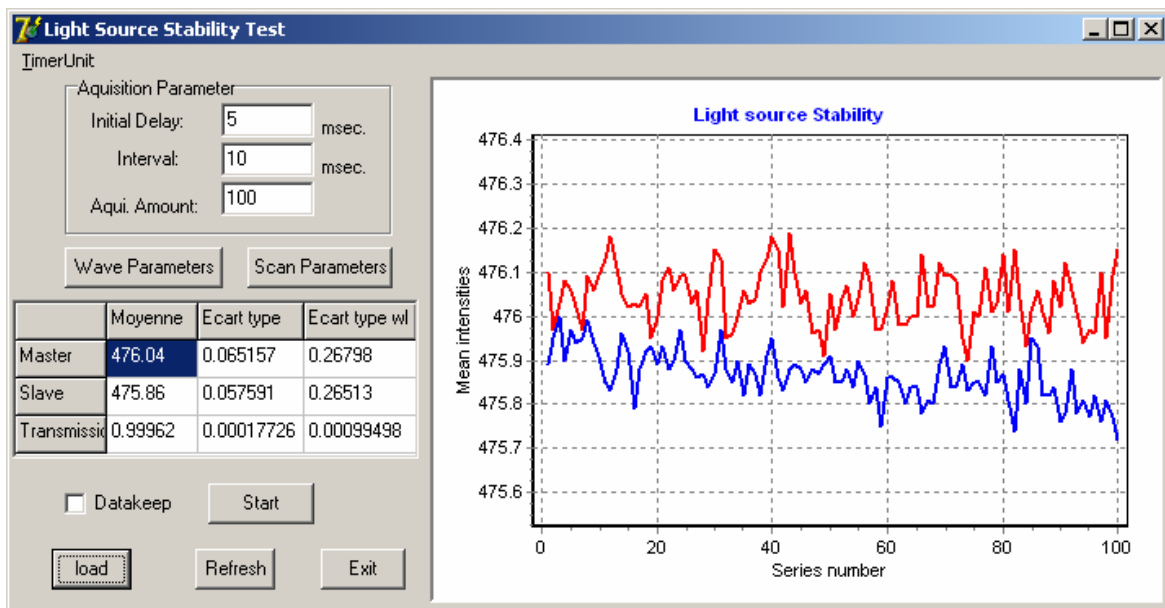
2). Demonstration of the extinction coefficient curve for a given refractive index of the particle



3). Direct calculation of the extinction spectrum and inversion algorithm test

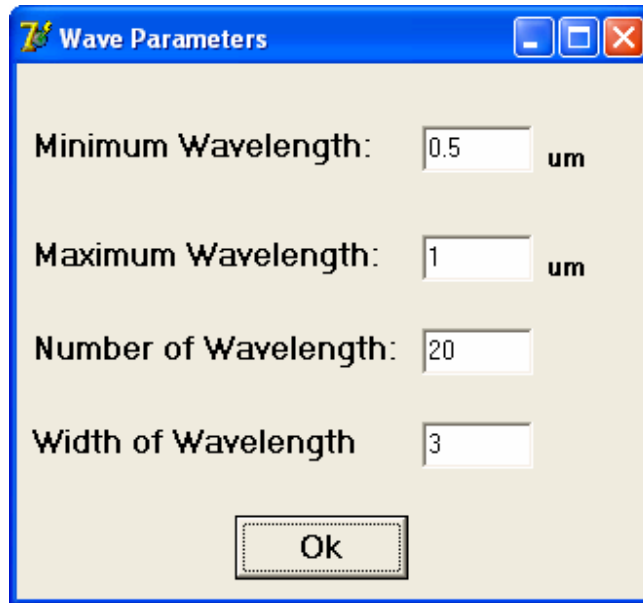


4). Interface for stability test of the light source

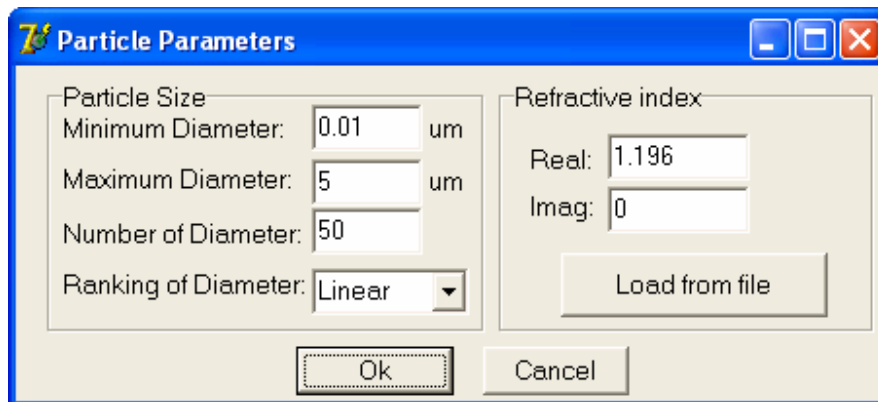


5). Interface for parameter input

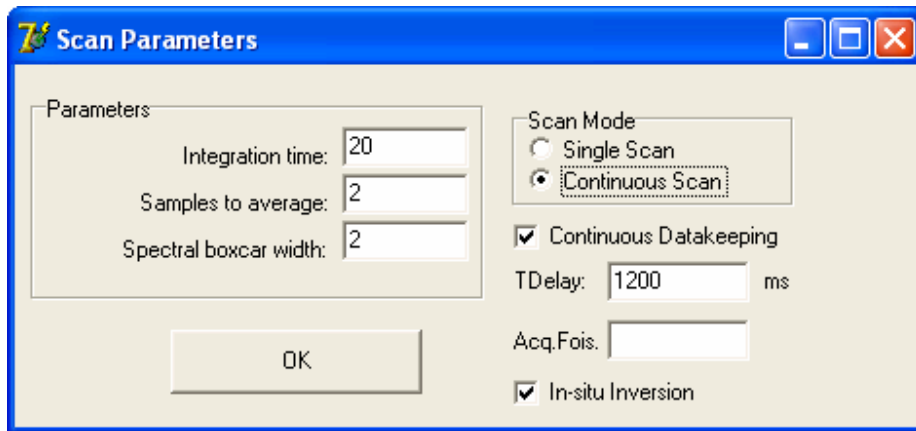
A. Wave parameters



B. Particle parameters

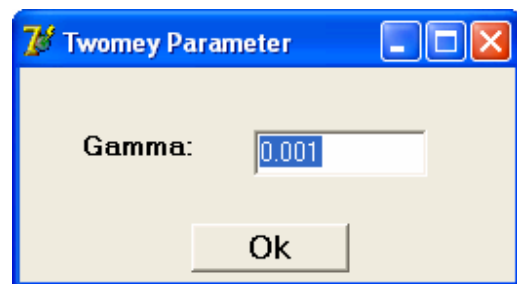
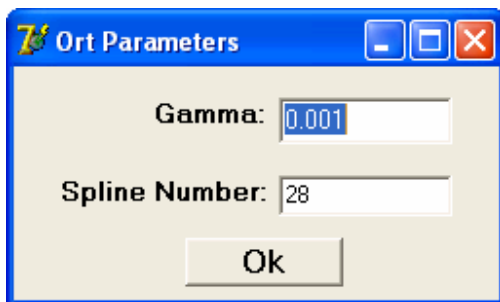


C. Scan parameters

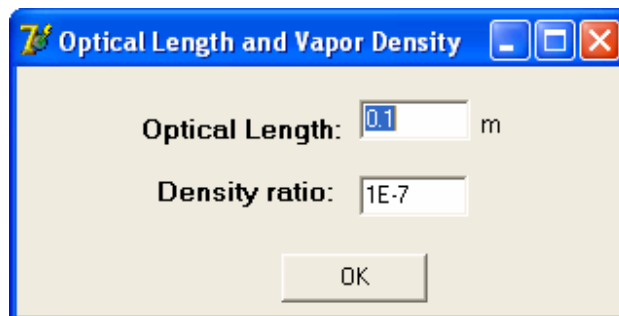


D. Parameters for inversion algorithms

D1). Optimized Regularization Technique (ORT) D2). Phillips-Twomey-NNLS (Twomey algorithm)



D3). Optical length and density ratio of the two phases of the water



Appendix G

Characteristics of the spectrometers

Type	SD 2000	HR 2000+
Detector	Sony ILX511 linear silicon CCD array	Idem
Range of wavelength	350 nm - 1100 nm (EDF)	200 nm - 1100 nm (EDF)
Pixels	2048 pixels	Idem
Signal : noise	250 : 1	250 : 1
Integration time	3 ms - 60 min	1 ms – 65 min
Linearity of intensity	< 0.3 %	Communication by telephone (Mr. Demezset)
Precision of wavelength	< 0.3 nm	

Appendix H

Characteristics of the light sources

Characteristics	HL 2000	DH 2000
Power supply	1.4 A @ 5VDC	0.3 A/85 V (D) and 1.67 A/11.5 VDC(H)
Range of wavelength	360-2000 nm	210-400 nm and 360-1500 nm
Stability	0.5%	$<5 \times 10^{-6}$
Current – voltage drift	$<0.3\%$ / hour	$<0.01\%$ / hour
Time for stabilization	~5 min.	~40 min. (D) and ~20 min. (H)

References

1. Adby P. R. and Demster M. A. H. (1974). *Introduction to Optimization Methods*. Chapman & Hall, London.
2. Aden A. L. and Kerker M. (1951). Scattering of electromagnetic waves from two concentric spheres. *J. Appl. Phys.* 22, 1242-1246.
3. Adler C. L., Lock J. A., and Stone B. R. (1998). Rainbow scattering by a cylinder with a nearly elliptical cross section. *Appl. Opt.* 37, 1540–1550.
4. Allen T. (1997). *Particle Size Measurement*. 5th Ed. Chapman & Hall, London.
5. Arfken G. (1985). *Mathematical Methods for Physicists*. Academic Press, Orlando.
6. Asano S. and Sato M. (1980). Light scattering by randomly oriented spheroidal particles, *Appl. Opt.* 19, 962-974.
7. Asano S. and Yamamoto G. (1975). Light scattering by a spheroidal particle. *Appl. Opt.* 14, 29-49.
8. Ashkin A. (1970). Acceleration and trapping of particles by radiation pressure. *Phys. Rev. Lett.* 24, 156-159.
9. Ashkin A. (1980). Applications of laser radiation pressure. *Science*, 210, 1081-1088.
10. Ashkin A. and Dziedzic J. M. (1977). Observation of resonances in the radiation pressure on dielectric spheres. *Phys. Rev. Lett.* 38, 1351-1354.
11. Ashkin A. and Dziedzic J.M. (1987). Optical trapping and manipulation of virus and bacteria. *Science* 235, 1517-1520.
12. Ashkin A., Dziedzic J. M. and Yamane T. (1987). Optical trapping and manipulation of single cells using infrared laser beams. *Nature* 330, 769-771.
13. Ashkin A. and Dziedzic J. M. (1989). Internal cell manipulation using infrared laser traps. *Proc. Natl. Acad. Sci. USA.* 86, 7914-7918.
14. Barth H. G. (1984). *Modern Methods for Particle Size Analysis*. Wiley, New York.
15. Barton J. P. (1988). Internal and near- surface electromagnetic fields for a

References

- spherical particle irradiated by a focused laser beam. *J. Appl. Phys.* 64, 1632-1639.
16. Barton J. P. (1995). Internal and near-surface electromagnetic fields for a spheroidal particle with arbitrary illumination. *Appl. Opt.* 34, 5542-5551.
 17. Barton J. P. (1997). Electromagnetic-field calculation for a sphere illuminated by a higher-order Gaussian beam. I. Internal and near-field effect, *Appl. Opt.* 36, 1303-1311.
 18. Barton J. P. (2000). Electromagnetic fields for a spheroidal particle with an arbitrary embedded sources. *J. Opt. Soc. Am. A* 17, 458-464.
 19. Barton J. P. (2001). Internal, near-surface and scattered electromagnetic fields for a layered spheroid with arbitrary illumination. *Appl. Opt.* 40, 3596-3607.
 20. Barton J. P. and Alexander D. R. (1989). Fifth order corrected electromagnetic field component for a fundamental Gaussian beam. *J. Appl. Phys.* 66, 2800-2802.
 21. Berne B. J. and Pecora R. (1976). *Dynamic Light Scattering*. Wiley, New York.
 22. Bohren C. F. and Huffman D. R. (1983). *Absorption and Scattering of Light by Small Particles*. Wiley, New York.
 23. Böckmann C. (2001). Hybrid regularization method for the ill-posed inversion of multiwavelength lidar data in the retrieval of aerosol size distributions. *Appl. Opt.* 40, 1329-1342.
 24. Born M. and Wolf E. (1999). *Principles of Optics*. 7th Ed. Cambridge U. Press, Cambridge.
 25. Brenn G. and Frohn A. (1993). An experimental method for the investigation of droplet oscillations in a gaseous medium. *Exp. Fluid* 15, 85-90.
 26. Britton J. P., Maheu B., Gréhan G., and Gouesbet G. (1992). Monte Carlo simulation of multiple scattering in arbitrary 3-D geometry. *Part. Part. Syst. Charact.* 9, 52-58.
 27. Brusaglioni P., Zaccanti G., Ismaelli A., and Pili P. (1987). Comparison between measured and calculated contributions of multiply scattered radiation to the transmittance of a light beam through a turbid medium. *Radio Sci.* 22, 899-905.
 28. Cashdollar K. L., Lee C. K., and Singer J. M. (1979). Three-wavelength light transmission technique to measure smoke particle size and concentration. *Appl. Opt.* 18, 1763-1769.

References

29. Chen G., Mazumder M. M., Chang R. K., Swindal J. C., and Acker W. P. (1996). Laser diagnostics for droplet characterization: application of morphology dependent resonances. *Prog. Energy Combust. Sci.* 22, 163-188.
30. Chevaillier J. P., Fabre J., and Hamelin P. (1986). Forward scattered light intensities by a sphere located anywhere in a Gaussian beam. *Appl. Opt.* 25, 1222-1225.
31. Chevaillier J. P., Fabre J., Gréhan G., and Gouesbet G. (1990). Comparison of diffraction theory and generalized Lorenz-Mie theory for a sphere located on axis of a laser beam. *Appl. Opt.* 29, 1293-1298.
32. Crawley G. M., Cournil M., and Benedetto D. D. (1997). Size analysis of fine particle suspensions by spectral turbidimetry. *Powder Techn.* 91, 197-208.
33. Czerwinski M., Mroczka J., Girasole T., Gouesbet G., and Gréhan G. (2001a). Light-transmittance predictions under multiple-light-scattering conditions. I. Direct problem: hybrid-method approximation. *Appl. Opt.* 40, 1514-1524.
34. Czerwinski M., Mroczka J., Girasole T., Gouesbet G., and Gréhan G. (2001b). Light-transmittance predictions under multiple-light-scattering conditions. II. Inverse problem: particle size determination. *Appl. Opt.* 40, 1525-1531.
35. Davis L. W. (1979). Theory of electromagnetic beams. *Phys. Rev. A*, 19, 1177-1179.
36. Debye P. (1909). Der lichtdruck auf kugeln von beliebigem material. *Ann. Phys.* 4, 57-136.
37. Deepak A. and Box M. A. (1978a). Forwardscattering corrections for optical extinction measurements in aerosol media. 1: Monodispersions. *Appl. Opt.* 17, 2900-2908.
38. Deepak A. and Box M. A. (1978b). Forwardscattering corrections for optical extinction measurements in aerosol media. 2: polydispersions *Appl. Opt.* 17, 3169-3176.
39. Dittmann R., Feld H-J., Samenfink W., and Wittig S. (1994). Multiple wavelength extinction technique for particle characterization in dense particle clouds. *Part. Part. Syst. Charact.* 11, 379-384.
40. Dorey J., David L., and Morel P. (2006). *Mesure d'humidité par extinction optique - Essais de sensibilité réalisée sur la PAT*. Technical Report, Department of Research and

References

- Development, EDF.
41. Durst F., Melling A., and Whitelaw J. H. (1981). *Principles and Practice of Laser Doppler Anemometry*. 2nd Ed. Academic, London.
 42. Ferri F., Giglio M., and Perini U. (1989). Inversion of light scattered data from fractals by means of the Chahine iterative algorithm. *Appl. Opt.* 28, 3074-3082.
 43. Flammer C. (1957). *Spheroidal Wave Functions*. Stanford U. Press, Stanford.
 44. Fraster A. B. (1983). Why can the supernumerary bows be seen in a rain shower? *J. Opt. Soc. Am. A* 73, 1626-1628.
 45. Ghatak A. (1977). *Optics*. Mcgraw-Hill, New Delhi.
 46. Glantschnig W. J. and Chen S-H. (1980). Light scattering from water droplets in the geometrical optics approximation. *Appl. Opt.* 20, 2499-2509.
 47. Golub G., Heath M., and Wahba (1979). Generalized cross-validation as a method for choosing a good ridge parameter. *Technometr.* 21, 215-223.
 48. Gouesbet G. (1999). Validity of the localized approximation for arbitrary shaped beams in the generalized Lorenz-Mie theory for spheres. *J. Opt. Soc. Am. A* 16, 1641-1650.
 49. Gouesbet G. (1990). Localized interpretation to calculate all the coefficients g_n^m in the generalized Lorenz-Mie theory. *J. Opt. Soc. Am. A* 7, 998-1007.
 50. Gouesbet G. and Gréhan G. (2000). Generalized Lorenz-Mie theories, from past to future. *Atomization and Sprays* 10, 277-333.
 51. Gouesbet G. and Lock J. A. (1994). Rigorous justification of the localized approximation to the beam-shape coefficients in generalized Lorenz-Mie theory. II. Off-axis beams. *J. Opt. Soc. Am. A* 11, 2516-2525.
 52. Gouesbet G., Gréhan G. and Maheu B. (1988). Computations of the coefficients g_n in the generalized Lorenz-Mie theory using three different methods. *Appl. Opt.* 27, 4874-4883.
 53. Gouesbet G., Maheu B., and Gréhan G. (1988). Light scattering from a sphere arbitrarily located in a Gaussian beam, using a Bromwich formulation. *J. Opt. Soc. Am. A* 5, 1427-1443.

References

54. Gouesbet G., Lock J. A., and Gréhan G. (1995). Partial-wave representations of laser beams for use in light scattering calculations. *Appl. Opt.* 34, 2133-2143.
55. Gouesbet G., Letellier C., Ren K. F., and Gréhan G. (1996). Discussion of two quadrature methods of evaluating beam-shape coefficients in generalized Lorenz-Mie theory. *Appl. Opt.* 35, 1537-1542.
56. Guck J., Ananthakrishnan R., Moon T. J., Cunningham C. C., and Käs J. (2000). Optical deformability of soft biological dielectrics. *Phys. Rev. Lett.* 84, 5451-5454.
57. Guck J., Ananthakrishnan R., Mahmood H., Moon T. J., Cunningham C. C., and Käs J. (2001). The optical stretcher: A novel laser tool to micromanipulate cells. *Biophys. J.* 81, 767-784.
58. Han Y. P. and Wu Z. (2001a). The expansion coefficients of a spheroidal particle illuminated by Gaussian beam. *IEEE Trans. Antenna Propagat.* 49, 615-620.
59. Han Y. P. and Wu Z. (2001b). Scattering of a spheroidal particle illuminated by a Gaussian beam. *Appl. Opt.* 40, 2501-2509.
60. Han Y. P., Gréhan G., and Gouesbet G. (2003). Generalized Lorenz-Mie theory for a spheroidal particle with off-axis Gaussian-beam illumination. *Appl. Opt.* 42, 6621-6629.
61. Hageman L. and Young D. (1981). *Applied Iterative Methods*. Academic Press, New York.
62. Hanke M. (1996). Limitations of the L-curve method in ill-posed problems. *BIT* 36, 287-301.
63. Hanson P. C. (1992). Analysis of discrete ill-posed problems by means of the L-curve. *SIAM Rev.* 34, 561-580.
64. Heintzenberg J. (1978). Particle size distributions from scattering measurements of nonspherical particles via Mie-theory. *Contrib. Atmos. Phys.* 51, 91-99.
65. Hirleman E. D. (1988). Modeling of multiple scattering effects in Fraunhofer diffraction particle size analysis. *Part. Part. Syst. Charact.* 5, 57-65.
66. Hirleman E. D. (1991). General solution to the inverse near-forward-scattering particle-sizing problem in multiple-scattering environments: theory. *Appl. Opt.* 30, 4832-4838.

References

67. Hodge D. B. (1970). Eigenvalues and Eigenfunctions of the spheroidal wave equation. *J. Math. Phys.* 11, 2308-2312.
68. Holve D. and Self S. A. (1979a). Optical particle sizing for in situ measurements. Part 1. *Appl. Opt.* 18, 1632-1645.
69. Holve D. and Self S. A. (1979b). Optical particle sizing for in situ measurements. Part 2. *Appl. Opt.* 18, 1646-1652.
70. Hovenac E. A. (1991). Calculation of far-field scattering from nonspherical particles using a geometrical optics approach. *Appl. Opt.* 30, 4739-4746.
71. Hovenac E. A. and Lock J. A. (1992). Assessing the contributions of surface waves and complex rays to far-field Mie scattering by use of the Debye series. *J. Opt. Soc. Am. A* 9, 781-795.
72. Hsiang L. P. and Faeth G. M. (1992). Near-limit drop deformation and secondary breakup. *Int. J. Multiphase Flow* 18, 635-652.
73. IAPWS (International Association for the Properties of Water and Steam) Industrial Formulation 1997 for the Thermodynamics of Water and Steam, IAPWS Release, IAPWS Secretariat.
74. James G. L. (1976). *Geometrical Theory of Diffraction for Electromagnetic Waves*. Peter Peregrinus Ltd., London.
75. Kandlikar M. and Ramachandran G. (1999). Inverse methods for analyzing aerosol spectrometer measurements: a critical review. *J. Aerosol Sci.* 30, 413-437.
76. Kerker M. (1969), *The scattering of Light and Other Electromagnetic Radiation*. Academic, New York.
77. Kim J. S. and Lee S. S. (1983). Scattering of laser beams and the optical potential well for a homogeneous sphere. *J. Opt. Soc. Am.* 73, 303-312.
78. King M. D. (1982). Sensitivity of constrained linear inversions to the selection of Lagrange multiplier. *J. Atmos. Sci.* 39, 1356-1369.
79. Kocifag M. and Horvath H. (2005). Retrieval of size distribution for urban aerosols using

References

- multispectral optical data. J. Phys. Conf. Ser. 6, 97-102.
80. Korn G. A. and Korn T. M. (1968) *Mathematical Handbook for Scientists and Engineers*. McGraw-Hill, New York.
 81. Kokhanovsky A. A. and Weichert R. (2001). Multiple light scattering in laser particle sizing. Appl. Opt. 40, 1507-1513.
 82. Kourti T., MacGregor J. F., and Hamielec A. E. (1987). Minimum number of turbidity measurements required for the determination of particle size distributions. J. Colloid and Interface Sci. 120, 292-295.
 83. Kusters K. A., Wijers J. G., and Thoenes D. (1991). Particle sizing by laser diffraction spectrometry in the anomalous regime. Appl. Opt. 30, 4839-4847.
 84. Lawson C. L. and Hanson R. J. (1974), *Solving Least Square Problems*. Prentice-Hall, New Jersey.
 85. Li L. W., Kang X. K., and Leong M. S. (2002). *Spheroidal Wave Functions in Electromagnetic Theory*. Wiley, New York.
 86. Li L. W., Leong M. S., Kooi P. S., and Yeo T. S. (2001). Spheroidal vector wave eigenfunction expansion of dyadic Green's functions for a dielectric spheroid. IEEE Trans. Antenna Propagat. 49, 645-659.
 87. Li L. W., Yeo T. S., Kooi P. S., and Leong M. S. (1998). Microwave specific attenuation by oblate spheroidal raindrops: an exact analysis of TCS's in terms of spheroidal wave functions. Prog. Electromagn. Res. 18, 127-150.
 88. Li L. W., Leong M. S., Yeo T. S., Kooi P. S., and Tan K. Y. (1998). Computations of spheroidal harmonics with complex arguments: A review with an algorithm. Phys. Rev. E 58, 6792-6806.
 89. Li M. and Wilkinson D. (2001). Particle size distribution determination from spectral extinction using evolutionary programming. Chem. Eng. Sci. 56, 3045-3052.
 90. Lienert B. R., Porter J. N., and Sharma S. K. (2001). Repetitive genetic inversion of optical extinction data. Appl. Opt. 40, 3476-3482.

References

91. Lienert B. R., Porter J. N., and Sharma S. K. (2003). Aerosol size distributions from genetic inversion of polar Nephelometer data. *J. Atmos. Ocean. Techn.* 20, 1403-1410.
92. Liu Y., Arnott W. P., and Hallett J. (1998). Anomalous diffraction theory for arbitrarily oriented finite circular cylinder and comparison with exact T-matrix results. *Appl. Opt.* 37, 5019-5030.
93. Liu Y., Arnott W. P., and Hallett J. (1999). Particle size distribution retrieval from multispectral optical depth: Influences of particle nonsphericity and refractive index. *J. Geophys. Res.* 104, 31753–31762.
94. Lock J. A. (1996a). Ray scattering by an arbitrarily oriented spheroid. I. Diffraction and specular reflection. *Appl. Opt.* 35, 500-514.
95. Lock J. A. (1996b). Ray scattering by an arbitrarily oriented spheroid. II. Transmission and cross-polarization effects. *Appl. Opt.* 35, 515-531.
96. Lock J. A. (2003). Role of the tunneling ray in near-critical-angle scattering by a dielectric sphere. *J. Opt. Soc. Am. A* 20, 499-507.
97. Lock J. A. and Adler C. L. (1997). Debye-series analysis of the first order rainbow produced in the scattering of a diagonally incident plane wave by a circular cylinder. *J. Opt. Soc. Am. A* 14, 1316-1328.
98. Lock J. A. and Gouesbet G. (1994). Rigorous justification of the localized approximation to the beam-shape coefficients in generalized Lorenz-Mie theory. I. On-axis beams. *J. Opt. Soc. Am. A* 11, 2503-2515.
99. Maheu B., Gouesbet G., and Gréhan G. (1988). A concise presentation of the generalized Lorenz-Mie theory for arbitrary location of the scatterer in an arbitrary incident profile. *J. Opt.* 19, 59-67.
100. Maheu B., Gréhan G., and Gouesbet G. (1989). Ray localization in Gaussian beams. *Opt. Commun.* 70, 259-262.
101. Marcuse D. (1974). Light scattering from elliptical fibers. *Appl. Opt.* 13, 1903-1905.
102. Markowski G. R. (1987). Improving Twomey's algorithm for inversion of aerosol

References

- measurement data. *Aerosol Sci. Techn.* 7, 127-141.
103. Michelewicz Z. (1996) *Genetic Algorithms+Data Structure=Evolution Programmes*. Springer, Berlin.
104. Mie G. (1908). Beiträge zur optik trüber Medien speziell kolloidaler metallosungen. *Ann. Phys.* 25, 377-452.
105. Möbius W. (1910). Zur Theorie des Regenbogens und ihrer experimentellen Prüfung. *Ann. Phys.* 33, 1493-1558.
106. Naqwi A.A. Liu X-Z, and F. Durst. (1990). Dual-cylindrical wave method for particle sizing. *Part. Part. Syst. Charact.* 7, 45-53.
107. Naqwi A.A. Liu X-Z, and F. Durst. (1992). Evaluation of the dual-cylindrical laser technique for sizing of liquid droplet. *Part. Part. Syst. Charact.* 9, 44-51.
108. Nefedov A. P., Petrov O. F., and Vaulina O. S. (1997). Analysis of particle sizes, concentration, and refractive index in measurement of light transmittance in the forward-scattering-angle range. *Appl. Opt.* 36, 1357-1366.
109. Niemann J. and Weichert R. (1995). Measurement of concentration and particle size distribution of soot particles in flames. *Proc. 4th Int. Congr. Optical Particle Sizing*, Nürnberg, 375-384.
110. Nussenzveig H. M. (1969). High-Frequency Scattering by a transparent sphere. I. Direct Reflection and Transmission. *J. Maths. Phys.* 10, 82-124.
111. Rayleigh L. (1881). "On the electromagnetic theory of light," *Philos. Mag.* 12, 81-101.
112. Ren K. F., Gouesbet G., and Gréhan G. (1998). Integral localized approximation in generalized Lorenz-Mie theory. *Appl. Opt.* 37, 4218-4225.
113. Ren K. F., Gréhan G., and Gouesbet G. (1992). Localized approximation of generalized Lorenz-Mie theory: faster algorithm for computations of beam shape coefficients g_n^m . *Part. Part. Syst. Charact.* 9, 144-150.
114. Ren K. F., Gréhan G., and Gouesbet G. (1994a). Symmetry relations in generalized Lorenz-Mie theory. *J. Opt. Soc. Am. A* 11, 1812-1817.

References

115. Ren K. F., Gréhan G., and Gouesbet G. (1994b). Evaluation of laser-sheet beam shape coefficients in generalized Lorenz-Mie theory by use of a localized approximation. *J. Opt. Soc. Am. A* 11, 2072-2079.
116. Ren K. F., Gréhan G., and Gouesbet G. (1994c). Electromagnetic field expression of the laser sheet and the order of approximation. *J. Opt.* 25, 165-176.
117. Ren K. F. (1995). *Diffusion des Faisceaux Feuille Laser par une Particule Sphérique et Application aux Ecoulements Diphasiques*. Thesis, Université de Rouen, France.
118. Ren K. F., Gréhan G., and Gouesbet G. (1996). Prediction of reverse radiation pressure by generalized Lorenz-Mie theory. *Appl. Opt.* 35, 2702-2710.
119. Ren K., Xu F., Dorey J., and Cai X. (2006). Development of a precise and in situ turbidity measurement system. The 5th International Symposium on Measurement Techniques for Multiphase Flows, Dec. 10-13, Macao, China.
120. Roth N., Anders K., and Frohn A. (1992). Simultaneous measurement of temperature and size of droplets in the micro-metric range. *J. Laser Appl.* 2, 37-42.
121. Schaub S. A., Alexander D. R., and Barton J. P. (1991). Theoretical model for the laser imaging of small aerosols: application to aerosol sizing. *Appl. Opt.* 30, 4777-4784.
122. Schnablegger H. and Glatter O. (1991). Optical sizing of small colloidal particles: an optimized regularization technique. *Appl. Opt.* 30, 4889-4896.
123. Schnablegger H. and Glatter O. (1995). Sizing of colloidal particles with light scattering: corrections for beginning multiple scattering. *Appl. Opt.* 34, 3489- 3501.
124. Secker D. R., Kaye P. H., Greenaway R. S., Hirst E., Bartley D. L., and Videen G. (2000a). Light scattering from deformed droplets and droplets with inclusions. I. Experimental results. *Appl. Opt.* 39, 5023-5030.
125. Secker D. R., Kaye P. H., Greenaway R. S., Hirst E., Bartley D. L., and Videen G. (2000b). Light scattering from deformed droplets and droplets with inclusions. II. Theoretical treatment. *Appl. Opt.* 39, 5031-5039.
126. Secker D. R., Kaye P. H., Greenaway R. S., and Hirst E. (2001). Real-time observation of

References

- the change in light scattering from droplets with increasing deformity. *Opt. Express* 8, 290-295.
127. Shen J., Riebel U., and Guo X. (2005). Measurements of particle-size distribution and concentration by transmission fluctuation spectrometry with temporal correlation. *Opt. Lett.* 30, 2098-2100.
128. Shettle E. P. and Fenn R. W. (1979). Models for the aerosols for the lower atmosphere and the effects of humidity variations on their optical properties. AFGL-TR-79-0214 Environmental Research Papers No. 676.
129. Siegman A. E. (1971). *An Introduction to Lasers and Masers*. McGraw-Hill, New York.
130. Siegman A. E. (1986). *Lasers*. University Science Books, Mill Valley.
131. Stevensen A. F., Heller W., and Wallach M. L. (1961). Theoretical investigations on the light scattering of colloidal spheres. XI. Determination of size distribution curves from spectra of the scattering ratio or from depolarization spectra. *J. Chem. Phys.* 34, 1789-1795.
132. Stratton J. A. (1941). *Electromagnetic Theory*. McGraw-Hill, New York.
133. Su M., Ren K., Gréhan G., Cai X., RozéC., and Girasole T. (2004). The effect of light multiple scattering on particle sizing by using light extinction method. *Acta Opt. Sin.*, 24, 696-699.
134. Swanson N. L., Billard B. D., and Gennaro T. L. (1999). Limits of Optical Transmission Measurements with Application to Particle Sizing Techniques. *Appl. Opt.* 38, 5887-5893.
135. Taylor T. D. and Acrivos A. (1964). On the deformation and drag of a falling viscous drop at low Reynolds number. *J. Fluid Mech.* 18, 466-476.
136. Teorell T. (1931). Photometrische Messung der Konzentration und Dispersität in kolloiden Lösungen. *Kolloid Z.* 54, 58-66.
137. Twomey S. (1979). *Introduction to the Mathematics in Remote Sensing and Indirect Measurement*. Elsevier, New York.
138. Ungut A., Gréhan G., and Gouesbet G. (1981). Comparisons between geometrical optics and Lorenz-Mie Theory. *Appl. Opt.* 20, 2911-2918.

References

139. Uthe E. E. (1982). Particle size evaluations using multiwavelength extinction measurements. *Appl. Opt.* 21, 454-459.
140. van Beeck J. P. A. J. and Riethmuller M.L. (1996). Rainbow phenomena applied to the measurement of droplet size and velocity and to the detection of nonsphericity. *Appl. Opt.* 35, 2259-2266.
141. van Beeck J. P. A. J., Zimmer L., and Riethmuller M. L. (2001). Global rainbow thermometry for mean temperature and size measurement of spray droplets. *Part. Part. Syst. Charact.* 18, 196-204.
142. van de Hulst H. C. (1957). *Light Scattering by Small Particles*. Dover, New York.
143. van Dongen M. E. H., Smolders H. J., Braun C. J. M., Snoeijs C. A. M., and Willems J. F. H. (1994). Spectral light extinction to characterize fast fog formation. *Appl. Opt.* 33, 1980-1988.
144. Vetrano M. R., van Beeck J. P. A. J., and Riethmuller M. L. (2005). Assessment of refractive index gradients by standard rainbow thermometry. *Appl. Opt.* 44, 7275-7281.
145. Walker J. D. (1976). Multiple rainbows from single drops of water and other liquids. *Am. J. Phys.* 44, 421-433.
146. Walters P. T. (1980). Practical applications of inverting spectral turbidity data to provide aerosol size distribution. *Appl. Opt.* 19, 2353-2365.
147. Walters P. T. and Skingley P. C. (1979). An optical instrument for measuring the wetness fraction and droplet size of wet steam flows in LP turbines. *IMEchE Proceedings: Steam Turbines for the 1980's*, London, 337-348.
148. Wang N., Zheng G., and Cai X. (1994). A theoretical and experimental study of total light scattering technique for particle size analysis. *Part. Part. Syst. Charact.* 13, 309-314.
149. Wang N., Wei J., Hong C., and Zhang H. (1996). Influence of refractive index on particle size analysis using the turbidimetric spectrum method. *Part. Part. Syst. Charact.* 13, 238-244.
150. Wessely B. (1999). *Extinktionsmessung von Licht zur Charakterisierung disperser Systeme*.

References

VDI-Verlag, Düsseldorf.

151. Widmann J. F., Yang J. C., Smith T. J., Manzello S. L., and Mulholland G. W. (2003). Measurement of the optical extinction coefficients of postflame soot in the infrared. *Combust. Flame* 134, 119-129.
152. Wilms J., Roth N., Arndt S., and Weigand B. (2004). Determination of the composition of multicomponent droplets by rainbow refractometry. 12th Int. Symp. Application of Laser Techniques to Fluid Mechanics, Lisbon.
153. Wilms J. (2005). *Evaporation of Multicomponent Droplets*. Thesis, Universität Stuttgart, Germany.
154. Wittig S., Zahoranski R. A., and Sakbani K H. (1981). The dispersion quotient technique in submicron particle size analysis. *J. Aerosol Sci.* 12, 183-184.
155. Xu F., Cai X., and Shen J. (2003). Geometrical approximation of light scattering in arbitrary diffraction regime for absorbing particles: application in laser particle sizing. *Acta Opt. Sin.* 12, 1464-1469.
156. Xu F., Cai X., and Ren K. F. (2004a). Geometrical optics approximation of forward scattering by coated particles. *Appl. Opt.* 43, 1870-1879.
157. Xu F., Cai X., Su M., and Ren K. F. (2005). "Inversion of refractive index in particle sizing by multi-spectral light extinction method," *China Powder Sci. and Tech.* 12(3), 1-5.
158. Xu F., Ren K. F., and Cai X. (2006a). Extension of geometrical-optics approximation to on-axis Gaussian beam scattering. I. By a spherical particle. *Appl. Opt.* 45, 4990-4999.
159. Xu F., Cai X., Ren K., and Gréhan G. (2004b). Application of genetic algorithm in particle size analysis by multispectral extinction measurements. *China Particuology* 2, 235-240.
160. Xu F., Ren K. F., Cai X., and Shen J. (2006b). Extension of geometrical-optics approximation to on-axis Gaussian beam scattering. II. By a spheroidal particle with end-on incidence. *Appl. Opt.* 45, 5000-5009.
161. Xu F., Ren K., and Cai X. (2007a). Expansion of arbitrarily oriented, located and shaped beam in spheroidal coordinates. *J. Opt. Soc. Am. A* 24, 109-118.

References

162. Xu F., Ren K., Gouesbet G., Gréhan G., and Cai X. (2007b). Generalized Lorenz-Mie theory for arbitrarily oriented, located and shaped beam scattering by a homogeneous spheroid. *J. Opt. Soc. Am. A* 24, 119-131.
163. Xu F., Ren K., Gouesbet G., Cai X., and Gréhan G. (2007c). Theoretical prediction of radiation pressure force exerted on a spheroid by arbitrarily shaped beam. *Phys. Rev. E* 75, 026613.
164. Xu R. (1996). Particle Size Distribution Analysis Using Light Scattering. in *Liquid and Surface-borne Particle Measurement Handbook*, J.Z. Knapp, T.A. Barber and A. Lieberman, eds. Marcel Dekker, New York, 745-777.
165. Yildiz D., van Beeck J. P. A. J., and Riethmuller M. L. (2002). Global rainbow thermometry applied to a flashing two-phase R134-A jet. in *Proceedings of Eleventh International Symposium on Application of Laser Techniques to Fluid Mechanics*. Instituto Superior Technico, Lisbon, Portugal.
166. Yong Y. and Sebak A. R. (2006). Radiation pattern of aperture coupled prolate hemispheroidal dielectric resonator antenna. *Prog. Electromagn. Res.* 58, 115-133.

Publication List of the Author

International Journals:

1. Xu F., Ren K. F., Gouesbet G., Cai X., and Gréhan G. (2007). Theoretical prediction of radiation pressure force exerted on a spheroid by arbitrarily shaped beam. *Phys. Rev. E* 75, 026613.
2. Xu F., Ren K. F., Gouesbet G., Gréhan G., and Cai X. (2007). Generalized Lorenz-Mie theory for arbitrarily oriented, located and shaped beam scattering by a homogeneous spheroid. *J. Opt. Soc. Am. A* 24, 119-131.
3. Xu F., Ren K. F., and Cai X. (2007). Expansion of arbitrarily oriented, located and shaped beam in spheroidal coordinates. *J. Opt. Soc. Am. A* 24, 109-118.
4. Xu F., Ren K. F., and Cai X. (2006). Extension of geometrical-optics approximation to on-axis Gaussian beam scattering. I. By a spherical particle. *Appl. Opt.* 45, 4990-4999.
5. Xu F., Ren K. F., Cai X., and Shen J. (2006). Extension of geometrical-optics approximation to on-axis Gaussian beam scattering. II. By a spheroidal particle with end-on incidence. *Appl. Opt.* 45, 5000-5009.
6. Shen J., Yu B., Xu Y, Xu F., and Shen J. (2006). Particle sizing by spectral analysis on transmission fluctuations. *Powder Techn.* 166, 91-99.
7. Xu F., Cai X., and Ren K. F. (2004). Geometrical optics approximation of forward scattering by coated particles. *Appl. Opt.* 43, 1870-1879.

National Journals:

1. Xu F., Cai X., Su M., and Ren K. F. (2005). Inversion of refractive index in particle sizing by multi-spectral light extinction method. *China Powder Sci. and Tech.* 12(3), 1-5.
2. Xu F., Cai X., Ren K. F., and Gréhan G. (2004). Application of genetic algorithm in particle size analysis by multispectral extinction measurements. *China Particuology* 2, 235-240 (in English).

3. Xu F., Cai X., Su M., Zhao Z., and Li J. (2004). Study of independent model algorithm for determination of particle size distribution. *Chinese J. Lasers* 31, 223-228.
4. Li J., Ding Y., Xu F., and Cai X. (2004). Influence of layered structure of particle on scattering characteristics and laser particle sizing. *China Powder Sci. and Tech.* 10(2), 1-3.
5. Su M., Cai X., Xu F., Zhang J., and Zhao Z. (2004). The measurement of particle size and concentration in suspensions by ultrasonic attenuation. *Acta Acustica* 29, 440-444.
6. Xu F., Cai X., and Shen J. (2003). Geometrical approximation of light scattering in arbitrary diffraction regime for absorbing particles: application in laser particle sizing. *Acta Opt. Sin.* 12, 1464-1469.
7. Xu F., Cai X., Zhao Z., and Shen J. (2003). Comparison of Mie theory and diffraction theory in laser diffraction particle size analysis. *China Powder Sci. and Tech.* 9(2), 1-6.

International Conferences:

1. Ren K. F., Xu F., Dorey J., and Cai X. (2006). Development of a precise and in situ turbidity measurement system. The 5th International Symposium on Measurement Techniques for Multiphase Flows, 10-13 December, Macao, China.
2. Xu F., Cai X., Ren K. F., Shen J., and Su M. (2004). Application of the geometrical optics approximation in particle size analysis by the forward scattering method. PARTEC, 16-18 March, 2004, Nuremberg, Germany.

National Conferences:

1. Xu F., Cai X., Su M., and Ren K. F. (2005). Inversion of refractive index in particle sizing by multi-spectral light extinction method. 6th national Conference of Particle Measurement Technology, 12-14 April, Jiangxi·Ji'an, China.

Report of Contracts:

1. Ren K. F. and Xu F., Final report of contract EDF-CORIA (2004-2005), Développement d'un logiciel pour la mesure de la vapeur humide, Mode d'emploi du logiciel TURACE, avril 2005.
2. Ren K. F. and Xu F., Final report of contract EDF-CORIA (2005-2006), Etude de la sensibilité et la précision de la mesure de concentration de gouttelettes icronique/submicronique par extinction lumineuse, April 2006.

Software:

1. Xu F. and Ren K. F., TURACE 1.0 - 5.0, developed since 2004 within the framework of the contracts EDF-CORIA 2004-2005 and EDF-CORIA 2005-2006. This software is used for the spectrum acquisition and data processing to obtain the droplet size distribution and wetness of the wet steam by using spectral light extinction method. The newest version of the software up to now, TURACE 5.0, permits to realize online measurement of the particle size distribution and concentration, off-line data analysis, as well as the numerical simulation of the spectral light extinction method.

论文摘要

本文分为理论和实验两部分。理论部分致力于研究均匀椭球颗粒对任意形状、任意位置和任意入射角的波束的散射，发展了互相独立的2种方法：广义米理论和扩展的几何光学方法。实验部分包括光谱消光法在线测量系统的开发及其在湿蒸汽测量中的应用。全文摘要简述如下：

理论研究：

1. 精确理论：系统地解决了椭球形颗粒对任意激光束（有形波束）的散射问题，包括波束在椭球坐标系中的展开，散射场，散射系数，消光系数，辐射压力等物理量的解析解。理论体系的建立主要基于Gouesbet等人自80年代起创立的球形颗粒对有形波束散射的广义米理论和Asano等人70年代创立的椭球平面波散射理论；

2. 近似理论：提出了几何光学描述球和椭球颗粒对有形波束散射的方法，研究了在轴入射的情况下，球和椭球对高斯光束的散射。该方法弥补了精确理论在计算大颗粒散射场方面的缺陷，为几何光学研究非球形颗粒对有形波束的散射奠定了基础。特别地，该方法可用于计算任意形状椭球的彩虹角位置，突破了Moebius于1910年提出的椭球彩虹角近似计算理论中对椭球两轴之比 κ 的限制 ($0.95 \leq \kappa \leq 1.05$)。

实验研究：

开发了基于光谱消光法的颗粒测量系统。为评估测量误差和系统的稳定性，进行了标准颗粒测量和灵敏度测试实验；之后，成功地在法国国家电力公司（EDF）的实验汽轮机上进行了湿蒸汽在线测量。数值模拟和实验结果表明：所开发系统可用于颗粒系统浓度和粒径分布瞬态变化的测量，为相关工业过程检测和控制提供可靠的依据。